Parallel transmission for magnetic resonance imaging of the human brain at ultra high field : specific absorption rate control & flip-angle homogenization

Martijn Anton Hendrik Cloos

UNIVERSITÉ PARIS-SUD XI

ÉCOLE DOCTORALE : *STITS*
Laboratoire de : *NeuroSpin*

DISCIPLINE : *Physique*

THÈSE DE DOCTORAT

soutenue le 17/04/2012

par

Martijn Anton Hendrik CLOOS

Parallel Transmission for Magnetic Resonance Imaging of the Human Brain at Ultra High Field

Specific Absorption Rate Control & Flip-Angle Homogenization

Directeur de thèse :	Denis Le Bihan	Dr. MD.	(Directeur de NeuroSpin)

Composition du jury :

Président du jury :	Luc Darrasse	Dr.	(Directeur de l'IR4M au CNRS)
Rapporteurs:	Cornelis van den Berg	Dr. Ir.	(Directeur de recherche à l'Hôpital de l'Université d'Utrecht)
	Maxim Zaitsev	Dr.	(Directeur de recherche à l'Hôpital de l'Université de Freiburg)
Examinateur :	Hans-Peter Fautz	Dr.	(Ingénieur chercheur à Siemens Healthcare)
Encadrant :	Alexis Amadon	Dr.	(Ingénieur chercheur à NeuroSpin)

date of print: May 15, 2012

Preface

This thesis is submitted in partial fulfillment of the requirements for the Degree of Doctor of Philosophy at University Paris-Sud XI. The results presented herein are based on the author's scientific endeavors performed between February 2009 and January 2012 at NeuroSpin. In the framework of the Franco-German Iseult-INUMAC project, and in anticipation of the whole body 11.7-Tesla magnetic resonance imaging setup, this work focuses on the development of parallel-transmission strategies to maximize the performance of current and future ultra-high field systems. Apart from aspiring to the realization of the above-mentioned goals, the author hopes this writing will assist scientists new to the field of parallel-transmission and that it will help in the continuation of this work at NeuroSpin.

Aknowledgements

I would like to express my appreciation to all those who gave me the possibility to complete this thesis.

I thank Denis Le Bihan, Frank Lethimonnier, and Cyril Poupon for orchestrating the opportunity to work and learn in a great environment such as Neurospin, not only providing the best of tools and excellent colleagues to interact with, but also the freedom to explore my own ideas.

I am grateful to Alexis Amadon and Nicolas Boulant for their continuous support throughout all my scientific endeavors presented in this work. Their attitude towards work was most inspiring and I fondly recall the many discussions we had, the scope of which vastly exceeds the field of MRI. Over the years I learnt to admire Alexis' relaxed attitude and patience, as well as Nicolas' dedication to understand every concept down to the smallest detail. In addition, I would like to thank them both for proofreading my manuscripts including this thesis.

It has been a pleasure interacting with all members at NeuroSpin. Among them, in particular, I thank: Bachir Jarraya (for introducing me to NeuroSpin), Christopher Wiggins (for his efforts to maintain and improve the 7-Tesla system, in addition to inspiring me with his creative thinking), Eric Giacomini and Marie-France Hang (for their support, always at the ready to help troubleshooting and repairing electronics even under the time pressure of a waiting subject), Karl Edler (for the invigorating discussions, and explaining numerous concepts particular to RF-engineering), the new PhD students Aurelien Massire and Alfredo Lopez (who will be continuing the group effort to enhance the multi-transmit capabilities available to the lab).

In addition, I would like to thank Antoine Dael and Michel Luong for allowing me to benefit from the resources available at Institute de Recherche sur les Fondamentales de l' Univers (IRFU). I particularly enjoyed the many discussions about RF-coil design and electromagnetic simulations.

I am thankful to all my colleagues at IRFU with whom I had the pleasure to work. In particular, I would like to thank my fellow PhD student Guillaume Ferrand who dedicated most of his time to the development of the transmit-array coils used throughout this work.

The technical support from the Siemens Healthcare team was especially appreciated. For this I thank: Franz Schmitt, Ulrich Fontius, Hans-Peter Fautz, Philippe Rouffiat, Luc Renou, and Alexandre Vignaud.

Finally, and most importantly, I would like to thank: my brother Peter and sisters Kitty and Jacqueline (whom I admire for setting an example of what could be achieved by hard work and dedicated study), my nephews and nieces (who had to tolerate my near complete absence throughout most of their years), and my parents Anton and Joke, for their unconditional love and support.

Martijn A. H. Cloos

Gometz-la-Ville, France

January 2012

Contents

Résumé

Les hauts champs magnétiques constituent une solution prometteuse dans la poursuite d'une résolution toujours plus fine des images IRM. Alors que la montée du champ statique améliore progressivement le signal RMN (Ocali and Atalar, 1998), elle augmente simultanément la fréquence de Larmor des protons. Si on considère les systèmes cliniques à 3 Tesla, la longueur d'onde RadioFréquence (RF) est déjà comparable aux dimensions transverses du corps humain. En conséquence, lors d'investigations sur les grands organes tels que l'abdomen ou les cuisses, des zones d'ombre et des pertes de contraste faussent l'image (Bernstein et al., 2006). En passant à 7 Tesla, les disparités de répartition spatiale du champ RF sont si fortes que les artefacts de contraste se développent aussi dans des régions plus petites telles que le cerveau humain. Dans la perspective des premiers systèmes à 11.7 Tesla actuellement en cours de réalisation à NeuroSpin et au NIH, il devient crucial de fournir des solutions pour atténuer les non-uniformités de l'excitation des spins. A défaut de quoi, de tels systèmes à très haut

champ ne pourront atteindre leur plein potentiel.

Pour relever ce défi, un système de transmission parallèle (pTx) à 8 canaux a été installé auprès de notre imageur à 7 Tesla. Alors que la plupart des systèmes IRM cliniques n'utilisent qu'un seul canal d'émission, l'extension pTx permet de jouer différentes formes d'impulsions RF de concert sur plusieurs canaux. Si cette méthode offre une grande souplesse dans la conception d'impulsions RF, elle autorise également une pléthore de distributions d'énergie RF dans le corps exposé (Angelone et al., 2006). Les dépôts d'énergie (Taux d'Absorption Spécifique ou TAS) locaux et globaux devant être limités afin d'assurer la sécurité des patients (IEC, 2010), il s'agit de rechercher les formes d'impulsions RF qui permettront d'exciter le motif désiré sans introduire de « points chauds ».

Les degrés de liberté supplémentaires fournis par l'extension pTx peuvent être mis à profit pour orienter la solution RF vers des distributions d'énergie favorables. Dans ce travail de thèse, cette considération est démontrée par l'optimisation itérative d'un ensemble de paramètres

Tikhonov indexés par canal d'émission RF dans le but de supprimer les points chauds (Cloos et al., 2010c). On montre que si cette approche intuitive est robuste et gérable sur le plan computationnel, elle impose en revanche une légère dégradation de la fidélité d'excitation en général. Des méthodes récentes plus élaborées ont été publiées permettant à la solution RF d'être optimisée vis à vis du TAS, tout en conservant un niveau de fidélité fixe (Brunner and Pruessmann, 2010; Lee et al., 2010). Cependant, ces méthodes sont encore limitées à l'approximation des petits angles de bascule de l'aimantation (Pauly and Nishimura, 1989). Compte tenu de la robustesse et de la flexibilité offerte par l'approche du contrôle optimal (Xu et al., 2008), les contraintes de TAS local et global pourraient être complètement intégrées à la conception des impulsions RF même si des Angles de Bascule (AB) élevés sont ciblés.

Au cours de cette thèse, la gestion du TAS local dans la conception d'impulsions RF a été principalement un exercice théorique pour illustrer la flexibilité de l'approche pTx. En effet, jusqu'à présent,

l'application de ces méthodes a été entravée par les systèmes de sécurité RF installés, la phase et l'amplitude transmises n'étant pas surveillées en temps réel sur chaque canal, ce qui oblige à considérer la pire des interférences de champ électrique en chaque instant et en chaque voxel. Même si une approche pratique de l'évaluation en ligne du TAS ainsi surestimé a été mise en œuvre, cette méthode conservatrice ne permet pas d'exploiter les véritables et souhaitables interférences destructives du champ E. Par conséquent, l'optimisation du vrai TAS local ne fournit que des avantages limités dans ce cadre de travail bridé. Cependant, des systèmes de surveillance de TAS plus sophistiqués finiront par rendre possible les bénéfices de la conception d'impulsions sous contrainte de TAS local (Graesslin, 2008; Gagoski et al., 2009). Notre approche conservatrice a néanmoins permis de valider de nouvelles stratégies de conception d'impulsions in-vivo.

La conception d'impulsions RF non-sélectives de type « k_T-points », introduite dans ce travail pour homogénéiser l'AB sur des volumes étendus, est largement testé dans le contexte de la pTx en imagerie

du cerveau humain à 7 Tesla (Cloos et al., 2012). L'idée de principe est de limiter la trajectoire de l'espace-k de transmission (parcourue avec les gradients) à un petit groupe de points autour du centre de cet espace. De cette façon, comme les inhomogénéités RF sont dominées par de basses fréquences spatiales, la limitation des excursions dans l'espace-k garantit qu'aucune énergie n'est gaspillée à des fréquences spatiales élevées d'un faible intérêt pour l'uniformisation de l'AB. De plus le temps requis pour couvrir les quelques k_T-points est minimisé, permettant une faible durée des impulsions simultanées résultantes.

En définitive, le véritable test de la stratégie des k_T-points est démontré par sa capacité à regagner un excellent contraste entre les tissus cérébraux au cours de séquences 3D traditionnelles comme la MP-RAGE (Mugler and Brookeman, 1990). En généralisant la conception d'impulsions RF à des impulsions à grand AB (inversions) grâce à l'approche du contrôle optimal, les impulsions adiabatiques gourmandes en TAS peuvent être remplacées par des impulsions basées sur les k_T-points plus efficaces et moins énergivores, restorant le contraste

attendu entre matière grise et matière blanche partout dans le cerveau. Ainsi ces inversions, rendues possibles par la pTx, améliorent simultanément la qualité d'image, le TAS déposé, et ce avec une durée d'impulsion réduite. Les effets de susceptibilité magnétique, qui augmentent avec le champ statique, peuvent toutefois représenter un défi aux impulsions d'inversion basées sur les k_T-points. Bien qu'on montre que ces effets peuvent être mitigés si on prend en considération les régions touchées dans la conception des impulsions, la qualité du résultat final dépend grandement de la précision avec laquelle la région d'intérêt (ROI) est démarquée. En ce qui concerne les applications en neuro-imagerie, des logiciels dédiés sont disponibles pour extraire le volume du cerveau à partir d'images de qualité. Cependant, quand on définit la ROI pour la conception d'impulsions, de telles images ne sont pas encore disponibles. Ainsi, de tels programmes doivent s'accommoder d'images faiblement contrastées avec une résolution grossière, pour lesquels ils ne sont pas optimisés. Malgré ces

conditions défavorables, on montre qu'il est possible d'automatiser le processus de démarcation de ROI, cependant que des améliorations de robustesse sont encore désirables.

Dans le travail présenté ici, seules des séquences de type Echos de Gradients sont considérées. Pour étendre la portée des k_T-points aux séquences de type Spin-Echo, l'algorithme de conception devrait être généralisé pour inclure les impulsions refocalisantes. Des premiers jalons ont été posés dans ce sens, de sorte à pouvoir incorporer de telles impulsions dans des séquences 3D comme la SPACE (Mugler et al., 2000).

Si on observe plus en détail notre conception d'impulsions RF à grand AB, l'approche de contrôle optimal commence avec une solution initiale basée sur l'approximation des petits angles. Cependant ceci impose des limitations sévères sur la solution optimisée : le minimum local de la fonction de coût trouvé n'est pas garanti proche du minimum global. Par ailleurs, l'inclusion de la trajectoire de l'espace-k comme sous-ensemble de paramètres au sein de l'optimisation fait de

la recherche de la solution optimale un défi encore plus grand. Intuitivement, il semble qu'en améliorant la conception d'impulsions à grand AB, le dépôt d'énergie pourrait être encore plus réduit.

Finalement, l'implémentation de la pTx elle-même est reconsidérée dans cette thèse. Bien que nous ayons pu montrer d'excellents résultats avec une extension à 8 canaux, les coûts et l'expérience technique nécessaires pour exploiter un tel système posent problème pour un usage en routine clinique. Par conséquent plusieurs configurations simplifiées sont envisagées par le biais de la simulation, pour évaluer le potentiel d'une solution hardware à moindre coût avec un nombre réduit de canaux de transmission. De premiers résultats montrent que, au moins dans le régime des petits angles de bascule, deux canaux parallèles (ou mêmes séquentiels) sont suffisants pour homogénéiser l'AB dans le cerveau humain à 7T. Pour le moment, ces résultats sont basés sur des cartes de B_1^+ mesurées in-vivo avec notre système pTx à 8 canaux. Une des étapes suivantes est de réaliser le hardware capable de piloter une antenne à N éléments de transmission en utilisant

seulement 2 voies de transmission. En plus, pour confirmer l'applicabilité de cette approche dans un environnement clinique, ce concept devrait être évalué sur d'autres parties du corps humain et en considérant tous les AB possibles. En particulier, pour chaque application clinique particulière, les limitations en termes de TAS devraient être investiguées pour déterminer si un système à 2 canaux est suffisant ou si davantage de voies sont requises au regard de la fidélité d'excitation désirée.

General Introduction

Medical imaging concerns a wide variety of methods dedicated to aid the diagnostic process and further the understanding of pathological conditions. From the perspective of both patient comfort and clinical performance, in particular when considering delicate anatomical structures with limited regenerative capabilities such as the brain, non-invasive techniques are often preferable. Although neuroplasticity facilitates some structural reorganization to mitigate the impact of lesions (Cao et al., 1994; Buonomano and Merzenich, 1998), recent studies suggest that the vast majority of neurons in the human neocortex are created at a prenatal stage and persists throughout most of each individual's life without replacement (Nowakowski, 2006).

Over the years, several tomography methods have been developed to provide clinically relevant brain images (Abraham, 2011). Among the most well known three-dimensional imaging techniques to date are: Computed Tomography (CT), Positron Emission Tomography (PET) and Magnetic Resonance Imaging (MRI). Although each of the aforementioned techniques has its merits, the first two of them both involve ionizing radiation and offer either limited soft tissue contrast or a relatively coarse resolution. On the contrary, MRI allows images to be resolved down to a sub-millimeter voxel size, while facilitating multiple contrast mechanisms that can be exploited to differentiate between tissues or indicate various pathological conditions. In addition, functional MRI (fMRI) provides cognitive neuro-scientists with a window into the human mind.

Considering the microscopic scale of the laminar and columnar structures in the cortex, there is a strong desire to perform measurements with high spatial and temporal resolution. Although planar multielectrode arrays (Strumwasser, 1958) and later linear multicontact electrodes (Barna et al., 1981) allow neural activation to be measured among neighboring columnar structures or different cortical layers, these invasive techniques are hampered by technical and ethical constraints. Apart from their limited spatial coverage, their tendency to result in glial scar formation limits their clinical applications and precludes them as investigational devices for neuroscience concerning the healthy human brain (Cheung, 2007). What is more, none of these techniques offers the opportunity to provide the anatomical reference necessary to account for inter-subject morphological variability.

Magnetic resonance imaging, on the other hand, facilitates both the acquisition of functional data and the anatomical reference requisite for the averaging or comparison between multiple subjects (Friston et al., 1995; Ardekani et al., 2005). Furthermore, highly-resolved structural brain imaging provides excellent tissue delineation, which has already provided profound insights into the ageing brain (Gur et al., 1991) and the progression of neurodegenerative diseases such as Alzheimer (Silbert et al., 2003) and Huntington's disease (Thieben et al., 2002). Moreover, recent findings support the notion that various pathological conditions result in a regional-dependent deterioration of the cortical ribbon (Dickerson et al., 2009; Kirk et al., 2009). These findings have initiated a demand for high-quality highly-resolved cross-sectional and longitudinal studies focusing on isolated regions, such as the hippocampus (Breyer et al., 2010).

In pursuit of a MRI-based technique to satisfy the above-mentioned needs, ever-higher main magnetic field strengths are explored. In the 11 years since the introduction of the first 7-Tesla MRI system suitable for human imaging, close to fifty such ultra-high-field (UHF) systems, including several 9.4-Tesla systems, have been installed around the world. Combined with recent advances in phased-array-coil technology and sequence development, these UHF systems start to probe spatial resolutions comparable to those of the cytoarchitectonic structures in the brain (Yacoub et al., 2008; Von Economo and Koskinas, 1927). This allows cognitive neuroscientists to investigate the cortical activation with better spatial precision aiding them in their understanding of the processing and computations carried out by individual cortical columns (Grinvald et al., 2000).

However, already at 3-Tesla the radio frequency (RF) wavelength corresponding to the proton Larmor frequency becomes comparable to the dimensions of some imaged human body parts. This results in zones of shade and losses of contrast distributed across the images of large organs such as the abdomen or thighs (Bernstein et al., 2006). When migrating to 7-Tesla, dielectric resonances and RF interferences cause inhomogeneous excitation profiles to develop in the human brain (Yang et al., 2002; Van de Moortele et al.,

2005). Consequently, a sub-optimal signal-to-noise ratio is obtained and a strong bias introduced on the desired contrast, hampering tissue delineation with high confidence. With the first 11.7 Tesla systems now in active development at NeuroSpin and NIH, it becomes increasingly urgent to provide adequate solutions to mitigate these excitation non-uniformities so that these systems can reach their full potential.

Scientific goals addressed in this work

Although there are many technical challenges associated with UHF-MRI, this study focuses on the mitigation of excitation non-uniformities and restoring the desired contrast. Considering the origin of these artifacts (Yang et al., 2002), parallel transmission (pTx) is one of the most promising solutions available to eradicate these undesired effects. Originally proposed by Katscher et al. (2003) and Zhu (2004), pTx utilizes multiple independently driven coil-elements to facilitate relatively short excitation pulses with the flexibility to obtain nearly any excitation pattern. However, there are certain risks inherent in this approach, stemming mainly from the potential occurrence of a highly localized energy deposition in the exposed volume. Therefore, special care must be taken to prevent tissue ablation. In spite of the fact that the relevant parameter is the RF induced temperature rise, for simplicity the specific absorption rate (SAR) is often considered instead. This measure of the energy deposition may then be constrained according to standardized guidelines (IEC, 2010) to provide adequate safety with respect to temperature (Massire et al., 2012).

While various interesting applications benefit from the enhanced degrees of freedom introduced by the pTx-approach (Setsompop et al., 2008a; Schneider et al., 2010; Katscher et al., 2010), the objective of this thesis is the development and demonstration of pTx-based techniques to provide substantial advances towards:

- High quality volumetric human brain imaging in UHF-MRI.
- Specific absorption rate assessment and control.

Overview of this thesis

First the fundamental concepts of MRI are introduced in chapter 1, concluding with the advantages and challenges encountered at UHF. Subsequently, the concepts and techniques particular to the pTx approach are detailed in chapter 2, followed by an overview of the experimental setup (chapter 3) used throughout the succeeding chapters. Because SAR management is essential to perform in-vivo experiments, we present in chapter 4 an progression of SAR evaluation methods that allowed along the course of this thesis to gain latitude in RF pulse design and in MRI exams. The rest of this manuscript is devoted to radio-frequency pulse design. After presenting an original approach to iteratively minimize the local SAR by penalizing different transmit-pathways (chapter 5), a new strategy named "k_T-points" for non-selective excitations achieving excellent flip angle homogenization over the whole brain is demonstrated in chapter 6. Encouraged by the small-tip-angle results and low energy excitations, its application to the large flip-angle regime is investigated by combining it with optimal control theory (chapter 7). Ultimately, and via the progress made in SAR assessment, the method was tested in the MP-RAGE (Mugler and Brookeman, 1990), one of the most commonly used T_1-weighting 3D sequences. The results of in-vivo experiments at 7 Tesla presented in chapter 8 prove the viability of the technique as well as good mitigation of the RF and B_0-field inhomogeneity artifacts for this sequence. Finally in chapter 9, simplifications in the global design of the pTx-implementation are studied to investigate more cost-effective solutions and more manageable SAR scenarios. Chapter 10 concludes this thesis with a summary of the most substantial scientific contributions and a brief outlook on possible future developments.

1 Background

1.1 Nuclear Magnetic Resonance

Most particles have, besides classical properties such as mass and charge, an intrinsic property referred to as spin[1]. This quantum mechanical property endows each of the nucleons with a spin value of $1/2$. Although nuclei can be comprised of multiple nucleons, it turns out that the simplest configuration, the Hydrogen proton, is the most abundant spin $1/2$ nucleus in organic tissues.

When immersed in a static magnetic field (B_0) oriented along the z-axis, the Hamiltonian matrix corresponding to the resulting potential energy is:

$$H = -\frac{\gamma B_0 \hbar}{2}\sigma_z = -\frac{\gamma B_0 \hbar}{2}\begin{pmatrix} 1 & 0 \\ 0 & -1 \end{pmatrix} \tag{1.1}$$

where γ is the gyromagnetic ratio ($\frac{\gamma}{2\pi} = 42.6\ 10^6 Hz\ T^{-1}$), $\hbar$ is Planck's constant divided by 2π, and σ_z is Pauli's spin matrix matching the selected direction of the magnetic field (Griffiths, 1994). The corresponding eigenstates are:

$$\begin{array}{lll} \chi_- & with\ energy: & E_- = -\frac{\gamma B_0 \hbar}{2} \\ \chi_+ & with\ energy: & E_+ = +\frac{\gamma B_0 \hbar}{2} \end{array} \tag{1.2}$$

where χ_- is the lower energy state co-aligned with the main magnetic field, and χ_+ the anti-aligned state. Consequently, this system could interact with a (virtual) photon of energy $\gamma B_0 \hbar$, corresponding to a frequency of:

$$\nu = \frac{E_- - E_+}{2\pi\hbar} = \frac{\gamma B_0}{2\pi}\ , \tag{1.3}$$

which is commonly referred as the proton Larmor frequency[2].

Bloch Equations

Thus far, only a single particle was considered. All biological tissues contain many nuclei of which, in terms of body mass percentage, Hydrogen is the third most abundant in the human body (Zumdahl and Zumdahl, 1999)[3]. The canonical ensemble of such spin $1/2$ nuclei, when at thermal equilibrium immersed in the above-mentioned static magnetic field, yields the following density of magnetization (Schroeder, 1999) :

$$M_0 \hat{e}_z = \frac{\rho\gamma\hbar}{2}\tanh\left(\beta E_+\right)\hat{e}_z \tag{1.4}$$

where ρ is the proton spin-density, $\beta \overset{def}{=} (kT)^{-1}$ is defined as the reciprocal of the Boltzmann's constant times the temperature in Kelvin[4]. When perturbed by an RF-field, the magnetization vector $\mathbf{M} = \{Mx(t), My(t), Mz(t)\}^T$ obays the Bloch equation:

$$\frac{\partial}{\partial t}\mathbf{M} = -\gamma\mathbf{B}\times\mathbf{M} - \begin{pmatrix} 1/T_2 & 0 & 0 \\ 0 & 1/T_2 & 0 \\ 0 & 0 & \frac{1-M_0/M_z}{T_1} \end{pmatrix}\mathbf{M} \tag{1.5}$$

[1] The interpretation of spin is by no means trivial; for those who are interested the author recommends a most intriguing article by Ohanian (1986).

[2] Strictly speaking, real photons do not constitute the dominant energy quanta considered in the context of MRI. It has been suggested that the virtual photons often considered in quantum field theory are more fitting. More background regarding these considerations can be found in (Hoult and Bhakar, 1997).

[3] Oxygen is first followed by Carbon, both of which, in their natural abundant form, have an effective spin of 0.

[4] Most textbooks on NMR emphasize on the first order Taylor expansion: $M_0\hat{e}_z \approx \frac{\rho\gamma^2\hbar^2}{4kT}B_0\hat{e}_z$.

where $B = \{Bx(t), By(t), Bz(t)\}^T$ is the magnetic field which may depend on time and whose static main component remains oriented along the z-axis, T_1 is the longitudinal relaxation time, and T_2 the transverse relaxation time (Bloch, 1946; Wangsness and Bloch, 1953). Instead of describing the magnetization from the perspective of an observer in the laboratory frame of reference, it is often more convenient to consider the transverse and longitudinal magnetization in the frame rotating at the Larmor frequency $\Omega = \gamma B_0$. To this end, the transformation matrix:

$$\mathbf{\Lambda}(\Omega t) = \mathbf{SR}(\Omega t) = \begin{pmatrix} 1 & i & 0 \\ 1 & -i & 0 \\ 0 & 0 & 1 \end{pmatrix} \begin{pmatrix} \cos(\Omega t) & -\sin(\Omega t) & 0 \\ \sin(\Omega t) & \cos(\Omega t) & 0 \\ 0 & 0 & 1 \end{pmatrix} \tag{1.6}$$

can be used to carry the observer into a more convenient frame of reference. Defining $\tilde{\mathbf{M}} = \mathbf{\Lambda}(\Omega t)\mathbf{M} = \left\{M_T(t), \overline{M_T}(t), M_z(t)\right\}^T$ (where $M_T(t) = M_{\tilde{x}}(t) + iM_{\tilde{y}}(t)$, $\overline{M_T}(t) = M_{\tilde{x}}(t) - iM_{\tilde{y}}(t)$, and $M_{\tilde{x}}(t)$ & $M_{\tilde{y}}(t)$ are the Cartesian magnetization components in the rotating frame), $\tilde{\mathbf{B}} = \mathbf{\Lambda}(\Omega t)\mathbf{B} \overset{def}{=} \left\{B_1^+(t), \overline{B_1^+}(t), B_0 + \Delta B_0\right\}^T$ (where, after neglecting the off-resonance components (Hoult, 2000b)[5], $2B_1^+(t) \approx B_{\tilde{x}}(t) + iB_{\tilde{y}}(t)$ and $B_{\tilde{x}}(t)$ & $B_{\tilde{y}}(t)$ are the Cartesian magnetic field components in the rotating frame, and ΔB_0 accounts for localized deviations from the static magnetic field B_0), and exploiting $\widehat{[\mathbf{B}]_\times} = \mathbf{\Lambda}(\Omega t)[\mathbf{B}]_\times \mathbf{\Lambda}^{-1}(\Omega t)$ (where $[\mathbf{B}]_\times$ is a matrix such that $[\mathbf{B}]_\times \mathbf{M} = \mathbf{B} \times \mathbf{M}$ (Jaynes, 1955)), allows Eq. 1.5 to be rewritten as:

$$\frac{\partial}{\partial t}\tilde{\mathbf{M}} = -i\gamma \underbrace{\begin{pmatrix} M_T(t)\Delta B_0 - M_z B_1^+(t) \\ 0 \\ \frac{\overline{M_T}(t)B_1^+(t) - M_T(t)\overline{B_1^+}(t)}{2} \end{pmatrix}}_{\text{"Conventional description"}} + i\gamma \underbrace{\begin{pmatrix} 0 \\ \overline{M_T}(t)\Delta B_0 - M_z(t)\overline{B_1^+}(t) \\ 0 \end{pmatrix}}_{\text{"Conjugate description"}} - \underbrace{\begin{pmatrix} M_T(t)/T_2 \\ \overline{M_T}(t)/T_2 \\ \frac{M_z(t) - M_0}{T_1} \end{pmatrix}}_{\text{Relaxation}}. \tag{1.7}$$

According to these definitions, the first two rows of equation 1.7 both describe the time-evolution of the transverse magnetization. Therefore, traditionaly, the "*Conjugate description*" is disregarded in favor of a more concise expression[6]. Consequently, the co-rotating component of the magnetic field (B_1^+) constitutes that component of the transmit-field suitable to introduce a transverse component (M_T) in to the magnetization vector. In the context of NMR, the flip-angle (FA or θ) is often adopted to express the result of a B_1^+ excitation: $\theta = \gamma B_1^+ \int_0^T f(t)\, dt$, where T is the duration and $f(t)$ is the pulse shape. If the initial state of the magnetization is $M_0\hat{e}_z$, and M_z is the longitudinal component after the excitation, then:

$$\theta = \arccos\left(\frac{M_z}{\|\mathbf{M}\|}\right) . \tag{1.8}$$

T_1 Relaxation

The longitudinal relaxation time T_1 is a tissue-specific characteristic constant related to the time required for the substance in question to (re-)establish its net thermal equilibrium magnetization. This can be seen when considering the immersion of the object into the main magnetic field at t = 0:

$$\frac{\partial}{\partial t}M_z = -\frac{M_z - M_0}{T_1} , \tag{1.9}$$

which has the solution:

$$M_z(t) = M_0\left(1 - e^{-t/T_1}\right) . \tag{1.10}$$

During this process, energy is transferred to the spin-lattice as the population of the eigenstates is changed (Eq. 1.2). This characteristic time constant is inversely proportional to the efficiency at which energy can be dissipated to other nuclei in the lattice.

[5] Hence the factor 1/2 in: $B_1^+(t) \approx \frac{B_{\tilde{x}}(t) + iB_{\tilde{y}}(t)}{2}$.

[6] Note that $\overline{B_1^+}$ should not be confused with B_1^- which is related to the receive sensitivity, i.e., it contains no additional information.

T_2 Relaxation

The transverse relaxation time T_2 is a measure of how long the resonating protons remain coherent, i.e. in phase, following an excitation. Considering a simplified model where only the transverse component is considered:

$$\frac{\partial}{\partial t} M_T = -\frac{M_T}{T_2} \ , \tag{1.11}$$

the following solution is found:

$$M_T\left(t\right) = M_T\left(0\right) e^{-t/T_2} \ , \tag{1.12}$$

where $M_T\left(0\right)$ is the transverse component at $t = 0$. The resulting decay in transverse magnetization is due to magnetic interactions occuring between protons. For example, neighboring protons bound to macromolecules locally change the magnetic field sensed by the free protons. These local field non-uniformities cause the free protons, which constitute the dominant component in the MR signal, to precess at slightly different frequencies. Thus, following an excitation pulse, the protons lose coherence and the net transverse magnetization is gradually lost.

The NMR signal

The previous sections briefly explained how an ensemble of protons immersed in a magnetic field may be excited, and the mechanisms that allow it to relax back to equilibrium. However, in order to exploit this behavior in the framework of NMR, a measurable signal needs to be extracted. To this end, let us consider a Hertzian loop placed close to the sample and prependicular to the transverse plane. Following an ideal 90° excitation, the magnetic moment precesses in the xy-plane (at the Larmor frequency). The rotating magnetic field of the nuclear magnetization induces an electromotive force (EMF) in the loop, much like a bicycle dynamo (Hoult and Bhakar, 1997). Since the induced EMF is proportional to the field produced by the oscillating magnetic moment, a suitable analog-to-digital converter (ADC) may be used to observe the time evolution of the system and facilitate subsequent computerized post-processing. Because the current induced in the Hertzian loop (or a more optimized receive-coil) is directly proportional to the transverse magnetization, the loss of coherence due to T_2^* relaxation will result in the recording of an attenuating signal[7]. This measurement corresponds to what is referred to as the free induction decay (FID) (Hahn, 1950a).

1.2 Magnetic Resonance Imaging

Historic introduction

Originally only published in a PhD thesis, the first transitional steps from NMR to MRI were pioneered by Carr (1952). This was later extended by Lauterbur, P.C. (1973) to produce the first 2D images, followed by the first cross-sectional image of a living mouse (Lauterbur, P.C., 1974). These experiments were still performed using a standard NMR spectrometer with an added field gradient, thus introducing the concept of frequency encoding. In the absence of a magnetic field gradient, the Fourier transform of the FID results in a peak corresponding to the Larmor frequency of the sample (Fig. 1.1**a**). When a linear gradient is applied, multiple frequencies are introduced into the FID dependent on the location of the source. Consequently, the Fourier transform now corresponds to the spatial distribution of the sample along the direction of the field gradient (Fig. 1.1**b**). Although this 1D technique was a milestone in the development of MRI, this first implementation was far from practical. Considering the fixed nature of the field gradient in these experiments, the object under investigation had to be physically rotated to resolve a two-dimensional image.

Much faster imaging techniques involving multiple linear field gradients were pioneered by Kumar et al. (1975); Mansfield and Maudsley (1976); Mansfield (1977). These techniques resemble more closely to what is now common practice, rather than the projection technique originally used by Lauterbur, P.C. (1974). Current clinical MRI systems provide time variable linear magnetic-field gradients in three orthogonal directions (Fig. 1.2) to allow 2D- and 3D-Fourier-transform based spatial encoding techniques.

[7] The measured attenuation corresponds to the time constant T_2^*, which incorporates the loss of coherence due to T_2 relaxation, magnetic susceptibility effects, and imperfections in the external static-field.

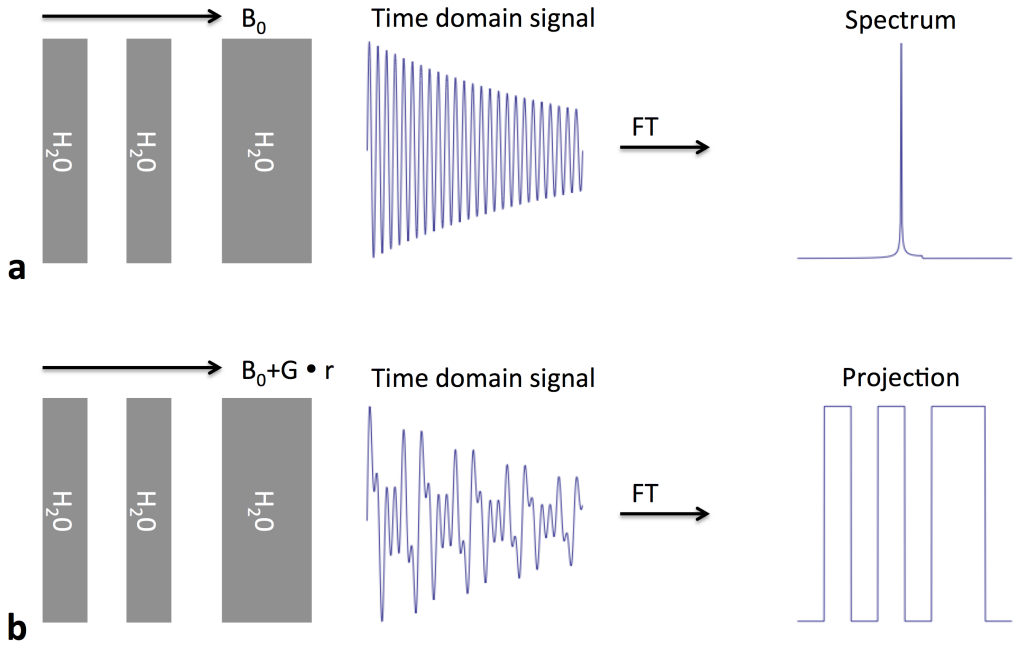

Figure 1.1: Frequency encoding in MRI. **a**: Three compartments filled with water immersed in a static magnetic field B0 result in a FID whose spectrum shows the Larmor frequencies present in the sample, e.g., a single proton peak in this case. **b**: Three compartments filled with water immersed in a linear field gradient on top of a static magnetic field B_0 result in a FID whose spectrum is the projection of the sample along the direction of the linear field gradient.

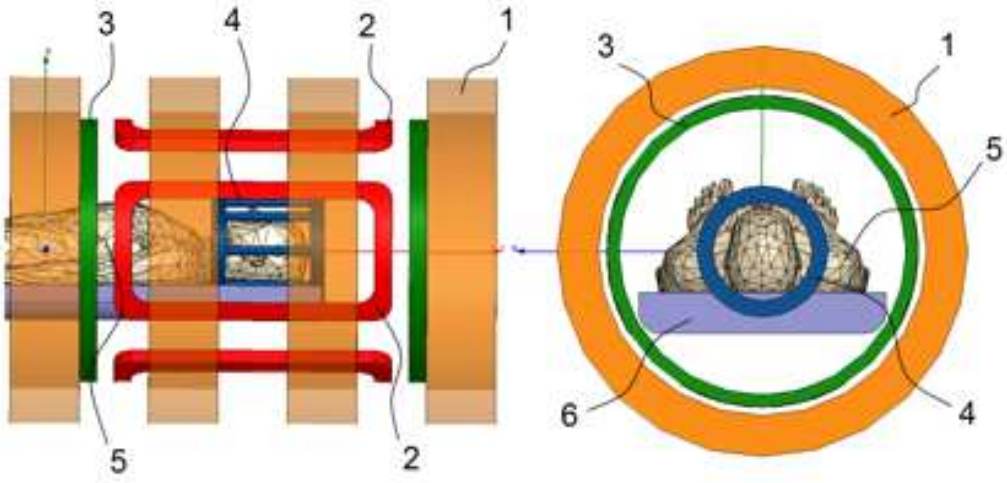

Figure 1.2: Schematic overview of the basic coil configuration in current MRI systems. 1: The main magnet responsible for the static magnetic field in the z-direction (B_0). Nowadays this typically entails a superconducting magnet cooled with liquid helium (Minkoff et al., 1977). 2: Gradient coils used to produce linear field gradients along the x and y direction through the subject (in a limited region of interest). 3: Gradient coils used to produce linear field gradients along the z-axis. 4: Head coil used for RF excitation and NMR signal reception. Many clinical systems are also equipped with a larger RF transmission coil for whole body applications (not shown), comparable in size to the gradient coil diameter. 5: Subject. 6: Patient table.

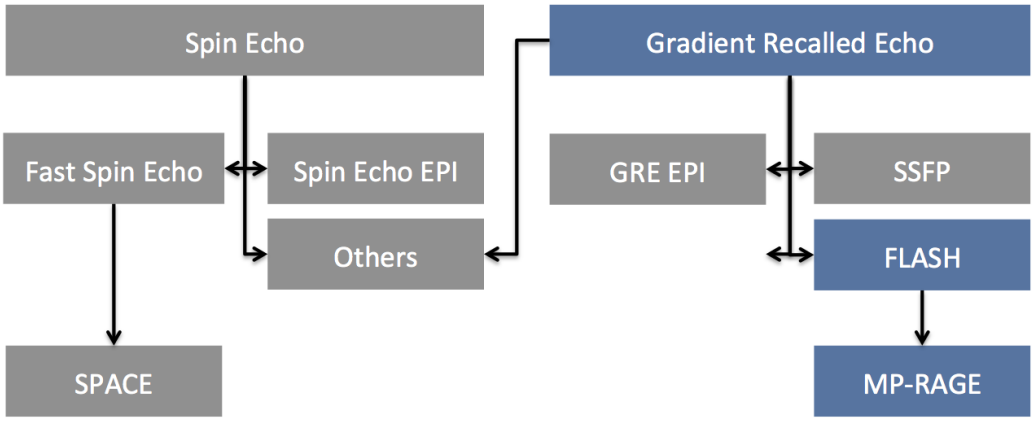

Figure 1.3: Schematic overview of the basic pulse sequences in MRI. Spin Echo (Hahn, 1950b), Fast Spin Echo (Feinberg et al., 1985b), Echo Planar imaging (EPI (Mansfield, 1977)), SPACE (Mugler et al., 2000), Gradient Recalled Echo (GRE), Steady-State Free precession (SSFP (Oppelt, 1986))), Fast Low Angle Shot (FLASH, (Haase et al., 1986)), Magnetization-Prepared RApid Gradient Echo (MP-RAGE, (Mugler and Brookeman, 1990)), Others (Bernstein et al., 2004; Haacke et al., 1999).

Current Imaging Sequences

Over the years, numerous imaging methods have been introduced, commonly referred to as acquisition sequences. Loosely speaking, two classes of sequences exist, the Gradient-Recalled-Echo (GRE) and the Spin-Echo (SE) branches (Fig. 1.3). Stepping over many important advances in the field[8], only those sequences most relevant to the work presented in this thesis will be considered in more detail (Fig. 1.3, Blue). First the GRE is explained in the context of a volumetric acquisition. Then the FLASH sequence is presented in the framework of slice selective excitation. Finally the Magnetization-Prepared RApid Gradient Echo (MP-RAGE) sequence, one of the most commonly used methods to obtain T_1-weighted images of the whole brain, is summarized.

Gradient Echo and 3D imaging

Rather than adopting a fixed field-gradient for frequency encoding, it is often more convenient to consider a field echo. This may be accomplished using two gradient lobes (Fig. 1.4, red & blue). First the prephasing lobe (Fig. 1.4, red) dephases the transverse mechanization such that the subsequent readout lobe with opposite polarity (Fig. 1.4, blue) refocuses the spins to produce the desired echo.

Mathematically, this can be seen as follows: after an excitation, the prephasing gradient introduces a spatial dependence ($\mathbf{r}$) to the precession frequency:

$$\omega\left(\mathbf{r},t\right)=\gamma\left(B_0+\mathbf{G}_{pre}\left(t\right)\cdot\mathbf{r}\right) \tag{1.13}$$

where $\mathbf{G}_{pre}\left(t\right)$ is the gradient waveform during prephasing. Therefore, in the rotating frame of reference, the relative phase accumulated during the prephasing gradient is:

$$\phi_{pre}\left(\mathbf{r},t\right)=\gamma\int_0^t\mathbf{G}_{pre}\left(t\right)\cdot\mathbf{r}\;dt\;. \tag{1.14}$$

Neglecting relaxation effects and assuming a spin density distribution $\rho(\mathbf{r})$, the following expression for the signal just after the prephasing gradient ($t=t_1$) is obtained:

$$S\left(t_1\right)=\gamma\sin\left(\theta\right)\int_{-\infty}^{\infty}\rho\left(\mathbf{r}\right)e^{-i2\pi k_{pre}(\mathbf{r})}\;d^3\mathbf{r} \tag{1.15}$$

[8]For a more complete overview of the different imaging techniques, the reader is directed to one of the numerous textbooks such as (Bernstein et al., 2004; Haacke et al., 1999).

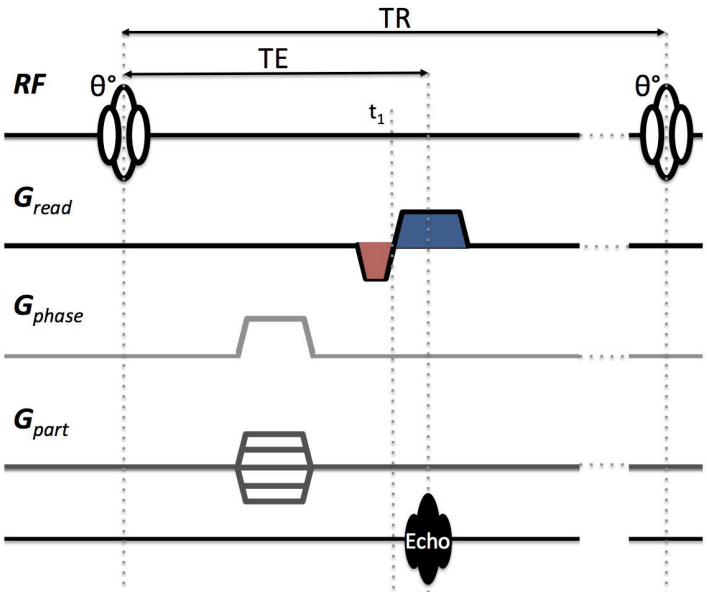

Figure 1.4: Schematic overview of the basic gradient recalled echo sequence. (The prephasing gradients, including phase an partition gradient lobes, may be played at the same time to allow shorter echo times.)

where $k_{pre}(\mathbf{r}) \overset{def}{=} \frac{1}{2\pi}\phi(\mathbf{r}, t_1)$ is the k-space offset, and θ is the flip angle produced by the excitation. In order to obtain the desired echo centered on the readout gradient lobe $G_{read}(t)$, the following conditions need to be satisfied:

$$\int_{t_1}^{TE} G_{read}(t) \cdot \mathbf{r}\ dt = \int_{0}^{t_1} G_{pre}(t) \cdot \mathbf{r}\ dt \tag{1.16}$$

where TE is the time of echo commonly specified relative to the center of the excitation (Fig. 4). Considering a GRE-based sequence, the prephase and imaging gradient lobes may be concatenated into one single continuous gradient waveform (Fig. 1.4).

To illustrate more clearly the Fourier relation between the signal and spatial distribution of the spin density, consider the following substitution:

$$\hat{\rho}(\mathbf{r}) = \rho(\mathbf{r})\, e^{-2\pi i k_{pre}(\mathbf{r})}\ . \tag{1.17}$$

Assuming that the gradient is constant during the readout, we can rewrite the signal corresponding to the echo as:

$$S_{Echo}(t) = \gamma \sin(\theta) \int_{-\infty}^{\infty} \hat{\rho}(\mathbf{r}) e^{-\gamma i \mathbf{G}_{read}\cdot\mathbf{r}t}\ d^3\mathbf{r}\ , \tag{1.18}$$

which simply constitutes a one-dimensional Fourier-transform of the spin density. However, so far, only a projection of the image along the read direction of $\mathbf{G}_{read}$ can be obtained, whereas the other two directions are just integrated. In theory it is possible to reconstruct the entire volume by acquiring multiple projections along different directions. More commonly, the full k-space is acquired with the aid of phase encoding gradients (Fig. 1.4, gray). Including these phase encoding gradient lobes we find:

$$S_{Echo}(t,\ u,\ v) = \gamma \sin(\theta) \int_{-\infty}^{\infty} \rho(\mathbf{r}) e^{-2\pi i k_{pha}(\mathbf{r})u} e^{-2\pi i k_{part}(\mathbf{r})v} e^{-2\pi i k_{pre}(\mathbf{r})} e^{-\gamma i \mathbf{G}_{read}\cdot\mathbf{r}t}\ d^3\mathbf{r} \tag{1.19}$$

where u and v are repetition-dependent scaling factors of the maximum k-space excursions (k_{pha}, k_{part}) orthogonal to one another and the read direction ($\mathbf{G}_{read}$). Iterating this strategy with a time of repetition TR, allows k-space to be sampled uniformly and the spin density distribution $\rho(\mathbf{r})$ to be recovered via the 3D Fourier transform. However, when implemented on a physical scanner, the temporal signal has to be discretized (sampling), and images have to be reconstructed adopting the discrete Fourier transform. Moreover, additional system limitations such as gradient amplitude, gradient slew-rate, and ADC bandwidth have to be taken into account when building an acquisition sequence (Bernstein et al., 2004; Haacke et al., 1999). Nonetheless, the basic principles remain untouched.

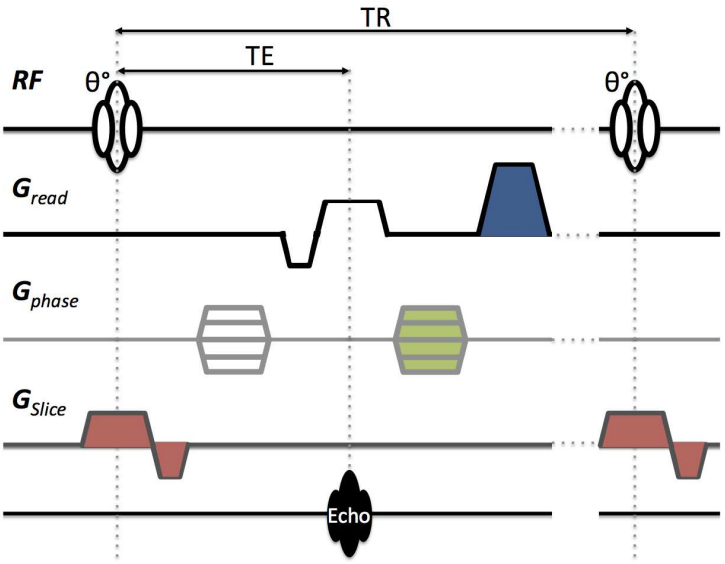

Figure 1.5: Schematic overview of the basic FLASH sequence.

Fast Low Angle Shot and 2D imaging

The basic GRE sequence described in the previous section assumes the initial magnetization prior to any RF pulse is longitudinal in all voxels. This is true if TR is very long compared to the T_2 of the sample. When the TR becomes comparable or shorter than T_2, unwanted stimulated echoes may arise[9], corrupting the final image. This poses a problem for most clinical applications as the total scan time would become too long. To allow high-quality images with a short TR, some modifications to the basic GRE sequence are necessary (Fig. 1.5).

In order to circumvent unwanted stimulated echoes, the spoiler gradient (Fig. 1.5, blue) combined with incremental quadratic RF phase shifts are introduced (Haacke et al., 1999; Bernstein et al., 2004). The idea behind the spoiler gradient is to dephase the spins inside every voxel so that no transverse magnetization is left when restarting RF transmission. Considering a voxel of size $\Delta\mathbf{r}$, the minimum necessary gradient envelope is:

$$\gamma \int \mathbf{G}_{spoil}(t) \cdot \Delta\mathbf{r} = 2\pi \ . \tag{1.20}$$

In addition to the spoiler, re-winder gradient lobes are generally introduced (Fig. 1.5, green). These additional lobes are the exact opposite of the phase encoding gradients, restoring the spin coherence in the phase encode directions[10].

While the spoilers destroy the spin-coherence at the end of the TR, the longitudinal component of the magnetization remains untouched by them. After several repetitions, this leads to a steady state where T_1 relaxation and excitation effects stabilize. Then the following steady state signal equation applies:

$$S(TR,\ TE\ ,\theta) \propto \sin(\theta)\,\rho(\mathbf{r})\,\frac{\left(1-e^{-TR/T_1}\right)}{1-\cos(\theta)\,e^{-TR/T_1}}e^{-TR/T_2^*}\ , \tag{1.21}$$

which allows the Ernst angle corresponding to the maximum signal for a given TR to be calculated via:

$$\theta_E = \arccos\left(e^{-TR/T_1}\right)\ . \tag{1.22}$$

Thus, for very short TR, the maximum signal will be reached for a small FA.

Although this sequence can be used to obtain volumetric images, as described in the previous section, the example depicted in Figure 1.5 illustrates the principles of a 2D image acquisition. The rationale is to limit

[9] Stimulated echoes can occur due to the refocusing of magnetization initialized by RF exposure in earlier repetitions, i.e., magnetization created more than $n \times TR + TE$ $(n \in N)$ ago. These echoes do not necessarily result in an artifact, some sequences use this to their advantage (Oppelt, 1986; Mugler et al., 2000).

[10] Neglecting ΔB_0 and relaxation effects

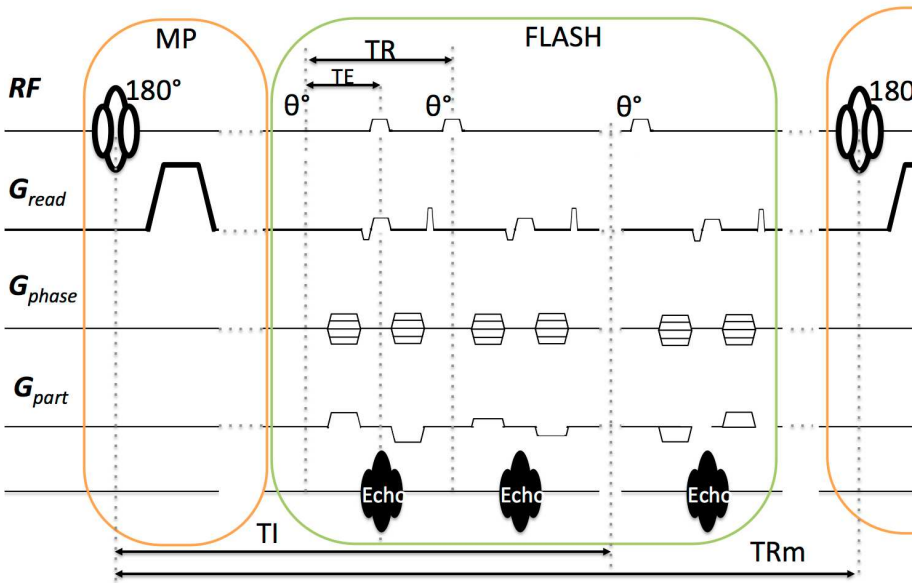

Figure 1.6: Schematic overview of one TRm of the MP-RAGE sequence. Orange: Magnetization preparation (MP) element including a non-selective inversion followed by a spoiler. Green: FLASH-based readout for a single k-space partition. TI: Time of Inversion, defined from the center of the inversion pulse to the center of the k-space partition in the FLASH train. TRm: the time between consecutive inversion pulses.

the excitation to a single slice through the volume, such that the integrated signal in the direction orthogonal to the slice is limited to the slice profile itself. To this end, a gradient of amplitude $\mathbf{G}$ is applied during the RF pulse (Fig. 1.5, red) to introduce a spatial linear dependency in the Larmor frequency distribution (Eq. 1.13). Combined with an RF-pulse of limited bandwidth (BW), a single slice with a finite thickness is excited. However, during this slice selection gradient, the transverse component of the spins is dephased along the slice profile. Therefore, a second gradient lobe with opposite polarity and half the time integral is concatenated after the RF pulse to restore coherence. The slice selection eliminates the necessity for partition encoding and allows the image to be reconstructed with a 2D Fourier transform. Nevertheless, the principle of slice-selective excitation can also be paired with volumetric imaging techniques to acquire a 3D slab through the exposed sample.

Magnetization-Prepared Rapid Gradient Echo

The magnetization-prepared rapid gradient echo sequence (Mugler and Brookeman, 1990), referred to as "MP-RAGE", is among the most commonly employed 3D sequences to obtain T_1-weighted anatomical images of the brain (Fig. 1.6). To this end, an inversion pulse is used (Fig. 1.6, orange) followed by a FLASH train (Fig. 1.6, green) acquiring one partition plane in k-space per repetition time TRm. Careful adjustment of the delay TI between the inversion and the acquisition block, as well as of the usual imaging parameters (θ, TR, TE), allows excellent contrast between gray matter, white matter, and cerebrospinal fluid (Deichmann et al., 2000; Mugler and Brookeman, 1990).

1.3 Specific Absorption Rate

During an MRI exam, radio frequency waves are transmitted to acquire images of a subject. These RF waves deposit energy into the subject, resulting in an increase of temperature that could potentially lead to tissue damage. Therefore committees provide guidelines indicating the maximum allowed energy deposition in human subjects (IEC, 2010). These guidelines refer to the energy deposition as the specific absorption rate (SAR), given by :

$$SAR\left(\mathbf{r}\right) = \frac{1}{T}\frac{\sigma\left(\mathbf{r}\right)}{2\rho\left(\mathbf{r}\right)}\int_0^T \left\|\mathbf{E}\left(\mathbf{r},t\right)\right\|_2^2 \; dt \; . \tag{1.23}$$

This depends on the conductivity $\sigma(\mathbf{r})$, the density $\rho(\mathbf{r})$, the electric field distribution $\mathbf{E}(\mathbf{r},t)$ inside the subject, and the time of integration T during which instantaneous energy deposition is averaged.

The aforementioned guidelines refer to a set of 4 limits considering the maximum allowed energy deposition in the human head. These limits pertain to the global SAR, i.e. the SAR averaged over the entire head, and the local SAR, defined as the SAR averaged over any closed 10-g volume of tissue. The 4 limits provided by the guidelines consider both the T=10-second average and T=6-minute average. The following provides a summary of the SAR limits as defined for diagnostic experiments exposing the human head to an RF field:

- Guideline local SAR #1 — 30 W/kg per 10-s window of integration, averaged over any closed 10-g volume.
- Guideline local SAR #2 — 10 W/kg per 6-min window of integration, averaged over any closed 10-g volume.
- Guideline global SAR #1 — 9.6 W/kg per 10-s window of integration, averaged over the entire head.
- Guideline global SAR #2 — 3.2 W/kg per 6-min window of integration, averaged over the entire head.

In the case of human subjects, the exact fields and anatomical details are often unknown. As a result, the SAR cannot be determined with absolute accuracy for each individual. The conventional method for SAR assessment revolves around simulations based on subject models to estimate the global and peak local SAR. In order to provide secure operation, suitable 10-s and 6-min average power limits are derived for the RF transmitter to ensure compliance with the SAR guidelines.

1.4 Ultra High Field MRI

So far, the impact of the main magnetic field strength has not been considered in detail. However, both the signal-to-noise ratio (SNR) and contrast-to-noise ratio (CNR) are dependent on the field strength. In general the MR signal is proportional to:

$$\begin{aligned} SNR_{3D} &\propto M_0 B_1^- \Delta x \Delta y \Delta z \sqrt{\frac{N_{phase} N_{par} N_{read} N_{avrg}}{BW}} S_{seq}(TR, TE, \theta) \\ SNR_{2D} &\propto M_0 B_1^- \Delta x \Delta y \Delta z \sqrt{\frac{N_{phase} N_{read} N_{avrg}}{BW}} S_{seq}(TR, TE, \theta) \end{aligned} \tag{1.24}$$

where M_0 is the thermal equilibrium magnetization, B_1^- the receive sensitivity (RF magnetic field per unit current in the receive coil), $\Delta x \Delta y \Delta z$ are the spatial dimensions of the voxels, N_{phase} the number of phase encoding steps, N_{part} the number of partition encoding steps, N_{read} the number of samples in the readout, N_{avrg} the number of averages, BW is the readout bandwidth, and $S_{seq}(TR, TE, \theta)$ is a factor dependent on the other sequence parameters[11]. Therefore, once receive coils and sequence parameters are adjusted to their optimal performance, the only options left to improve the MR signal are to increase M_0 or decrease the resolution. When high(er) resolution images are desired, the only remaining possibility is to increase magnetization. Looking back at equation 1.4, the net magnetization can be increased in two ways. Either the temperature of the object under investigation can be reduced, or the magnetic field can be increased[12]. Considering living biological tissues, significantly decreasing the temperature is not possible, leaving only the magnetic field strength as a free parameter.

Advantages

Apart from the direct improvement in SNR due to to an increased M_0, pushing up the main magnetic field strength brings other advantages. Most notably are the enhanced T_2^* contrast, and performance boost when adopting parallel imaging methods (Sodickson and Manning, 1997; Pruessmann et al., 1999; Griswold et al., 2002).

[11] In the case of a FLASH-based acquisition scheme, $S_{seq}(TR, TE, \theta)$ would be Eq. 1.21.
[12] Alternatively, contrast-agents or hyperpolarization may be used to locally increase the signal.

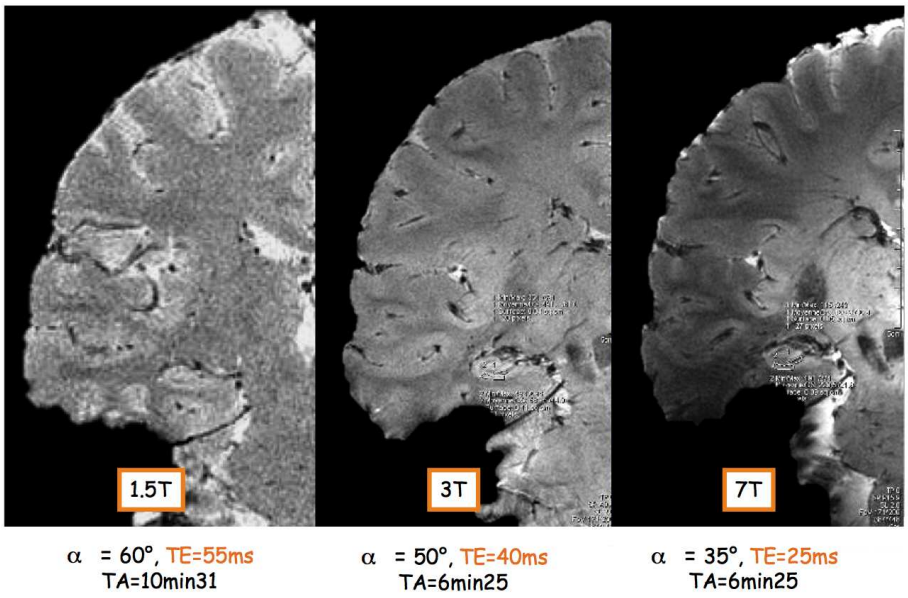

Figure 1.7: Comparison of the contrast-to-noise ratios, comparing gray matter and white matter, obtained at different field strengths on a coronal slice through the brain. All images were acquired with a T_2^*-weighted sequence and quadrature head coil.

Comparing T_2^*-weighted images obtained at different field strengths, a substantial improvement in CNR can be obtained when migrating from 1.5 to 7 Tesla (Fig. 1.7). This increased T_2^* contrast is not only beneficial for structural brain imaging. Considering BOLD-based fMRI for example, the physiological noise contributions (veinous blood) are expected to decrease with increased resolutions while the BOLD signal increases with field strength (Triantafyllou et al., 2005).

In general, it is desirable to constrain the acquisition time to a minimum, not only because of patient comfort and cost efficiency, but also to minimize motion artifacts. As the acquisition time becomes longer, it becomes increasingly difficult for the subject to refrain from moving. Furthermore, even small artifacts due to involuntary movements such as swallowing and breathing can be problematic when considering ultra-high-resolution structural imaging. Moreover, in the context of probing the microscopic scale of the laminar and columnar structures in the cortex, even brain movement due to variations in the cerebral spinal fluid pressure (Maier et al., 1994; Alperin et al., 1996) is a potential source of artifacts.

Parallel imaging (Sodickson and Manning, 1997; Pruessmann et al., 1999; Griswold et al., 2002) is one of the most potent tools available to decrease the acquisition time while maintaining contrast and resolution. This technique exploits the different sensitivity profiles from multiple receive elements (Roemer et al., 1990) to reconstruct an under-sampled image. The key principle behind these methods is the approximate orthogonality between the different receive sensitivities. With increased field strength, therefore shortened RF wavelengths, the receive profiles corresponding to each of the coil elements become more distinct. Consequently, higher acceleration factors can be reached with only limited image quality degradation (Ohliger and Sodickson, 2006).

Challenges

Alongside the opportunities provided by UHF-MRI, several challenges arise. As the external field (B_0) increases in strength, so does the induced magnetization ($\mathbf{M} = \chi_m \mathbf{H}$). Consequently, in those boundary areas where the difference between susceptibility constants (χ_m) is large, such as the air-tissue interface, substantial fluctuations are introduced into the static field observed by the spins. Due to the dependence on the external field, these non-uniformities become more pronounced in UHF-MRI. Although the bulk of these effects can be compensated with the aid of first and second-order shim coils, residual variations typically remain near intracranial cavities. These undesired disparities in the main field not only result in signal loss due to intravoxel dephasing, but also in geometrical distortions originating from the bias introduced in the frequency encoding. Looking back at the comparison shown in Figure 1.7, the appearance of an increasingly

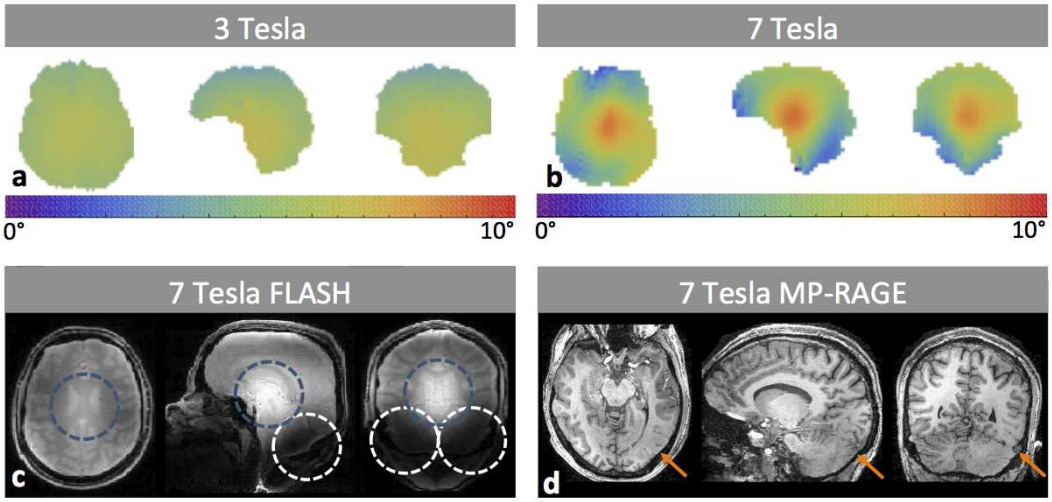

Figure 1.8: Comparison of the excitation uniformity obtained at 3 and 7 Tesla. **a**: Map of the flip-angle distribution obtained at 3 Tesla (Siemens Magnetom Tim Trio). **b**: Map the flip-agle distribution obtained at 7 Tesla (Siemens Magnetom, equipped with a home-built RF-coil). **c**: Image acquired with a FLASH sequence at 7 Tesla (equipped with a quadrature head coil). Blue rings indicate what is commonly referred to as the central brightening effect, whereas the white rings indicate the areas of signal loss. **d**: Image acquired with the MP-RAGE sequence at 7 Tesla (home-built RF-coil). Orange arrows indicate the approximate area where the contrast between gray and white matter is lost.

large cavity can be seen at the bottom of the temporal lobe. Although there may be some subject variability involved, to first order, this deviation is due to increased magnetic susceptibility effects introduced by the inner-ear proximity. Interestingly, the thriving potential of parallel imaging at UHF can in some cases be adopted to mitigate these geometrical distortions and signal losses (Weiger et al., 2002).

Apart from the increased sensitivity to magnetic field susceptibilities, UHF-MRI is hampered by an increased level of excitation non-uniformity (Fig. 1.8**a** & **b**). Although these effects are a hot topic with respect to current endeavors in UHF-MRI, Bottomley and Andrew in 1978 already predicted their impact on MRI. Looking back at the signal equation of the FLASH sequence (Eq. 1.21), it becomes apparent that a spatial variation of the FA will introduce unwanted contrast variations (Fig. 1.8**c**). Although this is just one example, various techniques, such as the MP-RAGE and SPACE sequence, are even more sensitive to these variations (Fig. 1.8**d**).

Besides the increased non-uniformity of the excitation field, Bottomley and Andrew (1978) also predicted an increased energy deposition. Considering the idealized case of a homogeneous spherical phantom centered in a quadrature coil, the following relation between absorbed power (W) and angular-frequency ($\omega = \gamma B_0$) is found (Hoult and Lauterbur, P.C., 1979; Hoult, 2000a):

$$W = \frac{2\pi\omega^2 B_1^{+2} a^5}{15} \tag{1.25}$$

where a is the radius of the sphere. Targeting a certain FA, for a fixed pulse duration the B_1^+-field necessary to yield it is independent of the main magnetic field strength B_0. Although there are some correction terms for the above-presented equation at high frequencies (Hoult, 2000a), it clearly illustrates the quadratic relation between global SAR and B_0. Moreover, depending on the setup at hand, the maximum local-SAR to global-SAR ratio may increase as a result of the reduced wavelength and enhanced interference effects. Consequently, certain SAR-demanding imaging protocols commonly adopted at low field strength need to be reconsidered before application at UHF.

2.1 A k-space analysis of small-tip-angle excitations

Much like the slice-selective excitation introduced in the previous chapter, tailored pairs of RF and gradient waveforms may be employed to selectively excite nearly any excitation pattern. Drawing an analogy to the Fourier encoding used in the imaging processes, the concept of k-space can also be extended to the domain of multi-dimensional RF pulse design (Pauly and Nishimura, 1989). This may be observed by studying the small-tip-angle (STA) approximation, which assumes that the longitudinal magnetization remains constant during RF exposure (Pauly and Nishimura, 1989). Indeed, when targeting a small flip-angle (FA , θ) and assuming an initial magnetization co-aligned with the static magnetic field, the transverse magnetization (M_T) is proportional to $sin(\theta) \approx \theta$, whereas M_z remains approximately constant. Consequently, when targeting a FA $< 30°$ while neglecting both off-resonance and relaxation effects, the cumbersome non-linear Bloch equation (1.7) can be linearized with the following approximation:

$$\frac{\partial}{\partial t} M_T(\mathbf{r}) = -i\gamma \left(\mathbf{G}(t) \cdot \mathbf{r}\ M_T(\mathbf{r}) - B_1^+(t) M_0 \right) \tag{2.1}$$

where $\mathbf{G}(t)$ and $B_1^+(t)$ are the time dependent gradient and RF waveforms, respectively. Solving this differential equation for the final magnetization at time T results in:

$$M_T(\mathbf{r}) = i\gamma M_0 \int_0^T B_1^+(t)\, e^{-i\mathbf{r}\cdot\mathbf{k}(t)}\ dt \tag{2.2}$$

where, similar to the spatial frequency covered during image encoding (1.14), $\mathbf{k}(t)$ is defined as $-\gamma \int_t^T \mathbf{G}(s)\ ds$. Hence the "k-space interpretation" is found, where $\mathbf{k}(t)$ constitutes a trajectory through k-space corresponding to a set of pre-defined gradient waveforms (Pauly and Nishimura, 1989). Then $M_T(\mathbf{r})$ is the Fourier Transform of the RF waveform as long as the latter is played while covering the whole k-space. Given a predefined trajectory, Equation 2.2 immediately suggests a multitude of spatially selective excitations to complement the earlier introduced slice-selective excitations. Considering the target $M_T(\mathbf{r})$ distribution shown in Fig 2.1**a**, the RF-pulse corresponding to this excitation is simply the inverse Fourier transform of $M_T(\mathbf{r})$ (Fig 2.1**b**) as it follows the Cartesian trajectory in Fig. 2.1**c**. This implies the RF-waveform is played in concert with the gradients, resulting in an excitation with the desired characteristics (Fig. 2.1**d**).

Albeit a powerful tool for spatial selection, most potential applications involving multidimensional RF pulses are hampered by hardware limitations. In particular, gradient slew-rate and amplitude constrain the minimal pulse duration due to the wide spatial-spectral range necessary to facilitate an arbitrary excitation profile. Although a judiciously chosen k-space design may be more favorable (Sersa and Macura, 1998), highly

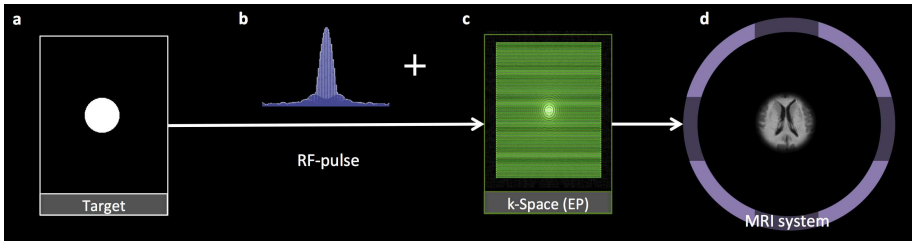

Figure 2.1: Schematic overview of the different steps involved in the design of a single-channel Fourier-based small-tip-angle 2D pulse. **a**: The desired target magnetization. **b**: The RF-waveform corresponding to the Fourier-transform of target excitation pattern. **c**: Echo-planar (EP) k-space trajectory super-imposed in green on top of the Fourier-transform of the target magnetization. **d**: Final image after application of the designed RF + gradient waveforms in a suitable imaging sequence.

selective excitations generally still result in unacceptably long pulse durations. These may not only exceed the repetition time desired in many ultra-fast sequences, but also deteriorate image quality due to off-resonance, relaxation, and magnetization transfer effects during the pulse.

2.2 Transmit-Arrays

As mentioned in the previous chapter, the RF-inhomogeneity increases with field strength, progressively introducing a stronger bias in the acquired images. To mitigate these effects, transmit-arrays consisting of multiple independent coil-elements were introduced (Duensing et al., 1998; Ibrahim et al., 2001a; Adriany et al., 2005). In contrast to the phased arrays used for reception (Roemer et al., 1990), most modern MRI systems are not equipped with multi-transmit capability. Those investigational devices fitted with a multi-transmit extension are typically limited to 8 independent channels, whereas the latest clinical MRI systems already offer up to 128 receive channels (Magnetom Skyra, Siemens Medical Systems, Erlangen Germany).

Circularly polarized eigenmodes

Cylindrically symmetric transmit-coils, such as the popular birdcage (Jin, 1998) and TEM resonator designs (Röschmann, 1987; Vaughan et al., 1994), are driven in their circularly polarized (CP)-mode. At field strengths well below 3 Tesla, the wavelength corresponding to the proton Larmor frequency is sufficiently large to justify the near-field approximation, at least in the human head. Under these conditions, conventional single-transmit-channel MRI systems employ a resonant coupled network of coil rungs to produce the aforementioned CP-mode (Jin, 1998). Similarly, cylindrically symmetric transmit-array coils can synthesize this mode by simply adjusting the relative phase between the transmit-elements according to their azimuthal angle (Adriany et al., 2005; Van de Moortele et al., 2005). However, when migrating to higher field strengths, the near-field approximation becomes less appropriate, causing the RF uniformity deteriorate.

The transmit-array system is not limited to the above-mentioned CP-mode. In addition, a N-channel design supports $N-1$ more orthogonal CP-eigenmodes(Alagappan et al., 2007), each of which may be obtained by shifting the relative phase between the coil-elements by $n \in [2; N]$ times the azimuthal angle. Although driving the transmit-array coil by its CP-eigenmodes has its merits (Alagappan et al., 2007; Setsompop et al., 2008a), the full set spans the same basis as the individually driven coil-elements (Fig. 2.2).

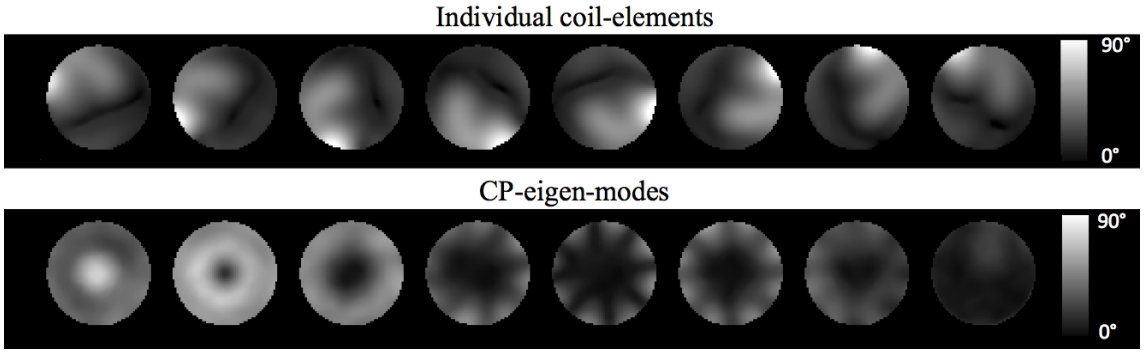

Figure 2.2: Top row: Transmit sensitivity profiles measured at 7 Tesla with the cylindrically symmetric transmit-array-coil shown on the left. Measurements were performed in a 16-cm diameter spherical water phantom. Bottom row: CP eigenmodes synthesized from the main CP mode (at the left), which was found by adjusting the phases of the transmit channels such that their propagation coincides in a constructive interference in the center of the phantom.

RF-shimming

At UHF, none of the CP-eigenmodes demonstrates a homogenous RF-field. Some improvement can be obtained by adjusting the relative phases and amplitudes between the coil-elements (or eigenmodes). When pushed to the extreme, .i.e., using a large number of channels, this method, referred to as RF-shimming, can substantially reduce the RF non-uniformity (Mao et al., 2006). In practice, at 7 Tesla, RF-shimming with a typical 8-channel multi-transmit configuration does not allow the desired level of FA uniformity to be reached throughout the entire human brain (Setsompop et al., 2008a; Cloos et al., 2012). However, recent advances in the field of transmit-array coil design could yield more flexible solutions(Kozlov and Turner, 2011).

B1-mapping

Before an optimized RF-shim configuration can be deduced, the spatially-dependent transmit sensitivities ($B^{+}_{1,n}(\mathbf{r})$) have to be estimated. These transmit-sensitivities quantify the amplitude and relative phase of the co-rotating RF-field produced by each coil-element. Because, on resonance, this field is proportional to the FA (1.21), the $B^{+}_{1,n}$-maps can be deduced from a dedicated MRI measurement. To this end, numerous techniques have been proposed (Hornak et al., 1988; Akoka et al., 1993; Stollberger and Wach, 1996; Cunningham et al., 2006; Yarnykh, 2007). Although B1-mapping sequence development is still an active field of research, the actual flip-angle imaging (AFI) sequence (Yarnykh, 2007), including various improvements proposed by Amadon and Boulant (2008), Boulant et al. (2010a) and Nehrke (2009), is currently among the most popular methods. Due to its steady-state implementation, short repetition times are feasible without the need for a SAR intensive reset pulse. Nevertheless, the AFI sequence applied to transmit-arrays is still relatively time-consuming and SAR-demanding. Considering that these calibrations have to be repeated for each subject before clinically relevant measurements can be started, various faster yet less accurate methods have been proposed (Van De Moortele et al., 2007; Fautz et al., 2008; Chung et al., 2010; Amadon et al., 2010; Cloos et al., 2011a; Amadon et al., 2012).

In a transmit-array, regions far away from the transmitting element under investigation are usually dominated by noise. To counteract this problem, Brunner and Pruessmann (2008) & Nehrke and Bornert (2010) proposed the matrix-based field mapping approach. This procedure combines the transmit-channels in different linear combinations, allowing the transmit-sensitivities corresponding to the individual transmit-channels to be retrieved after post-processing. To this end, typically the CP-mode is considered as a "reference", which is perturbed by cyclically adding π to the phase on each one of the channels. The advantage of this method is that the peak power per channel can be reduced while simultaneously obtaining a more favorable signal-to-noise distribution[1].

2.3 Transmit-Sense

Similar to the way parallel imaging allows the acquisition process to be accelerated, parallel-transmission (pTx) can be employed to reduce the duration of multi-dimensional RF pulses. The imaging SENSE method (Pruessmann et al., 1999) takes advantage of the distinct receive-sensitivity profiles of the coil-elements to reconstruct an un-aliased image from a reduced k-space acquisition (Fig. 2.3). In the same manner, Transmit-SENSE (Katscher et al., 2003; Zhu, 2004) allows a desired target excitation to be reached with a reduced k-space sampling during RF transmission (Fig. 2.4). Consequently, significantly shorter excitations can be designed while maintaining the desired excitation fidelity (Katscher et al., 2003; Zhu, 2004; Grissom et al., 2006). This enables multidimensional RF-pulses to be included in fast sequences with short repetition times, while simultaneously reducing the impact of relaxation and off-resonance effects during the RF pulse.

Based on the principles proposed by Pauly and Nishimura (1989), multidimensional RF pulse design was first formulated in the frequency domain (Katscher et al., 2003), and later in the spatial domain considering EP trajectories only (Zhu, 2004). Currently, the most popular method is the spatial domain method proposed by Grissom et al. (2006), which permits k-space trajectories of arbitrary shape and accounts for the measured off-resonance effects. This method is summarized in the Theory section of chapter 5 where we simultaneously introduce some minor modifications to improve the controllability of the RF power deposition.

[1] This method can be combined with any of the above-mentioned sequences.

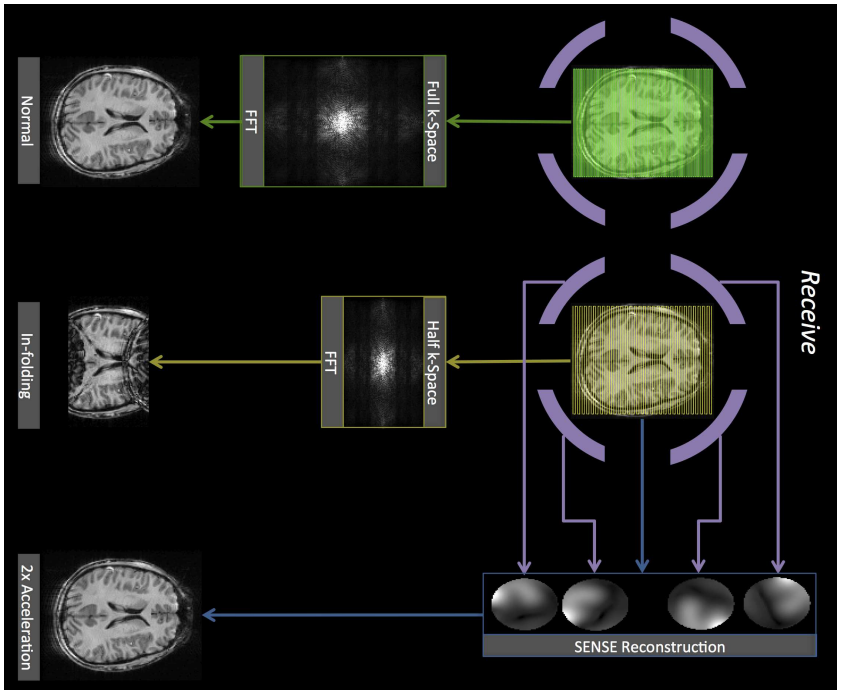

Figure 2.3: Schematic overview of 3 imaging strategies, each one indicated with arrows of a different color. Green: the standard reconstruction method (sum of squares) sampling the full k-space. Yellow: sum-of-squares reconstruction applied to a 2x under-sampled acquisition, resulting in an aliased image. Blue: parallel imaging (SENSE), using the receive sensitivities (purple) corresponding to the different coil-elements, applied to a 2x under-sampled acquisition.

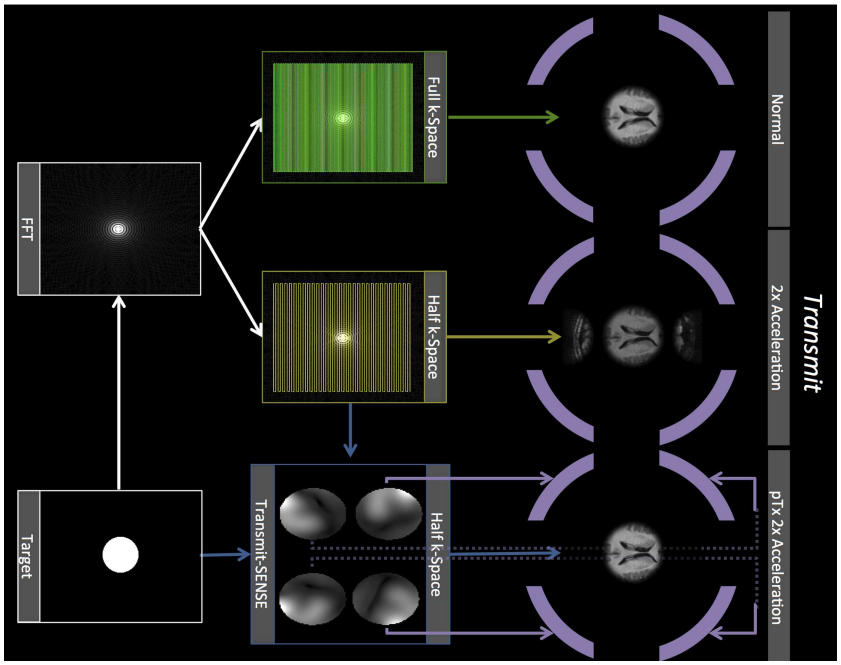

Figure 2.4: Schematic overview of 3 transmission strategies, each one indicated with arrows of a different color. Green: the standard single-channel-tailored RF-excitation as described in section 1 of this chapter. Yellow: the effect of under-sampling k-space by a factor 2 during transmission. Purple: adopting parallel transmission, taking into account the transmit-sensitivity of each coil-element, to produce the same target magnetization while under-sampling k-space by a factor 2.

Trajectories through k-space

Apart from the EP (Fig. 2.4) and 2D-Spiral trajectory (Fig. 2.5**a**), several other interesting designs have been published (Sersa and Macura, 1998; Saekho et al., 2005, 2006; Schneider et al., 2010; Cloos et al., 2012). Each of these techniques addresses a different goal, ranging from slice-selective RF non-uniformity mitigation to selectively exciting an arbitrarily shaped three-dimensional sub-volume.

Among the above-mentioned methods, the "fast-kz" trajectory (Saekho et al., 2006) is probably studied most extensively (Yip et al., 2006; Setsompop et al., 2006, 2008a; Zelinski et al., 2008d,c; Jankiewicz et al., 2010; Ma et al., 2010). The sparse design of this trajectory allows slice-selective uniform excitations with relatively short pulse durations. The key principle of this method resides in the combination of a dense k-space sampling along the slice direction interleaved with a few short gradient blips orthogonal to this direction. When viewed as a path through k-space, the fast-kz trajectory resembles a set of spokes (Fig. 2.5**b**), hence their nickname "spokes". Due to the fixed bandwidth necessary to assure the desired slice profile, the RF sub-pulses played in concert with each spoke are generally of a fixed duration. Consequently, in order to minimize the pulse duration, a sparse selection of optimally chosen spoke locations is desired (Yip et al., 2006; Zelinski et al., 2008d; Ma et al., 2010).

Recently, thanks to pTx enabled k-space acceleration, there has been some renewed interest in multidimensional RF pulse design dedicated to volumetric imaging. Designs that selectively excite an inner-volume are explored to facilitate un-aliased "zoomed" MRI (Feinberg et al., 1985a). Instead of a sparse k-space distribution, the 3D-selectivity necessitates sampling an extensive portion of 3D k-space by adopting accelerated stacks of 2D-spirals (Saekho et al., 2005) or 3D-spirals as proposed by Schneider et al. (2010) and Vahedipour et al. (2010) (Fig. 2.5**c**).

Finally, non-selective uniform excitations can benefit from the multidimensional tailored RF pulse design approach by only exploring a few locations in k-space (Fig. 2.5**d**). This is a novel strategy original to the work presented here and will be the topic of Chapter 6.

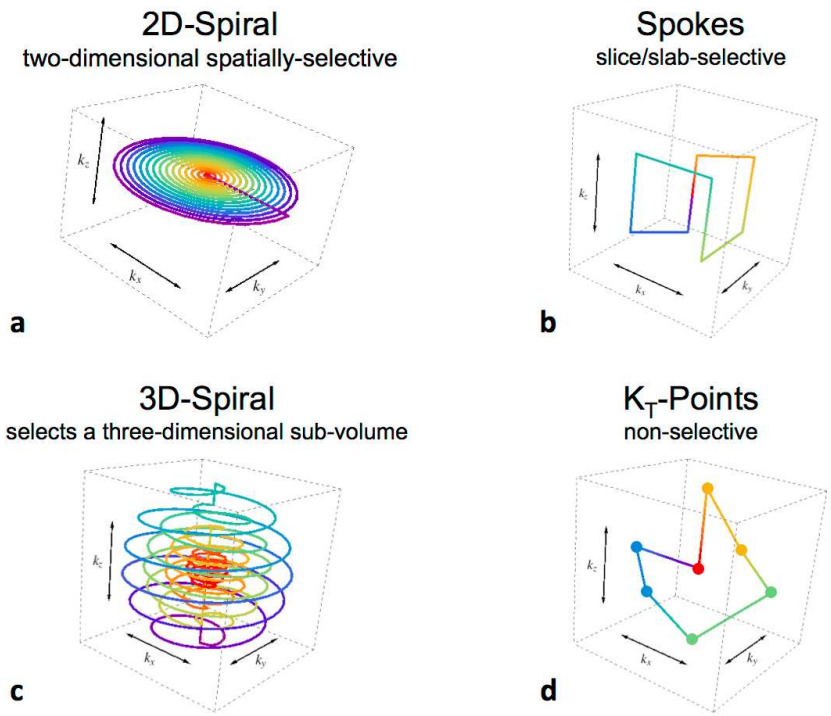

Figure 2.5: Different k-space trajectories considered for pTx applications, each one addressing a different goal. 2D-Spiral: 2-dimensionnal excitation pattern (**a**), Spokes: uniform slice (**b**), 3D-spiral: inner-volume selection (**c**), k_T-points: uniform non-selective excitation (**d**).

Magnitude-least-squares optimization

The spatial domain method as originally formulated by Grissom et al. (2006), summarized in the theory section of chapter 5, not only considerers a predefined $|M_T(\mathbf{r})|$ but also a spatial phase target $Arg(M_T(\mathbf{r}))$. Because the associated optimization method is convex, the global optimum can be approximated directly (Yip et al., 2005; Bazaraa et al., 1993). But selecting an alternative target phase distribution results in a different RF-solution. Considering that, in many cases, the quantity of interest is limited to the magnitude only (Katscher et al., 2007), the optimal solution among all possible phase distributions is desired[2]. To this end, the variable exchange method was introduced (Kassakian, 2006; Setsompop et al., 2008c). This method iteratively relaxes the target phase to the previously obtained phase pattern. In general, this magnitude-least-squares optimization procedure greatly reduces the RF power while enhancing the excitation fidelity (Chapter 5). Yet selecting an alternative initial target phase distribution may still result in a different RF-pulse, whose performance may vary significantly. In particular, some of the initial targets may not work well at all. Therefore, the initial phase distribution has to be selected with some care. Although not necessarily the optimal solution, selecting the phase distribution corresponding to the CP-mode as an initial target generally performs well (Kerr et al., 2007).

Specific Absorption Rate Considerations

Conventional MRI systems (without parallel transmission) evaluate the SAR based on the anticipated forward or transmitted power. This assessment typically relies on a single simulation of the RF coil in use, loaded with a human model exposed to a CP mode. This leads to a fixed scaling factor between the transmitted power and the maximum local/global SAR, which is tabulated on the console so the system can validate the compliance with a set of pre-defined limits such as those summarized in section 1.3 (IEC, 2010). When the proposed acquisition is expected to exceed these SAR limits, the system will prevent the user from starting the measurement. Otherwise, the imaging process is started during which both the 10-s and 6-min-averaged transmitted power is monitored to ensure that the RF-power remains within the appropriate limits. In the event that any of these power limits is exceeded, the acquisition is terminated.

Introducing a pTx-extension complicates the SAR evaluation due to the multiplicity of interference scenarios that can occur between the fields produced by the different transmit-channels playing in concert. For a given set of RF-sources in the array, the combination of incident amplitudes and phases can vary over time depending on the pulse design. Consequently, a generalized version of the single-channel SAR equation 1.23 must be considered:

$$SAR\left(\mathbf{r}\right) = \frac{1}{T}\frac{\sigma\left(\mathbf{r}\right)}{\rho\left(\mathbf{r}\right)}\int_0^T \left\| \sum_{n=1}^{N} \alpha_n\left(t\right)\mathbf{E}_n\left(\mathbf{r}\right) \right\|_2^2 dt \ , \tag{2.3}$$

which now includes a summation over the electric field distributions produced by the N RF sources. For a given pTx excitation pulse, i.e. a combination of complex coefficients $\alpha_n(t)$, the ratio between peak local and global SAR can be quite high (Collins et al., 2007). Therefore, in contrast to the conventional systems, it is no longer viable to derive the local and global SAR from a concise set of parameters (Mao et al., 2007). Nonetheless, based on the maximum ratio between peak local and global SAR, a conservative generalization of the conventional RF safety method is possible (Collins et al., 2007). However, this results in a large overestimation of the actual SAR, severely restricting pTx applications. To remedy this situation, equation 2.3 has to be evaluated for every RF pulse scenario ($\alpha_n(t)$), and the results compared to the guidelines. Only those acquisitions that are in compliance with the RF safety limits should be allowed by the system.

Only predicting the SAR before the measurement is not sufficient to fully guarantee patient safety. Without validating the implemented RF waveforms, the actual interference patterns may deviate from the anticipated. This not only involves the amplitude but also the relative phase, which precludes simply limiting the transmitted power, unless extra safety margins are considered. Although under certain conditions, it is still possible to use a set of dedicated time-averaged power-monitors, as will be detailed in chapter 4, deviations from the anticipated RF-wavefoms can result in substantially different SAR distribution. Therefore, ideally, the actual current-vectors in each coil-element (associated with $\alpha_n(t)$ should be monitored and validated in real-time (Graesslin, 2008; Graesslin et al., 2009; Gagoski et al., 2009) or enforced via Cartesian feedback

[2]It may also be desirable to enforce a certain level of smoothness on the phase distribution to prevent intra-voxel dephasing.

(Hoult et al., 2004; Zanchi et al., 2011)[3]. The setup currently available at NeuroSpin is detailed in the next chapter.

[3]When adopting Cartesian feedback, additional safety systems may be necessary to make sure the subject has not moved excessively (Boulant et al., 2010b).

3 Experimental Setup

3.1 Introduction

All experimental results presented in the subsequent chapters were obtained with the Siemens Magnetom 7 Tesla MRI system (Siemens Medical System, Erlangen, Germany) located at NeuroSpin. This system was built around an unshielded 90-cm-diameter-bore superconducting magnet (Magnex scientific, Oxford, England). The entire setup was enclosed in a Faraday cage to minimize RF noise from the outside and a 500-ton steel room to suppress stray fields outside the confines of the magnet room. Each of the subsequent sections provides details concerning the MR components most relevant to the work presented in the succeeding chapters.

3.2 Gradient & Shim Coils

Currently, the above-mentioned MRI system is equipped with two complete gradient sets, a whole-body gradient system (Siemens) and a head-only gradient insert (AC84, Siemens). The first closely resembles what is typically available on a high-end clinical MR system (slew-rate 200 T/m/s, max amplitude 45 mT/m). However, for economical reasons, this whole-body gradient is not operational at NeuroSpin for imaging purposes. Nevertheless, it can be used in static mode for shimming.

The gradient insert, on the other hand, can reach higher slew-rates (400 T/m/s) and larger gradient amplitudes (80 mT/m)[1] . However, due to its asymmetric design and smaller diameter (40 cm), gradient linearity is limited to a head sized elliptical volume oriented along the main axis of the magnet. Bearing in mind NeuroSpin's exclusive focus on brain imaging and particular interest in diffusion MRI, the benefits provided by the head gradient insert are generally considered to outweigh the constraints imposed by the restricted inner radius. However, with such a configuration, care needs to be taken not to introduce parasitic excitations (Robitaille and Berliner, 2006). Particularly at ultra high field, where the loaded magnet bore acts somewhat as a waveguide (Brunner et al., 2009), most head-only RF-coils demonstrate an increased sensitivity in the shoulder and chest regions. Due to the relatively small dimensions of the gradient insert and its dropping spatial encoding capacity beyond the above-mentioned ellipse, signal arising from these areas are aliased into the region of interest (Fig. 3.1**a**).

To mitigate these "third-arm" artifacts, the shim coils from the body gradient set can be utilized to dephase the signal originating from the shoulder regions (Wiggins et al., 2010). This technique, referred to as the double-shim method, applies opposing currents on the second order Z-shim coils of both gradient sets, effectively spoiling the signal arising from the shoulder regions (Fig. 3.1**b**). Nonetheless, depending on the sequence parameters, residual infolding into the brain stem area may persist. Although most prominent when using rapid non-selective sequences (such as MP-RAGE: Mugler and Brookeman (1990)), non-selective B_1^+-mapping techniques such as the AFI (Yarnykh, 2007) may also be affected. The later in particular was used extensively throughout this work, to provide the necessary transmit-calibration measurements required for the design of subject-specific excitations. Therefore, throughout the remainder of this work, the double-shim approach was adopted for all in-vivo experiments.

3.3 Radio-Frequency Chain

In contrast to current clinical MR systems, typically equipped with only a single transmit-channel, the 7-Tesla system at NeuroSpin has been equipped with a pTx-extension comprised of eight independent RF-pathways (Siemens). For later reference, a brief description of the architecture involved is provided here (Fig. 3.2**a**).

[1] In the context of this work, the slew-rate was limited to 333 $Tm^{-1}s^{-1}$ and the maximum gradient amplitude was constrained to 50 $mT\ m^{-1}$.

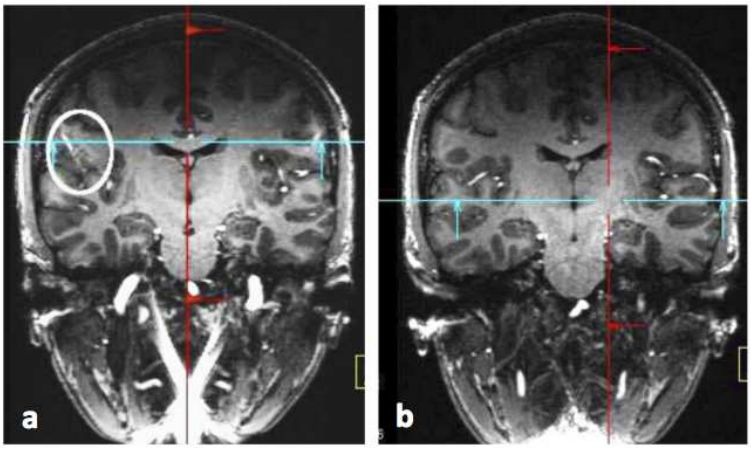

Figure 3.1: Coronal view from 3D MP-RAGE. **a**: The "V"-shaped signal artifact aliased from the neck region, extending through the brain (circled). **b**: Image acquired on same volunteer (without repositioning), but with opposing currents set in the body and head gradient shim coils.

Eight independent modulators are each attached to their own power amplifier, providing up to 1-kW peak power apiece (Dressler, Fort Collins, USA). Via a directional coupler, the forward power coming from each amplifier is monitored in real-time, allowing the peak, 10-s, and 6-min averaged power to be constrained (power monitors for channels 1 through 7 are located in the service room, whereas the monitor for channel 8 is located inside the scanner). In the event that one of the pre-specified limits is exceeded, the acquisition is terminated. However, it should be noted that currently, it remains the research institution's responsibility to derive the appropriate time-averaged power limits such that compliance with the SAR guidelines is ensured (see also Sections 1.3, 2.3 and Chapter 4). To protect the amplifiers, the reflected and coupled energy is dissipated in a dedicated set of circulators (Fig. 3.2**b**). Furthermore, these prevent unwanted interference effects that could arise via mutual coupling and subsequent reflection into the forward path (Fig. 3.2**c**). Although so called loop-back test were performed to evaluate the stability of the RF-waveform under different conditions, no detailed test were performed to evaluate potential additional power losses in the cables leading up to the coil due to the standing wave ratio.

3.4 Transmit-Array Coil

For pTx, a transmit-array coil is necessary. To this end, a home-made transceiver-array head coil was developed (Fig. 3.3) in collaboration with Institut de Recherche des lois Fondamentales de l'Univers[2] (Ferrand et al., 2010). The coil itself consists of 8 stripline dipoles distributed every 42.5° on a cylindrical surface of 27.6-cm diameter, leaving an 8.2-cm-wide window in front of the subject's eyes. The housing for the dipoles is made out of two polyoxymethylene half cylinders milled to provide close-fitting slots to hold each of the coil-elements.

The dipoles themselves consist of a 280 x 28 x 2 mm^3 high purity solid copper strip (Fig. 3.3e.103). Each of them is fed via a BALUN (BALanced UNbalanced transformer) that acts like an electrical transformer between the coaxial feedline and the symmetrical central feeding points (Fig. 3.3e.130). Air is used as the dielectric between ground plane (Fig. 3.3e.111) and dipole (spacing 3.2 mm). To first order, each element was tuned using capacitive disks (Fig. 3.3e C1 & C2); subsequent fine-tuning is provided via the pi-circuit incorporated into each element (Fig. 3.3e.150). At the end of the coil, a semi-circular polyoxymethylene "crown" is attached (Fig. 3.4) to provide the enclosure for the in-house-developed transmit/receive switches (-56-dB isolation between transmit and receive paths) and preamplifier circuits (23-dB amplification, 1.1-dB noise figure)[3]. To provide the necessary shielding, the inner surface of the crown was laminated with copper

[2]Design and implementation by Michel Luong and Guillaume Ferrand at Commissariat à l'Energie Atomique, Direction des Sciences de la Matière, Institut de Recherche des lois Fondamentales de l'Univers, Service des Accélérateurs, de la Cryogénie et du Magnétisme.

[3]Design and implementation by Marie-France Hang and Eric Giacomini at Commissariat à l'Energie Atomique, Direction des Sciences du Vivant, Institute d' Imagerie Biomédicale, NeuroSpin, Laboratoire de Résonance Magnétique Nucléaire.

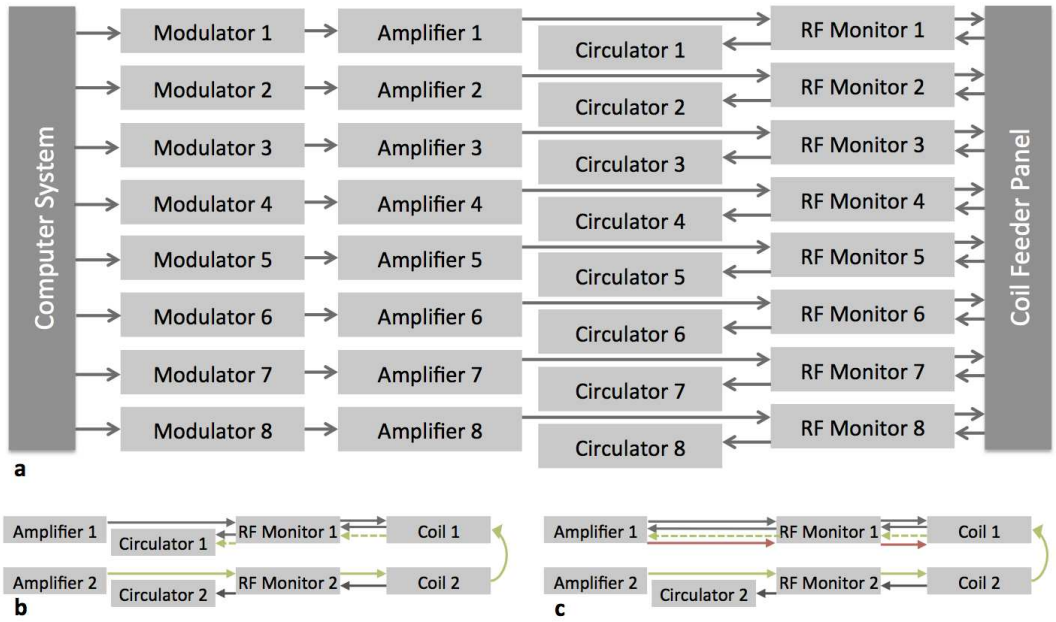

Figure 3.2: Schematic representation of the RF-chain corresponding to the 8-channel pTx-extension. **a**: Each of the individual transmit-channels is provided with its own modulator (this includes the mixing to the 297MHz carrier frequency) and amplifier. The forward power sent by each of the amplifiers is monitored (peak, 10-sec-, and 6-min-averaged power). In case any of the associated pre-defined limits is exceeded, the acquisition is terminated. The power monitors for channels 1 through 7 are located in the service room, whereas the monitor for channel 8 is located inside the scanner. **b**: Reflected power (black arrows to the left) and contributions from mutual coupling between coil-elements (green arrows) are dissipated in circulators. **c**: Illustration depicting currents introduced via coupling between the coil-elements (green arrow) reflecting back into the forward RF-chain (red arrow).

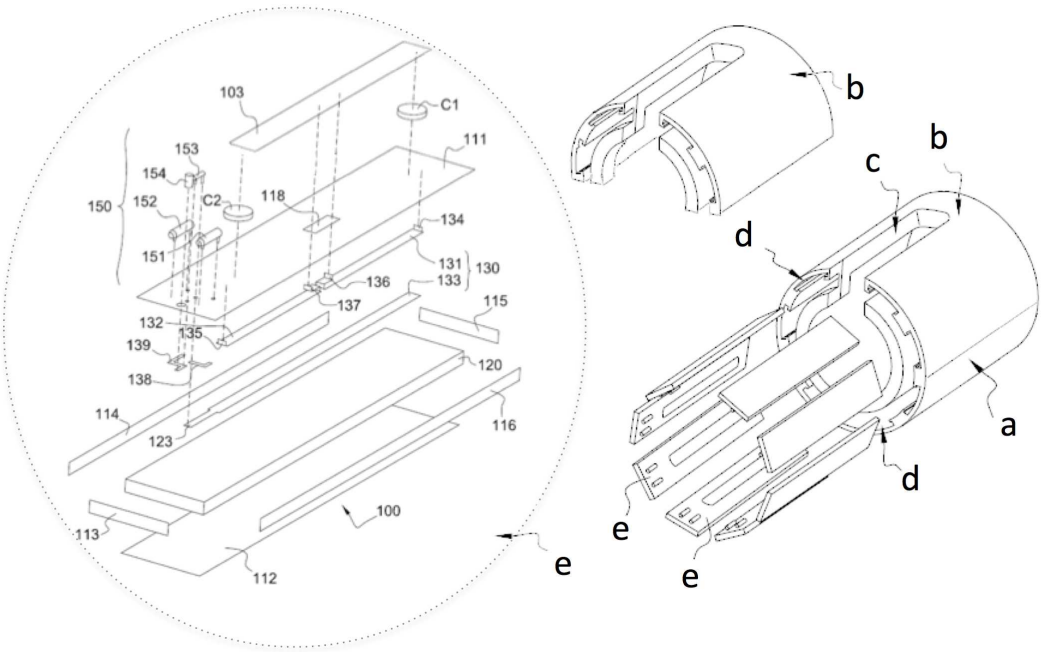

Figure 3.3: Exploded view of a dipole antenna and the transmit-array coil used throughout this thesis. The body of the coil consists of two halves (a & b). The top half (b), contain an opening (c) allowing the subject to look backwards out of the magnet bore via a mirror (non represented). Both parts of the coil body contain close-fitting slots to hold four dipoles in place (d). Each coil-element (e) consists of a substrate (120) that supports the balun, comprised out of two lines (131 + 132 & 133) separated by a 3.2 mm thick layer of TMM-4 (Rogers Corporation, Arizona, USA), one of which is cut in the center (131, 132). A shield on the six faces of the substrate protects the balun (111, 112, 113, 114, 115, 116). The ends of the top lines (131, 132) are connected to the shield (134, 135) and feed the dipole at the two dielectric blocks (C1 & C2) and the central feeding conductors (136-137). The auxiliary circuit has its own tracks (138, 139) to connect the elements (151, 152, 153, 154) used for frequency tuning and impedance matching (150). The central conductor of the coaxial input is connected to 154, whereas the outer shielding of the cable is attached to the ground plain.

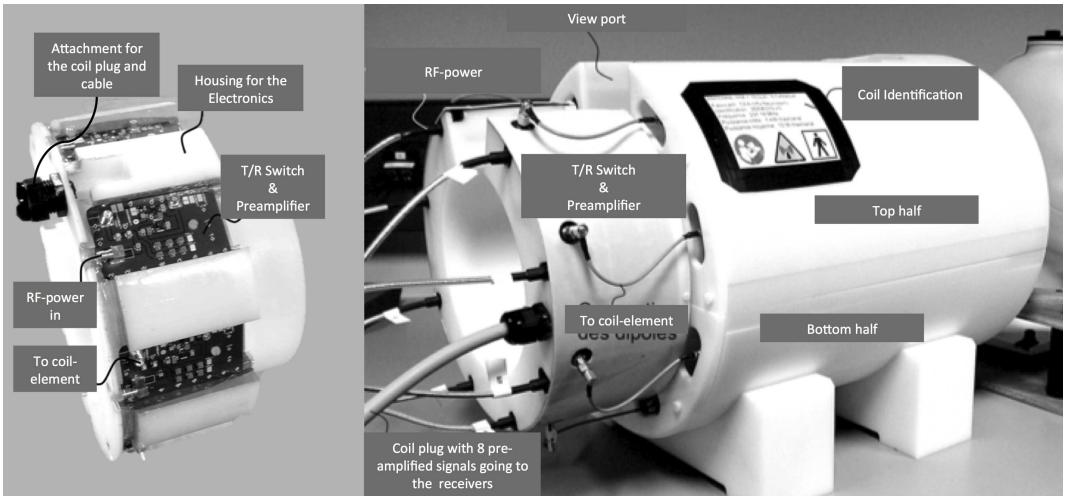

Figure 3.4: T/R-switches and complete coil assembly.

tape. Before application to studies involving human volunteers, standard electrical and mechanical tests were performed by an external company (Bureau Veritas, France) for compliance with EC labeling.

To provide the necessary resources for SAR assessment, Finite Element (FE)-based simulations were performed. To this end, the coil was modeled with HFSS (ANSYS, Canonsburg, PA, USA) along with a human head electrical load. Since the FE method allows volume elements of variable size and shape, it is particularly important to cut space into high-density regions near the coil-elements where strong spatial variations in the conservative electric fields are expected. This, in combination with the complexity of the human head model, requires a large number of tetrahedrons. Therefore a dedicated computer system equipped with 64 GB of working memory and 8 CPU cores was used (Dell, Precision T7500), thus allowing complex models made of approximately 1 million tetrahedrons to be evaluated within a reasonable time (approximately 10 hours for all eight channels simultaneously).

3.5 Computational Resources

The console used to operate the pTx-enabled system consists of 2 computer systems referred to as master and slave. The master controls a single transmit-channel (channel 8), and provides all the necessary tools to configure and prepare a new acquisition. The slave system allows any protocol prepared on the master system to be dispatched to all 8 transmit-pathways. Furthermore, the slave system was retrofitted with a high-performance-computing graphics card (CUDA-enabled C2050 Tesla, NVIDA, Santa Clara, CA, USA). This board, equipped with a Graphics Processing Unit (GPU) containing 448 cores, and 3 GB of error-code-correction DDR5 memory, facilitates massive numbers of concurrent threads for the parallel evaluation of both SAR and Bloch equations. All the software tools developed in-house on this GPU are based on a combination of C++ and CUDA (NVIDA). They are detailed in the subsequent chapters.

4 Specific Absorbtion Rate Assessment

This chapter contains methods & principles that were published as abstracts in the proceedings of the Annual Meeting of the International Society for Magnetic Resonance in Medicine 2010 and 2011.

M. A. Cloos, M. Luong, G. Ferrand, A. Amadon, D. Le Bihan, and N. Boulant. (2010) "Specific absorption rate monitor for in-vivo parallel transmission at 7 Tesla." p. 3871

N. Boulant, M. A. Cloos, M. Luong, G. Ferrand, C. J. Wiggins, and A. Amadon. (2011) "Method for monitoring safety in parallel transmission systems based on channel-dependent average powers." p. 3850

4.1 Introduction

Before the potential of pTx may be exploited in-vivo, an appropriate RF-safety system must be implemented (section 2.3). Although in principle both local and global SAR can be calculated from simulated field-maps, care must be taken to ensure safe operation in the event of a technical malfunction in order to always respect the current guidelines provided by the International Electrotechnical Commission (IEC, 2010)

Many methods for SAR assessment are available in the literature (Collins et al., 2007; Brunner et al., 2008; Graesslin et al., 2009; Gagoski et al., 2009; Boulant et al., 2011), some deriving more conservative power limits than others. The resulting safety margins in general depend on the monitoring equipment available, which must confirm all the information used in the SAR calculation (amplitude, phase, power etc), and on the accuracy of the simulated field maps. Thus the first part of this chapter describes our endeavors to validate of the electromagnetic simulations and characterize our transmit array coil via B_1^+ measurements, magnetic resonance thermometry and robustness tests of the tuning/matching network. During this thesis, the only monitoring available was based on power sensors placed at the output of each amplifier (section 3.3). The so-called Transmit Antenna Level Sensors (TALES) then provided the data necessary to enforce a predefined set of peak, the 10s and the 6 min average powers. Consistent with that information alone, three different methods to assure compliance with the SAR guidelines are compared in the second part of this chapter.

4.2 Part I: Validation of Electromagnetic Simulations

Throughout this work, the finite element method (FEM) was adopted to provide full-wave simulations (HFSS, ANSYS, Canonsburg, PA, USA) corresponding to our home-built 8-element transceiver-array coil (Section 3.4). All coil-elements were tuned ideally at 297 MHz corresponding to the proton Larmor frequency at 7-Tesla and matched identically to a 50-Ohm line impedance. However, each dipole resonated at a slightly different frequency due to the interaction with the subject-model placed in the coil. Electric and magnetic field maps thus obtained were normalized to 1 W incident power for each coil-element and projected onto a 5x5x5 mm Cartesian grid.

Comparison of Measured and Simulated B_1^+-maps

The first step towards establishing the validity of the FEM-based coil model was based on a comparison between simulated and measured B_1^+-maps. To this end, an acrylic sphere (15.5/16.0-mm inner/outer diameter) filled with dedicated liquid mimicking the averaged dielectric properties of the human brain was imaged (Fukunaga et al. (2005), $\sigma = 0.87$, $\epsilon_r = 45.3$). The actual flip-angle imaging sequence (Yarnykh, 2007) was employed to map the transmit sensitivity corresponding to each of the coil-elements in the using an interferometric acquisition method (Brunner and Pruessmann, 2008), and B_0 inhomogeneity effects were corrected as proposed by Boulant et al. (2010a). Sequence parameters were: TR1/TR2=40/200ms, (TE1/TE2/TE3 = 1/2/3.5ms), 5mm-isotropic. In addition, a single high-resolution Fast Low Angle Shot (FLASH) acquisition was performed to determine the exact position of the phantom relative to the coil.

Comparing the simulated and measured $\left|B_1^+\right|$-maps (Fig. 4.1), resulted in correlation factors well above 0.9 for all coil-elements (Fig 4.2**a**). However, demonstrating excellent correspondence between measured and simulated $\left|B_1^+\right|$-distributions alone is not sufficient to validate the electromagnetic-simulations with high confidence (Alon et al., 2011). Therefore, additional verifications were performed by incorporating the relative transmit-phase:

$$B_{n,k}^{rel}(\mathbf{r}) = B_{1,n}^+(\mathbf{r}) e^{-i\ arg(B_{n,k}^+(\mathbf{r}))}\ , \tag{4.1}$$

where $B_{n,k}^{rel}(\mathbf{r})$ is the measured transmit-sensitivity now including the transmit-phase relative the kth transmit-channel. Although this constitutes a more noise-sensitive measurement, a relatively good correspondence was obtained (Fig. 4.2**b**). Considering the obtained complex correlation factors, only the magnitude is of interest in the context of MR safety[1]. Adopting the nearest neighbor as a reference channel, the absolute complex correlation factors range between 0.89 and 0.93.

[1]The argument of the complex correlation factor constitutes the global phase offset between simulated and measured data sets which has no further consequence in the context of an MRI experiment.

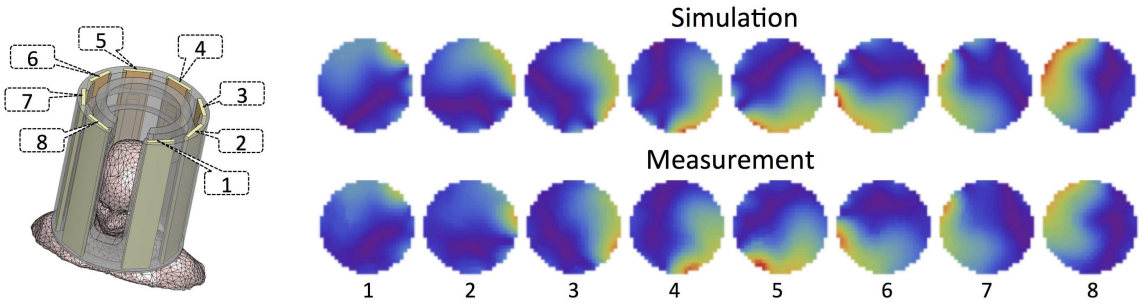

Figure 4.1: Simulated and measured transmit-sensitivity maps in a synthetic liquid phantom (Central axial slice).

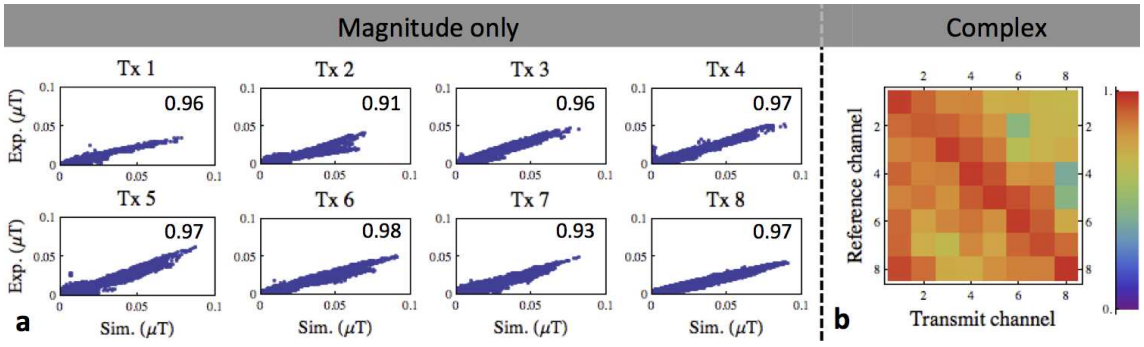

Figure 4.2: Correlation between the simulated and measured transmit-sensitivity maps. **a**: Scatter plots showing the correlation between simulated and measured $\left|B_1^+\right|$ in every voxel of the phantom. Corresponding correlation factors are included in the top right corner of each subfigure. **b**: The magnitude of the complex correlation matrix comparing simulated and measured relative complex transmit-sensitivity maps. Different voxels correspond to different combinations of transmission and phase-reference channels used to obtain the relative phase distribution. Consequently, the diagonal elements represent the correlation factors obtained by considering the magnitude only.

Temperature measurements

The magnitude of the correlation factors considered so far is invariant under scalar multiplication. Therefore, this metric only concerns the comparability of the relative spatial variations. To determine the unknown scalar, the slopes between the measured and simulated $\left|B_1^+\right|$-maps were calculated. Whereas during simulation, exactly 1 W of incident power was applied per channel, in practice the actual incident power depends on the amplifier output and cable losses. Because the aforementioned parameters were not included in the simulation, a set of calibration factors must be obtained before the SAR can be evaluated accurately for an arbitrary pulse.

Although all amplifiers demonstrated a linear response (Fig. 4.3**a**), as typically assumed during pulse design for transmit-SENSE applications, the level of output power varies by up to about 30%. Moreover, it was found that the relative performance of the amplifiers can change after maintenance or repairs, thus requiring the calibration factors to be updated. Taking into account the cable losses and amplifier characteristics, close quantitative agreement between simulated and measured field amplitudes was obtained.

Following these calibrations, additional measurements were performed on a Agar-gel phantom (acrylic sphere 15.5/16.0-mm inner/outer diameter, $\sigma = 0.78$, $\epsilon_r = 74.6$). This time, the scope of the experiment was extended to include MR temperature measurements based on the proton resonance shift method (Kuroda et al., 1997). Incorporating the previously found calibration factors, the simulated E-fields corresponding to this new phantom were adopted to simulate the expected temperature rise by solving numerically the heat conduction equation. Comparing the simulated and measured temperature rise, a mean error in temperature increase of 25% was revealed (corresponding to a 12% discrepancy between simulated and measured$|\mathbf{E}|$-fields). When calculating the SAR for in-vivo applications, this 25 % accuracy was incorporated as a safety margin. (Fig. 4.3**b**).

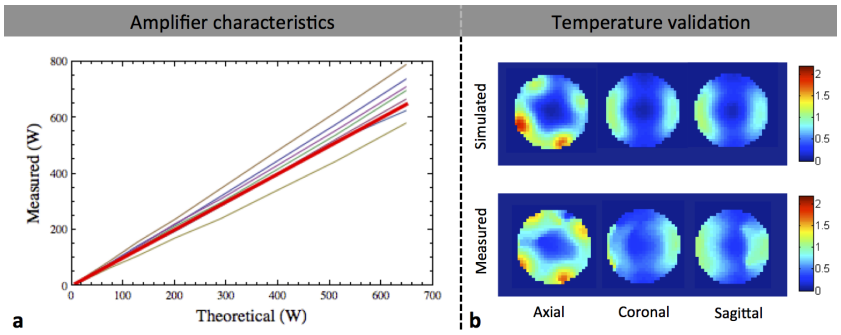

Figure 4.3: Amplifier linearity relative to the theoretical incident power, where the red line indicates the ideal situation (**a**). Results from the temperature rise simulations and corresponding MRI-based measurements (**b**).

Load sensitivity of the coil

Good correspondence between simulated fields obtained for a given head model and an arbitrary real subject requires that the coupling between coil-elements is relatively load-insensitive. In that way, even though none of the simulations was performed specifically for the subject under examination, the field-maps remain representative. This is particularly important, as the energy dissipated via mutual coupling between coil-elements is included in the simulation. Consequently, different RF-shim combinations not only effect the local SAR distribution but also the global SAR as the amount of energy dissipated in the circulators depends on both the phase and amplitude combination played on all channels.

To investigate the coil load-dependence, a series of measurements was performed outside of the MRI scanner. With a two-port network analyzer (MS2024A, Anritsu, Kanagawa, Japan) attached directly to the coil, the coupling coefficients between coil-elements were measured on the bench (Tables 4.1 & 4.2). This way, several realistic coil loadings were evaluated, including 6 different volunteers positioned with two different cushion configurations (Fig. 4.4).

Due to the self-shielded coil-design, measurements in the absence of the gradient shielding do not significantly affect the S-parameters. Although the coupling coefficients demonstrated some variation between volunteers and different subject positions, the overall deviations remained acceptable (Tables 4.1 & 4.2). In particular when adopting the first cushion configuration, the variation between subjects may be expected to remain well below 15%. Limiting the scope to the nearest neighboring elements only, which exhibit the highest levels

of mutual-coupling, the setup can be considered reasonably robust (-14dB ± 3%). Therefore, this cushion arrangement (Fig. 4.4**a**) was adopted as the standard for future studies.

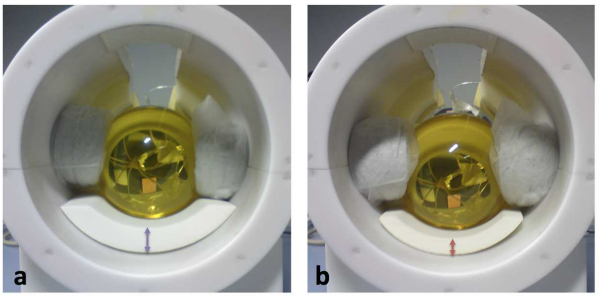

Figure 4.4: Two different cushion configurations. **a**: Configuration 1 (thick padding). **b**: Configuration 2 (thin padding).

	Tx 1	**Tx 2**	**Tx 3**	**Tx 4**	**Tx 5**	**Tx 6**	**Tx 7**	**Tx 8**
Tx 1	$-29 \pm 8\%$	$-11 \pm 4\%$	$-20 \pm 3\%$	$-29 \pm 3\%$	$-31 \pm 8\%$	$-34 \pm 5\%$	$-32 \pm 7\%$	$-22 \pm 4\%$
Tx 2		$-32 \pm 10\%$	$-12 \pm 2\%$	$-21 \pm 3\%$	$-29 \pm 4\%$	$-32 \pm 9\%$	$-37 \pm 10\%$	$-33 \pm 10\%$
Tx 3			$-25 \pm 3\%$	$-14 \pm 3\%$	$-23 \pm 4\%$	$-30 \pm 5\%$	$-34 \pm 11\%$	$-37 \pm 6\%$
Tx 4				$-19 \pm 6\%$	$-14 \pm 3\%$	$-24 \pm 4\%$	$-30 \pm 4\%$	$-32 \pm 9\%$
Tx 5					$-19 \pm 7\%$	$-13 \pm 3\%$	$-22 \pm 3\%$	$-30 \pm 4\%$
Tx 6						$-23 \pm 6\%$	$-12 \pm 3\%$	$-21 \pm 4\%$
Tx 7							$-21 \pm 5\%$	$-12 \pm 4\%$
Tx 8								$-25 \pm 5\%$

Table 4.1: Measured $S_{i,j}$ (dB±SD) coefficients corresponding to the first cushion configuration. Mean value corresponding of the diagonal: -24dB±6%. Mean value of the $S_{i,i+1}$ elements: -14dB±3%.

	Tx 1	**Tx 2**	**Tx 3**	**Tx 4**	**Tx 5**	**Tx 6**	**Tx 7**	**Tx 8**
Tx 1	$-28 \pm 11\%$	$-11 \pm 6\%$	$-21 \pm 7\%$	$-31 \pm 6\%$	$-31 \pm 9\%$	$-36 \pm 5\%$	$-33 \pm 6\%$	$-22 \pm 4\%$
Tx 2		$-30 \pm 11\%$	$-12 \pm 3\%$	$-23 \pm 6\%$	$-31 \pm 5\%$	$-33 \pm 8\%$	$-46 \pm 21\%$	$-33 \pm 7\%$
Tx 3			$-22 \pm 12\%$	$-15 \pm 4\%$	$-27 \pm 8\%$	$-32 \pm 7\%$	$-34 \pm 5\%$	$-39 \pm 11\%$
Tx 4				$-16 \pm 10\%$	$-17 \pm 7\%$	$-27 \pm 9\%$	$-31 \pm 5\%$	$-33 \pm 8\%$
Tx 5					$-19 \pm 8\%$	$-13 \pm 6\%$	$-22 \pm 5\%$	$-31 \pm 3\%$
Tx 6						$-23 \pm 7\%$	$-12 \pm 3\%$	$-20 \pm 3\%$
Tx 7							$-20 \pm 4\%$	$-11 \pm 3\%$
Tx 8								$-24 \pm 14\%$

Table 4.2: Measured $S_{i,j}$ (dB±SD) coefficients corresponding to the second cushion configuration. Mean value corresponding of the diagonal: -24dB±10%. Mean value of the $S_{i,i+1}$ elements: -14dB±5%.

Practical Considerations

Due to the construction of the gradient insert, the maximum depth of the patient-table into the bore of the magnet is limited. As the rather long coil can only be placed in a fixed position at the end of the bed, the setup prevents most subjects from positioning the center of their brain at gradient isocenter (Fig. 4.5**b**). So they are asked to put their head as far inside the RF coil as they can, which is typically about 3 cm deeper than originally assumed during RF simulation (Fig. 4.5**a**). Re-evaluating the simulations with a more realistically positioned head-model, resulted in a $\sim 15\%$ increase of the 10-g local SAR[2]. Furthermore, this non-ideal placement requires the shoulders of the subject to touch the edge of the coil. Therefore, the severity of the third-arm artifact is increased due to the enhanced receive-sensitivity of the coil in the shoulder region (Section 3.2). In addition, the obtainable B_0-shim quality and SNR are diminished due to sub-optimal placement relative to the shim- and receive-coils, respectively.

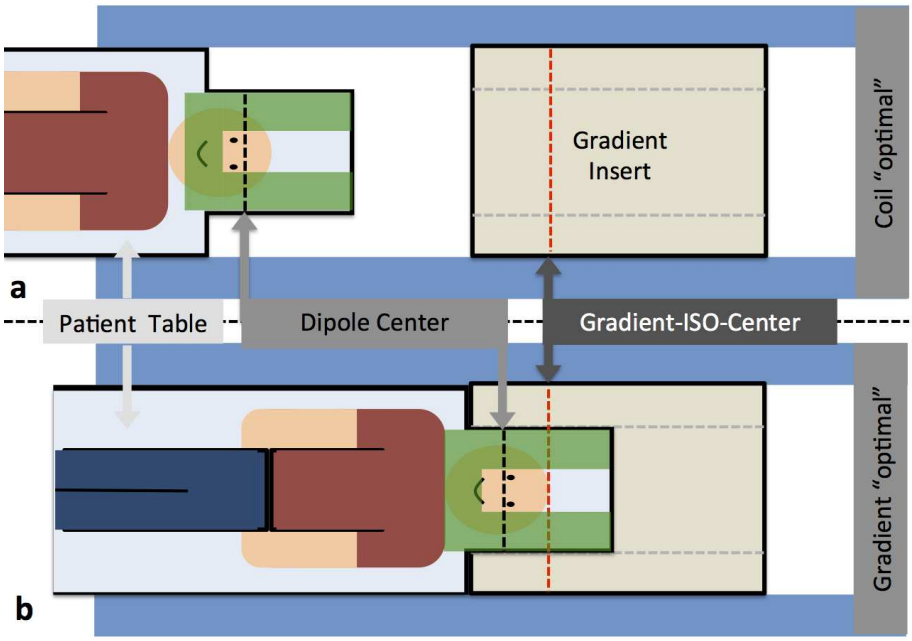

Figure 4.5: Patient positioning relative to the RF coil and gradient insert. **a**: Patient in the RF coil optimal position, with the brain approximately centered relative to the dipole coil-elements. **b**: Actual subject position, shoulders touching the edge of the coil, and brain positioned as close as possible to gradient isocenter.

[2]When applying 1W of incident power per channel and assuming constructive interference.

4.3 Part II: Online SAR Assessment Based on Time-Averaged Power Measurements

After validating the simulation methods necessary to assess the SAR distribution corresponding to our particular setup, the electric fields produced in a realistically positioned anatomically accurate human head-model were evaluated. To this end, our FEM-compatible implementation of the MRI-based MGH head-model (Makris et al., 2008; Massire et al., 2012) was considered (Fig. 4.6). Based on these simulated field-maps, three different methods to derive appropriate time-averaged power limits were evaluated.

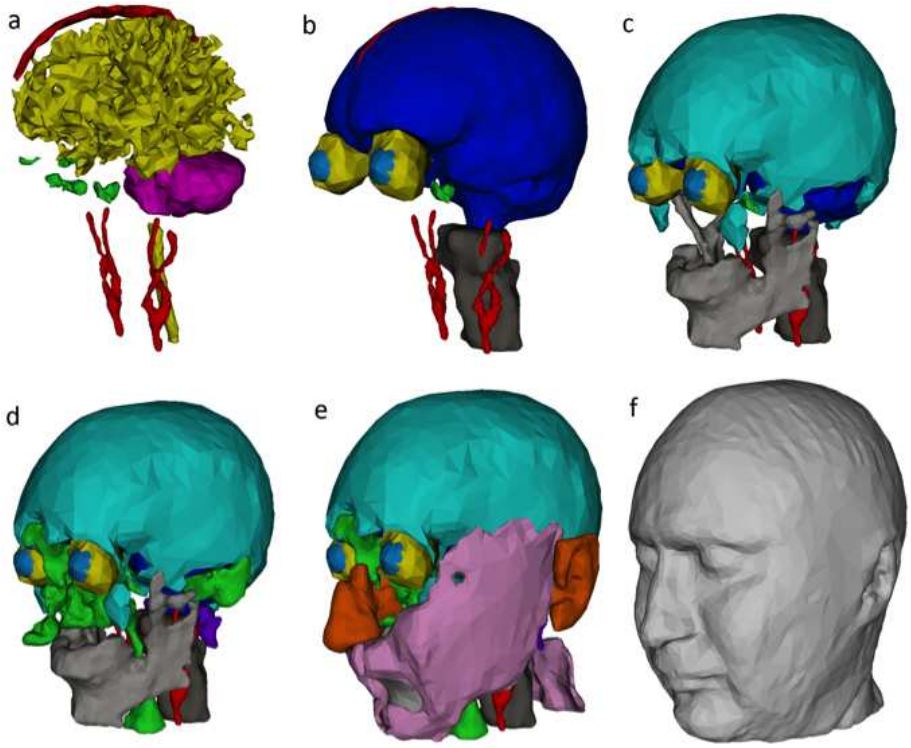

Figure 4.6: Three-dimensional rendering of the in-house-developed, finite-element-compatible implementation of the MGH-head model. **a**: White Matter (yellow), blood vessels (red), nerves (green) & Cerebellum (purple). **b**: Grey Matter (dark blue), orbital fat (yellow), eyes (blue), vertebral column (black). **c**: Skull (cyan), facial bones (gray). **d**: Air & mastoid cells (green), adipose (purple). **e**: cartilage (orange), subcutaneous muscles (pink). **f**: Whole head (neck and shoulders not shown).

"Constructive interference"

Because the time-averaged power monitors do not allow the relative phase between RF-channels to be evaluated, all possible phase combinations have to be covered (chapter 3). One way to facilitate this is to assume constructive interference of the E-fields at every point in space. The corresponding upper limit of the SAR can then be found by:

$$SAR(\mathbf{r}) \leq \alpha \frac{\sigma(\mathbf{r})}{2\rho(\mathbf{r})} \frac{1}{T} \int_0^T \left(\sum_{n=1}^{N} \| b_n(t) \mathbf{E}_n(\mathbf{r}) \| \right)^2 dt \ , \tag{4.2}$$

where α is the duty cycle, $\mathbf{E}_n(\mathbf{r})$ is the electric field produced by the nth coil-element, $\sigma(\mathbf{r})$ the local conductivity (S/m), $\rho(\mathbf{r})$ the local density (kg m^{-3}), $b_n(t)$ the waveform played at the nth coil-element, and T the pulse duration.

For this basic safety assessment we will consider two quantities: the local 10-g averaged SAR when assuming constructive interference of the E-fields at every point (SAR_{wl}), and the worst-case global SAR corresponding

to the comulative forward power divided by the exposed body mass (SAR_{wg}). Taking the ratio between the aforementioned parameters, we define the ratio:

$$R = \frac{SAR_{wl}}{SAR_{\text{wg}}} \ . \tag{4.3}$$

Assuming that the power is equally distributed over all available transmit-channels a conservative time averaged power limit (P_{lim}) can be deduced as follows:

$$P_{lim} = \frac{1}{N}\frac{SAR_{lim}}{R} M \times 0.9 \ , \tag{4.4}$$

where N is the number of transmit-pathways, M is the head mass, and SAR_{lim} is the local SAR limit specified in the guidelines (IEC, 2010). To take the approximately ±10% accuracy of the power meters in to consideration, the enforced limits are scaled down by a factor 0.9. For simplicity, and to provide an additional safety margin, both the 10-s and 6-min time averaged power limits were restricted to the more conservative guidelines corresponding to the 6-min SAR limits. Furthermore, a conservative average head mass of 5 kg is assumed to provide a subject independent power limit[3].

Sending 1 W of power to each of the coil-elements results in a simulated worst-case global SAR of 1.54 W/kg and a maximum local 10-g SAR of 8.12 W/kg. This results in a 10-s time-averaged power limit of 0.7 W per channel. At this point the 25% accuracy of our simulations is assumed to be well within the safety margins of these conservative power constraints. Thus assuming constructive interference, no cable loss, complete absorption of the incident power by the head, and a relatively light average head, a very conservative but usable time-averaged power constraint was derived

"Total incident power"

Alternatively, a suitable time-averaged power limit can be calculated based on the method proposed by Brunner et al. (2008). In contrast to the assumption of constructive interference at every point, which is physically impossible, this approach incorporates the effects of destructive interference. Consequently, the thus obtained maximum 10-g local SAR could be lower than the worst-case scenario considered in the previous section. However, this method is very general and does not allow channel dependent constraints to be incorporated.

When applied to our 8-channel transmit-array, considering a 1 W total power budget at the coil level, we obtain a maximum local 10-g SAR of 2.74 W/kg. Assuming that the guidelines for the local SAR will be exceeded before the global one, another conservative time-averaged power limits can be obtained from:

$$P_{lim} = \frac{1}{N}\frac{SAR_{lim}}{2.74} \times 0.9 = 0.41W \ , \tag{4.5}$$

where N is the number of transmit-pathways, SAR_{lim} is the local SAR limit specified in the guidelines (IEC, 2010), and again assuming that there are no cable losses. Although this method provided a clean analytical solution for the peak 10-g local SAR, it does not provide a more favorable set of time-averaged power limits. Investigating this worst-case scenario in more detail reveals that 70% of the power was deposited on a single channel. This situation, effectively, corresponds to what most closely resembles a single surface coil configuration, which is of limited interest in the context of pTx. Because this approach does not allow channel specific limits to be considered, the benefits of channel dependent time-averaged power-monitors cannot be exploited. On the other hand, compared to the previous method, this approach does allow a much larger time-averaged power limit to be applied on one channel, provided that the power transmitted through the other channels is negligible.

"CEASAR"

Theory

Omitting the assumption that the energy is distributed evenly among channels, a less restrictive yet also conservative approach can be derived to enforce compliance with the SAR guidelines (Boulant et al., 2011).

[3]It should be noted that currently only adults are allowed in the 7-Tesla scanner at NeuroSpin.

Considering the set of N RF-waveforms $f_n(t)$ to be played on each of the coil elements, the SAR at point $\mathbf{r}$ is defined as:

$$SAR(\mathbf{r}) = \frac{\sigma(\mathbf{r})}{2\rho(\mathbf{r})}\frac{1}{T}\int_0^T \left\| \sum_{n=1}^{N} \mathbf{E}_n(\mathbf{r}) f_n(t) \right\|_2^2 dt \ . \tag{4.6}$$

Again discarding the phase information and assuming constructive interference at every point, we obtain the following conservative expression:

$$SAR(\mathbf{r}) \leq \frac{\sigma(\mathbf{r})}{2\rho(\mathbf{r})}\frac{1}{T}\int_0^T \left(\sum_{n=1}^{N} \|\mathbf{E}_n(\mathbf{r}) f_n(t)\| \right)^2 dt \ . \tag{4.7}$$

Limitation of the average incident power on each transmit channel implies the following constraints:

$$\frac{1}{T}\int_0^T |f_n(t)|^2 \, \mathbf{d}t \leq P_n \ . \tag{4.8}$$

Taking these inequalities into account, Eq. 4.7 can be simplified to:

$$SAR(\mathbf{r}) \leq \frac{\sigma(\mathbf{r})}{2\rho(\mathbf{r})} \left(\sum_{n=1}^{N} \|\mathbf{E}_n(\mathbf{r})\|_2^2 \, P_n + C(\mathbf{r}) \right) \ , \tag{4.9}$$

where $C(\mathbf{r})$ is defined as

$$C(\mathbf{r}) = \frac{2}{T} \sum_{n=1}^{N} \sum_{m=n+1}^{N} \left(\|\mathbf{E}_n(\mathbf{r})\| \, \|\mathbf{E}_m(\mathbf{r})\| \int_0^T |f_n(t)| \, |f_m(t)| \, \mathbf{d}t \right) \ . \tag{4.10}$$

Applying the Cauchy-Schwarz inequality, we find that

$$C(\mathbf{r}) \leq 2 \sum_{n=1}^{N} \sum_{m=n+1}^{N} \left(\|\mathbf{E}_n(\mathbf{r})\| \, \|\mathbf{E}_m(\mathbf{r})\| \sqrt{P_n P_m} \right) \ . \tag{4.11}$$

This way, tailored to the set of RF waveforms at hand, a set of appropriate average power limitations can be derived for each one of the available transmit-cannels[4].

Implementation

In order to reach the full potential of the above proposed SAR-assessment, the time-averaged power limits have to be re-evaluated based on the RF pulses to be played. To this end, our SAR assessment tool (Fig. 4.7), referred to as "CEASAR", evaluates both the global and local 10-g SAR over several pre-simulated data sets (Cloos et al., 2010a)[5]. Each one of them contains the simulated fields corresponding to all of the transmit-elements in the presence of a human head-model. In addition, a pre-calculated "averaging-matrix" is included to facilitate rapid evaluation of the corresponding 10-g-averaged SAR. Although inter-subject variability precludes predictions with absolute certainty regarding local SAR, these differences may be encompassed, to some extent, by evaluating different head-models. Therefore, in addition to our 20-anatomical-structure head-model (Fig. 4.6), the 8-anatomical-structure head from the Ansoft human body model (Aarkid, East Lothian, Scotland) was considered et slightly different positions relative to the coil.

When operating in pTx-mode, before the subject enters the scanner, CEASAR is started (on the slave console). At this point, all available simulations corresponding to the selected coil are loaded. First a default protocol is evaluated to obtain a set of initial time-averaged power limits for each of the individual transmit-channels. These limits typically facilitate all the calibration acquisitions such as B_0-shimming, frequency adjustments, and transmit-sensitivity mapping. Nevertheless, every time a new protocol is prepared,

[4] Note that eq 4.9 applies regardless of the RF waveform, i.e., only the average power need to be monitored.

[5] With the current GPU-enabled implementation of CEASAR, protocols including 10-ms transmit-SENSE pulses defined at a 1-μs raster-time can be evaluated over all models in seconds, thus introducing only a minimal delay between acquisitions.

CEASAR evaluates the SAR and if necessary provides an appropriate set of alternative time-averaged power limits. When excessive SAR is predicted, the option to alter the repetition time or FA is provided (Fig. 4.7**a**). Only protocols that passed the CEASAR evaluation may be played on the scanner (Fig. 4.7**b**&**c**). Effectively, this is enforced by only copying validated protocols to the slave-system used to operate the pTx-extension. Meanwhile, the power out of the amplifiers is measured through the use of directional couplers and time-averaged power meters (Section 3.3). In the event that one of the limits is exceeded, the acquisition is terminated[6].

Taking into account the cable losses, amplifier variability, the 10% accuracy of our power monitors, the 25% accuracy of our SAR simulations, the initial time-averaged power limit is now approximately 1.2 W per channel. Adjustments are then only made if a particular protocol requires it. The possibility to fix different average power limits on different channels gives additional flexibility in pulse design, while strictly enforcing safety. Although a plethora of said subspaces exist, most of them only partially overlap one-another. Therefore, depending on the pTx pulses configuration, CEASAR may suggest a different combination of time-averaged power constraints. In this way, transmit-SENSE-based acquisitions with substantially higher time-averaged forward power levels on some channels are possible (up to about 3.0 W).

Comparison

Each of the three approaches SAR-assessment considered above have their advantages. Although the method proposed by Brunner et al. provides an elegant solution to obtain the peak 10-g local SAR corresponding to fixed total-power input, it does not provide the tools necessary to exclude scenarios that are of limited interest in the context of pTx. This is illustrated by the peak 10-g local SAR corresponding to our setup, where approximately 70% of the power deposited on a single channel.

Simply assuming constructive interference, on the other hand, allows the additional constrains enforced by channel-depend power monitors to be incorporated. Consequently, a much higher average power per channel can be achieved when adopting this method. Considering our interest in pTx-enabled FA-homogenization, where relatively uniform levels of power among channels may be expected, the initial in-vivo pTx experiments presented in chapter 6 were performed based on the assumption of constructive interference.

Although CEASAR is also based on the assumption of constructive interference, it is more refined allowing the power to be distributed differently between acquisitions. Moreover, "CEASAR" is calibrated differently, directly considering the global and 10-g local SAR rather then a fixed ratio. Although this method still incorporates a substantial safety margin compared to the true SAR (Buchenau et al., 2010), adopting CEASAR allowed slightly more RF intensive sequences to be explored, such as the MPRAGE in chapter 8. However, even more RF intensive applications, such as spin-echo based sequences, would likely require a more elaborate safety system that allows the true SAR limits to be approached more closely (Graesslin, 2008; Graesslin et al., 2009; Gagoski et al., 2009).

[6]Note that all protocols that can operate within the enforced time-averaged power limits are (IEC, 2010)-compliant. Therefore, running an invalid protocol would not endanger the subject. However, the acquisition may be terminated even if the SAR limits were not reached.

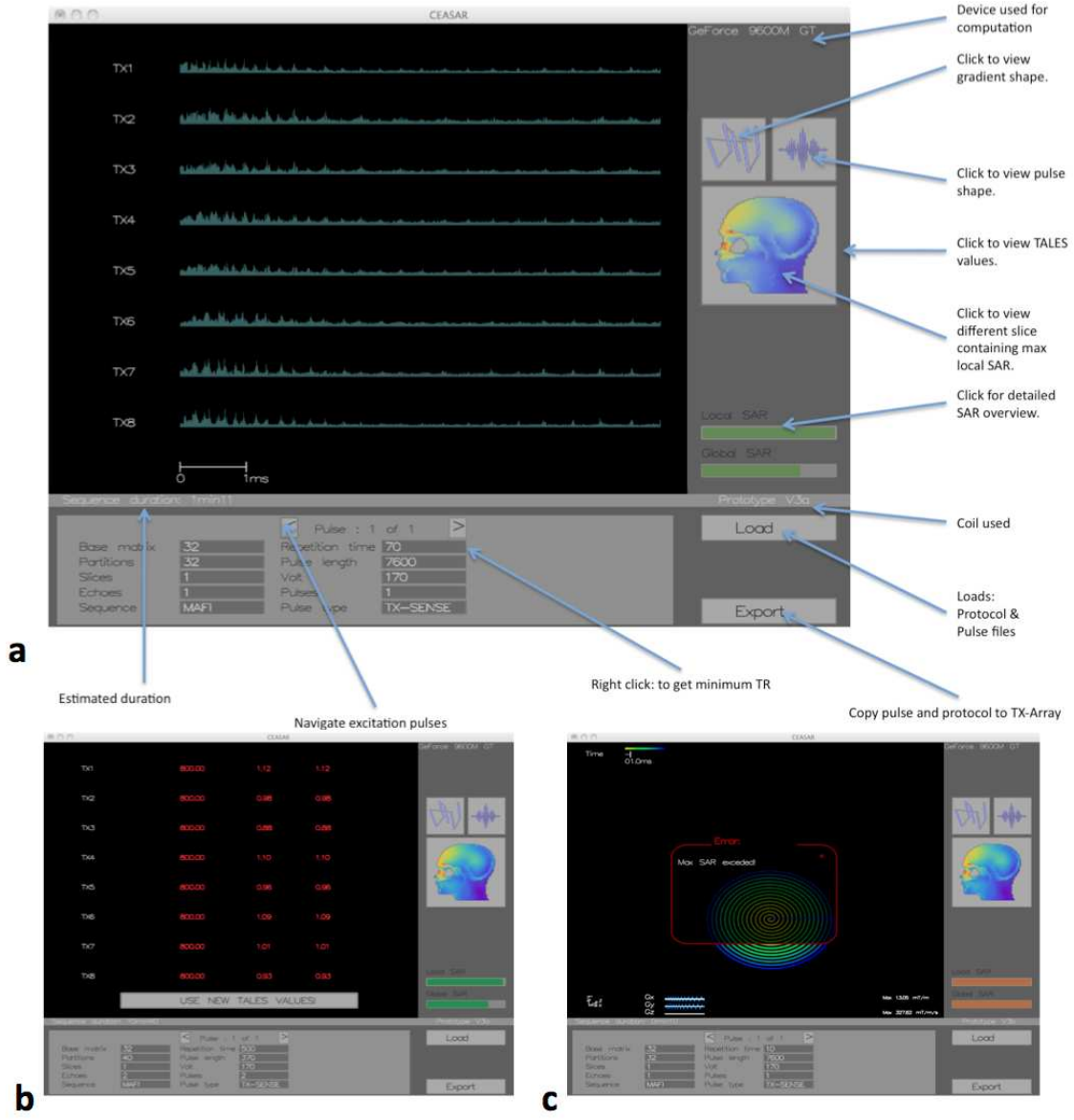

Figure 4.7: Screenshots taken from CEASAR. **a**: The main screen showing a 10-ms pTx RF-waveform. Some of the main features are indicated with arrow and labels. **b**: Example of a protocol that is in compliance with the SAR guidelines, but requires the time-averaged power-limits to be updated. **c**: Example hosting a protocol exceeding the SAR-guideline specifications. Apart from the message window, the SAR level indicators are orange indicating an excess of the guidelines. Note that, in the background the k-space trajectory and gradient waveforms are shown. Although not relevant in the SAR assessment, CEASAR also validates the compliance of the gradient waveforms with respect to the system limitations.

5 Local SAR Reduction in Parallel Excitation Based on Channel-dependent Tikhonov Parameters.

This chapter has been accepted for publication as: Martijn Anton Cloos, Michel Luong, Guillaume Ferrand, Alexis Amadon, Denis Le Bihan, and Nicolas Boulant. "Local SAR Reduction in Parallel Excitation Based on Channel-Dependent Tikhonov Parameters" Journal of Magnetic Resonance Imaging 2010 November; 32(5):1209-16.

The priciple idea described in this chapter was filed as patent application 09290696.5 (EP 2 296 000 A1), "Parallel excitation of nuclear spins with local SAR control".

Abstract

Purpose: To reduce the local SAR obtained with tailored pulses using parallel transmission while obtaining homogenous flip angle distributions.

Materials and Methods: Finite-element simulations on a human head model were performed to obtain the individual magnetic and electric field maps for each channel of a parallel transmit array. Based on those maps, SAR calculations were carried out for "spoke" pulses designed to homogenize the flip angle in an axial slice of a human brain at 7 Tesla. Based on the assumption that the coil element nearest to the maximum local energy deposition is the dominant contributor to the corresponding hot spot a set of channel-dependent Tikhonov parameters is optimized. Resulting SAR distributions are compared to the ones obtained when using standard pulse design approaches based on a single Tikhonov parameter.

Results: In both the small- and large-tip-angle domain the simulations show local SAR reductions by over a factor of 2 (4) for a well-centered (off-centered) head model at the expense of roughly 1% increment in flip-angle spread over the slice.

Conlusion: Significant SAR reductions can be obtained by optimizing channel-dependent Tikhonov parameters based on the relation between coil elements and SAR hot spot positions.

5.1 Introduction

High local specific absorption rates (SAR) have become an important problem severely limiting the potential of ultra high field MRI. Increased field strength yields an improved signal-to-noise ratio (Collins and Smith, 2001), and therefore promises better image resolution. However, as the Larmor frequency is proportional to the static field strength, at high field spin excitation requires high radio frequencies (RF). Compared to vacuum, the wavelengths inside the body are reduced considerably due to the dielectric properties of the tissues (Gabriel et al., 1996; Yang et al., 2004). Wavelengths comparable to or shorter than the dimensions of the body create interferences inside the patient, which can result in complex magnetic and electric field distributions. These field distributions can lead to strongly inhomogeneous excitation profiles (Collins and Smith, 2001; Ibrahim et al., 2001b), resulting in non-uniform tissue contrast and signal intensity. Various methods have been proposed to achieve homogenous excitation at high field strengths, including alternative coil designs (Brunner et al., 2009), passive B1 shimming (Yang et al., 2006), shaped pulses (Boulant et al., 2008; Bernstein et al., 2004), static B1 shimming (Ibrahim et al., 2001b; Metzger et al., 2008), and transmit-SENSE (Katscher et al., 2003; Zhu, 2004). With the latter technique, excellent excitation homogeneity was demonstrated both in vitro (Ullmann et al., 2005; Setsompop et al., 2006, 2009) and in vivo (Angelone et al., 2006; Setsompop et al., 2008a). Independent control over phase and amplitude for each of the coil elements during parallel transmission provides a great wealth of possible RF schemes, which can distribute energy differently over the patient's anatomy. Furthermore it was shown that for tailor-made excitation pulses using parallel transmission, local SAR could show considerable variations (Zelinski et al., 2008b) and high peak values (Collins et al., 2007). Hence taming the SAR during parallel transmission requires extensive studies and calculations (Angelone et al., 2006; Zelinski et al., 2008b; Collins et al., 2007; Mao et al., 2007).

For patient safety reasons, both global, i.e. averaged over the whole exposed body, and local SAR limits must be enforced (IEC, 2002). Currently, methods are in development to measure the dielectric properties and estimate the SAR (Katscher et al., 2008; Voigt et al., 2009; Cloos and Bonmassar, 2009) using transmit sensitivity maps (B_1^+). Alternatively, pre-calculated patient models can be used to evaluate the SAR (Graesslin et al., 2009; Kini et al., 2009). In the end, the local SAR peak value imposes more restrictive conditions than the global SAR limit on the application of parallel transmission (by limiting repetition times and/or flip angles). Zhu (2004) indicated that if the electric-field distribution is known, global SAR minimization could be encompassed in the design procedure of the excitation pulse. Extending this method by adding a limited number of control points during pulse design (Graesslin et al., 2008), i.e. by imposing a quadratic constraint at these particular points, also allows the local SAR to be reduced at those points.

In this work, we present a new method allowing the maximum local SAR to be reduced via an optimization technique that considers the entire object. The procedure iteratively optimizes a set of channel-dependent regularization parameters, effectively applying channel-specific power penalties. We assume that the coil-element closest to the maximum local SAR location contributes the most to the corresponding hot spot, an assumption that we will justify later on. By using this property, a minimal number of calculations is needed to determine the next iterative step, significantly reducing the overall calculation time.

In the theory section of this paper we first introduce channel-dependent (also possibly time-dependent) Tikhonov regularization parameters in the spatial domain method (Grissom et al., 2006). Following the details about the computation of the electric and magnetic field maps, the optimization procedure for local SAR reduction using channel-dependent Tikhonov parameters is provided in the method section. Results obtained using the proposed technique are then reported, analyzed and compared with a global SAR minimization approach (Zhu, 2004; Zelinski et al., 2007).

5.2 Theory

Using the small-tip-angle approximation (STA), RF pulses can be designed for a given k-space trajectory ($\mathbf{k}(t)$) with the spatial domain method reported by Grissom et al. (2006). The STA allows the transverse plane magnetization $m(\mathbf{r})$ to be approximated by the Fourier integral of complex RF pulses $b_n(t)$ spatially weighted by their transmit sensitivity maps $B_{1,n}^{+}$ (associated with coil element n), over a predefined excitation k-space trajectory :

$$m(\mathbf{r}) = i\gamma m_0 \sum_{n}^{N} B_{1,n}^{+}(\mathbf{r}) \int_0^T b_n(t) e^{i\gamma \Delta B_0(\mathbf{r})(t-T)} e^{i\mathbf{r}\cdot\mathbf{k}(t)} dt \tag{5.1}$$

where γ is the gyromagnetic ratio, m_0 is the equilibrium magnetization magnitude, T is the pulse length, and $i\gamma\Delta B_0(\mathbf{r})(t-T)$ represents the phase evolution due to static field inhomogeneity $\Delta B_0(\mathbf{r})$. The k-space trajectory $\mathbf{k}(t)$ is equal to the time-reversed integration of the gradient waveforms to be played during excitation. Linearity in the STA regime was assumed to allow summation over the N coil elements available for parallel transmission. By discretizing space and time with N_s and N_t samples respectively, the transverse magnetization can be written as a column vector $\mathbf{m}$:

$$\mathbf{m} = [\mathbf{D}_1\mathbf{A}, \cdots, \mathbf{D}_N\mathbf{A}] \begin{bmatrix} \mathbf{b}_1 \\ \vdots \\ \mathbf{b}_N \end{bmatrix} = \mathbf{A}_{tot}\mathbf{b}_{tot} \tag{5.2}$$

where $\mathbf{D}_n(\mathbf{r}) = \text{diag}\{B_{1,n}^{+}(\mathbf{r})\}$ is a $N_s \times N_s$ diagonal matrix containing spatial samples of the transmit sensitivity map of coil element n, and $\mathbf{A}$ is a $N_s \times N_t$ matrix whose elements are $a_{i.j} = i\gamma m_0 \Delta t e^{i\gamma\Delta B_0(\mathbf{r_i})(t_j-T)} e^{i\mathbf{r}_i\cdot\mathbf{k}(t_j)}$. Given a target transverse magnetization profile vector $\mathbf{d}$, finding the RF pulse $\mathbf{b}_{tot}$ is a linear inverse problem. In order to produce a well-conditioned convex optimization problem, a Tikhonov regularization is often introduced with a scaling parameter λ (Grissom et al., 2006). Effectively, it adds to the least squares residual a cost function proportional to the RF power integrated over time and coil elements, thereby suppressing solutions with large integrated RF powers. The standard method uses the same Tikhonov parameter for all the elements in the coil (Setsompop et al., 2006, 2008a, 2009; Zelinski et al., 2008b; Grissom et al., 2008; Zelinski et al., 2007; Setsompop et al., 2008c; Zelinski et al., 2008d) to reduce the overall RF power by solving the following problem:

$$\min_{\mathbf{b}_{tot}} \{ \|\mathbf{d} - \mathbf{A}_{tot}\mathbf{b}_{tot}\|_2^2 + \lambda \|\mathbf{b}_{tot}\|_2^2 \} \tag{5.3}$$

where the subscript "2" designates the ubiquitous L_2 norm, i.e. the square root of the sum of magnitude squares of the elements. Depending on coil design and patient orientation, interaction between each coil element and patient may vary. To reduce the maximum local SAR, we propose to optimize the diagonal matrix λ_M with the new problem formulation:

$$\min_{\mathbf{b}_{tot}} \{ \|\mathbf{d} - |\mathbf{A}_{tot}\mathbf{b}_{tot}|\|_2^2 + \|\boldsymbol{\lambda}_M\mathbf{b}_{tot}\|_2^2 \} \tag{5.4}$$

where $\boldsymbol{\lambda}_M = \text{diag}\{\sqrt{\lambda_1}\mathbf{I}, \cdots, \sqrt{\lambda_N}\mathbf{I}\}$, I being the $N_t \times N_t$ identity matrix. Note that in addition to the introduction of the $\boldsymbol{\lambda}_M$ matrix, the phase constraint in Eq. [5.4] was relaxed by adopting the Magnitude Least Square approach (MLS) proposed in (Setsompop et al., 2008c).

5.3 Methods

Field Map Computations

The head coil used in this study consisted of eight stripline dipoles distributed every 40° on a cylindrical surface with 27.6-cm diameter, leaving an open space in front of the eyes of the patient for fMRI studies (Fig. 5.1**a**). Full-wave simulations with the finite element method (FEM) using HFSS (Ansoft, Pittsburgh,

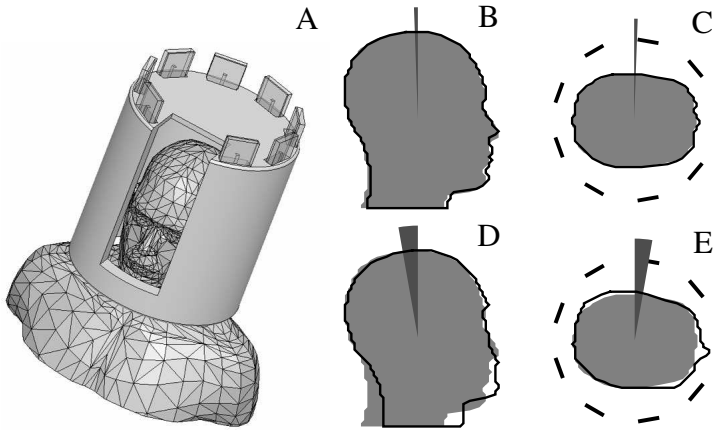

Figure 5.1: **a**: The coil and nominal head position used for magnetic and electric field simulation. **b**–**e**: Head positions used for simulation: the centered human head is shown in gray. a: Dark gray wedge and the black outline of the head indicate rotations in the transverse and sagittal plane. **b**: 2^{o}- rotation in sagittal plane. **c**: 2^{o}-rotation in transverse-plane. **d**: 10^{o}-rotation in the sagittal plane. **e**: 10^{o}-rotation in the transverse-plane.

PA) (Vogel and Kleihorst, 2007; Kozlov and Turner, 2009) provided the electric and magnetic field maps normalized to 1 W incident power for each dipole. All dipoles were tuned ideally at 297 MHz corresponding to the proton Larmor frequency at 7 Tesla, and matched identically to a 50-Ohm line impedance. However each dipole resonated at a slightly different frequency due to the interaction of the human head model placed in the centre of the coil; but the reflected power coefficient on all channels was still maintained below 0.1 at the common field excitation frequency. The head and shoulders of the Ansoft human body model (Aarkid, East Lothian, Scotland) were used to provide an 8-anatomical-structure head model. The FEM uses tetrahedrons of various sizes and shapes, instead of the Cartesian Yee cells frequently used in finite difference time domain (FDTD) methods. Appropriate tetrahedron density distributions were provided by the HFSS mesh adaption tool. Nonetheless, it was validated that a further increase in the tetrahedron density by a factor of 3 results in nearly identical field-distributions. To facilitate fast SAR evaluation and pulse optimization, the field maps obtained using the FEM were projected onto a 5x5x5mm^3 Cartesian grid (Kozlov and Turner, 2009). Before performing SAR computations, the electric field maps were verified by computing a histogram of their amplitudes. Voxels corresponding to relatively high isolated peak values were then inspected and removed if affected by partial voluming.

Using non-patient specific models, inter-patient anatomical differences remain unaccounted. Furthermore, the position of the patient can be different from the model placement in the simulation. To test the robustness of our method with respect to head displacement, additional simulations were performed with the head model rotated (Fig. 5.1**b-e**), first rotated by φ around the z-axis followed by the same rotation around the x-axis ($\varphi = 2°, 10°$).

SAR Calculation

The local SAR is defined as a function of the local conductivity $\sigma(\mathbf{r})$, local mass density $\rho(\mathbf{r})$, the duration of the pulse T, and the local electric field strength $\mathbf{E}(\mathbf{r}, t)$:

$$SAR(\mathbf{r}) = \frac{\sigma(\mathbf{r})}{2\rho(\mathbf{r})} \frac{1}{T} \int_0^T \|\mathbf{E}(\mathbf{r}, t)\|_2^2 \, dt \tag{5.5}$$

Assuming linearity of the E-field with respect to the input currents in the coil elements, the complex sum of the $b_n(t)$-scaled electric field components of all coils was used to calculate the SAR value in each voxel:

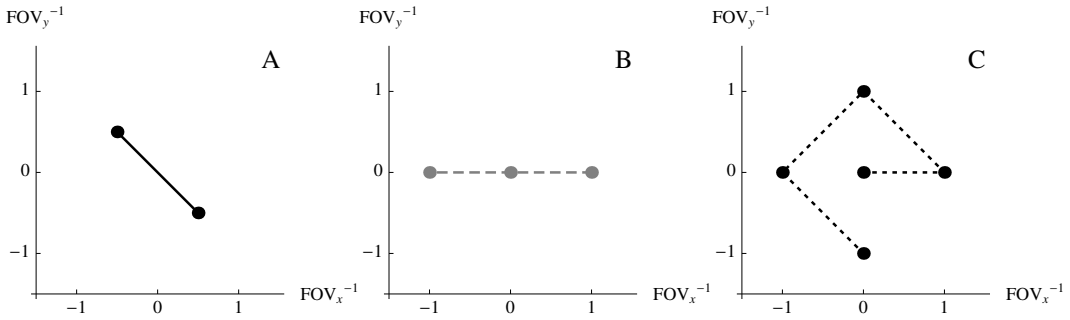

Figure 5.2: Spoke locations used for pulse design, in the (k_x, k_y) plane, where FOV denotes the field of view (x 1/4 23 cm, y 1/4 27 cm). Two (**a**), three (**b**), and five (**c**) spoke k-space trajectory used to generate homogenous excitation profiles.

$$\mathbf{E}(\mathbf{r},t) = \sum_{n}^{N} b_n(t)\mathbf{E}_n(r) \tag{5.6}$$

where $\mathbf{E}_n$ is the three-component electric field associated with coil element n, as found from the full-wave simulation. Local SAR distributions were averaged over 10-g closed volume elements, as specified in the IEC guidelines (IEC, 2002), by using a region growing algorithm. This algorithm was implemented in C++ by progressively increasing the size of an averaging box until 10 grams of matter were contained in it. Thus on average, the size of a 10-g box was about 82.7-voxels. The head model used in the simulations provided both the conductivity and mass density maps needed for this calculation. In this work, although the pulses were designed to homogenize the flip angle over an axial slice through the central region of the brain, SAR calculations were performed over the whole head and neck. In the remainder of this text, wherever local SAR is mentioned, it will refer to the 10-g averaged SAR.

Pulse Design and SAR Optimization

We focused on slice selective excitation pulses with a homogeneous excitation profile over a central axial slice of the brain using a spokes-shaped k-space trajectory (Saekho et al., 2006). We quantified the flip angle (FA) inhomogeneity by calculating the root mean square error of the flip angle, divided by the target FA. The latter was chosen to be either 20° or 90°, to explore different FA regimes. The linear model of Eq. 5.2 was used to compute an RF solution targeting 20°, while the additive flip-angle method was used to design RF solutions targeting 90° (Grissom et al., 2008). Full Bloch simulations were performed to quantify the performance of each pulse. Trajectories with 2, 3, and 5 spokes (Fig. 5.2) were tested. Individual sub-pulses were 0.7-ms sinc waveforms apodized with Hanning windows and time-bandwidth product equal to 4. Blips used to travel between k-space locations (duration = 80 μs maximum slewrate = 200 mT/m/s) were played barely overlapping with the excitation pulses. The placement of the spokes was not optimized but could potentially be determined with sparsity-enforced algorithms (Zelinski et al., 2008d).

For a given number of spokes, the optimization started from a pulse designed with the standard method using the spatial domain method (Grissom et al., 2006) with the MLS approach (Setsompop et al., 2008a) Eq. 5.4, by using a set of identical Tikhonov parameters ($\lambda_M = \lambda\mathbf{I}$) obtained from the L-curve criterion (Hansen, 1992). For the 90° pulse, which no longer fulfills the STA, first a pulse with target flip angle of 45° was designed and then simply multiplied by 2 to provide a first order solution. Results from the full Bloch simulations were then used to design the correction term in the additive flip angle method (Grissom et al., 2008). For any set of regularization parameters, the local variable exchange method (Setsompop et al., 2008c) was implemented in order to disregard the phase information in the output transverse magnetization, hence only taking into account the flip angle distribution. Subsequently the 10-g average local SAR map was calculated by using the returned initial RF pulses. Then for each iteration in the optimization procedure, the

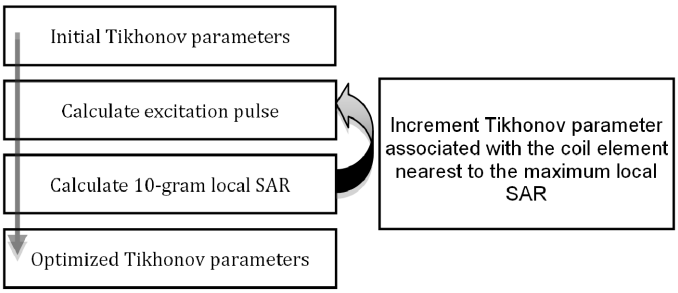

Figure 5.3: Flowchart illustrating the iterative optimization procedure used to optimize the coil-element-dependent Tikhonov parameters.

Tikhonov parameter of the coil element closest to the spatial location of the maximum local SAR value was incremented by a small number Δ, 1/5 of the initial value, while leaving the other parameters unchanged. For instance, if the penalty on coil 1 is incremented, the new matrix containing the updated Tikhonov parameters now becomes $\widetilde{\boldsymbol{\lambda}_M} = diag\{\sqrt{\lambda_1 + \Delta}\mathbf{I}, \ldots, \sqrt{\lambda_N}\mathbf{I}\}$. In this way, a higher penalty on the RF power is imposed on the coil mainly responsible for the maximum local SAR. By redesigning the RF pulse using the updated Tikhonov parameters, the location of the maximum local SAR shifts from its previous position and its value decreases. Depending on the application, the procedure can then be stopped if the desired local SAR criteria have been satisfied, for instance if the maximum local SAR drops below a given threshold, or if a maximum number of iterations is reached. The procedure is illustrated in Fig. 5.3.

Pulses designed assuming a well-centered head were directly applied to the head model rotated by 2° or 10° to assess the robustness of our optimization result with respect to the head position. In these simulations, the full effects of detuning and dematching of the coil elements due to changed head position were taken into account. Subsequently both B_1^+ and E-maps obtained with the rotated head models were used to evaluate the performance of the proposed method under these new conditions.

For comparison we also implemented global SAR minimization as proposed by Zelinski et al. (2007). First we construct a matrix where is a single vector containing the concatenation of the complex SAR contributions $\sqrt{\frac{\sigma(\mathbf{r})}{2\rho(\mathbf{r})}}\mathbf{E}_j(\mathbf{r})$ at every point $\mathbf{r}$ from the jth coil element. Using this expression Eq. 5.3 can be modified to include a cost function proportional to the global SAR:

$$min\{\|\mathbf{d} - |\mathbf{A}_{tot}\mathbf{b}_{tot}|\|_2^2 + \lambda \mathbf{b}_{tot}^H \mathbf{G}^H \mathbf{b}_{tot}\} \tag{5.7}$$

Where describes the interaction of the electric fields for each of the N sub-pulses, such that is proportional to the global SAR. Again the phase constraint was relaxed by adopting the MLS approach (Setsompop et al., 2008c). To allow fair comparison with our local SAR optimized pulses the Tikhonov scalar term was chosen to match the corresponding FA homogeneity. Pulse design and SAR calculations were implemented in C++ & CUDA^{TM}, while the results were analyzed with Mathematica (Wolfram Research, Champain, IL, USA).

5.4 Results

For each spoke trajectory, incrementing the Tikhonov parameter associated with the coil element closest to the maximum local SAR showed an approximately exponential decrease in peak local SAR (Fig. 5.4**a**). The cost of this decrease in maximum local SAR is a slight increase in the excitation inhomogeneity (Table 5.1). Compared to merely imposing a penalty on the total power, i.e. increasing the Tikhonov parameter in its scalar form, the proposed coil-specific optimization provides a more favorable trade-off (Fig.5.4**b**). Table 5.1 shows the proposed method reduces the maximum local SAR by more than 50% for a 1% increment of the FA inhomogeneity. In comparison, global SAR minimization demonstrated only minor local SAR reductions (see "Global SAR minimization 20°" results in Table 5.1). Furthermore, in some instances the local SAR was increased. Investigation of the local SAR evolution during the variable exchange method (Fig. 5.4**c**)

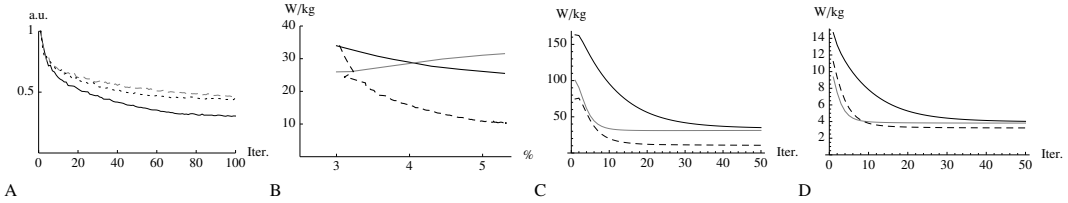

Figure 5.4: Local SAR and FA error evolution for a 20^{o} pulse. **a**: The ratio between the initial maximum local SAR and the max- imum local SAR after the Nth iteration. Results from the various k-space trajectories are indicated with different lines: solid black (2 spokes), dashed gray (3 spokes), dotted black (5 spokes). **b**: The same maximum local SAR ratio as a function of the FA inhomogeneity in the target slice (in %) for a 2-spoke excitation pulse. Results from various optimization strategies are indicated with different lines: solid black (the standard design method), solid gray (global SAR minimization), dashed black (channel-specific Tikhonov-parameters). **c**: The maximum 10-g SAR for a 2-spoke trajectory after the Nth iteration of the variable exchange method starting from a spatially invariant target phase. The final set of optimized values was used for the channel-specific Tikhonov-parameters. Results obtained using various design methods: same labeling as subfigure **b**. **d**: The global SAR evolution for the same conditions as in sub-figure **c**. Results obtained using various design methods: same labeling as used in subfigures **b** and **c**.

showed a significant initial SAR reduction. However, as the phase constraint is relaxed both methods, i.e. Zelinski's and the standard design method, converge to comparable local minima. Considering the global SAR, the coil specific Tikhonov parameter optimized pulse even outperforms the pulse designed using the global SAR optimization method (Fig. 5.4**d**).

Figure 5.5 shows the transverse slice of the head containing the maximum local SAR. SAR distributions for the initial pulses, obtained using the scalar Tikhonov parameter (L-curve criterion), are shown in the top row of Figure 5.5, while the results obtained after 100 iterations are shown in the bottom row. Coil-element-dependent Tikhonov parameters are displayed (Fig. 5.5) after optimization. For comparison the FA distributions obtained using a 3 spokes trajectory targeting a 90° FA, before and after SAR optimization, are also included in Figure 5.5.

Looking at the evolution of the SAR distribution over several optimization iterations (Fig. 5.6) reveals that the maximum hot spot changes position as expected. By comparing different pulse designs (for instance 20° vs 90°), it was found that the evolution of the SAR distribution may vary.

For both initial and optimized pulses, rotation of the head model by 2 or 10° significantly affected the local SAR while barely changing the global one (see Table 5.1). However, our optimized pulses initially designed for the head in the reference position always yielded a lower maximum local SAR than with the initial pulses obtained with a single Tikhonov parameter. Especially short pulses containing only 2 or 3 spokes got a large reduction in the maximum local SAR. Note that, a SAR reduction of more than a factor 3 was found at the cost of a 2.3% -increment in FA error using the 2 spoke trajectory, a 2-fold SAR reduction could be obtained with an $\sim$ 1% -increment by halting the optimization procedure at an earlier stage. In general, the local SAR maxima found for the rotated head models were all reduced by a factor larger than 1.84.

Finally, changing the reference position of the head model from centered to 10°-rotated and repeating the optimization procedure with the "rotated" E-fields & B1-maps allowed over a 4-fold reduction in local SAR if the head stays in the rotated configuration (result not reported in table above). For example, optimization of the 2-spoke 20° pulse reduced the maximum local SAR from 42 W/kg to less than 10 W/kg for 100% duty cycle. In general, the maximum local SAR could be reduced to values similar to the optimized results obtained from the centered head configuration.

		Centered				2° Rotation		10° Rotation	
		Local	Global	FA error	Mean FA	Local	Global	Local	Global
Initial 20°	**2**	33.9	3.87	3.0%	19.6°	30.6	4.48	42.7	3.85
	3	9.8	1.40	2.0%	19.7°	10.7	1.69	13.1	1.41
	5	4.8	0.67	1.4%	19.48°	4.7	0.80	6.1	0.67
Global SAR *minimization* 20°	**2**	31.5	3.84	5.3%	19.3°	34.3	5.30	46.9	4.56
	3	10.0	1.35	3.1%	19.7°	14.1	2.00	18.2	1.72
	5	6.3	0.65	2.1%	19.8°	5.9	0.79	7.7	0.65
Optimized 20°	**2**	10.3	3.11	5.3%	19.4°	16.5	4.33	12.8	3.02
	3	4.5	1.44	3.1%	19.6°	6.4	1.95	5.8	1.38
	5	2.1	0.62	2.1%	19.8°	3.3	0.85	2.7	0.62
Initial 90°	**2**	797.2	88.46	2.9%	88.0°	680.7	102.64	976.2	87.16
	3	238.6	30.75	1.6%	88.9°	250.0	37.06	310.8	30.91
	5	106.4	14.36	1.4%	89.0°	101.7	17.120	133.9	14.49
Optimized 90°	**2**	262.8	73.05	4.4%	86.7°	361.1	98.09	313.4	68.36
	3	107.7	30.72	2.4%	88.5°	143.8	41.51	139.9	29.45
	5	47.0	14.21	1.7%	88.5°	68.2	17.71	60.6	12.91

Table 5.1: 'Local' corresponds to the maximum 10-g local SAR while 'Global' stands for the SAR averaged over the entire head (both in W/kg). Bold numbers indicate the number of spokes used in the k-space trajectory. RF pulses were designed and optimized for the head model in the centered position. Global and maximum local SAR were calculated when applying these pulses to the centered and rotated head models.

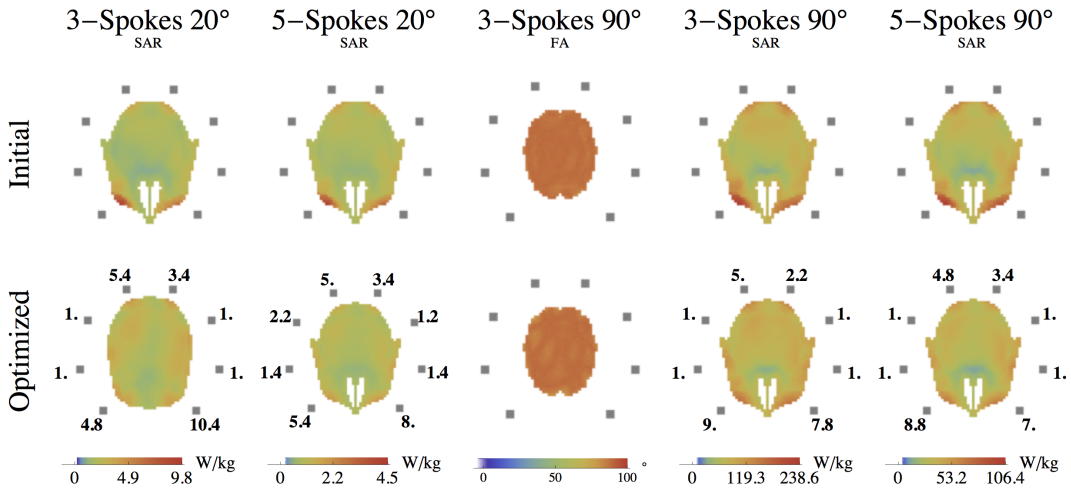

Figure 5.5: Ten-g local SAR distributions found for slice selective excitation pulses with a homogeneous excitation target profile (100% RF duty cycle is assumed). SAR distributions for pulses designed with respectively 3- and 5-spoke k-space trajectories are shown for both 20° and 90° FA targets. The top row shows the slice that includes the maximum 10-g local SAR for the initial excitation pulses. The bottom row shows the displaced equivalent slice for the optimized excitation pulses. Coil element positions are indicated by the gray squares. Optimized coil-element-dependent Tikhonov parameters are shown next to their associated coil elements (to be multiplied by 10^{-6}). For the 90°-tip-angle target, the initial pulse has the same scalar Tikhonov parameter as for the 20° FA. Optimized coil-element-dependent Tikhonov parameters for the correction term are shown (to be multiplied by 10^{-6}) next to their associated coil elements, while the parameters for the first-order term were the same as for the 20° FA scenario. In the center the FA distribution in the target slice (brain only) is shown before (top) and after optimization (bottom).

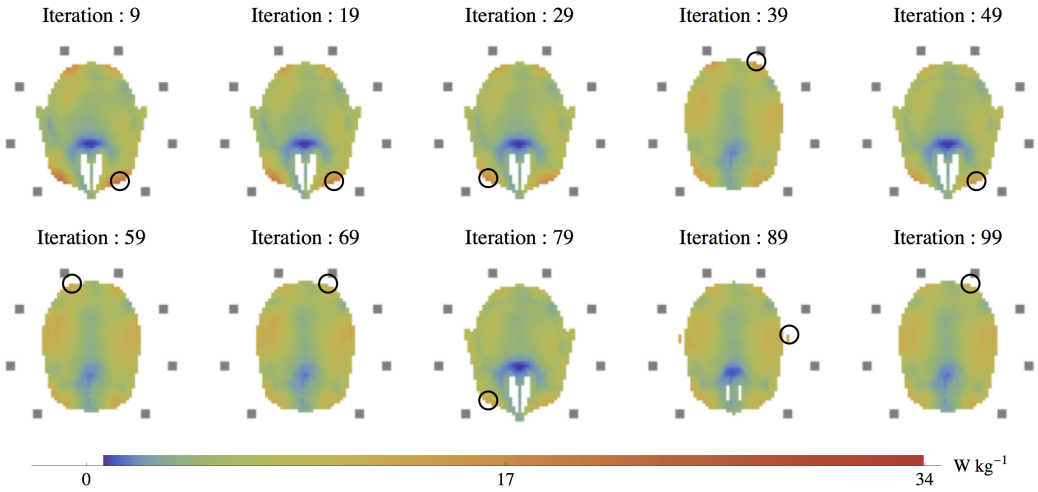

Figure 5.6: Ten-g local SAR distributions found for a 2-spoke slice selective excitation pulse with a 20° homogeneous excitation target profile (100% duty cycle). Slices containing the maximum local SAR at different stages during the optimization procedure are shown. The location of the maximum hot spot is indicated with a circle for each iteration.

5.5 Discussion

The above results show that coil-element-dependent Tikhonov parameters can be used to reduce and move hot spots. The assumption that it is the coil closest to the hottest spot that contributes the most to the maximum local SAR was a key element in our optimization procedure. This assumption originates from the observation that for the studied microstrip coil, the electric fields inside the head are strongly attenuated. Then it was indeed confirmed by observing the change of location of the hottest spot with our optimization iterations. However this assumption could break with different coil geometries, in particular if the diameter of the coil is much larger than the one proposed in this study[1]. By applying the optimization in a coil-element-dependent fashion, we showed that reductions of more than a factor of 2 in the maximum local SAR are possible on a well-centered head at the expense of approximately a 1%-increment in FA inhomogeneity[2].

As an alternative to the nearest coil element approach, algorithms such as the simplex or the gradient descent could be used to optimize the coil-dependent Tikhonov parameters. However, the 10-g local SAR would have to be evaluated for every parameter change in the design, greatly increasing the computational task. Even with the NVIDIA® CUDA^{TM}-based optimizations available to us at this time, local SAR evaluation integrating all degrees of freedom can still be a tremendous constraint. On the other hand, the channel-dependent Tikhonov parameter method has a more restricted number of degrees of freedom and could therefore be easily applied to k-space trajectories with large numbers of time steps. For instance, it could be potentially used in combination with variable density spirals (Liu et al., 2008), to obtain an additional SAR reduction. Furthermore, although the hot spot can often be found at similar initial positions, many different hot spot positions can be found during optimization. The channel-dependent method allows all these scenarios to be optimized without increasing the computational complexity, unlike adding additional control points needed to minimize possible new hot spot locations. Based on the performance of relatively standard hardware (2.4GHz Intel® Core^{TM} 2 Duo laptop including a NVIDIA® GeForce® 9600m graphics card), pulses optimized over 100 iterations can be found in less than 1 min. In the demonstrated optimization procedure, the parameters were incremented equally for all time steps based on the maximum 10-g local SAR location, a "step" being a spoke in the reported work. By replacing the identity matrix $\mathbf{I}$ in $\boldsymbol{\lambda}_M$ with an optimized diagonal matrix, independent Tikhonov parameters can be defined for each time step t_i

[1] Since the publication of the work presented here (Cloos et al., 2010c), generalized local SAR optimization techniques have underlined the relation between local SAR of the coil geometry for close fitting micro-strip array-coils (Sbrizzi et al., 2012). In these scenarios such methods indirectly enforce our assumption that it is the coil-element closest to the hottest spot that contributes the most to the maximum local SAR.

[2] Although the performance of the off-slice magnetization suppression was not explicitly validated in this work, it may be expected to remain relatively unaffected by the optimization procedure, at the very least in the linear domain of the small-tip-angle approximation, as long as the selectivity of the individual sub-pulses is of sufficient quality.

defining the amplitude of the sub-pulses $b_n(t_i)$. To keep the problem reasonably simple, we have chosen to keep the regularization parameters the same for every time step while allowing them to vary among coil elements. Nevertheless, allowing the Tikhonov parameters to vary with time steps could yield a better solution since a larger number of degrees of freedom would be available for optimization. Compared to other SAR-reducing methods such as global SAR optimization and increasing the scalar Tikhonov parameter, the method proposed here showed considerable advantages. Increasing the Tikhonov parameter in its scalar form allows the local SAR to be decreased (Fig. 5.4**b**) at the expense of a large FA error. Global SAR optimization can potentially result in significant SAR reductions (Fig. 5.4**c**&**d**). However, in combination with the variable exchange method sub-optimal local-minima can be found. Furthermore, the local SAR can also be increased while the global one is reduced (Table 5.1). Considering a head displaced from the coil centre, the local SAR can be increased substantially. For all the head positions we tried, pulses obtained by the proposed method from the centered reference head model yielded a lower peak SAR value than the one found by the standard design method, making our approach more robust with respect to head displacement. Furthermore, using Tikhonov regularization in its scalar form somewhat assumes that all coil elements deposit similar amounts of power in the patient, therefore that the head is round, well-centered and that all channels transmit equally well. In practice it might be hard to perfectly centre each patient's head due to differences in size and asymmetries in head geometry. The 4-fold reduction in peak local SAR we obtained for the head model rotated by 10° suggests that the more asymmetric the geometry/position of the head is in the coil, the more likely the optimization method reported here can help decrease the peak SAR value. Also often the power available per channel is limited. Under these conditions, it can be advantageous to optimize pulses based on the method described here. Incrementing the coil-element-dependent Tikhonov parameters based on the power per channel allows pulses to be found that maximize the utilizable power and suppress solutions where too large amplitudes occur on a single channel.

In conclusion, a novel method was demonstrated to reduce the local SAR in excitation pulses for magnetic resonance imaging systems using parallel transmission. Patient-specific local SAR mitigation is possible in both the small and the large-tip-angle domain by introducing coil-element-dependent regularization parameters. Under the assumption that the coil element closest to the maximum local SAR is the dominant contributor, the local SAR could be reduced by a factor of 2 to 4 for a variety of spoke-based k-space trajectories. This should be useful in high field applications where reductions of local SAR in parallel excitation are strongly desired.

6 k_T-Points: Short Three-Dimensional Tailored RF Pulses for Flip-Angle Homogenization Over an Extended Volume

This chapter has been accepted for publication as: M. A. Cloos, N. Boulant, M. Luong, G. Ferrand, E. Giacomini, D. Le Bihan, and A. Amadon."k_T-Points: Short Three-Dimensional Tailored RF Pulses for Flip-Angle Homogenization Over an Extended Volume" Magnetic Resonance in Medicine 2012 January; 67 (1): 72–80.

The priciple idea described in this chapter was filed as patent aplication 10290205.3 (WO 2011/12 8847 A1), "Method and apparatus for compensating for B1 inhomogenity in magnetic resonance imaging by nonselective tailored RF pulses".

Abstract

With Transmit-SENSE, we demonstrate the feasibility of uniformly exciting a volume such as the human brain at 7T through the use of an original minimalist transmit k-space coverage, referred to as "k_T-points". Radio-frequency energy is deposited only at a limited number of k-space locations in the vicinity of the center to counteract transmit sensitivity inhomogeneities. The resulting non-selective pulses are short and need little energy compared to adiabatic or other B_1^+-robust pulses available in the literature, making them good candidates for short-TR 3D sequences at high field. Experimental verification was performed on 3 human volunteers at 7 T by means of an 8-channel transmit array system. On average, whereas the standard circularly polarized excitation resulted in a 33% flip angle spread (standard deviation over mean) throughout the brain, and a static RF-shim showed flip angle variations of 17% and up, application of k_T-point-based excitations demonstrated excellent flip angle uniformity (8%) for a small target flip angle and with sub-millisecond durations.

6.1 Introduction

Increased static magnetic fields enhance the signal-to-noise ratio so that finer spatial resolutions can be achieved. However at high field, the proton Larmor frequency increases to the extent where the wavelength becomes smaller than the volumes of interest (VOI). As a result of dielectric resonances and radio-frequency (RF) interferences, inhomogeneous transmit profiles (B_1^+) develop through the body to be observed (Yang et al., 2002; Van de Moortele et al., 2005). This translates into zones of shade and losses of contrast distributed across the image.

Several methods have been proposed to counteract the B_1^+ inhomogeneity issue. Already in the fifties, Carr, Purcell, Meiboom and Gill noticed that shifting the phase by 90° of a train of pulses with respect to the phase of an initial pulse cancels the B_1^+ inhomogeneity errors at zero order (Carr and Purcell, 1954; Meiboom and Gill, 1958). In the eighties, a plethora of RF pulsing techniques was developed to counteract that same problem, in particular frequency-sweeping adiabatic pulses (Baum et al., 1985; Silver et al., 1985; Staewen et al., 1990), nowadays used in many standard sequences to invert the magnetization. Optimal performance of these methods usually requires long pulses and high power, i.e. highly energetic pulses. This results in a notable specific absorption rate (SAR) contribution, limiting their applicability.

In more recent years, several techniques have appeared to tackle these problems. Strongly modulating pulses have shown to be useful at 3T and 7T (Boulant et al., 2008, 2009), but have also shown their limits. Using RF pulses in combination with magnetic field gradients (Pauly and Nishimura, 1989) have demonstrated their ability to counteract minor spatial B_1^+ variations in both volumes (Saekho et al., 2005) and single slices (Saekho et al., 2006). In the presence of stronger B_1^+ variations, as observed in the brain at 7 Tesla, again long pulses are needed to obtain a homogeneous excitation profile (Zelinski et al., 2008c). To further facilitate B_1^+-inhomogeneity mitigation at high fields, parallel transmission (Katscher et al., 2003; Zhu, 2004; Grissom et al., 2006) was introduced, providing better control of the RF distribution and helping homogenization of the spins flip angle (FA) within the VOI. Static RF shimming solely relies on setting fixed optimized amplitude and phase combinations on each transmitting channel to reach good homogenization of the B_1^+ distribution in a limited VOI (Mao et al., 2006). Dynamic RF shimming, or "Transmit-SENSE" (Katscher et al., 2003; Zhu, 2004), addresses instead a FA target distribution by allowing RF waveforms to be different on every channel as gradient pulses are played to cover a predetermined k-space trajectory. "Spokes-based" waveforms (Saekho et al., 2006) perform especially well in the framework of parallel transmission due to the extra degrees of freedom available for pulse design with good FA homogenization over a slice in the human brain at 7 Tesla (Setsompop et al., 2008a). But until now, no demonstration was made which shows similar performance in 3D over an extended volume such as a human brain. Although multishot 3D coverage of the transmission k-space has been proposed with trajectories such as a stack of spirals (Saekho et al., 2005), it has never led to successful application at high fields because, again, it is penalized by lengthy RF pulse durations, bringing B_0-inhomogeneity, relaxation and magnetization transfer issues up front (Boulant, 2009; Matson and Liu, 2010).

In this paper, we introduce a concept that provides spatially uniform excitation in an extended volume with tailored, yet non-selective, RF pulses. These pulses rely on an original transmit k-space trajectory which covers a minimal number of locations, the so-called "k_T-points", so as to not waste time and energy at spatial frequencies which need not be addressed in the context of smooth RF inhomogeneities. Applied in conjunction with parallel transmission, sub-millisecond pulses are thus possible, leading to a broad spectrum of potential applications in 3D-acquired sequences with short repetition time (TR). While the original method was first reported in (Cloos et al., 2010b; Amadon and Cloos, 2010), a more comprehensive description is given here, alongside a demonstration of its application to 3D fast low angle shot sequences (FLASH) in the human brain at 7 Tesla. Results are analyzed and discussed by comparing them with those obtained by more standard methods such as static RF shimming.

6.2 Methods

Pulse design

The method presented below allows the design of RF-inhomogeneity-counteracting pulses which are non-selective based on an original transmit k-space trajectory, hereafter referred to as "k_T-points" (Cloos et al., 2010b). It is inspired from the slice-selective Fast-kz trajectory (Saekho et al., 2006), often referred to as "spokes" in the literature (Setsompop et al., 2008a; Zelinski et al., 2008c,d; Setsompop et al., 2008c), which is used to homogenize the excitation in a single slice, therefore solving a 2D problem even though spokes spread in 3D k-space. The location of spokes in the (k_x, k_y) plane proves to be very sparse in the context of parallel transmission, with only 2 spokes being sufficient to homogenize to a good extent an axial slice in the center of the human brain at 7T (Setsompop et al., 2008a). In the same manner, for a homogeneous 3D excitation, k_T-points embody a limited number of excitation sub-pulses interleaved with gradient blips to travel between transmission sites in three-dimensional k-space. In our case, sub-pulses will simply be square and no gradient is played a priori whilst pulsing RF. The name "k_T-points" indicates that RF-power is applied only while stationary in k-space, "k_T" standing for Transmission k-space. Attributable to the similarity to the spoke trajectory in the (k_x,k_y) plane (Saekho et al., 2005), techniques introduced to refine spoke placement (Zelinski et al., 2008d; Yip et al., 2006; Ma et al., 2010) can also be applied to find k_T-point locations. In this work, such locations were obtained by applying a threshold on the inverse Fourier transform of the mask, similarly to the method introduced by Ma et al. (2010). Although more thorough methods could potentially improve excitation uniformity, the aforementioned approach was selected for its computationally simplicity allowing real-time evaluation for in-vivo experiments.

To show the validity of the method, we applied it to homogenize the FA over the entire human brain at 7T, by implementation on a transmit-array system with 8 independently-driven channels. The brain volume was first extracted from initial images acquired with a short B_0-mapping sequence (preliminary step detailed later on). Subsequent to the Fourier transform of the 3D brain mask, the k_T-point locations were determined by the position of the N largest magnitude components in k-space[1]. From these N locations, the trajectory was deduced by solving the associated traveling salesman problem. Then, pulse design was performed with Mathematica (Wolfram Research, Champaign, IL, USA) using the small tip approximation in the spatial domain (Grissom et al., 2006), and the local variable exchange method to solve the magnitude least squares (MLS) problem (Setsompop et al., 2008a). Optimal Tikhonov parameters were found by applying the L-curve criteria (Hansen, 1992; Cloos et al., 2010c). All pulse design calculations were performed on the same grid as was used for B_1^+-mapping, taking into consideration only the voxels inside the VOI (the entire brain in our case).

As k_T-points are targeted towards 3D sequences with no spatial selectivity and small TR, such as the MP-RAGE sequence (Bernstein et al., 2004), short excitation pulses are favored. Repeating the design procedure over several iterations, as illustrated in Fig. 6.1, facilitated the optimization of the individual sub-pulse durations. First an initial candidate is obtained by designing an excitation pulse with extremely short sub-pulse durations (10-μs). Comparing this initial candidate's sub-pulse amplitudes to a pre-defined maximum voltage, a set of new sub-pulse durations was obtained by keeping the sub-pulse time integrals the same between iterations. From these sub-pulse durations, a new candidate excitation pulse was found taking ΔB_0 evolution into account. Due to the change in ΔB_0 evolution between iterations, this procedure had to be repeated a few times until an RF solution was found that both minimized sub-pulse duration and satisfied the amplitude constraint. In order to allow relatively low TR values, the amplitude was constrained to 90 V per channel, so as to keep the output RF power below the threshold later discussed in the SAR monitoring section.

Setup & B_0 shimming

Three volunteers were scanned to demonstrate the k_T-point method as a way to homogenize excitation in their entire brain. Informed consent was obtained from them in accordance with guidelines of our institutional review board. Experimental validation was performed on a Siemens 7T Magnetom scanner (Erlangen, Germany), equipped with an 8-channel transmit array (1 kW peak power per channel). Our AC84 head

[1] Magnitude of FFT(Abs[CP-mode] - Abs[Target])

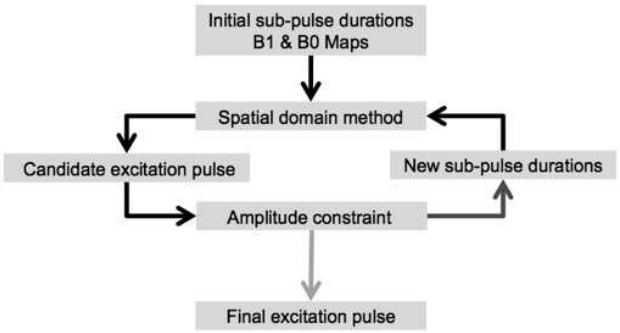

Figure 6.1: Schematic overview of the iterative method used to optimize the sub-pulse durations. To start, extremely short sub-pulses are set to provide a first candidate excitation pulse. New sub-pulse durations can be found by comparing the maximum amplitude to a predefined constraint. Redesigning the excitation pulse based on the appropriate sub-pulse durations produces a new and slightly different candidate excitation pulse. This cycle is repeated until an excitation pulse is found that minimizes the total pulse duration while satisfying the amplitude constraint.

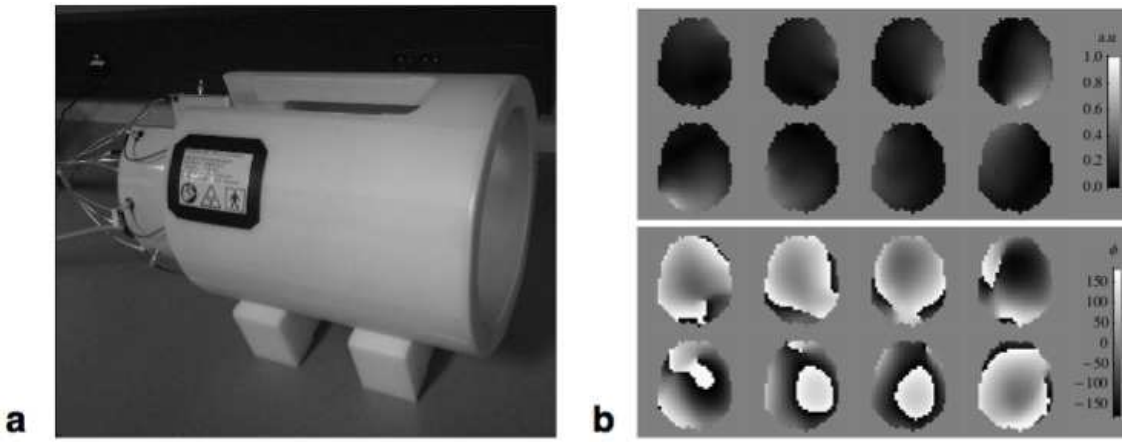

Figure 6.2: **a**: Eight channel transmit-array coil used in this work. **b**: Transmit sensitivity and relative phase maps measured in the brain for each of the 8 transmit elements (only central axial slice shown here).

gradient set allowed amplitudes up to of 50 mT/m and a slew rate of 333 mT/m/ms. Because of the RF field at 7T propagating to body regions well outside the RF coil and of the rapidly-dropping linearity of the head gradient coil along z, signal arising from the region below the neck (hereafter referred as "shoulders") is encoded in such a way that it aliases into the main image (third-arm artifact). To reduce such contributions, both body and head shim coil sets, having a different coverage along the z-axis, were exploited to dephase the signal from the shoulders without affecting the signal from the head. To this end, strong opposing currents were set on the 2nd-order z-affecting shim coils, effectively spoiling the signal originating from shoulder area (Wiggins et al., 2010). B_0-shimming was then performed with our own procedure after acquiring a short (30 s) three-echo FLASH sequence using all transmit channels in an approximately circularly-polarized (CP) mode. This typically leads to B_0 standard deviations of approximately 45 Hz with peak values up to 250 Hz near the sinus cavity. For both RF transmission and reception, a home-made transceiver-array head coil was used (Ferrand et al., 2010), which consists of 8 stripline dipoles distributed every 42.5-degrees on a cylindrical surface of 27.6-cm diameter, leaving a small open space in front of the subject's eyes (Fig. 6.2**a**). All dipoles were tuned ideally to the proton Larmor frequency at 7T and matched identically to a 50 Ω line impedance.

Specific Absorbtion Rate Monitoring

Both the 10-sec- and 6-min-averaged RF power levels were monitored in real-time for each transmit-channel. To account for the plethora of possible E-field interference patterns, a conservative approach was adopted

to ensure patient safety and compliance with the SAR guidelines (IEC, 2002). Power limits were derived from finite element simulations (HFSS, Ansoft, Pittsburgh, PA) (Cloos et al., 2010c; Kozlov and Turner, 2009) performed for this specific coil loaded with different human head models in various positions, taking the worst-case scenario amongst those. Trust in our simulations was gained by matching B_1^+-maps obtained from them with that obtained from measurements on a spherical phantom of well-known electric permittivity and conductivity. Then, assuming E-field constructive interference in every voxel of the human-head models, a conservative power constraint was found for both 10-sec and 6-min averages.

B_1^+& B_0-mapping

Currently, non-selective B_1^+-mapping is particularly difficult due to the combination of time and conservative SAR constraints for parallel transmission studies on human volunteers. Measuring relative B_1^+-maps in the low-tip-angle regime provides a low SAR solution that can be upgraded to provide quantitative FA maps using a single high angle measurement (Setsompop et al., 2008a; Van De Moortele et al., 2007). In order to minimize T_1-weighting, these relative B_1^+-maps are obtained from a small-tip-angle spoiled-gradient-echo sequence (FLASH) with relatively long TR (0.2-1.0s) to remain in the domain where the signal intensity is linearly dependent on the FA over a sufficiently large range. Considering 3D tailored excitation pulses, such TR values extend the total duration of the B_1^+-mapping and pulse validation procedures beyond the maximum scan time appropriate for a single human volunteer. Still, fast B_1^+-mapping is desired to validate non-selective tailored RF-pulses such as k_T-points. Considering the T_1 values corresponding to the main tissues in the human brain, gray and white matter ($T_1 < 2$s (Rooney et al., 2007)), the signal intensity difference is approximately 5% or less if FA $< 6°$ and TR $\leq$ 50ms at 7T. In this domain, intensity attenuation due to T1 in a FLASH image can then be corrected, to first order, for a known FA distribution, by assuming an average T_1 in the signal equation (Bernstein et al., 2004). In order to increase the overall accuracy, the relative B_1^+-mapping procedure was implemented in the framework of the matrix-based method proposed by Brunner et al. (Brunner and Pruessmann, 2008). To this end, from an approximately CP-mode, a FLASH image set was obtained with 8 different phase combinations by cyclically shifting the transmit-phase by 180° on each one of the transmit-channels. The FLASH sequence parameters were: TR = 50 ms, 5-mm isotropic resolution with a 48x48x36 matrix in sagittal acquisition, and 8 simultaneous 100-µs 30V broad pulses later validated to yield peak FAs smaller than 6°. Subsequently, more time-consuming quantitative complex FA-maps, AFI_i & AFI_j, were obtained for two approximately orthogonal phase combinations contained in the set of FLASH acquisitions. Two quantitative measurements were performed rather than a single one in order to increase the accuracy of the resulting FA-maps in regions with low SNR. For this purpose, the AFI sequence (Yarnykh, 2007), including spoiling improvements (Nehrke, 2009) and two additional echoes for ΔB_0 mapping (Amadon and Boulant, 2008), was used with the following sequence parameters: TR1/TR2 = 40/200ms, TE1/TE2/TE3 = 1/2/3ms, same acquisition matrix as for FLASH, and 8 simultaneous 900-µs 60V broad pulses. From the 8 FLASH images and the 2 AFI maps, a complete set of 8 FA-maps (FA_n) was obtained in the following way:

$$FA_n = \begin{cases} c\frac{FLASH_n(|AFI_1|+|AFI_2|)}{|FLASH_1|+|FLASH_2|} & if \quad n \neq 1,2 \\ cAFI_n & otherwhise \end{cases} \tag{6.1}$$

where $FLASH_n$ indicates acquisitions obtained with the nth phase combination in the set and c is the scaling factor between the AFI_i & $FLASH_i$ excitations. The B_1^+- or equivalent FA-map for each individual transmit-channel can then be retrieved by inverting the corresponding encoding matrix (Brunner and Pruessmann, 2008). Typical individual B_1^+-maps obtained with our coil on a human brain at 7T are shown in Fig. 6.2**b**.

Validation

Substituting the tailored pulses for the square pulses in the FLASH sequence allows validation of their performance. To this end, the two previously acquired AFI acquisitions and their associated FLASH images now allow the results to be quantified by:

$$FA_{res} = c\frac{FLASH_{res}(|AFI_1| + |AFI_2|)}{|FLASH_1| + |FLASH_2|} \tag{6.2}$$

where $FLASH_{res}$ is the image obtained using the tailored excitation pulse under consideration and c is the scaling constant introduced in the B_1^+-mapping section. For comparison, both a pseudo CP-mode and a static RF shim were considered. The pseudo CP-mode was synthesized by aligning the 8 transmit phases in the center of the brain. The static shim was obtained with the same method as for the k_T-points pulse design, now limited to only one sub-pulse played at the center of k-space. For each case, a suitable target FA was selected based on the criterion that the expected peak would remain below 6°, bearing in mind that too low FA would result in poor SNR. Measured FA variations in the VOI were quantified by means of the standard deviation over the mean.

Qualitive comparison

Both square pulses in a pseudo CP-mode and k_T-point-based excitation pulses were inserted in a higher resolution multi-echo FLASH sequence. Sequence parameters were: target FA = 6°, TR = 50 ms, TE = 4 ms and 20 ms, 2-mm isotropic resolution with a 128x128x80 matrix in sagittal acquisition. The shorter echo time yielded a mostly proton-density weighted image whereas the second echo led to a T_2*-weighted image. Receive sensitivity correction was applied during image reconstruction to provide a direct qualitative comparison between the different excitation pulses (Wang et al., 2005).

Off-resonance & k-space location sensitivity

To investigate the sensitivity of the proposed method with respect to off-resonance effects and k_T-point placement, a series of simulations was performed. Measured B_1^+ and ΔB_0 maps from subject #3 were used to design k_T-point-based excitations from both our implementation of the inverse Fourier method and a greedy-algorithm. In the latter, similar to the sequential optimal selection method proposed by Ma et al. (2010), k-space is searched to yield the next best k_T-point location. To incorporate the magnitude least squares approach (Setsompop et al., 2008c) and pulse duration optimization, the complete pulse design procedure was performed when evaluating each potential k-space location, finally leading to an optimized k_T-point trajectory. Subsequently, full Bloch simulations of the obtained excitation pulses were evaluated under different off-resonance conditions, by introducing an artificial ΔB_0 offset ranging from -300 to +300Hz in 100Hz increments. In addition, some indication of the pulse bandwidth was provided by calculating the full width at half maximum of the central lobe averaged over all transmit-channels as well as the standard deviation.

6.3 Results

Quantitative analysis

As anticipated from earlier phantom studies (Cloos et al., 2010b), we found the low spatial frequency components to dominate k-space upon Fourier-transforming the 3D brain mask. Bloch simulations indicated that, for our setup, 5 k_T-points were sufficient to achieve spatial excitation uniformity better than 10% in the human brain. Although the exact locations showed some variations between subjects, they were commonly contained within a / FOV radius around the DC component (Fig. 6.3**a**). The associated k-space trajectories, targeting a 5°-FA everywhere in the brain, resulted in excitation pulses of less than 450-µs (Fig. 6.3**b**). These solutions were typically found in 3 to 4 iterations of the pulse duration optimization procedure. Based on the performance of an Intel core 2 duo 2.4-Ghz with 4-GB RAM, the complete pulse design procedure could be performed in roughly 30 s.

Results obtained with different excitations pulses are shown in Fig. 6.4 for subject #1. In addition to the central brightening effect, the pseudo CP-mode demonstrated low FA's in the frontal lobe and cerebellum (Fig. 6.4**a** – 31.7% FA variation across the whole brain). As expected, the static-shim (a single k_T-point optimized at the center of k-space) produced a significant improvement over the synthesized CP-mode (Fig. 6.4**b**). Still, large spatial variations remain in the excitation profile (16.7% FA variation). Using 5 k_T-points, good FA homogenization was achieved throughout the volume of the brain (Fig. 6.4**c** – 7.8% FA spread). Considering the many potential experimental inaccuracies, the measured and simulated result corresponds

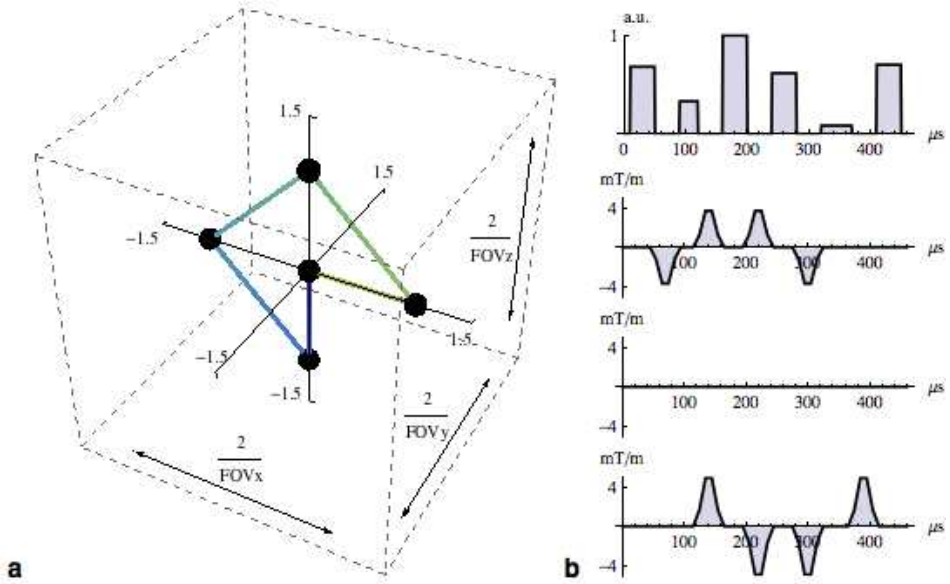

Figure 6.3: Example kT-point-based k-space trajectory, RF subpulse train and gradient blips designed for FA homogenization in the human brain at 7T. **a**: The trajectory used to move between the different points in transmission k-space. Spheres indicate stationary points where RF-power is applied. **b**: The RF amplitude solution found for one of the 8 channels and the corresponding gradient blips along x, y and z. The different sub-pulse durations are optimized to minimize the total duration of the excitation without exceeding the maximum allowed amplitude on transmit-channels. A long low power sub-pulse on one channel implies that at least one of the other channels requires a high level of power.

well with the full Bloch simulation (Fig. 6.4**d**, – 5.5% FA spread). Still, adding two additional k_T-points can provide a further improvement at the expense of an increase in pulse duration (Table 6.1).

In addition to the homogeneity results obtained for each experiment of this study, Table 6.1 depicts the total energy required by the RF coil in each case, i.e. the sum of the integrals of the squared pulse voltage amplitudes (assuming 50 Ω load). It becomes clear that the trade-off for the improved FA distribution is an increase in total incident energy. In this case, we observe that the pseudo CP-mode requires on average about 2/3 of the energy required by the 5 k_T-point excitation. Interestingly, although the k_T-points deposit significantly more energy than the RF-shim, the energy is much more evenly distributed among the transmit-channels, as shown from the maximum total energy per channel in Table 6.1.

Qualitative comparison

The impact of the FA-homogenizing quality of the excitation strategies can clearly be seen in the proton-density-weighted 3D FLASH images (Fig. 6.5). The very low FA's produced by the CP-mode (FA = 6°, pulse duration = 270-μs) in the cerebellum, occipital, frontal and temporal lobes are manifest by the lack of signal in these regions (Fig. 6.5**a**). With 5 k_T-points (FA = 6°, pulse duration = 490-μs), the signal in these areas is mostly recovered (Fig. 6.5**b**). Most dramatic is the improvement obtained in the cerebellum, which is now clearly visible with the same uniform excitation as throughout the rest of the brain, even in T_2*-weighted images (Fig. 6.5). Yet complete FA-recovery did not occur near the brain stem region, because this is the most affected by the residual third-arm artifact mentioned in the B_0-shimming section.

Off-resonance & k-space location sensitivity

Empirically we found that the proposed implementation of the inverse Fourier method produced adequate k-space locations for FA homogenization throughout the human brain by means of k_T-point-based excitation (Table 6.1). Nonetheless, simulations indicate that more thorough methods such as a greedy algorithm can

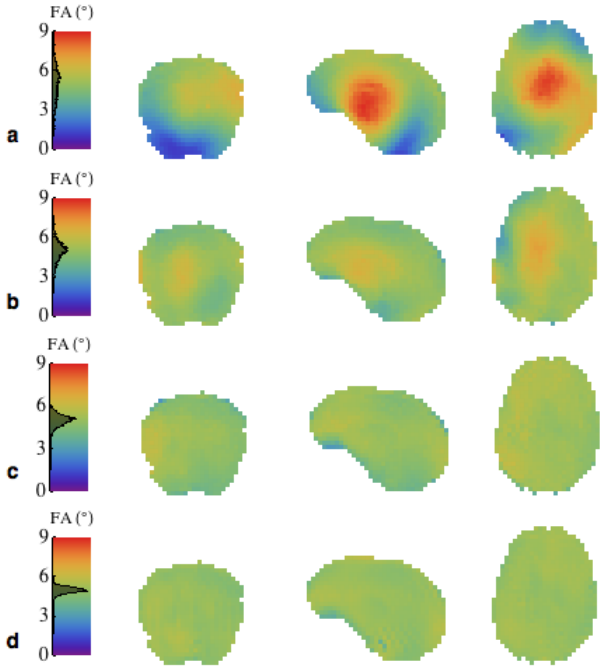

Figure 6.4: Measured and simulated FA distributions in subject #1. They are displayed in central coronal, sagittal and axial brain cross-sections for three RF strategies: **a**: CP-mode (measured). **b**: Static shim (measured). **c**: 5 kT-points (measured). **d**: 5 kT-points (full Bloch simulation). The CP-mode and RF-shim were scaled to produce an average of 5°. For each measurement, the corresponding histogram is superimposed on the color bar.

	Subject 1				**Subject 2**				**Subject 3**				
	CP-mode	RF-shim	5 k_T-points	7 k_T-points	CP-mode	RF-shim	5 k_T-points	7 k_T-points	CP-mode	RF-shim	5 k_T-points	7 k_T-points	
Pulse duration	100	100	440	570	100	100	430	540	100	100	430	630	μs
Fore-& midbrain	28.9	17.0	7.2	7.0	29.2	25.6	7.4	8.3	35.4	16.7	8.0	6.2	%
Cerebellum	47.8	13.8	11.3	10.6	53.2	38.6	16.0	18.7	60.4	19.4	15.5	11.0	%
Total Brain	31.7	16.7	7.8	7.5	31.5	26.6	8.3	9.4	35.5	17.0	8.9	6.8	%
Total energy	67.8	88.7	95.4	108	71.5	111.0	102.0	111.0	81.6	113.6	103.0	80.2	mJ
MTE channel	8.5	29.8	19.0	22.6	8.9	42.0	16.4	20.6	10.2	40.2	17.6	31.4	mJ

Table 6.1: Measured FA homogeneity and energy-balance obtained with different excitation pulse strategies. The CP-mode and RF-shim pulse amplitudes were scaled to produce an average of 5°. The spatial variation of the FA in different regions (Fore- & midbrain, Cerebellum, Total brain) of the brain is expressed as the standard deviation as percentage of the mean. Total Energy: the total incident energy per RF excitation on all channels. MTE channel: the maximum total incident energy per pulse per channel. Considering that the simulation consistently predicts improved results with an increased number of k-space locations, that the decreased excitation fidelity obtained with 7 rather than 5 k_T-points in subject 2 is most likely related due to subject movement between.

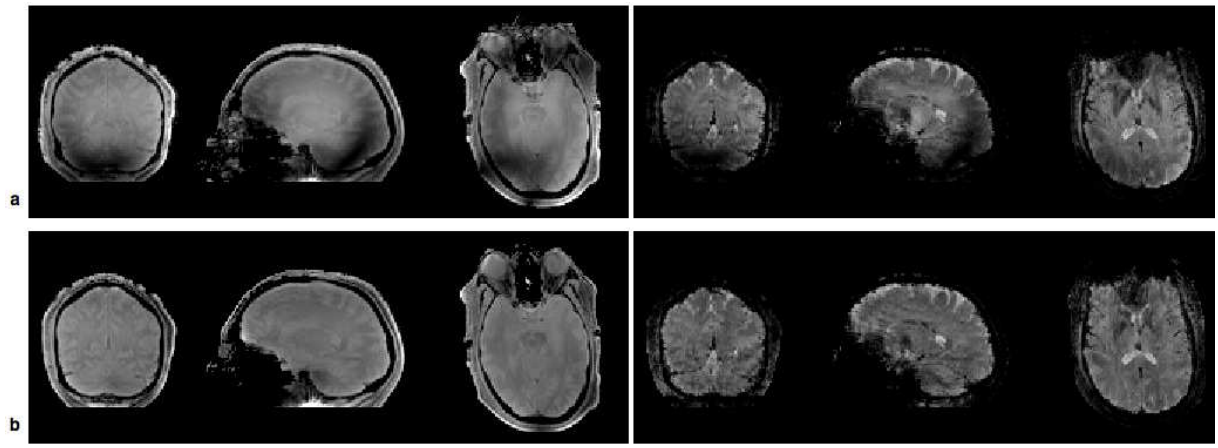

Figure 6.5: FLASH images obtained using the pseudo CP-mode and 5 k_T-points (subject #2). The receive profile was removed in post processing. **a**: Proton-density-weighted followed by T_2*-weighted images from the CP-mode (pulse duration: 270-µs). **b**: Same using 5 k_T-points (490-µs).

further improve the excitation uniformity (Table 6.2). However, this method produced trajectories traveling slightly further out in k-space (up to 2/FOV). Therefore, in order to accommodate the slew-rate constraints, some of the gradient blips would need to be lengthened from 40 to 60 µs. When small FA's are targeted, this results in significantly longer excitation pulses (Table 6.2). Considering off-resonance effects, we observe that not only the mean FA decreases as may be expected from the average bandwidth, but also the FA homogeneity achieved by the proposed method degrades with increased frequency offsets. Yet even with a ±300 Hz offset, this degradation does not reach the level of FA variation obtained at resonance with the static RF-shim. This is especially true for k_T-points found from the inverse Fourier-method as they are shorter than those found from the greedy algorithm, which therefore demonstrates their robustness against B_0-offsets. Although slightly different results are obtained depending on the sign of the frequency offset, significant deviations only appear with long excitation pulses applied to a large frequency offset.

6.4 Discussion

We have introduced a novel 3D k-space trajectory, the k_T-points, towards B_1^+ inhomogeneity mitigation over an extended volume. It is comprised of a minimal number of k-space locations in conjunction with non-selective sub-pulses. Implemented on an eight-channel parallel transmit-array, spatially uniform excitation was demonstrated in the entire brain at 7 Tesla. In a previous work by Setsompop et al. (2008a), slice-selective FA homogenization was demonstrated in central transversal slices of the brain, with 7.5% FA variation across the slice. Our results obtained in the entire brain volume showed comparable FA variations (Table 6.1). It should be noted that although this method provided good excitation uniformity in the brain, artifacts related to external effects remain. With our setup, depending on the patient position, some residual in-folding was observed in the cerebellum as mentioned above. This not only affected the validation procedure but also the B_1^+-maps and consequently the pulse design. Furthermore, small discrepancies between the designed and executed k-space trajectory may be expected as well as minor temporal variations in transmit and receive sensitivity due to patient movement. Nonetheless, good correspondence between the simulated and measured FA distributions was observed, as shown in Fig. 6.4**d**.

To find the location of the k_T-points, although the inverse Fourier method (Yip et al., 2006) has been shown to be sub-optimal, it provides a less computationally-demanding alternative to methods such as the sparsity-enforced algorithm (Zelinski et al., 2008d). When optimizing the FA over an extended volume, the inverse Fourier method allows adequate k_T-point placement in a time-scale compatible with human in-vivo studies. Nonetheless, further improvements in FA uniformity can be achieved by improved optimization of the k-space trajectory (Table 6.2). In particular excitations targeting higher FA's could benefit from optimized k-space trajectories as the sub-pulse durations become significantly longer than the interleaving gradient-blips. Although our implementation of the greedy algorithm required more time than appropriate for in-vivo studies, a computationally optimized implementation such as suggested by Ma et al. (2010) could possibly

	RF-shim	3 k_T-points FFT	3 k_T-points GA	5 k_T-points FFT	5 k_T-points GA	7 k_T-points FFT	7 k_T-points GA	
Pulse duration	500	320	410	430	590	630	810	μs
Bandwidth	2.4±0.0	3.5±0.9	3.0±0.8	2.7±0.5	2.0±0.3	1.8±0.1	1.4±0.3	Hz
FA variation B_0	4.9±17.1	4.9±8.8	4.9±7.7	4.9±6.9	5.0±6.1	4.9±6.1	5.0±5.5	º ± %
FA variation B_0 +100Hz	4.8±17.1	4.9±8.8	4.9±7.7	4.9±6.9	5.0±6.6	4.8±6.5	4.9±6.1	º ± %
FA variation B_0 -100Hz	4.8±17.1	4.9±8.9	4.9±7.7	4.9±7.0	4.9±6.4	5.0±6.4	4.9±6.0	º ± %
FA variation B_0 +200Hz	4.8±17.1	4.9±9.2	4.8±7.8	4.8±7.0	4.9±7.4	4.7±7.7	4.7±7.8	º ± %
FA variation B_0 -200Hz	4.8±17.1	4.9±9.1	4.9±7.9	4.9±7.2	4.7±7.6	4.9±7.4	4.7±8.1	º ± %
FA variation B_0 +300Hz	4.7±17.1	4.8±9.8	4.7±8.0	4.7±7.3	4.8±8.8	4.4±9.8	4.3±11.0	º ± %
FA variation B_0 -300Hz	4.7±17.1	4.8±9.6	4.9±8.0	4.7±7.6	4.5±9.6	4.7±8.6	4.3±12.3	º ± %

Table 6.2: Simulated results obtained with different excitation pulses targeting an average FA of 5°. The reported bandwidth (Mean±SD) is estimated from the full width at half maximum of the Fourier transform of the excitation pulses played on all 8 channels. Excitation pulses designed for the measured B_0-map were evaluated (mean FA° ± FA variation %) in the presence of an additional B_0-offset.

mitigate this problem. Considering parallel transmission, additional improvements in excitation uniformity or pulse duration could possibly be obtained by inclusion of coil elements segmented along the magnet main axis, as in our setup, the azimuthal segmentation of the coil could a priori only provide a reduction of the number of k_T-points in the transverse direction. Furthermore, such tri-directional coil segmentations would potentially allow FA homogenization over volumes larger than the brain like the thighs, pelvis or abdomen.

In this work, k_T-points were implemented as a set of discrete sub-pulses interleaved with 40-µs gradient blips. We also investigated on the side whether pulsing RF continuously while covering the same trajectory without stopping at the k_T-points could yield some gain in pulse duration or energy. Simulations indicated that continuous RF solutions could indeed provide even shorter pulse durations, but with higher energy demand. Depending on the k-space trajectory and the pace at which it is followed, increased power deposition can occur, especially when the velocity at which the k_T-point is transected is not slow enough with respect to the energy deposition required in its vicinity (Lee et al., 2009). Furthermore, even without trajectory optimization, the increased number of time points involved along the trajectory prolongs the pulse design procedure by over 5 min. Interestingly, although these solutions provide increased degrees of freedom, only minor improvements in FA homogeneity were found. Possibly, this could be related to the close proximity of the k-space locations. Therefore, if the pulse duration at the end of Fig.6.1's algorithm is found to be sufficiently short for the application under study, a further decrease in pulse duration at the expense of an increase in power and SAR seems unfavorable. On the other hand, the slew-rate required to execute these continuous excitations can be less demanding and could benefit systems with lower gradient specifications.

By comparing the energy deposited by different excitation pulses, we saw from Table 6.1 that the trade-off for an improved FA distribution is an increase in energy deposition. In particular, the maximum total energy per channel shows a significant increase for the RF-shim, while the CP-mode and k_T-point-based excitations distribute the energy more evenly over the available coil elements. Based on the pulses demonstrated, the k_T-point method requires roughly 6 times the total energy used by the CP-mode. Although this is a substantial difference, for many applications, this energy increase seems manageable. Simulations indicated that, a 5° FA obtained with a 5 ms BIR4 adiabatic pulse (Bernstein et al., 2004) requires several hundred times more energy even when the coil was driven in RF-shim configuration. Moreover, even strongly-modulating pulses (Boulant et al., 2008), 3.9 ms duration targeting the same FA and error, needed over 50 times more energy than required by the k_T-points based excitations. Although these differences might be less severe when targeting high FA's, the proposed method clearly excels at small angles, thus making them ideally suited for small excitations in fast sequences. For example in the MP-RAGE sequence, where typical conventional excitation pulses in the turbo-FLASH echo train are typically 100-µs in duration (12.0 kHz bandwidth), replacing these with 440-µs k_T-point excitations (2.7 kHz bandwidth) will only increase the total RF deposition by approximately a factor 3/2 (Table 6.1). Furthermore, it is important to note

that an increase in total energy deposition does not necessarily imply a similar increase in local SAR. Due to the increased number of degrees of freedom available in Transmit-Sense, the energy can be distributed more evenly over the volume, potentially reducing the local SAR. This is suggested by the results of Table 6.1 which show large differences in the maximum total energy per channel. In our RF coil configuration, where the transmit elements are fairly close to the head, this points to a somewhat better management of the local SAR with k_T-points compared to the static RF shim. Moreover, various optimization methods have been proposed to facilitate local SAR minimization (Cloos et al., 2010c; Lee et al., 2010; Brunner and Pruessmann, 2010). Under current conditions, where the average RF power per transmit-path is monitored, channel-dependent Tikhonov parameters (Cloos et al., 2010c) could readily be implemented to improve the minimum TR and/or maximum FA. Another important factor that should be taken into consideration is the region of interest. Here the comparison was performed considering the entire brain. However, some regions in the brain would require a significant increase in power to obtain the same FA by simply using the CP-mode. In these areas, k_T-point excitations could outperform the CP-mode even in terms of total energy deposition. Although the small tip angle approximation was assumed in the work reported here, k_T-points can allow to design large tip angles by using extensions such as the additive method (Grissom et al., 2008) or optimal control theory (Xu et al., 2008). With the former method, our simulations show that RF pulses can be found with angles up to at least 90° yielding good FA-homogeneity (less then 9.0%) performance in the brain. Additional work is being pursued to reach equivalent homogeneity with 180° pulses. However, the increased power requirements preclude high-FA in-vivo validation with our current setup because our conservative power thresholds would be exceeded. In the future, we plan to use a different approach to evaluate the SAR, which includes real-time amplitude and phase monitoring on every transmit-channel (Gagoski et al., 2009). This, coupled to future improvements of our coil design, should allow us to raise our power thresholds substantially, which will then open up the possibility to demonstrate high-FA k_T-points in-vivo. Then, virtually all non-selective 3D sequences could benefit from the k_T-points. This includes not only GRE-based sequences like the MP-RAGE sequence (Bernstein et al., 2004), but also Turbo-Spin-Echo-type sequences with variable FA refocusing pulses like the SPACE sequence (Busse et al., 2006). This is the subject of future work.

In this study, k_T-point-based excitation pulses have been demonstrated in the framework of parallel transmission. In principle, the presented method could also be implemented on a conventional single channel transmit MRI system, provided that the excitation coil produces sufficient B_1^+ throughout the ROI. Simulations assuming a synthesized single channel system constructed from the RF shim of our transmit-array coil could indeed homogenize the FA throughout the brain. To obtain such results, we found from the inverse-Fourier method that 30 distinct k-space locations were necessary to reduce the corresponding FA variation to approximately 10%. Presumably, in this case, the sparsity-enforced method could provide a more manageable solution by optimizing the visited k-space locations (Zelinski et al., 2008d; Ma et al., 2010). Still, significantly longer excitation pulses should be expected when implementing k_T-points on a single channel at high field.

6.5 Conclusions

Spatially uniform excitation throughout the volume of the human brain by means of Transmit-SENSE has been demonstrated in 3 volunteers at 7 Tesla, through the use of an original minimalist k-space coverage, the k_T-points. This limited number of k-space locations where RF energy is deposited to counteract B_1^+-inhomogeneities leads to short non-selective excitation pulses with good FA uniformity over extended volumes. Thus a whole range of 3D sequences with short TR can be targeted for applications at high fields, with less SAR limitations than energy-consuming pulses like standard adiabatic or strongly-modulating pulses on single channel systems.

7 Non-Selective Excitations with an Arbitrary Flip-Angle

This chapter contains methods & principles that were accepted for publication as abstracts in the proceedings of the Annual Annual Meeting of the International Society for Magnetic Resonance in Medicine 2012.

M.A. Cloos, N. Boulant, M. Luong, G. Ferrand, E. Giacomini, M-F. Hang, C.J. Wiggins, D. Le Bihan, and A. Amadon. (2012) "k_T-points-based Inversion Pulse Design For Transmit-sense Enabled MP-RAGE Brain Imaging At 7T."

7.1 Introduction

Since the introduction of Transmit-SENSE (Katscher et al., 2003; Zhu, 2004), various methods have been proposed to design dedicated pTx-enabled RF-waveforms (Katscher et al., 2003; Zhu, 2004; Grissom et al., 2006; Xu et al., 2007; Setsompop et al., 2008b; Grissom et al., 2008; Xu et al., 2008; Grissom et al., 2009). Initially, most of these approaches were limited to the small-tip-angle (STA) regime, where the transverse magnetization upholds an approximately linear relation with the excitation field (Pauly and Nishimura, 1989). Beyond this domain, i.e. targeting a FA exceeding $\sim 30°$, the non-linear behavior of the Bloch equations must be considered to achieve a high excitation fidelity. Nonetheless, a careful analysis of this non-linear system revealed that under certain conditions, the STA approximation may also yield viable large-tip-angle (LTA) results (Pauly et al., 1989). In a similar fashion, large FA excitations may also be designed in the framework of pTx (Xu et al., 2007).

Although the pTx-approach allows excellent STA excitation fidelity in conjunction with under-sampled excitation k-space trajectories (Grissom et al., 2006; Setsompop et al., 2006), adhering to constraints imposed by the linear class of LTAs significantly impairs its potential to reach the desired result with a short RF exposure (Xu et al., 2007). Therefore, optimization techniques have been proposed to mitigate excitation defects that arise due the non-linear behavior of the Bloch equations. Although not ensuring a global optimum, LTA excitations designed via optimal control methods have been demonstrated to provide robust results (Xu et al., 2008; Grissom et al., 2009).

So far, the sparse non-selective uniform excitations introduced in the previous chapter have only been demonstrated in the STA domain. In this chapter, the methods relevant to the design of k_T-point excitations targeting an arbitrary FA are detailed. Although some of these principles could also be considered for applications such as spin-echo pulse design, the focus of this chapter lays on inversion pulses. To this end, a series of Bloch simulations will be considered based on the B_1^+ and B_0 profiles measured in 6 different human brains at 7 Tesla. Thus allowing the different design parameters to be explored without the need for time consuming pulse validation experiments. All the data, perquisite for this study, was acquired conform the methods described in the previous chapter.

This chapter is structured as follows, firstly, to aid the LTA pulse design, an observation on the STA approximation is brought forward which broadens the STA scope. Subsequently, the optimal control approach (OCA) introduced by Xu et al. (2008) is recast into the form of a magnitude-least-squares optimization problem constrained by the hardware limitations. The performance of this method, hereafter referred to as the magnitude optimal control approach (MOCA), is then compared to the original implementation proposed by Xu et al. (2008). Subsequently, the joint k-space design method (Grissom and Pauly, 2010) is introduced to adjust k_T-point locations, and integrated into MOCA. Finally, several considerations specific to in-vivo applications are illustrated and discussed.

7.2 Limitations of the (Extended) Small Tip Angle Approximation

Methods

The STA approximation (Pauly and Nishimura, 1989) assumes that the longitudinal magnetization remains constant during the RF pulse (Section 2.1). Albeit not an exact representation of the physics involved, this simplification can be applied to small FA excitations. In this domain, the transverse magnetization demonstrates an approximately linear dependence on the applied excitation field. Therefore, excitations pulses based on the STA approximation generally perform well when targeting a FA up to $\sim 30°$. Outside of the STA domain, the magnetization no longer upholds a linear relation, and variation of the longitudinal magnetization can no longer be neglected (Fig. 7.1). Consequently, when designing LTA pulses based on the STA approximation, sub-optimal levels of excitation fidelity are obtained.

The following observation leads to a simple trick aiding the design of LTA RF-pulses. Supposing a FA of 90° is desired, the STA approximation suggests that the normalized transverse magnetization of $M_T = M_0 = 1$ should be targeted. However, due to the non-linear dynamics in the Bloch equations, a FA of 1 rad ($\sim 57°$) will be obtained (Fig. 7.1, brown). Extrapolation based on this observation indicates that a "virtual transverse magnetization" of $\pi/2$ should be targeted instead (Fig. 7.1, green). In general, it turns out

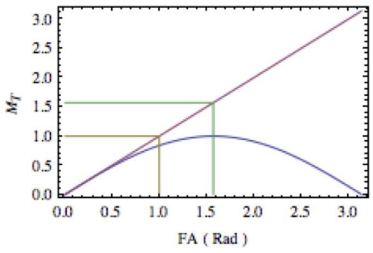

Figure 7.1: The normalized transverse magnetization (M_T) as a function of the flip-angle (FA).

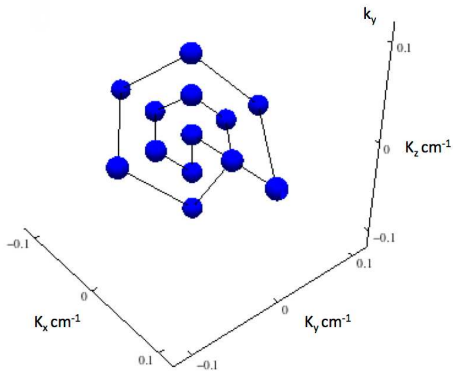

Figure 7.2: Symmetrically distributed 13-k_T-points k-space trajectory.

that substituting the transverse magnetization with the FA (in radians) in the Bloch equation yields an appreciably better excitation fidelity when targeting LTA based on the STA assumptions. This was recently derived more rigorously by Boulant and Hoult (2012).

Based on this extended STA method, 13-k_T-point-based excitations were designed targeting 5°, 90°, and 180° FA's[1]. To this end, a symmetric excitation k-space trajectory was adopted (Fig. 7.2), approximating one of the design constraints of the linear-class LTA approach (Pauly et al., 1989). Based on the B_1^+ and B_0 maps measured in-vivo, the obtainable normalized root mean square error (NRMSE) was evaluated. To this end, the FAs obtained throughout the brain were simulated as a function of the Tikhonov regularization parameter λ introduced in section 5.2.

Results and Discussion

When targeting a 5° FA, the characteristic shape of the L-curve is revealed (Fig. 7.3**a** & **b**). By selecting a suitable Tikhonov parameter at the L-corner, a good compromise between excitation fidelity and RF-power is obtained (Fig. 7.3**c**). Regarding 90°-excitations, the proposed method still allows high quality solutions to be found (Fig. 7.3**d**). However, in order to assure a near optimal NRMSE, the Tikhonov parameter must to be evaluated more carefully (Fig. 7.3**a** & **b**). When targeting an 180°-inversion pulse, on the other hand, the corresponding L-curve only shows a shallow minimum with relatively poor performance (Fig. 7.3**e**).

7.3 The Optimal Control Approach

Although the OCA has been shown to be a robust LTA pulse design tool, the implementations published up until now are subject to sub-optimal constrain (Xu et al., 2008; Grissom et al., 2009). In particular, both demonstrations enforce a pre-defined target phase distribution, while in most cases, the quantity of interest is limited to the magnitude of the magnetization (Katscher et al., 2007; Setsompop et al., 2008c). Moreover, neither method takes the peak RF-power limitations into account.

Optimal Control Theory applied to MR pulse design

As proposed by Xu et al. (2008), in the rotating frame of reference, the Bloch equation without relaxation terms can be written as:

$$\frac{d}{dt}\mathbf{M}(\mathbf{r},t)=\gamma\begin{pmatrix}0 & \mathbf{G}(t)\cdot\mathbf{r}+\Delta B_0(\mathbf{r}) & -B_{1,y}^+(\mathbf{r},t)\\ -\mathbf{G}(t)\cdot\mathbf{r}-\Delta B_0(\mathbf{r}) & 0 & B_{1,x}^+(\mathbf{r},t)\\ B_{1,y}^+(\mathbf{r},t) & -B_{1,x}^+(\mathbf{r},t) & 0\end{pmatrix}\mathbf{M}(\mathbf{r},t), \tag{7.1}$$

[1] 14 sub-pulses, but 13 k_T-points (starting and ending at $\mathbf{k}=0,0,0$).

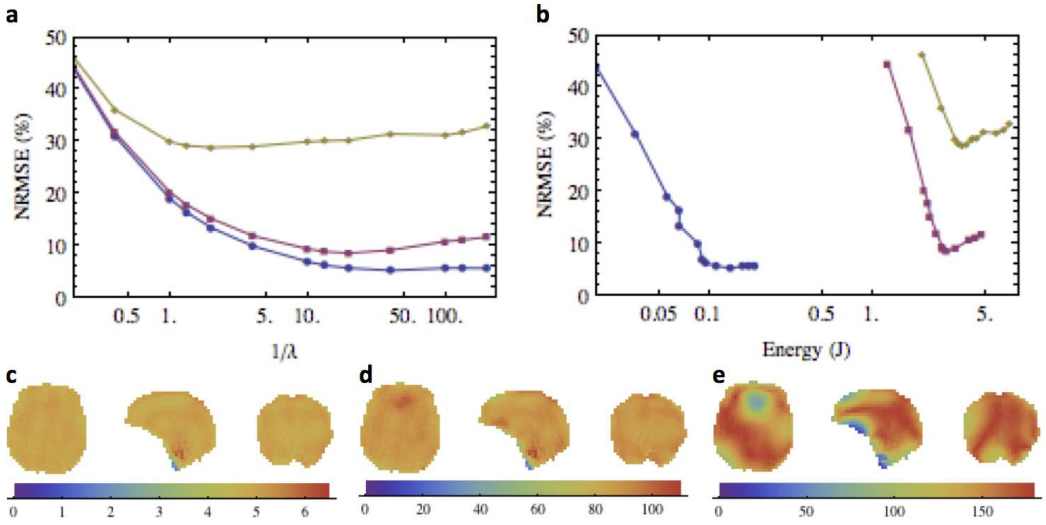

Figure 7.3: Pulse design based on the small-tip-angle approximation. **a**: The "L-curve" showing the relation between the normalized root mean square excitation error (NRMSE) and the inverse of the regularization parameter λ, corresponding to 3 different target flip-angles (blue: 5°, purple: 90°, yellow: 180°). **b**: The "L-curve" showing the relation between NRMSE and the cumulative incident energy at the coil (same color coding as sub-figure **b**). **c**-**e**: Three orthogonal central brain slices showing the flip angle distribution (color code in deg) obtained with a near-optimal Tikhonov parameter when targeting an excitation of **c**: 5° (NRMSE $\sim$ 5%); **d**: 90° (NMRSE $\sim$ 8%); **e**: 180° (NMRSE $\sim$ 30%).

where $\mathbf{M}(t) = (M_x(t), M_y(t), M_z(t))^T$, $\mathbf{G}(t) = (G_x(t), G_y(t), G_z(t))^T$, ΔB_0 the offset with respect to the RF carrier frequency, and $\mathbf{r} = (x, y, z)^T$. Then for a pTx system utilizing N individual transmit-pathways we find:

$$B_1^+(\mathbf{r}, t) = \sum_{n=1}^{N} s_n(\mathbf{r}) b_n(t), \tag{7.2}$$

where $s_n(\mathbf{r})$ represents the transmit-sensitivity of the nth coil, and b_n denotes the RF pulse waveform to be played at the nth transmit-pathway. Rewriting $s_n^R(\mathbf{r}) = Re\{s_n(\mathbf{r})\}$, $s_n^I(\mathbf{r}) = Im\{s_n(\mathbf{r})\}$, $u_n(t) = Re\{b_n(t)\}$, and $v_n(t) = Im\{b_n(t)\}$ we find:

$$B_{1,x}^+(\mathbf{r}, t) = \sum_{n=1}^{N} [s_n^R(\mathbf{r}) u_n(t) - s_n^I(\mathbf{r}) v_n(t)], \tag{7.3}$$

$$B_{1,y}^+(\mathbf{r}, t) = \sum_{n=1}^{N} [s_n^I(\mathbf{r}) u_n(t) + s_n^R(\mathbf{r}) v_n(t)]. \tag{7.4}$$

Replacing Eq.7.3 & 7.4 in Eq. 7.1 yields:

$$\frac{d}{dt}\mathbf{M}(\mathbf{r}, t) = [\mathbf{A}(\mathbf{r}, t) + \sum_{n=1}^{N} \mathbf{B}_n(\mathbf{r}) u_n(t) + \sum_{n=1}^{N} \mathbf{C}_n(\mathbf{r}) v_n(t)]\mathbf{M}(\mathbf{r}, t), \tag{7.5}$$

where

$$\mathbf{A}(\mathbf{r}, t) = \gamma \begin{pmatrix} 0 & \mathbf{G}(t) \cdot \mathbf{r} + \Delta B_0(\mathbf{r}) & 0 \\ -\mathbf{G}(t) \cdot \mathbf{r} - \Delta B_0(\mathbf{r}) & 0 & 0 \\ 0 & 0 & 0 \end{pmatrix}, \tag{7.6}$$

$$\mathbf{B}_n(\mathbf{r}) = \gamma \begin{pmatrix} 0 & 0 & -s_n^I \\ 0 & 0 & s_n^R \\ s_n^I & -s_n^R & 0 \end{pmatrix}, \tag{7.7}$$

and

$$\mathbf{C}_n(\mathbf{r}) = \gamma \begin{pmatrix} 0 & 0 & -s_n^R \\ 0 & 0 & -s_n^I \\ s_n^R & s_n^I & 0 \end{pmatrix}. \tag{7.8}$$

Concatenating vectors and matrices in Eq. 7.5 along different $\mathbf{r}$ gives:

$$\frac{d}{dt}\mathbf{M}(t)=[\mathbf{A}(t) + \sum_{n=1}^{N} \mathbf{B}_n u_n(t) + \sum_{n=1}^{N} \mathbf{C}_n v_n(t)]\mathbf{M}(t), \tag{7.9}$$

where

$$\mathbf{M}(t) = [\mathbf{M}^T(\mathbf{r}_1, t), \mathbf{M}^T(\mathbf{r}_2, t), \cdots, \mathbf{M}^T(\mathbf{r}_p, t)]^T, \tag{7.10}$$

$$\mathbf{A}(t) = diag\{\mathbf{A}(\mathbf{r}_1, t), \mathbf{A}(\mathbf{r}_2, t), \cdots, \mathbf{A}(\mathbf{r}_p, t)], \tag{7.11}$$

$$\mathbf{B}_n = diag\{\mathbf{B}_n(\mathbf{r}_1), \mathbf{B}_n(\mathbf{r}_2), \cdots, \mathbf{B}_n(\mathbf{r}_p)], \tag{7.12}$$

and

$$\mathbf{C}_n = diag\{\mathbf{C}_n(\mathbf{r}_1), \mathbf{C}_n(\mathbf{r}_2), \cdots, \mathbf{C}_n(\mathbf{r}_p)], \tag{7.13}$$

with p equal to the number of voxels in the space.

Analogous to the "minimum-distance" formulation proposed by (Conolly et al., 1986), we minimize a cost functional J over all possible controls:

$$\begin{array}{c} \underset{[u_n(t), v_n(t)]_{n=1}^N}{min} \\ \end{array} \begin{array}{c} J[u_1(t), \cdots u_N(t), v_1(t), \cdots, v_N(t)] = \\ \varphi(\mathbf{M}(T)) + \int_0^T F(u_1(t), \cdots u_N(t), v_1(t), \cdots, v_N(t))dt, \end{array} \tag{7.14}$$

subject to the Bloch equation (Eq. 7.9). In 7.14, $\varphi(\mathbf{M}(T))$ is a weighted l_2 norm representing the deviation of the final state $\mathbf{M}(T)$ from the desired magnetization $\mathbf{D}$ via the metric:

$$\varphi(\mathbf{M}(T)) = (\mathbf{M}(T) - \mathbf{D})^T \mathbf{W} ([\mathbf{M}(T) - \mathbf{D}]), \tag{7.15}$$

where $\mathbf{W}$ is a diagonal matrix containing the weights for different spatial locations to emphasize regions of interest (e.g. binary weights to exclude the regions outside the object, and/or heuristically-chosen fractional weights for different regions-of-interest), and $F(u_1(t), \cdots u_N(t), v_1(t), \cdots, v_N(t))$ is a penalty function on RF power:

$$F(u_1(t), \cdots u_N(t), v_1(t), \cdots, v_N(t)) = \frac{1}{2}\alpha \left[\sum_{n=1}^{N} u_l^2(t) + \sum_{n=1}^{N} v_n^2(t) \right], \tag{7.16}$$

where α is a relative weighting parameter to balance the two terms in Eq. 7.14.

Adopting Lagrange multipliers $\boldsymbol{\lambda}(t)$, Eq. 7.14 can be recast in the from of an unconstrained problem:

$$\begin{array}{c} \underset{[u_n(t), v_n(t)]_{n=1}^N}{min} \\ \end{array} \begin{array}{c} J[u_1(t), \cdots u_N(t), v_1(t), \cdots, v_N(t)] = \\ \varphi(\mathbf{M}(T)) + \int_0^T H(\mathbf{M}(t), \lambda(t), u_1(t), \cdots u_N(t), v_1(t), \cdots, v_N(t))dt, \end{array} \tag{7.17}$$

where the Hamiltonian in the integral is:

$$\begin{array}{c} H(\mathbf{M}(t), \boldsymbol{\lambda}(t), u_1(t), \cdots u_N(t), v_1(t), \cdots, v_N(t)) = F(u_1(t), \cdots u_N(t), v_1(t), \cdots, v_N(t)) \\ +\boldsymbol{\lambda}(t) \left([\mathbf{A}(t) + \sum_{n=1}^{N} \mathbf{B}_n u_n(t) + \sum_{n=1}^{N} \mathbf{C}_n v_n(t)]\mathbf{M}(t) - \frac{d}{dt}\mathbf{M}(t) \right). \end{array} \tag{7.18}$$

Solutions of the corresponding two-point boundary-value problem, which does not have a closed-form solution (Bryson and Ho, 1975), can numerically be approximated using a first-order gradient algorithm (Xu et al., 2008):

Step 1 Initialize $u_n^0(t)$ and $v_n^0(t)$, $n = 1, 2, \cdots, N$, based on the STA aproximation (Pauly and Nishimura, 1989; Grissom et al., 2006).

Step 2 Given $\mathbf{M}(0)$, integrate Eq. 7.9 forward to obtain $M^0(t)$, for all $0 \leq t \leq T$.

Step 3 Evaluate $\boldsymbol{\lambda}(T) = \mathbf{W}(\mathbf{M}(T) - \mathbf{D})$. Integrate Eq. 7.9 backwards, substituting $\mathbf{M}(t)$ with $\boldsymbol{\lambda}(t)$ to obtain $\boldsymbol{\lambda}^k(t)$, corresponding to the kth iteration for all $0 \leq t \leq T$.

Step 4 Update $u_n(t)$ and $v_n(t)$ for $n = 1, 2, \cdots, N$:

$$u_n^{k+1}(t) = u_n^k(t) - \mu[(\boldsymbol{\lambda}^k)^T(t)\mathbf{B}_n\mathbf{M}^k(t) + \alpha u_n^k(t)], \tag{7.19}$$

$$, v_n^{k+1}(t) = v_n^k(t) - \mu[(\boldsymbol{\lambda}^k)^T(t)\mathbf{C}_n\mathbf{M}^k(t) + \alpha v_n^k(t)], \tag{7.20}$$

where μ is the step size.

Step 5 Given $\mathbf{M}(0)$, integrate Eq. 7.9 forward to obtain $M^{k+1}(t)$, for all $0 \leq t \leq T$.

Step 6

- If $(\mathbf{M}^{k+1}(T) - \mathbf{D})^T\mathbf{W}\left(\mathbf{M}^{k+1}(T) - \mathbf{D}\right)$ is smaller than a given error tolerance ε, the algorithm is stopped (the waveforms u_n^k & v_n^k, $n = 1, 2, \cdots, N$, have satisfactory performance).
- Else if $(\mathbf{M}^k(T) - \mathbf{D})^T\mathbf{W}\left(\mathbf{M}^k(T) - \mathbf{D}\right)$ is smaller than $(\mathbf{M}^{k+1}(T) - \mathbf{D})^T\mathbf{W}\left(\mathbf{M}^{k+1}(T) - \mathbf{D}\right)$, then half the step size μ and return to **Step 4**.
- Else if 4 consecutively correct updates have been performed, double the step size μ, increase k by one and continue to the next iteration (**Step 3**).
- Else, increase k by one and continue to the next iteration (**Step 3**).

7.4 Adaptation to k_T-points (with initial magnetization $M_z = M_0$)

To enhance the performance of arbitrary-FA pulses in the framework of the k_T-points method, several small modifications were made to the original optimal control implementation. Considering the non-selective nature of the k_T-points strategy, regions outside the volume of interest (ROI) can be excluded from the optimization process. Thus instead of nulling their relative weights in the diagonal matrix $\mathbf{W}$, all points $\mathbf{r}$ not in the ROI may be dropped from Eq. 7.15. In practice, when selecting a 3D brain mask from initial measurements, this dramatically reduces both the computational load and memory requirements for the optimization procedure. Furthermore, additional constraints are applied to the OCA procedure detailed-above: the voltage amplitude of each channel $b_n(t)$ is constrained to stay below a threshold set by the RF amplifier limitations (**Step 5** below). In-addition, the RF is nulled between the k_T-points, i.e. during the gradient blips (**Step 6** below).

Instead of solving $u_l(t)$ and $v_l(t)$ to find a specific $(\mathbf{M}(T)-\mathbf{D})^T(\mathbf{M}(T)-\mathbf{D}) < \varepsilon$, the following M_z magnitude-only criterion is targeted:

$$(\mathbf{M}_z(T) - \mathbf{D}_z)^T(\mathbf{M}_z(T) - \mathbf{D}_z) < \varepsilon, \tag{7.21}$$

and neglecting the phase contribution in the second boundary value:

$$\boldsymbol{\lambda}_z(T) = (\mathbf{M}_z(T) - \mathbf{D}_z) \quad \& \quad \boldsymbol{\lambda}_x(T) = \boldsymbol{\lambda}_y(T) \equiv 0 \ , \tag{7.22}$$

where the subscript z indicates the longitudinal magnetization and x,y correspond to the transverse components[2]. Solutions of the corresponding magnitude only two-point boundary-value problem, can numerically be approximated using the following implementation of the first-order gradient algorithm.

Step 1 Initialize $u_n^0(t)$ and $v_n^0(t)$, $n = 1, 2, \cdots, N$, based on the STA aproximation (Pauly and Nishimura, 1989; Grissom et al., 2006).

Step 2 Given $\mathbf{M}(0)$, integrate Eq. 7.9 forward to obtain $M^0(t)$, for all $0 \leq t \leq T$.

Step 3 Evaluate $\boldsymbol{\lambda}_z(T) = \left(\mathbf{M}_z^k(T) - \mathbf{D}_z\right)$ and set all transversal components of $\boldsymbol{\lambda}(T)$ equal to 0. Integrate Eq. 7.9 backwards, substituting $\mathbf{M}(t)$ with $\boldsymbol{\lambda}(t)$ to obtain $\boldsymbol{\lambda}^k(t)$, corresponding to the kth iteration for all $0 \leq t \leq T$.

[2] Alternativly, a constraint on the spatial phase variation can be enforced by replacing the previous target phase with a smoothed version of the obtained phase profile.

Step 4 Update $u_n(t)$ and $v_n(t)$ for $n = 1, 2, \cdots, N$:

$$u_n^{k+1}(t) = u_n^k(t) - \mu[(\boldsymbol{\lambda}^k)^T(t)\mathbf{B}_n\mathbf{M}^k(t) + \alpha u_n^k(t)], \tag{7.23}$$

$$v_n^{k+1}(t) = v_n^k(t) - \mu[(\boldsymbol{\lambda}^k)^T(t)\mathbf{C}_n\mathbf{M}^k(t) + \alpha v_n^k(t)], \tag{7.24}$$

where μ is the step size.

Step 5 If $\sqrt{\left(u_n^{k+1}(t)\right)^2 + \left(v_n^{k+1}(t)\right)^2} > \delta$ at any given $0 \le t \le T$:

$$\begin{aligned} u_n^{k+1}(t) &= \delta \frac{u_n^{k+1}(t)}{\sqrt{\left(u_n^{k+1}(t)\right)^2 + \left(v_n^{k+1}(t)\right)^2}}, \\ v_n^{k+1}(t) &= \delta \frac{v_n^{k+1}(t)}{\sqrt{\left(u_n^{k+1}(t)\right)^2 + \left(v_n^{k+1}(t)\right)^2}}, \end{aligned} \tag{7.25}$$

where δ corresponds to the maximum amplitude allowed by the system (or user).

Step 6 If $G(t)^T G(t) > 0$ at any given $0 \le t \le T$:

$$\begin{aligned} u_n^{k+1}(t) &= 0, \\ v_n^{k+1}(t) &= 0, \end{aligned} \tag{7.26}$$

thus ensuring that no RF is played during the gradient blips (Although this is not essential for the RF-pulse design at this stage, it will be beneficial when considering k-space optimization techniques originally designed for the spokes trajectory (Saekho et al., 2006).

Step 7 Given $\mathbf{M}(0)$, integrate Eq. (7.9) forward to obtain $M^{k+1}(t)$, for all $0 \le t \le T$.

Step 8

- If $\left(\mathbf{M}_z^{k+1}(T) - \mathbf{D}_z\right)^T \left(\mathbf{M}_z^{k+1}(T) - \mathbf{D}_z\right)$ is smaller than a given error tolerance ε, the algorithm is stopped (the waveforms u_n^k & v_n^k, $n = 1, 2, \cdots, N$, have satisfactory performance).
- Else if $\left(\mathbf{M}_z^k(T) - \mathbf{D}_z\right)^T \left(\mathbf{M}_z^k(T) - \mathbf{D}_z\right)$ is smaller than $\left(\mathbf{M}_z^{k+1}(T) - \mathbf{D}_z\right)^T \left(\mathbf{M}_z^{k+1}(T) - \mathbf{D}_z\right)$, then half the step size μ and return to **Step 4**.
- Else if 4 consecutively correct updates have been performed, double the step size μ, increase k by one, and continue to the next iteration (**Step 3**).
- Else, increase k by one and continue to the next iteration (**Step 3**).

Methods

Both OCA and MOCA were adopted to optimize initial candidate 90°-excitations and 180°-inversion pulses based on the STA approximation, as described in the previous section. To this end, the spatial domain method was adopted (Grissom et al., 2006) including the variable exchange method to relax the phase constraints (Setsompop et al., 2008c). It should be pointed out that the performance of this method depends heavily on the initial target phase. We found, as suggested by Kerr et al. (2007), that adopting the phase distribution corresponding to the CP-mode as an initial target yielded good results. Furthermore, because it is likely that the LTA optimized pulses will require additional power, the STA pulse design is constrained to $\sim 50\%$ of the available peak power (Cloos et al., 2012).

In contrast to 180°-refocusing pulses, the component of interest for inversion pulses is the longitudinal magnetization only. Therefore, the normalized root mean square inversion error (NRMSIE)[3] will be adopted to quantify the performance of the inversion pulses, whereas 90°-excitations will be quantified by the normalized root mean square excitation error (NRMSEE):

$$\begin{aligned} NRMSEE &= \frac{1}{\sqrt{p}} \sqrt{\sum_{\mathbf{r}} \left(M_z(\mathbf{r})\right)^2}, \\ NRMSIE &= \frac{1}{\sqrt{p}} \sqrt{\sum_{\mathbf{r}} \left(M_z(\mathbf{r}) + 1\right)^2}, \end{aligned} \tag{7.27}$$

[3]The NRMSIE varies between 0 and 2, i.e., without applying RF a NRMSIE 200% is obtained.

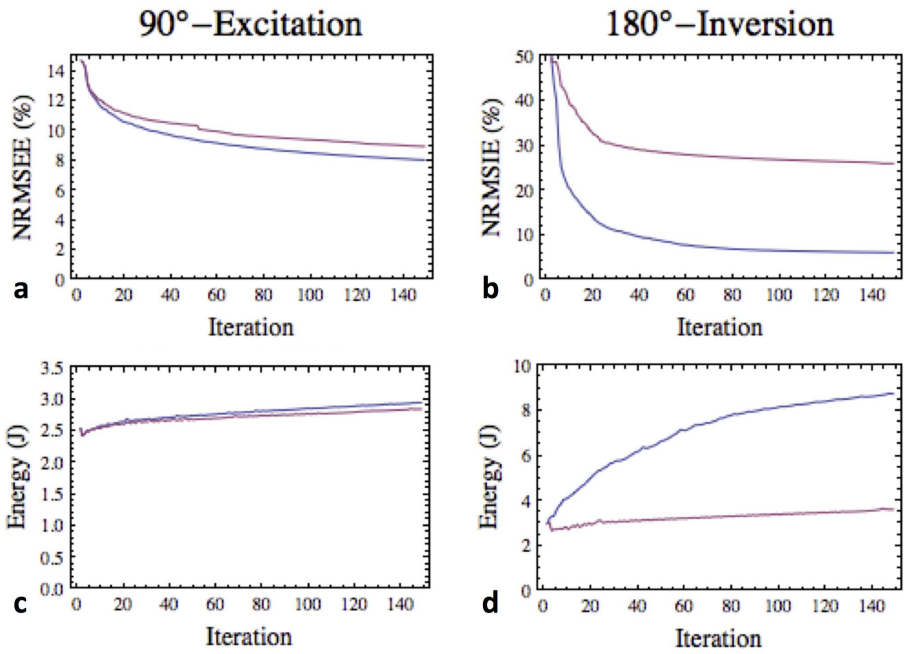

Figure 7.4: Comparison of the different optimal control implementations: OCA (purple), MOCA (blue). Results shown, correspond to the averaged results based on the calibration measurements performed on 6 different volunteers scanned at 7-Tesla. **a**: The evolution of the NRMSEE when targeting a 90°-excitation. **b**: The evolution of the normalized root mean square inversion error (NRMSIE) when targeting a 180°-inversion. **c-d**: The evolution of the cumulative incident energy at the coil, corresponding to the optimization illustrated in subfigure **a-b**.

with **r** designating a voxel location in the brain and p their number.

Because dipolar coupling among spins is ignored, the Bloch equations corresponding to each voxel in the ROI may be evaluated in parallel without introducing inter-thread latency issues. Consequently, most steps in the OCA and MOCA algorithm can be performed in parallel on a multi-core Graphic Processing Unit (GPU). Considering the numerical accuracy of this implementation, the waveforms were discretized with a $1\mu s$ time-step to assure reliable results.

Results & Discussion

The initial 90°-excitation candidates, based on the STA approximation, already demonstrate an acceptable level of performance. Nonetheless, both optimal-control-based solutions provide substantial improvements in excitation uniformity (Fig. 7.4**a**). Although the MOCA outperforms the original implementation suggested by Xu et al. (2008), either method could be used to obtain k_T-point-based tailored excitations of excellent quality, depositing similar levels of energy (Fig. 7.4**c**).

Considering 180°-inversion pulses, the phase constraint imposed in the OCA limits the obtainable excitation fidelity to a suboptimal 30% NRMSIE (Fig. 7.4**b**). It should be pointed out that the performance of the original OCA depends heavily on the initial target phase. Clearly the final target phase produced by the variable exchange method in the STA approximation (Setsompop et al., 2008c) is far from optimal when approaching 180°. Unfortunately, obtaining the optimal target phase corresponding to the desired LTA solution constitutes a non-trivial problem. However, neglecting the phase contribution, as proposed in MOCA, effectively extends the principle of the MLS approach into to inversion pulses. Nonetheless, the performance of these methods still depends on the initial "candidate" solution, which is then iteratively optimized. Therefore, alternative initial solutions could potentially better approach the global optimal.

Starting from the same STA-based candidate RF waveform, the MOCA outperforms the original implementation suggested by Xu et al. (2008). Although a near-perfect inversion fidelity is reached (5% NRMSIE), the final MOCA-based 180°-inversion pulse requires nearly 3 times the energy required for a high-fidelity 90°-

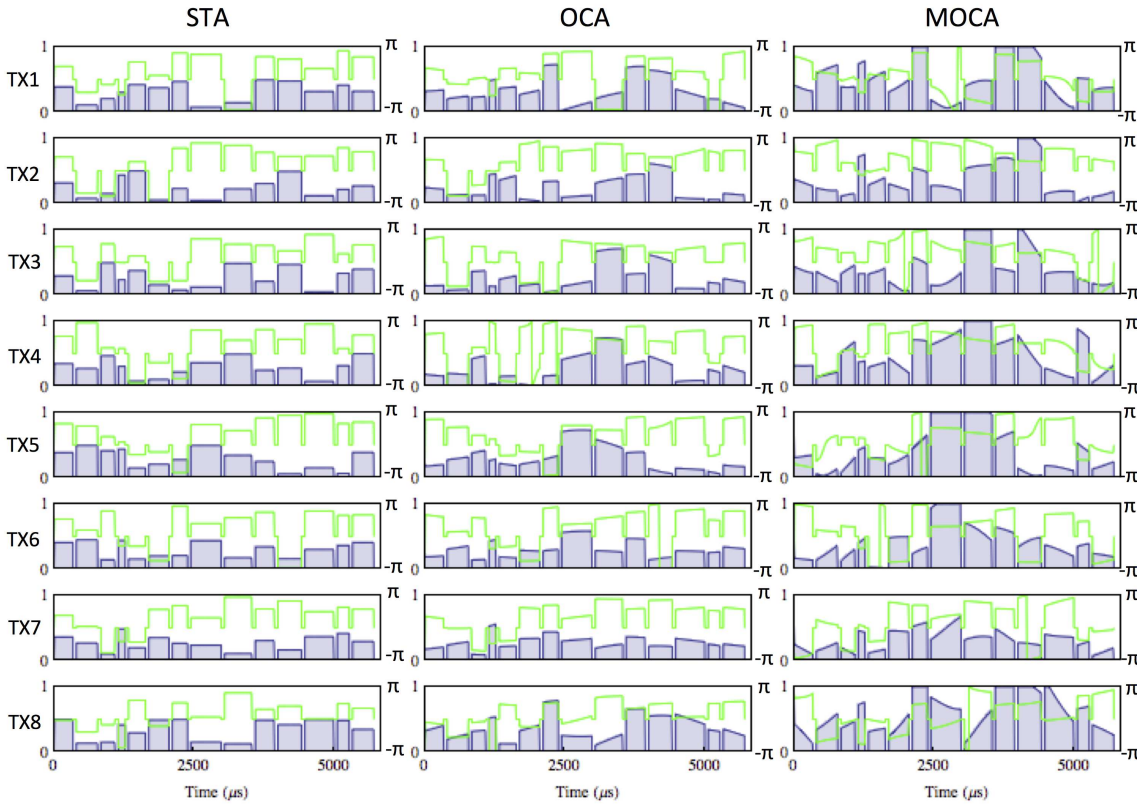

Figure 7.5: Comparison of the RF waveform targeting 180° before (STA) and after optimization (OCA & MOCA). The normalized amplitude (corresponding to a peak amplitude of 180V per channel) is depicted in blue, whereas the relative phase is superimposed in green.

excitation (Fig. 7.4**c**&**d**). To ensure that these solutions remain compatible with the hardware limitations, the cut-off filter implemented in step 5 of the MOCA is essential (Fig. 7.5).

7.5 Joint k-space optimization

Theory

Inspired by (Grissom and Pauly, 2010) the joint k-space optimization routine was incorporated into MOCA as an additional improvement towards a higher FA-fidelity to energy-cost ratio. Although, in the STA domain, square sub-pulses generally provide sufficient degrees of freedom to obtain good excitation fidelity (Fig. 7.6**a**), the sub-pulses obtained after optimal control can be of arbitrary shape (Fig. 7.6**b**).

Considering MOCA as detailed earlier, **Step 6** ensures that no RF is played during the gradient blips. Thus neglecting the relatively small ΔB_0 effects during the short gradient blips[4], a general operator $\mathbf{A}(\mathbf{g}_i^k)$ can be constructed:

$$\mathbf{A}(\mathbf{g}_j^k) = \prod_{i=t_{2j+1}}^{\Gamma} \left(\mathbf{ID} + \gamma \begin{pmatrix} 0 & \mathbf{g}_j^k(t_i)\cdot\mathbf{r} & 0 \\ -\mathbf{g}_j^k(t_i)\cdot\mathbf{r} & 0 & 0 \\ 0 & 0 & 0 \end{pmatrix} \Delta t \right), \tag{7.28}$$

where **ID** is the identity matrix, Δt corresponds to the duration of a single the time-step, $\mathbf{g}$ is a vector corresponding to the k-space segment from one k_T-point location to the next, and $\Gamma = (t_{2j+2} - t_{2j+1})/\Delta t$ such that the evolution of the magnetization vector during the gradient blips is described by:

[4] In general, this assumption is not necessary. Considering the short gradient blip durations, the phase variation induced by ΔB_0 effects may be expected to remain well below 5°. Therefore, their contribution was neglected in favor of a simplified implementation.

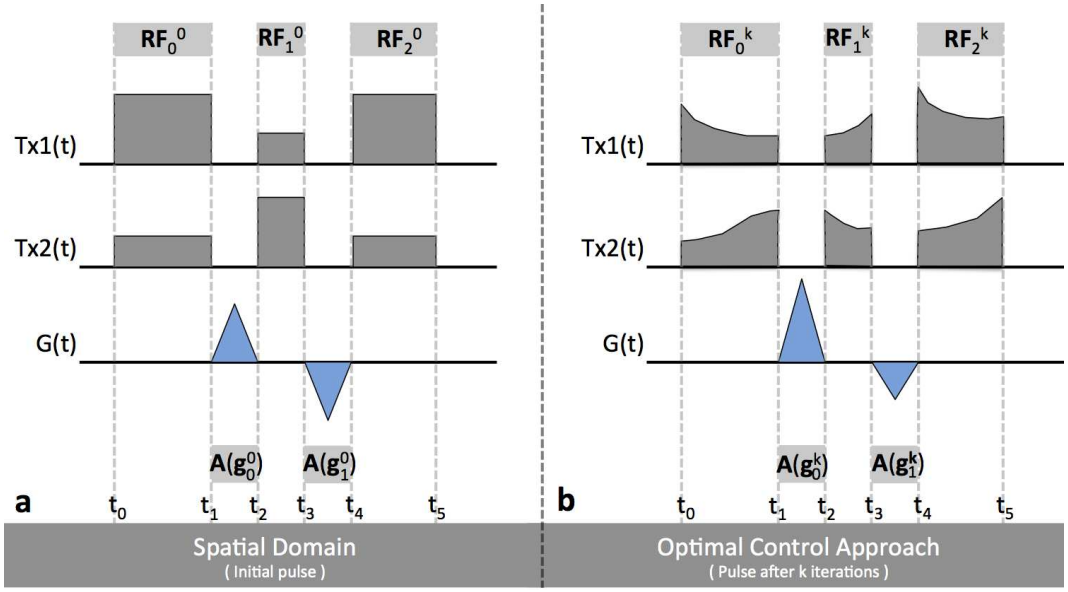

Figure 7.6: Simplified illustration showing k_T-points-based excitations during different stages of the joint k-space optimization procedure. **a**: Exemplary initial candidate RF waveform based on the small-tip-angle approximation. **b**: The RF waveform after the kth optimization iteration.

$$\mathbf{M}(t_{2i+2}) = \mathbf{A}(\mathbf{g}_i^k)\mathbf{M}(t_{2i+1}). \tag{7.29}$$

Although $\mathbf{A}(\mathbf{g}_i^k)$ does not constitute a proper rotation matrix, the approximations is adequate provided that the time-step Δt and gradient amplitude $\left\|\mathbf{g}_j^k\right\|$ are sufficiently small. Similarly, if the RF waveforms are known, an operator $\mathbf{RF}_j^k$ can be constructed for every sub-pulse j such that:

$$\mathbf{RF}_j^k = \prod_{i=t_{2j}}^{\Gamma} \left(\mathbf{ID} + \mathbf{A}\left(t\right)\Delta t + \Delta t \sum_{n=1}^{N} \mathbf{B}_n u_n^k(t) + \Delta t \sum_{n=1}^{N} \mathbf{C}_n v_n^k(t) \right), \tag{7.30}$$

where $\Gamma = \left(t_{2j+1} - t_{2j}\right)/\Delta t$ for each of the j sub-pulses such that:

$$\mathbf{M}(t_{2i+1}) = \mathbf{RF}_i^k \mathbf{M}(t_{2i}). \tag{7.31}$$

Again, this approximation requires a sufficiently small time-step to assure numerical stability. On the other hand, the advantage is that the operators $\mathbf{RF}_j^k$ have already been constructed during step 7 of the MOCA algorithm. Therefore, given a RF-waveform the performance of different k_T- point locations can efficiently be explored by varying $\mathbf{g}_i^k$ and concatenating the operators for each of the L sub-pulses as follows :

$$\mathbf{M}(T) = \left[\prod_{i=0}^{L-1} \mathbf{A}(\mathbf{g}_i^k)\mathbf{RF}_{2i}^k \right] \mathrm{M}(0). \tag{7.32}$$

The joint design is then inserted after **Step 8** before returning to **Step 3** for the next iteration. Encouraged by earlier results (Boulant et al., 2008), the simplex method (Nelder and Mead, 1965) was adopted to search for possible improvements in the k-space trajectory. To this end, an initial step size 1/FOV was adopted after which the algorithm was allowed to freely evolve. Note that although this does not take ΔB_0 in to account, the next iteration of **Step 7** will. Furthermore, this approach does not consider the energy deposition, as it has no direct influence on the RF-waveforms. Although at each step the improvements provided require no additional energy, the final RF-solution obtained may not be the most energy efficient.

Methods

First the norm of $\mathbf{M}$ was investigated after evaluating Eq. 7.32 to ensure that the time-step considered is sufficiently small to allow the gradient and RF induced rotations to be approximated by Eq. 7.28 and 7.30,

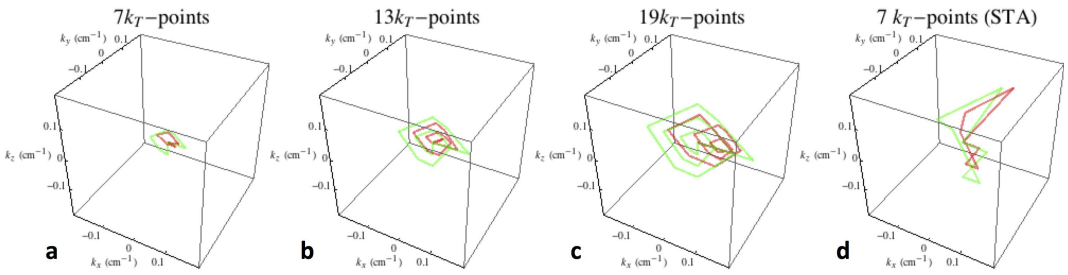

Figure 7.7: Different initial (green) and optimized (red) k-space trajectories evaluated in this work. Results shown correspond to a single subject. **a**: Symmetric 7-k_T-point-based trajectory. **b**: Symmetric 13-k_T-point-based k-space trajectory. **c**: Symmetric 19-k_T-point-based k-space trajectory. **d**: STA-optimized k-space trajectory consisting of 7 different k_T-point locations.

respectively. Based on these initial trails a $1/30\mu s$ time step was adopted, i.e., 30 sub-steps per sample point in the RF waveform[5].

To evaluate the impact of the joint k-space optimization, 180^{o}-inversion pulses were based on four different initial k_T-point trajectories. The first three (Fig. 7.7**a-c**) are symmetric patterns, loosely approximating the design constraints suggested in the linear-class of LTA pulses (Pauly et al., 1989), where the initial k_T-point locations are on the k_x, k_y, k_z axes, 1/FOV away from one-another, adding one more layer at a time. The fourth trajectory (Fig. 7.7**d**) is a STA optimized design based on a greedy algorithm (Ma et al., 2010). Simulated results, obtained from MOCA with or without a simplex-based joint k-space optimization (Nelder and Mead, 1965; Grissom and Pauly, 2010), were evaluated based on B_1^+ and B_0 profiles measured in a total of 6 different subjects.

Results & Discussion

All k-space trajectories considered in this evaluation allow inversion pulses to be found with a NRMSIE of less than 8% (Fig. 7.8). Nonetheless, adopting our implementation of the joint k-space design generally results in a slightly better inversion fidelity. Advantages in energy deposition, on the other hand, only become apparent when considering large numbers of k-space locations (Fig. 7.8**c**). Considering that the results shown in Fig. 7.8 start after the first complete iteration of the MOCA algorithm, the initial energy and NRMSIE reduction suggest that these initial trajectories are less optimal. Inaddition, adding more k-space locations tends to lengthen the overal pulse duration. Consequently the off resonance effects become even more challenging, thus mitigating the advantage of the additional degrees of freedom. In general, the initial gradient waveform appears to be of greater significance than the added degrees of freedom provided by our implementation of the joint design method. Moreover, optimization of the k-space trajectory based on the STA approximation does not seem to improve the overall performance. Therefore, these results illustrate the need for a more direct method to design optimized k-space trajectories when targeting LTA excitations. Nonetheless, in the absence of such a method, with our current setup, the presented 13 k_T-point-based design can be adopted to provide high fidelity inversion pulses.

Conclusions

The joint-design method provides some additional robustness by allowing the initial k-space trajectory to evolve to a more suitable one. However, our current implementation quickly converges to a local optimum, thus providing only minimal improvements. More elaborate search methods, such as originally proposed by Grissom and Pauly (2010), could perhaps yield better results. Nonetheless, the problem originates from the application of the STA approximation in the initial design stage. Consequently, to obtain truly optimized RF-wavefroms, a more direct LTA design method is needed.

[5]The same internal time-step as used in the forward and backwards integration steps of the OCA and MOCA

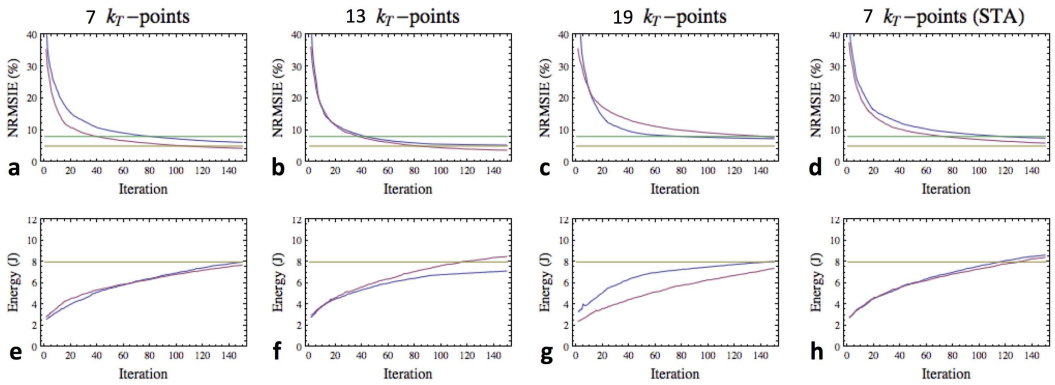

Figure 7.8: Comparison of the optimal control implementations: MOCA (blue), MOCA + joint k-space optimization (purple). Results correspond to the k-space trajectories illustrated in Figure 7.7. Top row: evolution of the NRMSIE when targeting a 180°-inversion. To aid comparison between subfigures, the 8% NRMSIE line is indicated in green, whereas the 5% NRMSIE line is marked in brown. Bottom row: evolution of the cumulative energy deposition when targeting a 180°-inversion. To aid comparison between subfigures, the 8 J mark is indicated with a brown line.

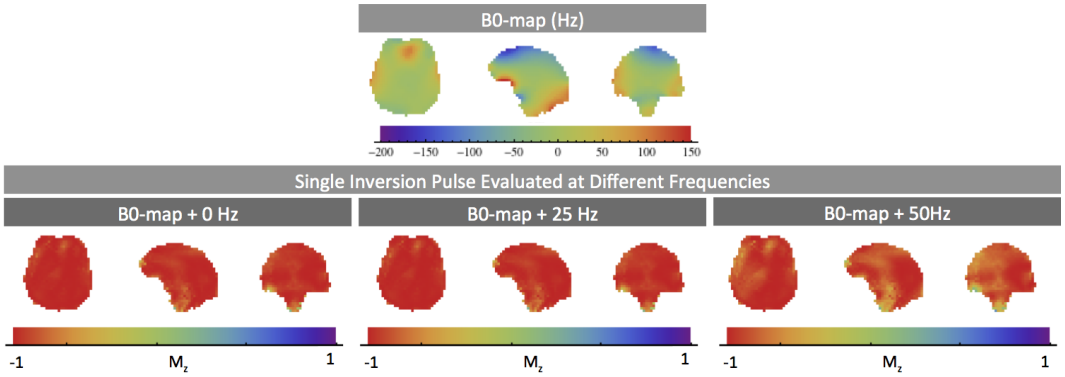

Figure 7.9: Effective bandwidth of a 6-ms 13-k_T-point-based inversion pulse. Top: Three orthogonal slices through the brain showing the measured B_0-field. Bottom row: Effect of a single inversion-pulse based on the perturbed B_0-maps. From left to right: the simulated excitation fidelity from the measured B_0-map, the same assuming a 25Hz offset on top of the measured B_0-map, the same with double the frequency offset.

7.6 LTA pulse design: B_1^+ versus B_0

In the previous sections, it was demonstrated how the B_1^+ inhomogeneities can be mitigated considering an arbitrary target FA. However, potential inaccuracies in the calibration measurements were not considered. Apart from systematic errors in the B_1^+-estimation method (Pohmann, 2011), the biased demarcation of the region of interest and partial volume effects at the edges of the brain-mask also affect the final excitation fidelity.

Although STA excitations are also influenced by the aforementioned error sources, the short pulse durations allow for a sufficiently large bandwidth to moderated the impact of minor deviations from the measured B_0 field. Therefore, minor edge defects in the ROI, where generally the strongest B_0 variations occur, bear little impact on the final excitation fidelity.

Due to the SAR constraints and limited peak RF-power permissible on the amplifiers LTA excitations require much longer pulse durations. Consequently, the effective pulse bandwidth is substantially reduced. In the context of inversion pulses, the bandwidth may even become comparable to the spatial variations in the B_0 field (Fig 7.9). Therefore, in the subsequent sections, special attention is given to brain masking and RF-bandwidth.

Region of Interest (Brain masking)

For optimal performance, the k_T-points-based RF-pulse optimization should be limited to the ROI only. Although this region can manually be defined, it is both a cumbersome and error-prone procedure. Therefore it is most desirable to have a fast and robust automated method to identify the ROI. Currently, various software packages are available that allow the brain volume to be extracted automatically (BrainVisa, FreeSurfer, FSL). However, measurements obtained for this purpose, during the pTx calibration stage, generally yield a relatively poor contrast. Indeed a short calibration time is used to maximize the time available for subsequent optimized pTx acquisitions. Taking this into consideration, the FSL brain extraction tool (Smith, 2002) appears to be suitable[6].

So far, attempts to perform brain delineation based on images with a 5-mm isotropic resolution have not yielded robust results. Due to partial-volume effects, the skull-brain interface is often not well defined, causing portions of non-brain tissue to be included into the ROI, or brain tissue to be excluded from it. More robust automated brain extraction was achieved by selecting an in-plane resolution of 2.5 x 2.5 mm paired with a slice thickness of 5 mm (FLASH with TR=25ms, FA $\sim 10°$, TE1/TE2=10/15ms, total acquisition time ~ 1.5 min). After post-processing, the obtained brain mask may be down-sampled to match the B_1^+ and B_0 calibrations. Even so, it may still be beneficial to allow some T_2*-weighting to suppress signal originating from areas outside of the brain.

Comparing inversion pulses based on two different brain masks, one with 15-ms and the other with 10-ms echo-time, it becomes clear how important the accuracy of the brain mask is in the context of LTA pulse design (Fig. 7.10). Although the longer TE results in a visually more appealing brain mask, some crucial areas close to intracranial cavities are excluded due to intra-voxel dephasing. Evaluating the waveform obtained from either mask on a more accurate delineated brain volume (the union of both masks) reveals substantial defects in the excitation profile (Fig. 7.10, black arrows). The brain mask obtained with the shorter TE, on the other hand, mostly includes these cavity-neighboring regions, resulting in better overall excitation fidelity. Nonetheless, some small defects can still be observed in areas where the mask excluded small parts of the brain.

Bandwidth

Compared to the STA excitations detailed in the previous chapter, the LTA inversions demonstrate a much smaller bandwidth. Although the measured B_0-map is taken into account during the pulse design, its coarse resolution may average out some of the high magnetic susceptibility effects at the edges of the brain. In principle, a higher resolution B_0-map could be incorporated in the pulse design to mitigate these effects. This not only substantially lengthens the calibration procedure, but also enhancing the resolution by a factor x increases the computational load by a factor x^3. Alternatively, an extended bandwidth can be enforced locally. To this end, the broad bandwidth pulse design method proposed by Setsompop et al. (2009) can be adopted. This allows the pulse design to be optimized simultaneously at multiple frequency offsets in every voxel. In order not to overly constrain the problem, this approach can be confined to potential trouble areas. To automate the determination of such regions, the ROI can be convolved with an edge detection filter to obtain the boundaries most sensitive to magnetic susceptibility effects. Specifying different frequency offsets for these regions, i.e., $\pm 25\%$ on top of the measured value, and incorporating them into MOCA for simultaneous optimization, an extended bandwidth is enforced in these regions only (Fig. 7.11).

Initial results

Based on the simulations presented in this chapter, the impact of automated brain masking for the purpose of LTA pulse design was evaluated in-vivo (Fig. 7.12). This experiment clearly illustrates the negative impact associated with the exclusion of small critical brain areas (Fig. 7.12**a**). Although the above detailed approach is still under evaluation, initial measurements suggest that, once a good brain mask is obtained, it is generally sufficient to enforce a 25% margin around the measured B_0-field near the intracranial cavities (Fig. 7.12**b**).

[6] At first sight, FreeSurfer appears to be relatively computationally demanding, whereas BrainVisa seems to rely heavily on the contrast. Nonetheless, both BrainVisa and FreeSurfer may prove equally reliable and efficient, when optimized by an experienced user.

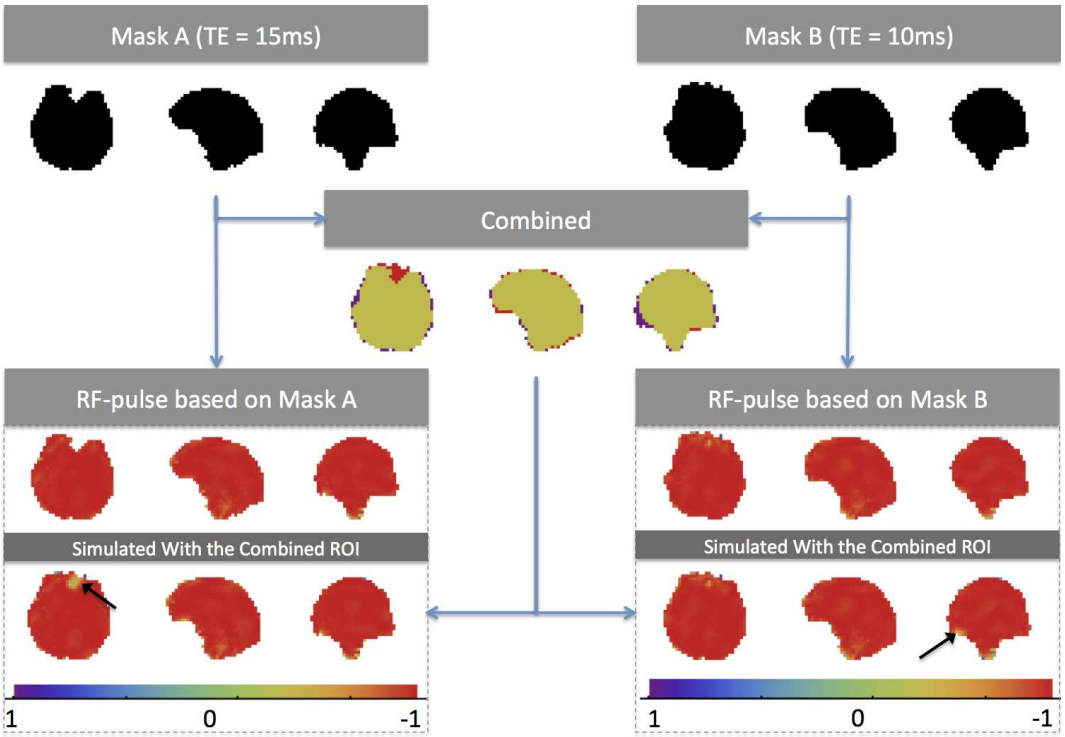

Figure 7.10: Illustration of the sensitivity of LTA pulse design with respect to imperfections in the definition of the ROI.

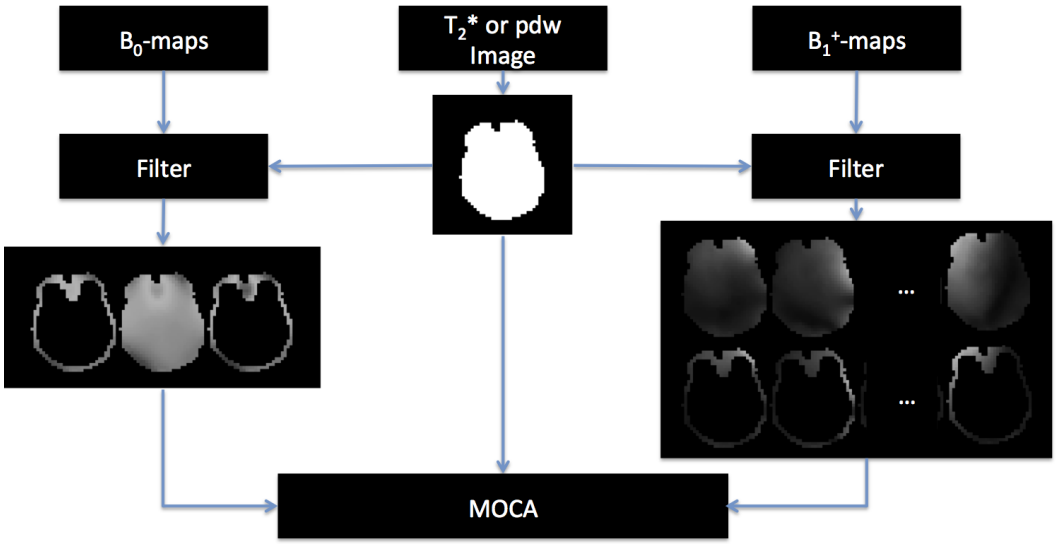

Figure 7.11: Illustration of the procedure adopted to define localized areas where an extended bandwidth will be enforced during MOCA-based optimization. On the left hand side: application of the brain mask and edge detection filter, are used to produce a set of 3 distinct B_0-maps for consideration during pulse design. The central one of these three corresponds to the measured ΔB_0-map throughout the entire brain, whereas the ones next to it correspond to a $\pm 25\%$ deviation to be incorporated on the edges only. On the right hand side: the same mask and filter is applied to obtain the B1-maps corresponding to this extended space, where the voxels on the edges of the brain mask are now represented 3 times (collectively covering a $\pm 25\%$ bandwidth around the expected off-resonance frequencies) during the MOCA based optimization.

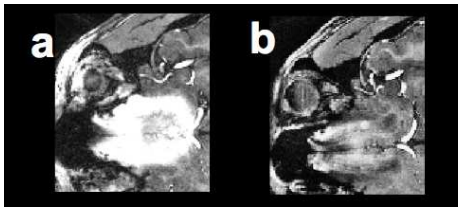

Figure 7.12: Preliminary result illustrating the impact of the pulse bandwidth on the image quality. Both subfigures were acquired with the MP-RAGE sequence including a 13-k_T-point-based inversion pulse (same subject). **a**: Inversion pulse designed with MOCA, based on a brain mask with a 15-ms echo time. **b**: Inversion pulse designed with broad-bandwidth MOCA, based on a brain mask with a 10-ms echo time.

7.7 Summary and Recommendations

Although the spatial domain method (Grissom et al., 2006) with the magnitude least squares approach (Setsompop et al., 2008c) can readily be adopted to design LTA excitations up to $\sim 90°$, provided transverse magnetization is substituted by the target FA in radians (Boulant and Hoult, 2012) the excitation significantly deteriorates as the targeted FA approaches 180°. Going to the presented MOCA provides a robust optimization procedure to account for the non-linear dynamics of the Bloch equations. Nonetheless, the optimal control-based solutions presented in this chapter could still be improved. For instance to enhance the control of the RF-deposition, the sub-pulse duration could be considered as a free parameter, like in the STA approach. Recasting the problem formulation into the spin-domain (Jaynes, 1955; Pauly et al., 1991) as proposed by Grissom et al. (2009), would reduce the computational load, and could provide valuable tools to enforce limited-phase constraints when designing refocusing pulses. Ultimately a direct (very) large-tip-angle pulse design method, omitting the small-tip-angle approximation and including a direct k-space optimization routine, is desired to approximate a truly optimized RF solution. However, such a method has hitherto remained elusive.

8 Parallel-Transmission-Enabled Magnetization-Prepared Rapid Gradient-Echo T_1-Weighted Imaging of the Human Brain at 7 Tesla

This chapter contains methods & principles that were accepted for publication as abstracts in the proceedings of the Annual Annual Meeting of the International Society for Magnetic Resonance in Medicine 2012.

M.A. Cloos, N. Boulant, M. Luong, G. Ferrand, E. Giacomini, M-F. Hang, C.J. Wiggins, D. Le Bihan, and A. Amadon. (2012) "k_T-points-based Inversion Pulse Design for Transmit-SENSE Enabled MP-RAGE Brain Imaging at 7T."

M.A. Cloos, A. Amadon, N. Boulant, M. Luong, G. Ferrand, E. Giacomini, M-F. Hang, C.J. Wiggins, and D. Le Bihan. (2012) "Parallel-Transmission-Enabled T_1-Weighted Human Brain Imaging for Robust Volumetric and Morphologic Studies at 7T."

Abstract

One of the promises of UHF MRI scanners is to bring finer spatial resolution in the human brain images due to an increased signal to noise ratio. However, at such field strengths, the spatial non-uniformity of the RF transmit profiles challenges the applicability of most MRI sequences, where the signal and contrast levels strongly depend on the FA homogeneity. In particular, the MP-RAGE sequence, one of the most commonly employed 3D sequences to obtain T_1-weighted anatomical images of the brain, is highly sensitive to these spatial variations. These cause deterioration in image quality and complicate subsequent image post-processing such as automated tissue segmentation at UHF.

In this work, we evaluate the potential of pTx to obtain high-quality MP-RAGE images of the human brain at 7 Tesla. To this end, non-selective transmit-SENSE pulses were individually tailored for each of 8 subjects under study, and applied to an 8-channel transmit-array. Such RF pulses were designed both for the low-FA excitation train and the 180° inversion preparation involved in the sequence, both utilizing the recently introduced k_T-points trajectory. The resulting images were compared with those obtained from the conventional method and from subject-specific RF-shimmed excitations. In addition, four of the volunteers were scanned at 3 Tesla for benchmarking purposes (clinical setup without pTx). Subsequently, automated tissue classification was performed to provide a more quantitative measure of the final image quality.

Results indicated that pTx could already significantly improve image quality at 7 Tesla by adopting a suitable RF-Shim. Exploiting the full potential of the pTx-setup, the proposed k_T-points method provided excellent inversion fidelity, comparable to what is commonly only achievable at 3 Tesla with energy intensive adiabatic pulses. Furthermore, the cumulative energy deposition was simultaneously reduced by over 40% compared to the conventional adiabatic inversions. Regarding the low-FA k_T-points based excitations, the FA uniformity achieved at 7 Tesla surpassed what is typically obtained at 3 Tesla. Subsequently, automated white and gray matter segmentation confirmed the expected improvements in image quality, but also suggest that care should be taken to properly account for the strong local susceptibility effects near cranial cavities. Overall, these findings indicate that the k_T-point-based pTx solution is an excellent candidate for UHF 3D imaging, where patient safety is a major concern due to the increase of specific absorption rates.

8.1 Introduction

The magnetization-prepared rapid gradient echo sequence (Mugler and Brookeman, 1990) referred to as "MP-RAGE", is among the most commonly employed 3D sequences to obtain T_1-weighted anatomical images of the brain. To this end, typically an inversion pulse is used followed by a spoiled fast low angle shot (FLASH) train acquiring one partition plane in k-space per repetition (TR). Careful adjustment of the delay between the inversion and the acquisition block, as well as of the usual imaging parameters, allows excellent contrast between gray matter (GM), white matter (WM) and (CSF) at field strengths up to 3 Tesla (Deichmann et al., 2000; Han et al., 2006; Mugler and Brookeman, 1990).

Strong GM/WM/CSF contrast is a prerequisite for both manual and automated tissue segmentation. Analysis based on such segmented data allows the study and potentially diagnosis of various pathological conditions. Measurements of change in GM, WM and CSF volume for example provide profound insights into the ageing brain (Gur et al., 1991) and pathologic progression in neurodegenerative diseases such as Alzheimer (Silbert et al., 2003) and Huntington's disease (Thieben et al., 2002). Moreover, thinning of the cerebral cortex is often region-dependent, stressing the importance of high quality highly-resolved images. Aside from its applications in pathology, the MP-RAGE sequence has become the current standard for anatomical reference images in functional studies such as in fMRI, PET, EEG and MEG. In the quest for ever more detailed images of the human brain, increasingly higher main-magnetic field strengths are being explored to reap the benefits of increased signal and contrast (Ocali and Atalar, 1998). Already at 3 Tesla, the RF wavelength corresponding to the proton Larmor frequency becomes comparable to the dimensions of some imaged human body parts. Consequently, non-uniformities arise in the transmit sensitivity (B1+), which results in zones of shade and losses of contrast distributed across the images of large organs such as the abdomen or thighs (Bernstein et al., 2006). Considering the application of the MP-RAGE sequence to human brain imaging, a combination of adiabatic inversion-pulses (Bernstein et al., 2004) and hard excitations can still be considered adequate to obtain high quality T_1-weighted images at 3 Tesla (Han et al., 2006). Moving up in field strength to 7 Tesla and beyond, the increased Larmor frequency results in strong transmit sensitivity (B_1^+) variations throughout the volume of the human brain (Yang et al., 2002). Consequently, contrast artifacts form due to unwanted spatial variations of the flip-angle (FA). Coincidentally, the uniformity of the receive sensitivity (B_1^-) deteriorates with the decrease in wavelength. This results in additional unwanted signal intensity variations (bias-field) throughout the image.

Various methods have been proposed to alleviate both the deteriorated T_1 contrast and spatial B_1^- variation in MP-RAGE images. These include post-processing techniques exploiting the relatively low spatial frequencies in the bias-fields to remove unwanted signal intensity variations (Wald et al., 1995; Styner et al., 2000; Ashburner and Friston, 2005). Alternatively, an adaptation on the MP-RAGE sequence, referred to as the MP2RAGE sequence, has been proposed in the form of a second acquisition block following the inversion (Van de Moortele et al., 2009). Combined with a suitable post-processing scheme, the images produced by the two acquisition blocks can be combined to produce high-quality bias-field-corrected T_1-weighted images. Although this method is less sensitive to B_1^+ non-uniformities, the contrast may not be recovered in severely affected areas. At 7 Tesla, depending on the RF coil in use, such areas may typically reside in the cerebellum, potentially extending out into the occipital or temporal lobes (Van De Moortele et al., 2007; Marques et al., 2010). Post-processing-based correction of these contrast artifacts induced by strong B_1^+ non-uniformities requires a priory knowledge of the anatomical structures, therefore defeating the general purpose of most T_1-weighted imaging techniques (Wang et al., 2005). Considering the foreseeable continued increase in field strength, several 9.4 Tesla scanners readily in operation and the development of an 11.7-Tesla human MRI system at our site, increased B_1^+ artifacts may be expected, possibly limiting the applicability of the MP-RAGE and MP2RAGE approaches. Furthermore, the inclusion of the second acquisition block in the MP2RAGE significantly lengthens the TR (Marques et al., 2010). Thus high parallel imaging acceleration factors must be employed, at the expense of SNR, to achieve acceptable acquisition times (Sodickson and Manning, 1997; Pruessmann et al., 1999; Griswold et al., 2002).

Parallel transmission (pTx) was proposed to alleviate these limitations (Katscher et al., 2003; Zhu, 2004). This technique utilizes multiple independently-driven coil elements distributed around the subject. In its simplest form, referred to as RF-Shimming (Adriany et al., 2005), the B_1^+-fields from all coil elements are combined to optimize the B_1^+-distribution in a region of interest (ROI). Similarly to the conventional Circularly-Polarized (CP) mode utilized by most clinical systems today, a single pulse shape is transmitted at any particular time point in the pulse sequence. However, the RF-Shimming technique allows the amplitude

and phase combination between coil-elements to be tailored to a specific ROI. Further generalization of this concept led to the introduction of Transmit-SENSE (Katscher et al., 2003; Zhu, 2004), exploiting the full potential of the transmit-array by tailoring the RF-waveforms to be applied to each of the individual coil-elements. This transmission generally occurs in concert with magnetic field gradients (usually used for spatial selectivity) so as to provide additional degrees of freedom to maximize the final excitation uniformity. Thus the RF pulses are played while pursuing a trajectory in k-space, where $\mathbf{k}$ is the spatial frequency vector: $\mathbf{k}(t) = -\gamma \int_t^T \mathbf{G}(\tau) \cdot \mathbf{r} d\tau$, T being the RF pulse duration and $\mathbf{G}(t)$ the controlled linear magnetic field gradient at time t.

In the framework of Transmit-SENSE, whole-brain non-selective uniform excitations were recently demonstrated at 7 Tesla with the k_T-points method introduced by the authors (Cloos et al., 2012). This technique proposes a minimalist transmit k-space coverage in the vicinity of the k-space center to compensate for the smooth RF inhomogeneities without depositing high levels of energy. The few k-space locations where RF is transmitted are the so-called k_T-points. The objective of this manuscript is to extend this work beyond the small-tip-angle regime (Pauly and Nishimura, 1989) and validate the applicability of k_T-point pulses to T_1-weighted whole brain imaging in the MP-RAGE sequence. This would demonstrate the ability of such pulses to retain the desired contrast in short-TR sequences (here we refer to the FLASH inter-echo time), where earlier attempts have shown their limitations (Boulant, 2009). In addition, the in-vivo demonstration of pTx-based inversion pulses would provide a prospective on their potential to replace SAR-intensive adiabatic pulses in UHF MRI.

The RF energy control is an important issue, as it will directly impact the SAR level in the patient. To facilitate our demonstration, an approach to SAR management for parallel-transmission will be presented in the next section, which while conservative, is less restrictive than the commonly adopted worst-case approach (Collins et al., 2007; Brunner et al., 2008).

Experimental results obtained at 7 Tesla with both the conventional and proposed pTx methods were compared to images acquired at 3 Tesla without pTx. Subsequently, the potential impact of the attained image quality on volumetric and morphological studies is quantified by analysis of the outcome from automated tissue classification and evaluation of the cortical ribbon.

8.2 Methods

Pulse design

Prior to on-line RF pulse design, the main field offset ΔB_0-map as well as transmit and receive maps were collected with a low resolution (5-mm) as detailed in Cloos et al. (2012). From these calibration measurements, a brain mask was created with the brain extraction tool from the FSL software package (Smith, 2002) to define the three-dimensional ROI on which pulse design should focus.

The FLASH train excitation pulse design was performed in the small-tip-angle regime (Pauly and Nishimura, 1989). To this end, the spatial domain method (Grissom et al., 2006) was adopted including the Magnitude Least Squares approach introduced by Setsompop et al. (2008c), with an initial target transmit phase map obtained from the conventional CP mode. Non-selective uniform excitation of the brain volume was achieved by selecting a 5 k_T-point trajectory as described in Cloos et al. (2012). Targeting an average FA of 6.5°, the RF voltage per channel was limited to 45 Volts so as to constrain their SAR contribution.

Magnetization preparation pulses were designed in two stages. First a candidate pulse was obtained utilizing the tools developed for the excitation pulse design, now targeting 180° (Fig. 8.1**a**, step 1). Constraints on the inversion pulse duration are more lenient, hence 13 k_T-points were selected to reap the benefits provided by the increased degrees of freedom. The symmetric spread of the k_T-points in a diamond-like shape surrounding the center of transmission k-space (Fig. 8.1**b**) allowed to approximate the linear class of large tip angle pulses introduced by (Pauly et al., 1989). Subsequently the optimal control approach was applied to take into account the non-linear behavior of the Bloch-equations at large tip angles (Fig. 8.1**a**, step 2). Our implementation differs slightly from that demonstrated by Xu et al. (2008), since, for an inversion, the produced phase distribution can be neglected. Consequently a magnitude-only optimization problem is solved, where the normalized root mean square inversion error (NRMSIE) defined as $N^{-1/2}\sqrt{\sum_{\mathbf{r}} (M_z(\mathbf{r}) + 1)^2}$ is minimized, with $\mathbf{r}$ designating a voxel location in the brain and N their number. In addition, the phase

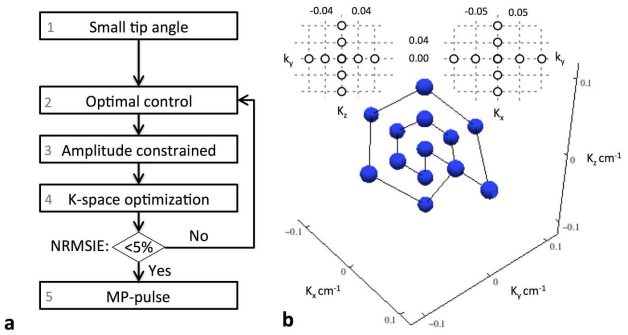

Figure 8.1: Schematic overview of the large tip angle pulse design method used to design inversion pulses. **a**: Step 1: Small-tip-angle pulse design as described by Cloos et al. (2012). Step 2: Optimal control approach as described by Xu et al. (2008) modified to optimize the longitudinal magnetization magnitude only while taking the ΔB_0 evolution into account. Step 3: Cut-off filter to constrain the peak amplitude. Step 4: Nelder–Mead search of k-space for improved k_T-point locations. **b**: k-space trajectory used for the k_T-point-based parallel transmission inversion pulses. RF energy is deposited only at the k-space locations indicated by the spheres. Gradient blips (60-µs, no RF) are played in-between to move to the next k-space location.

evolution due to $\Delta B_0(\mathbf{r})$ was encompassed in the optimization procedure. In the end, for optimal flexibility, the sub-pulse shapes at each k_T-point are allowed to vary rather than staying square as was the case in Cloos et al. (2012). The peak amplitude of the designed waveforms was constrained to almost the maximum voltage available per channel (180 V). For this purpose, a cutoff filter was applied to the obtained RF waveforms between iterations in the optimal control approach (Fig. 8.1**a**, step 3). Inspired by Grissom and Pauly (2010), the Nelder–Mead method (Nelder and Mead, 1965) was applied to search k-space for improved k_T-point locations (Fig. 8.1**a**, step 4). These steps (2-4) were iterated until either the NRMSIE dropped below 5%, 120 such iterations were performed, or the cumulative energy on a single channel reached 1.8 Joules. The later constraint was selected to exclude solutions where the RF energy was not properly distributed over the brain, in which case the last solution obtained still fulfilling the constraints was adopted.

The complete procedure was implemented in C++ including GPU-enabled CUDA extensions allowing subject-specific inversion pulse design within a time scale compatible with in-vivo studies performed on human subjects.

For comparison at 7 Tesla, 7-ms hyperbolic-secant adiabatic inversion pulses (Silver et al., 1985) in combination with 500-µs hard-pulse excitations were set for both the conventional CP mode and subject-specific static RF-shims. The latter were obtained by applying the small-tip-angle pulse design method to a single k_T-point at the center of k-space. Channel-dependent Tikhonov parameters (Cloos et al., 2010c) were used to constrain the maximum amplitude variation among channels in the RF-shim, thereby minimizing the maximum local SAR deposited in the head while allowing the adiabatic condition to be satisfied as much as possible with the peak power available in our setup. The 7- and 0.5-ms durations of the conventional pulses were chosen so as to not exceed the SAR limitations and yet keep as close as possible to the pulse durations obtained with the k_T-points approach.

At 3 Tesla, standard native pulses were applied in the MP-RAGE sequence. Because of a lower RF energy demand, their durations varied slightly from the ones we used at 7 Tesla: adiabatic hyperbolic secant and excitation hard pulse durations were 10.2 ms and 0.1 ms respectively.

Setup

Four volunteers were scanned at 7 Tesla to evaluate the applicability of the proposed methods for adaptation in the MP-RAGE sequence. In addition, B_1^+-maps were measured in four more volunteers to investigate the variation in energy deposition and achievable excitation fidelity. Our institutional review board approved the study and informed consent was obtained from all volunteers. Experimental validation was performed on a 7 Tesla Magnetom scanner (Siemens, Erlangen, Germany), equipped with an 8-channel transmit array (1 kW peak power per channel) and an AC84 head gradient system (Siemens, Erlangen) allowing amplitudes up to of 50 mT/m and a slew rate of 333 mT/m/ms.

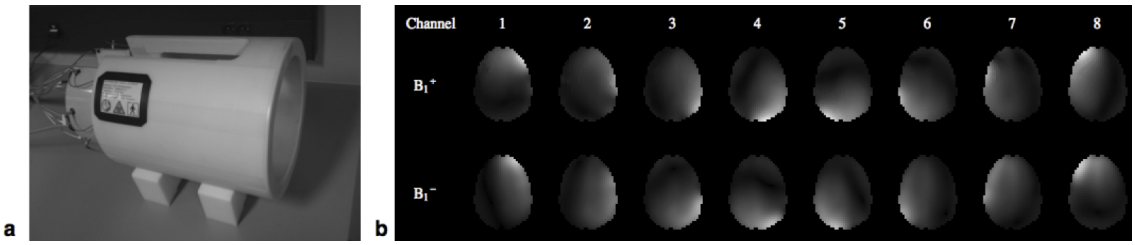

Figure 8.2: Transmit-array coil used at 7 Tesla in this study (**a**) and the corresponding transmit (B_1^+) and receive (B_1^-) sensitivity profiles measured in the human brain (**b**).

For both RF transmission and reception, a home-made transceiver-array head coil was used (Ferrand et al., 2010). The array consists of 8 stripline dipoles distributed every 42.5-degrees on a cylindrical surface of 27.6-cm diameter, leaving a small open space in front of the subject's eyes (Fig. 8.2**a**). All dipoles were tuned ideally to the proton Larmor frequency at 7 T and matched identically to a 50-Ω line impedance. Transmit and receive sensitivity profiles as well as ΔB_0-maps were determined as described in Cloos et al. (2012). Typical transmit and receive profiles measured in the human brain are shown in Fig. 8.2**b**. Variations in B_0 demonstrated standard deviations of approximately 45 Hz with peak values up to about 300 Hz near the sinus cavity.

In addition, for benchmarking purposes, the same volunteers were also scanned at 3 T (without parallel transmission). The clinical system used for that purpose was a Magnetom Tim Trio (Siemens, Erlangen) equipped with a whole-body transmit RF coil and a 12-channel receive head coil.

Sequence parameters and validation

Each of the pulse shapes as described by the above designs was inserted into the MP-RAGE sequence and applied to the human brain at 7 Tesla. Sequence parameters were: inversion time TI = 1.1 s, inversion TR = 2.6 s, FLASH TR or IET = 7.1 ms, TE = 3.5 ms, FA = 6.5°, 0.8-mm isotropic resolution with a 256x256x192 matrix in sagittal acquisition and a phase-encode SENSE factor of 1.33 (Pruessmann et al., 1999), total acquisition time ∼ 8 min. First-order receive sensitivity correction (Wang et al., 2005) was applied to provide a more direct qualitative comparison between the different MP-RAGE implementations. The somewhat strong AC84 gradient spatial non-linearities were corrected for at the end of the image reconstruction procedure. Both the RF-shim and k_T-point-based approaches were compared to the conventional CP-mode configuration obtained at 3 T and 7 T.

The MP-RAGE images obtained at 3 Tesla were acquired with routinely-used parameters: 1.04x1.0x1.1mm resolution, TI = 0.9 s, TR = 2.3 s, TE/IET = 3.0/7.1ms, FA = 9°, partial Fourier 7/8, 256x230x160 matrix in sagittal acquisition, total acquisition time ∼ 8 min.

Considering that the images obtained with the conventional combined transmission at 3 Tesla are often deemed to be of sufficient quality to be used in a variety of studies, they may be regarded as a frame of reference. Moreover, they provide a gauge to estimate the applicability of the proposed method for automated GM/WM/CSF segmentation. To this end, automated tissue classification was attempted with two commonly employed software packages: SPM (distributed through the website http://www.fil.ion.ucl.ac.uk/spm/) and FreeSurfer (freely available to the research community through the website http://surfer.nmr.mgh.harvard.edu/). In addition, the latter tool also provided a more quantitative metric for the assessment of the obtained tissue classification in the form of localized cortical gray matter thickness measurements (Fischl and Dale, 2000).

8.3 Results

Pulse design

Based on the B_1^+-maps measured in all eight volunteers, full Bloch simulations were performed to evaluate the theoretical performance of the inversion pulses (Fig. 8.3**a**). On average, the 7-ms hyperbolic secant

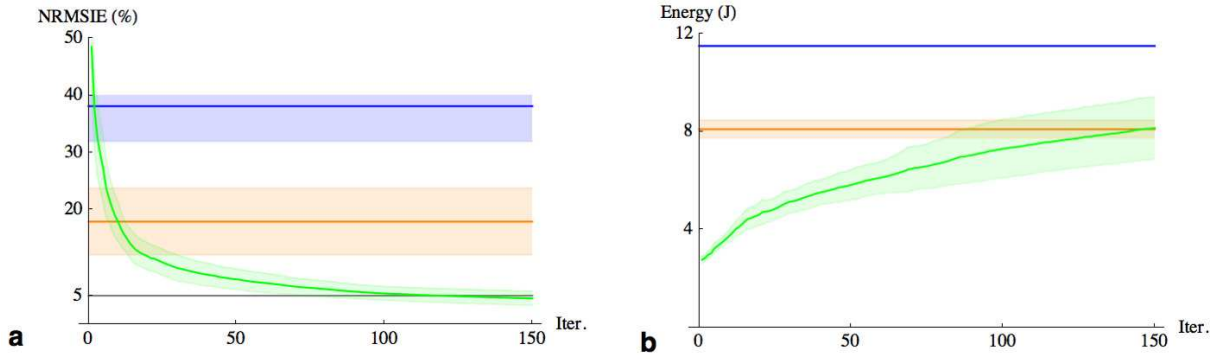

Figure 8.3: A comparison of the different inversion pulses tailored for all 8 subjects. **a**: The normalized root mean square inversion error (NRMSIE) as a function of the iteration number in the optimal control approach. The CP-mode, RF-shim and k_T-points method are indicated in blue, orange and green respectively. The dark lines indicate the mean values whereas the light areas indicate standard deviation from the mean. **b**: The total RF energy required as a function of the iteration number in the optimal control approach. The same color-coding was used as in **a**.

adiabatic inversion applied to the conventional CP-mode resulted in a 38±6% NRMSIE (cerebrum only: 22±8%). Similar to what is achieved at 3 Tesla (Fig. 8.4**a**), typically good inversion is established in the parietal and frontal lobes. However, extremely poor results are obtained in the cerebellum in this case, extending up into the lower parts of the occipital lobe (Fig. 8.4**b**). Note that although these values may seem relatively large for adiabatic pulses, adopting the same metric for optimally-chosen square pulses resulted in a 63±6% NRMSIE (cerebrum only: 49±8%). Application of a subject-specific RF-shim with the above adiabatic pulse improved the inversion quality to 18±6% NRMSIE (cerebrum only: 14±4%). Nevertheless, substantial FA variations remained in the cerebellum. Furthermore, additional fluctuations were sometimes introduced along the edges of the parietal, frontal and temporal lobes (Fig. 8.4**c**).

Although the initial candidate k_T-point-based inversions typically result in an NRMSIE in excess of 40%, application of the optimal control approach rapidly improves the performance beyond what was achieved with the adiabatic pulses (Fig. 8.4**d**). On average the optimization reaches a NRMSIE of 5±2% (cerebrum only: 5±1%) within about 100 iterations (Fig. 8.3**a**). Based on the performance of a 3-Ghz Intel Xenon system paired with an NVIDIA Tesla C2050 GPU, these pulses, optimized with 1-µs raster time, can be found within about 3 minutes. Considering the cumulative energy deposition, the k_T-points method demonstrates a clear tradeoff between inversion quality and the energy required (Fig. 8.3**b**). Although improvement of the NRMSIE results in an increased energy deposition, the 5%-target is achieved with less energy than needed by the RF-shim, and requires 40% less energy than the conventional CP mode. Another way of comparing the pulse performance is to fix the level of NRMSIE to that of the RF-shim (18%), and look at the energy required by the k_T-points to reach it: this energy (4 J) is half the one used by the RF-shimmed adiabatic pulse whereas the k_T-point pulse duration is 1-ms shorter. This tends to show optimally-controlled k_T-points are not only excellent candidates for FA homogenization, but also with respect to SAR management.

In addition to the inversion, the excitation pulses also have an impact on the contrast (Deichmann et al., 2000). The relatively minor spatial variations in the transmit sensitivity at 3 Tesla are generally of little concern for clinical human brain imaging applications (Fig. 8.4**e**). On the other hand, at 7 Tesla, the conventional method clearly shows a strong central brightening effect (Fig. 8.4**f**), that even the application of a subject-specific RF-shim cannot completely subdue (Fig. 8.4**g**). However, adopting the k_T-points method, superior excitation fidelity was achieved compared to what is typically obtained at 3 Tesla (Fig. 8.4**h**).

Image quality

The combined impact of inversion and excitation can be seen in the T_1-weighted MP-RAGE images (Fig. 8.5). Whereas the images obtained at 3 Tesla with a transmit body coil are barely affected by B_1^+-inhomogeneities (Fig. 8.5**a**), the conventional method applied at 7 Tesla results in strong contrast artifacts (Fig. 8.5**b**). Due to

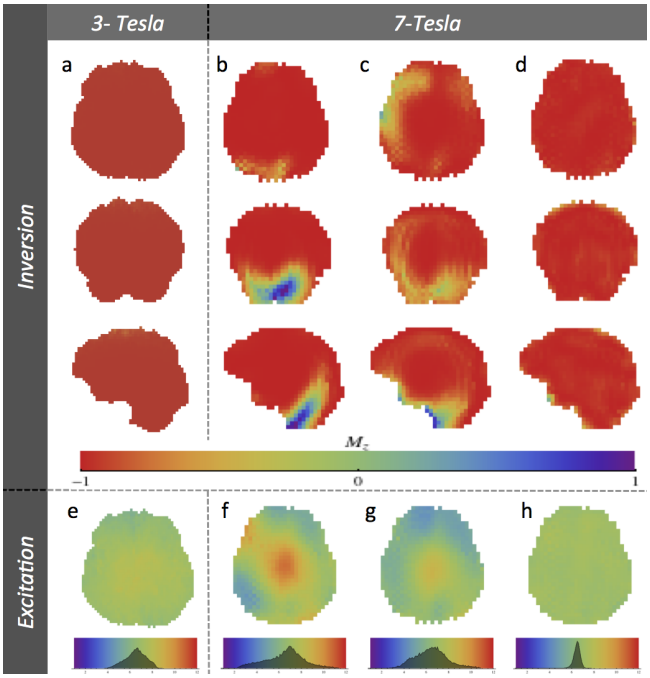

Figure 8.4: A comparison of the different inversion and excitation pulses applied to a representative subject (simulation only). The inversion pulses from left to right: **a**: hyperbolic secant adiabatic inversion pulse at 3 Tesla (NRMSIE 1.3%), **b**: CP-mode with a 7-ms hyperbolic secant adiabatic inversion pulse (NRMSIE 30.1%), **c**: RF-shim with the same pulse (NRMSIE 15.7%), and **d**: k_T-point-based 6.1-ms inversion pulse (NRMSIE $\approx$ 5%). The FA-maps of excitation pulses, all targeting an average of 6.5°, are shown alongside their corresponding FA histogram. From left to right: **e**: 3 Tesla, **f**: conventional method at 7 T, **g**: subject-specific RF-Shim at 7 T, **h**: k_T-point-based excitations at 7 T.

the poor inversion quality produced, distinction between GM and WM is no longer possible in the cerebellum. Furthermore, as expected from the simulation (Fig. 8.4**b**), the contrast artifact can also be seen extending into the occipital lobe.

Application of a subject-specific RF-shim significantly improved image quality (Fig. 8.5**c**), thus allowing cerebellar GM/WM to be distinguished. Even so, residual B_1^+ non-uniformities (Fig. 8.4**c**) introduced artificial contrast variations complicating distinction between GM & WM with confidence. This can be seen, for example, in the frontal part of the temporal lobe (Fig 8.5**g**). Furthermore, the arachnoids cyst, a CSF-filled lesion observable in front of the temporal lobe of this subject (white arrow), now appears slightly brighter than the CSF in the ventricles.

The proposed combination of k_T-point-based inversion and excitation pulses significantly reduces the aforementioned residual contrast artifacts (Fig. 8.5**d**). In particular, intricate structures can now be resolved in greater detail (Fig. 8.5**h**). Regarding the central part of the brain, where the conventional methods typically produce fair results, a reduction in signal intensity is observed. This coincides with the absence of a central brightening effect typical of the CP-mode and, to a lesser extent, RF-shim excitations. Therefore, even though all excitations were designed to produce an average FA of 6.5°, both the CP-mode and RF-shim produce substantially higher FA in the center of the brain. Consequently they demonstrate relatively more signal in this area. However, these deviations from the target FA also lead to a change in contrast, whereas the k_T-point-based method produces a uniform FA distribution resulting in the expected contrast.

Considering off-resonance effects, only the k_T-point-based method incorporated the measured ΔB_0 spatial variations in its design. This allowed greater inversion and excitation fidelity in the regions with significant frequency offsets. Although this is of little concern for the excitation pulses, which, even with a 500-µs duration, have sufficient bandwidth to uniformly cover the entire volume, the adiabatic inversion pulses can deteriorate significantly with large ΔB_0 variations. This can be observed, for example, near the orbito-frontal sinus cavity on the sagittal slice (Fig. 8.5**b**). This is corrected by the k_T-points-based pulses (Fig. 8.5**d**), except for the orbital gyrus where a hypersignal remains because of either localized inaccuracies in the ΔB_0-measurement or brain mask.

Histograms of the brain voxel intensities obtained with the different methods provide a first indication towards their applicability for automated tissue segmentation. Before bias correction, a small plateau was found in the histogram at 3 Tesla indicating the presence of separable GM and WM peaks (Fig 8.6**a**, gray). Moving to 7 Tesla, such a plateau was no longer present with either the conventional CP-mode (Fig 8.6**a**) or RF-shim (Fig 8.6**b**). Only with the application of the k_T-points method, a small dip appears suggesting the coexistence of two populations (Fig 8.6**c**, black). However, with the advanced tools available, the existence of such a local minimum before bias-field correction is by no means an absolute criterion to estimate the suitability of these images for automated tissue classification [1]. Analysis of the bias-field corrected data as returned by SPM (Ashburner and Friston, 2005) facilitated a more straightforward comparison of the obtained histograms. Application of the conventional approach at 7 Tesla revealed a significantly diminished contrast compared to what was obtained at 3 Tesla (Fig 8.6**d**). Adopting a suitable RF-shim improves the contrast substantially (Fig 8.6**e**). Again, the proposed k_T-point-based method approximated most faithfully what was observed at lower field strength (Fig 8.6**f**).

Automated Tissue Segmentation

To investigate the fidelity of the automated tissue classification, the spatial distributions of the labeled voxels have to be considered. Bearing in mind that minor imperfections in the obtained GM/WM delineation may still be anticipated, a comparison can be made to the 3 Tesla benchmark (Fig. 8.7**a**). Moving to 7 Tesla, images acquired with the conventional strategy can essentially no longer be used for automated tissue segmentation throughout the entire volume of the brain. Utilizing the SPM software package, the observed contrast deterioration in portions of the cerebellum, temporal and occipital lobes no longer allows proper GM/WM differentiation (Fig. 8.7**b**). Application of a suitable RF-shim configuration largely mitigates this problem. Nonetheless, minor artifacts remained scattered throughout cerebral hemispheres. One example of this is indicated with a white arrow in Fig. 8.7**c**. Using the proposed combination of k_T-point-based

[1] Note that; although bias-field correction is a powerful tool, if due to excitation defects the contrast is lost it may not be recovered by post-processing only. In addition, bias-field correction methods may also remove valuable information regarding local intra GM T_1 relaxation variations.

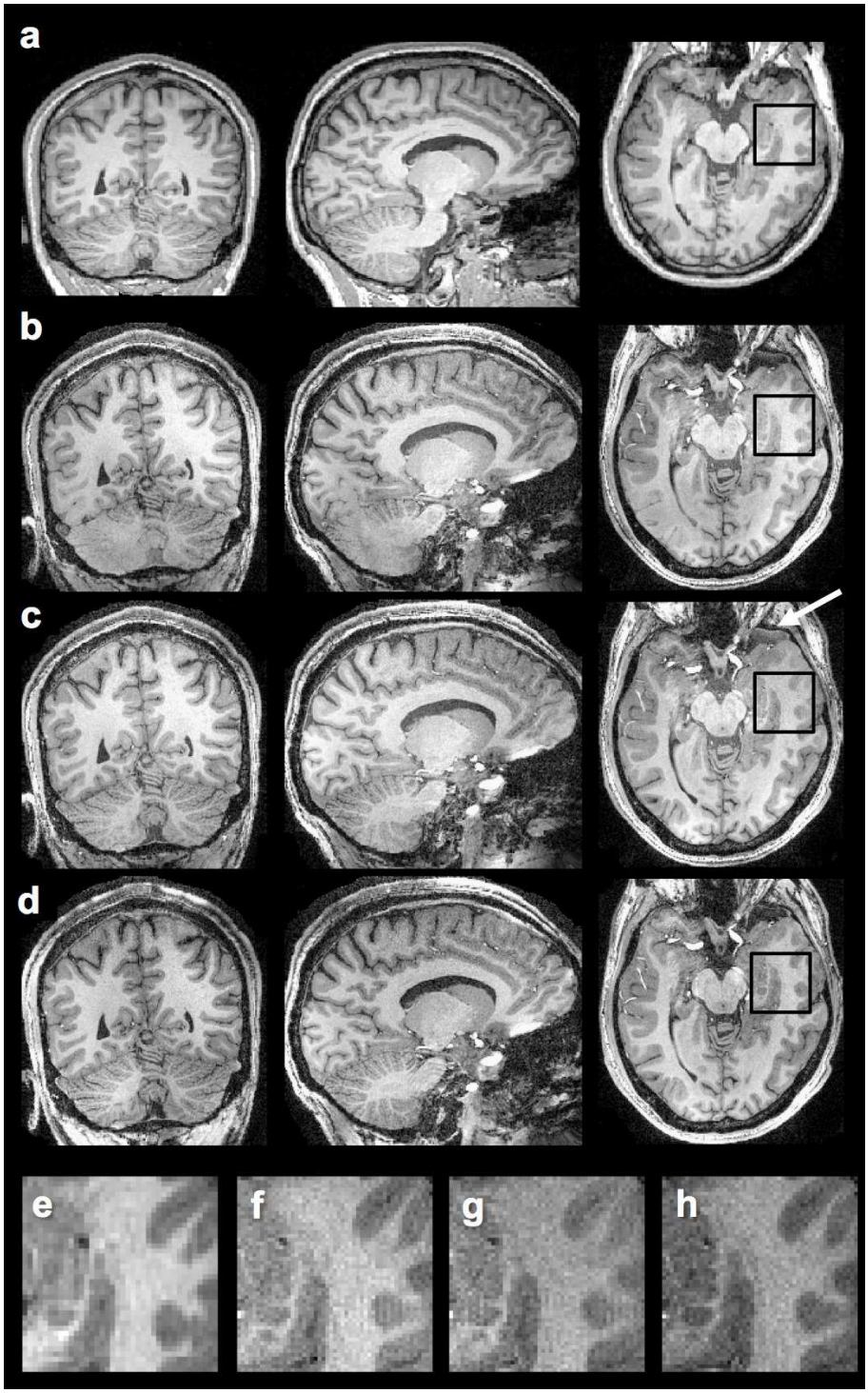

Figure 8.5: A qualitative comparison of the different pulses applied to the MP-RAGE sequence at 7T and the conventional 3T implementation (Subject #1). **a**: 1-mm-resolved images obtained with the conventional adiabatic inversion and non-selective excitation at 3 T (CP-mode). **b**: Same method as in a applied at 7 T with isotropic 0.8-mm resolution (NRMSIE 34.7%). **c**: Application of the conventional adiabatic inversion and non-selective excitation at 7 T using a subject-optimized RF-shim (NRMSIE 19.6%). **d**: Image acquired with the proposed k_T-points method (NRMSIE 6.7%). Zoomed sections corresponding to the region indicated in the axial view (**a**-**d**) illustrate the more subtle differences in contrast and signal. From left to right: 3T (**e**), conventional method at 7T (**f**), subject-specific RF-shim (**g**), the proposed method (**h**). White arrow: contrast artifact resulting in the relatively bright appearance of CSF in the arachnoids cyst.

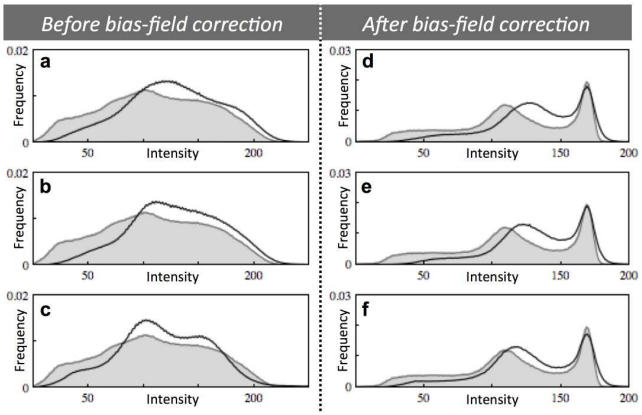

Figure 8.6: A quantitative comparison of the different pulse strategies applied to the MP-RAGE sequence at 7 Tesla with the conventional 3 Tesla implementation (Subject #2). Each subfigure shows a histogram of the voxel signal intensities measured throughout the volume of the brain. Results from the 3 methods used at 7 T are superimposed (black line) on the histogram corresponding to the conventional method at 3 Tesla (gray surface). The first column shows the histograms before bias correction, followed by the histograms corresponding to the bias-field-corrected and noise-filtered data (median filter r=1). From top to bottom: the conventional method (**a**, **d**), subject-optimized RF-shim (**b**, **e**), the proposed k_T-points method (**c**, **f**).

inversion and excitation pulses mitigated these last residual contrast artifacts. In addition, the improved excitation fidelity restored the signal in the peripheral regions of the brain where both CP-mode and RF-shim produce low FAs. This ameliorates the delineation of the cortical ribbon in the parietal lobe (Fig. 8.7**d**). Furthermore, the adiabatic inversions resulted in a deteriorated tissue classification near the sinuses due to magnetic susceptibility artifacts (gray arrows), whereas the pTx-based inversions (RF-Shim and k_T-points), which take the measured B_0 variations into account, provide a superior contrast in these regions.

Further investigation of the obtained cortical ribbon provided some insight in the potential impact of the discrepancies observed in the segmentation process. To this end, both global volumetric and morphological results were considered (FreeSurfer). A basic comparison of the cortical GM and subcortical WM volume fractions revealed a discrepancy between the different imaging techniques (Table 8.1). Systematically, the conventional method applied at 7 Tesla reveals a GM/WM ratio deviating from the one anticipated from 3 Tesla. Although the RF-shim demonstrates improved results, the proposed k_T-points method produces the best match with the 3 Tesla reference.

Concerning the measured gray matter distribution over the cortical ribbon, baseline results obtained using the conventional method at 3 Tesla coincide well with the nominal values expected from the literature. Focusing on the anterior and posterior banks of the central sulcus (Table 8.2), such measurements demonstrated values in close agreement with the 2.7/1.8 mm reported by Meyer and Roychowdhury (1996). Although this area does not lie in the regions most affected by reduced inversion fidelity (Fig. 8.4), variations in the cortical thickness were measured depending on the transmission technique (Table 8.2). Confirming earlier results, both the RF-shim and k_T-point implementations reflect more closely what was expected based on the measurements performed at 3 Tesla. A similar trend was observed comparing the gyral and sulcal regions, where, on average, the gyral regions are expected to be significantly thicker. However, due to the localized nature of the contrast artifacts, their impact is relatively small when averaging over large surfaces.

Commonly, morphologic studies are performed on an extended population to obtain a representative average that is less dependent on subject inter-variability. Coincidentally, this approach also averages out contrast-artifact-related discrepancies, provided that the overlap between subjects is minimal. Averaging results obtained from our 4 subjects, the localized impact of the observed contrast artifacts remains apparent (Fig. 8.8). Implementation of the conventional approach at 7 Tesla results in a large yet localized area with significant deviations from the anticipated results (Fig. 8.8**b** versus 8.8**a**). This confirms that the artifacts, observed with this setup, typically appear in the same location. Improvements obtained by adopting a suitable RF-shim configuration can be seen clearly, especially in the occipital lobe (Fig. 8.8**c**). Adopting the k_T-points methods, further improvements are obtained in the frontal lobe where the thicker middle frontal gyri can now be distinguished more clearly (Fig. 8.8**d**). However, the cortical thickness in some of the

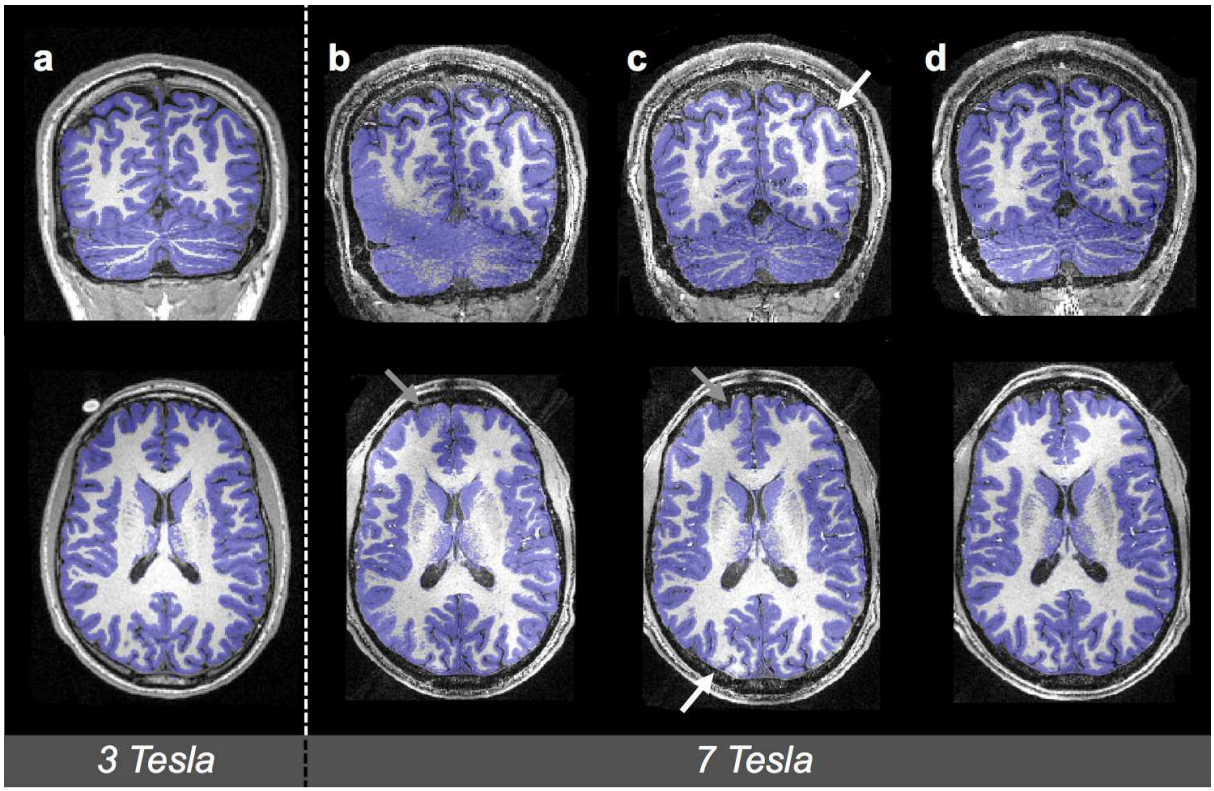

Figure 8.7: Results of automated tissue segmentation (SPM version 8) for each of the different imaging techniques (Subject #2). Voxels identified as GM are superimposed in blue, from left to right: conventional method at 3 Tesla (**a**), conventional method at 7 T (**b**), RF-shim (**c**), the proposed k_T-points method at 7 T (**d**).

Subject	**Method**		**NRMSIE** (%)		**cGM/sWM**
			Brain	Cerebrum	
#1	3T	CP-mode	NA*	NA*	1.07
	7T	CP-mode	34.7	22.6	1.03
	7T	RF-shim	19.6	15.8	1.08
	7T	k_T-points	6.7	5.5	1.07
#2	3T	CP-mode	NA*	NA*	1.07
	7T	CP-mode	46.5	29.8	0.95
	7T	RF-shim	22.9	16.8	1.05
	7T	k_T-points	5.0	5.0	1.07
#3	3T	CP-mode	NA*	NA*	1.00
	7T	CP-mode	39.1	17.4	0.97
	7T	RF-shim	24.1	17.7	1.01
	7T	k_T-points	8.1	5.4	1.00
4#	3T	CP-mode	NA*	NA*	0.99
	7T	CP-mode	35.6	15.0	0.92
	7T	RF-shim	21.2	12.8	1.01
	7T	k_T-points	9.9	6.0	1.01

Table 8.1: Results from automated segmentation analysis (FreeSurfer). For each of the different imaging techniques, the ratio of the cumulative cortical gray matter (cGM) and subcortical white matter (sWM) volumes of the two hemispheres is reported in the last column. NMRSI simulation results have also been reported here for the sake of completeness. *Based on the B_1^+-map measured in a different volunteer, the 10.2-ms adiabatic inversion applied at 3 Tesla, a NRMSIE of 1% (cerebrum only: 1%) may be expected.

Source	**Subject**	**Method**		**Central sulcus**		**Gyral regions**	**Sulcal regions**
				Anterior bank	Posterior bank		
This study	#1	3T	CP-mode	2.6 ± 0.60	1.4 ± 0.32	2.8 ± 0.63	2.4 ± 0.56
		7T	CP-mode	2.6 ± 0.66	1.7 ± 0.32	2.6 ± 0.75	2.3 ± 0.64
		7T	RF-shim	2.6 ± 0.51	1.7 ± 0.33	2.7 ± 0.70	2.3 ± 0.60
		7T	k_T-points	2.6 ± 0.71	1.6 ± 0.31	2.7 ± 0.72	2.3 ± 0.58
This study	#2	3T	CP-mode	2.7 ± 0.63	1.7 ± 0.42	2.9 ± 0.62	2.5 ± 0.53
		7T	CP-mode	2.5 ± 0.72	1.8 ± 0.48	2.6 ± 0.77	2.4 ± 0.66
		7T	RF-shim	2.6 ± 0.75	1.8 ± 0.38	2.7 ± 0.73	2.4 ± 0.61
		7T	k_T-points	2.8 ± 0.79	1.8 ± 0.42	2.8 ± 0.75	2.4 ± 0.63
This study	#3	3T	CP-mode	2.6 ± 0.58	1.5 ± 0.31	2.7 ± 0.63	2.3 ± 0.53
		7T	CP-mode	2.4 ± 0.59	1.7 ± 0.36	2.5 ± 0.67	2.2 ± 0.59
		7T	RF-shim	2.5 ± 0.58	1.6 ± 0.31	2.6 ± 0.68	2.3 ± 0.55
		7T	k_T-points	2.6 ± 0.64	1.6 ± 0.30	2.6 ± 0.67	2.2 ± 0.55
This study	#4	3T	CP-mode	2.6 ± 0.51	1.5 ± 0.61	2.8 ± 0.60	2.4 ± 0.53
		7T	CP-mode	2.6 ± 0.63	1.7 ± 0.56	2.7 ± 0.69	2.3 ± 0.57
		7T	RF-shim	2.5 ± 0.64	1.6 ± 0.58	2.7 ± 0.69	2.3 ± 0.57
		7T	k_T-points	2.6 ± 0.69	1.6 ± 0.51	2.7 ± 0.60	2.3 ± 0.57
(Fischl and Dale, 2000)	*Averaged over* 30 *subjects*	1.5T	CP-mode	2.6 ± 0.4	1.9 ± 0.2	2.7 ± 0.3	2.3 ± 0.3

Table 8.2: Cortical thickness (in mm) measured by automated analysis (FreeSurfer) for the banks of gray matter anterior and posterior to the central sulcus and averaged over both hemispheres. In addition, the average thicknesses measured in the gyral and sulcal regions are reported.

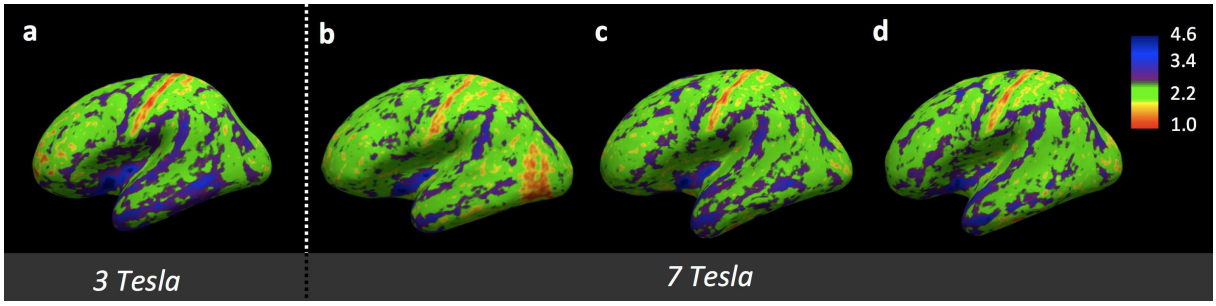

Figure 8.8: Cortical thickness (in mm) of the inflated brain from automated analysis (FreeSurfer). For each of the different imaging methods, the measured thickness of cortical ribbon is averaged over all 4 subjects. From left to right: the conventional method at 3 Tesla (**a**), the conventional method applied at 7 Tesla (**b**), subject-specific RF-Shim (**c**), the proposed k_T-point method (**d**).

lower parts of the temporal lobe was still underestimated, especially near the middle ear where strong ΔB_0 variations occur.

8.4 Discussion

Pulse design

Due to the low-energy demand of the k_T-point RF pulses, the absence of relaxation-related contrast deterioration (Boulant, 2009) confirms their applicability as excitations in short-TR echo trains such as used in the MP-RAGE sequence. Furthermore, their extension beyond the small-tip-angle domain provided inversion pulses with excellent spatial uniformity throughout the human brain at UHF, not only outperforming the conventional adiabatic hyperbolic secant pulses (Silver et al., 1985) in terms of NRMSIE, but also simultaneously reducing the cumulative energy deposition.

These results are especially compelling considering the ambitions of various institutions to explore field strengths well beyond 7 Tesla, where the T_1-contrast quality obtained with conventional imaging methods may be expected to deteriorate even further due to stronger B_1^+ inhomogeneities and the relative T_1 convergence between white and gray matter. Coincidently, the average energy deposition is expected to rise on account of the increased Larmor frequency. Thus although, in theory, increased power levels may be used to enhance the performance of adiabatic pulses, unacceptable levels of energy deposition may be required to minimize residual artifacts. With the adiabatic pulses used in this work, the relative energy deposition between the 7-ms adiabatic inversion and 0.5-ms excitation pulse train was approximately 2:1. Thus when nearing the SAR limit, such adiabatic pulses may limit the obtainable resolution by constraining the maximum number of partitions per TR or demanding the elongation of the acquisition time. Thus, if such compromise was deemed acceptable, simulations based on the measured B_1^+-maps suggest that substantial improvements of the inversion fidelity could be obtained using more energetic adiabatic inversions (Table 8.3). However, increasing the pulse duration reduces its bandwidth, therefore diminishing the performance in regions strongly affected by susceptibility effects.

The use of adiabatic sech pulses with application of a suitable subject-specific RF-shim demonstrated the ability to produce significant improvements in image quality while reducing the total energy deposition. Nonetheless, small residual artifacts may remain especially if the available power per channel is limited. On all accounts, significantly better inversion quality was achieved using the k_T-points method while decreasing both pulse duration and total energy deposition. Although the total energy deposition is only a first indication towards the actual SAR, techniques such as channel-dependent Tikhonov parameters (Cloos et al., 2010c) or virtual observation points (Eichfelder and Gebhardt, 2011) can be employed to further control the local SAR distribution produced by the k_T-point-based excitations if necessary.

Additional improvements in performance may be obtained with the continued advancements in pulse design techniques for parallel transmission. In this work, ΔB_0-maps with a 5mm-isotropic resolution were used to optimize the k_T-point-tailored inversion pulses. When later applied to high resolution imaging sequences,

Field	**Method**	**Duration** (ms)	**Energy** (J)	**NRMSIE** (%)	
				brain	cerebrum
3T	CP-mode	10.2	14.9	1	1
3T	CP-mode	8.2	12.0	3	3
7T	CP-mode	7.0	11.5	38 ± 6	22 ± 8
7T	CP-mode	8.5	14.0	31 ± 6	18 ± 6
7T	CP-mode	10.0	16.4	27 ± 5	17 ± 5
7T	RF-shim	7.0	8.1 ± 0.4	18 ± 6	14 ± 4
7T	RF-shim	8.5	9.8 ± 0.4	12 ± 4	10 ± 3
7T	RF-shim	10.0	11.6 ± 0.5	12 ± 4	11 ± 4
7T	k_T-points	5.9 ± 0.7	7.3 ± 0.6	6 ± 2	5 ± 1

Table 8.3: Simulated gain observed on the inversion sech pulse performance when lengthening its duration, based on B_1^+-maps measured at 7 Tesla in all 8 volunteers. For comparison, the result from the canonical 3-Tesla system was based on the B_1^+-map measured on a single volunteer.

such as MP-RAGE, some of the strongly localized susceptibility gradients may remain unaccounted for, due to coarse-voxel averaging. This may explain the observed residual artifacts near the sinus cavity (Fig. 8.5**d**) and middle ear. Instead of incorporating higher resolution maps in the pulse design, it may be beneficial to optimize the pulse design over a more extended bandwidth near the cranial cavities (Setsompop et al., 2009). This would make the pulses more robust to deviations from the measured B_0-map.

Although simulations based on the measured B_1^+-maps confirmed the robustness of the proposed pulse design method, it is known to be sensitive to the initial pulse candidate (Xu et al., 2008). In addition, selecting the optimal k-space locations can have a significant impact on the pulse duration and energy deposition (Grissom and Pauly, 2010). The initial k-space locations selected in this work were the same for each subject. Presumably, this is not the optimal solution and extensions to methods such as the sparsity-enforced (Zelinski et al., 2008d) and joined-design (Ma et al., 2010) approaches into the large-tip-angle domain would be favorable. Nonetheless, the fixed k-space trajectory adopted in this manuscript produced robust results without the need for long additional computations. It allowed, with our current setup, the tailored pulses to be designed in approximately 3 minutes. Additional improvements in both code and hardware could help to further reduce the computation time limiting the delay between consecutive sequences.

Beyond the scope of the MP-RAGE sequence, k_T-points may be applied advantageously as non-selective pulses in a variety of 3D-imaging sequences, which are becoming more and more prominent at high field. This will be the topic of future work.

Image Quality

High-quality MP-RAGE images of the human brain were acquired with pTx and the k_T-points method. Previous studies have shown that, at least up to 7 Tesla, the MP2RAGE approach can be utilized to obtain high-quality T_1-weighted images, provided the setup allows adequate performance of the adiabatic inversion over the entire ROI. However, even then, the MP2RAGE demands at least double the TR needed for the conventional MP-RAGE sequence between inversion pulses, thereby doubling the acquisition time for equivalent parallel imaging acceleration factors. Thus potentially higher-resolution images could be obtained within the same allotted time using the k_T-point-based pulse design in MP-RAGE.

With our current transmit-array coil, 0.8-mm isotropic is approximately the maximum achievable resolution for an $\sim$ 8-min acquisition. However, this coil uses stripline transceiver-elements that may be considered sub-optimal for reception, especially in the top part of the brain, as shown on the sagittal images. Improvements in SNR by about a factor 3 have been reported with the aid of dedicated multiple-loop receive arrays closely fitting the patient's head (Wiggins et al., 2006). Nonetheless, we were able to demonstrate higher-resolution MP-RAGE images than at 3 T, with a factor 2 smaller voxel volume and less receive elements, in approximately the same acquisition time, even though the longitudinal relaxation time is lengthened at 7 Tesla (Rooney et al., 2007).

Adopting the k_T-points method, the residual contrast losses observed with the RF-shim can be corrected resulting in robust tissue segmentation with results most comparable to what may be expected with a conventional 3 Tesla setup. This was also reflected by the histograms, where measurements with the proposed solution demonstrated a close match with the 3 Tesla data (Fig. 8.6). Due to the shortening of T_2 and lengthening of T_1 on top of the increased excitation non-uniformity observed at UHF strengths, lower field systems are generally expected to be more reliable for whole-brain T_1-weighted imaging. Even at 3 Tesla, transmit non-uniformities produced by the excitation pulses may produce minor contrast artifacts and undesired spatial variation in signal intensity (Fig. 8.4**e**). Using the proposed method at 7 Tesla resulted in an excitation fidelity surpassing what is commonly observed at 3 Tesla (Fig. 8.4**h**). Therefore, even clinical 3-Tesla systems could benefit from the proposed method if equipped with parallel transmission hardware (Malik et al., 2012).

Considering the measurements of the cortical thickness, on average sulcal regions seem to be least affected. Presumably this is related to their more central location where the adiabatic condition can be satisfied more easily. On the other hand, in the gyral areas, the proposed method appears more reliable. Apart from the improved magnetization preparation, this may be attributed to the increased excitation FA in the peripheral regions resulting in increased signal levels.

Even when averaged over several subjects, areas with severely under- and over-estimated cortical thickness were observed when applying the conventional transmission in our 7 Tesla setup. This suggests that these localized artifacts have a tendency to overlap between volunteers scanned in the same setup. Thus adopting a larger subject population may not be sufficient to average out the erroneous data (Fig. 8.8). On the other hand, the most dramatic deviations may be resolved by adopting a suitable RF-shim. Nonetheless, the best results were obtained using the proposed method. Especially in the frontal cortex where now the presence of a thicker middle frontal gyrus region can be distinguished, as was also observed in a more extensive study performed on healthy volunteers at 1.5 Tesla (Fischl and Dale, 2000). Although, good inversion fidelity may be expected at 3 Tesla (Table 8.3), spatial variation in the excitation profile may still introduce a bias in the measurements (Fig. 8.4). The superior excitation homogeneity produced at 7-Tesla by the k_T-points method could explain the observed difference in this region. On the other hand, all three methods implemented at 7-Tesla showed a reduced cortical thickness near the middle ear. Presumably, these regions could be improved by increasing the bandwidth of the k_T-point-based inversion pulses as discussed in the previous section.

So far, no particular care was taken to include the dura in the ROI when producing the brain mask for excitation homogenization. In general, segmentation of the dura from the GM remains challenging in some areas (Van der Kouwe et al., 2008). When adopting the k_T-point approach, the FA distribution is only optimized in a low-resolution brain mask. However tissue outside of the brain will still be excited with FAs that are arbitrary. This potentially leads to anomalous contrast effects just outside the brain. Thus care should be taken not to exclude any essential volume of interest in the mask used to define the optimized region of excitation.

8.5 Conclusions

We have demonstrated the soundness of the k_T-points method in the framework of parallel transmission applied to T_1-weighted 3D-imaging of the human brain at 7 Tesla. The derived inversion pulses provided excellent spatial uniformity throughout the human brain (NRMSIE $\sim$ 5%), outperforming the adiabatic pulses played in the conventional CP-mode (NRMSIE $\sim$ 38%) and in subject-specific RF-shim ($\sim$ 18%), while simultaneously reducing the cumulative energy deposition. Thus the proposed method showed that the merits of T_1-weighted human brain imaging could remain accessible at UHF without the need of SAR-intensive adiabatic inversion pulses. Although there has been some suspicion in the neuro-radiology community that high field systems are not competitive for T_1-weighted imaging, this study shows that a 7 Tesla system is able to produce high-quality highly-resolved T_1-weighted images with allotted time equivalent to those used at lower field strength, provided it is equipped with a true parallel-transmit capability. Still, because of shorter and relatively more distinct T_1's for white and gray matter at lower field strengths, similar or better contrast may be obtained at 1.5 or 3 Tesla especially if a parallel transmission setup can also be used. Nonetheless, for equivalent coil technology and voxel resolution, the SNR will be lower in these cases.

9 A Minimalistic approach to Transmit-SENSE

This chapter contains methods & principles that were published as abstracts in the proceedings of the Annual Meeting of the International Society for Magnetic Resonance in Medicine 2011.

M. A. Cloos, G. Ferrand, N. Boulant, M. Luong, C. J. Wiggins, D. Le Bihan, and A. Amadon. (2011) "Dual-channel transmit-SENSE for flip-angle homogenization in the human brain at 7 Tesla: a feasibility study." p. 325

Abstract

Purpose: To investigate the minimal number of independent RF-channels necessary to obtain FA homogenization in the framework of Transmit-SENSE.

Materials and Methods: Imposing fixed linear combinations on an 8-channel pTx-setup, four different RF-transmit configurations were investigated. These synthesized configurations, comprised out of 1, 2, 4, or 8 independent RF-pathways, by means of Bloch simulations. To this end, transmit-sensitivity profiles were measured at 7 Tesla in 10 human volunteers. In addition, full-wave electromagnetic-simulations were considered to evaluate the impact on the SAR.

Results: It is possible to design a dual-channel pTx-setup, suitable for clinical neuro-imaging applications at 7 Tesla. Such a setup could even be simplified to a serial mode configuration, witch a single amplifier. However, compared to the dual-channel approach, the here-evaluated 4-channel implementation reduces the level of FA non-uniformity and energy deposition by almost a factor 2. The best performance is obtained when all coil-elements are driven independently.

Conclusion: The level of FA uniformity obtainable, in the human brain at 7 Tesla, with only two independent channels can easily outperform conventional clinical system operating at 3 Tesla. Although it is feasible to reduce the number of transmit-channels to a bare minimum, overly constraining them may limit the applicability to SAR lenient protocols only.

9.1 Introduction

In the previous chapters, we exhibited the potential of the pTx-solution for FA-homogenization at UHF MRI. However, the 8-channel configuration used in these demonstrations entails a substantial increase in complexity compared to current clinical MR systems. More specifically, as described in Chapter **3**, the implementation of the transmit-SENSE approach with 8 parallel channels requires numerous duplicate MR components. In addition, the necessary safety systems are complicated, requiring specialized components to facilitate secure operation without imposing overly conservative constraints (Chapters 2 and 4). Apart from the added financial expenses, additional calibration measurements are mandatory to exploit the full potential of the pTx system. Typically this includes the mapping of the subject specific transmit-sensitivities associated with each of the transmit-channels, in addition to ΔB_0 variations (Chapter 2).

To properly balance the benefits and costs associated with the implementation of a pTx-enabled MRI system, some insight towards the minimal number of independent RF channels is desirable. Currently most UHF sites have adopted an 8-channel pTx-extension, while some actively explore the potential benefits provided by doubling the number of transmit-pathways. Although the general consensus seems to be that additional transmit-channels are advantageous when targeting short RF-pulse durations or exercising local SAR control, the necessity of this performance boost remains unclear. Furthermore, driving each of the coil elements separately may not be optimal. Considering an 8-transmit-element coil, it was shown that driving the coil with the 4 most efficient circularly polarized eigen-modes provides a level of performance comparable to what could be achieved when driving each of the 8 elements directly (Alagappan et al., 2007). Adopting this approach, sometimes referred to as mode-compression, a 2N-element transmit-array-coil can efficiently be driven with only N independent transmit-pathways (Alagappan et al., 2007, 2008).

When pursuing FA homogenization in the human brain at 7 Tesla with an 8-channel pTx-system, only a small number of k-space locations need to be visited to achieve excellent excitation uniformity (Setsompop et al., 2008a; Cloos et al., 2012). Although short excitation pulses are generally favorable, it could be considered to visit several additional k-space locations provided that this allows the complexity of the required pTx-setup to be reduced substantially. Moreover, clinically-viable MRI systems operating at 3 Tesla typically demonstrate less homogeneous excitation patterns than what can be achieved using an 8-channel pTx-setup at 7 Tesla (Chapter 8). With the understanding that the aforementioned clinical systems can be considered suitable for most medical applications focusing on the human brain we explore the viability of a minimalistic pTx-extension to facilitate similar levels of excitation fidelity at 7 Tesla.

9.2 Methods

Four different configurations were explored to provide some insight towards the minimum requirements to facilitate adequate FA non-uniformity mitigation for human brain imaging at 7 Tesla based on the Transmit-SENSE method:

`pTx:` 8-channel setup where every coil-element is driven independently.

`mTx:` 4-channel setup where an 8-element coil is driven using the four most efficient circularly polarized modes.

`dTx:` 2-channel setup where an 8-element coil is driven with two optimized linear combinations in parallel.

`sTx:` 1-channel setup where an 8-element coil is sequentially driven with two optimized linear combinations .

A more detailed description of the differences between the dTx and sTx configurations is detailed below.

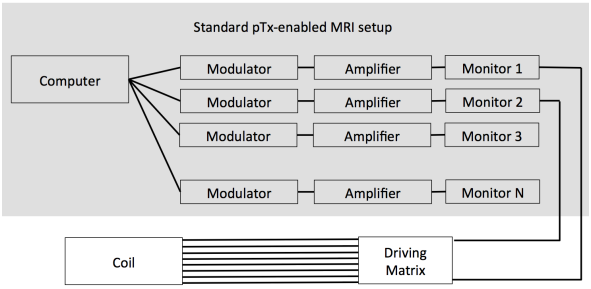

(a) Schematic overview of the dTx system. The gray surface indicates the RF-related components present in a typical N-channel pTx-enabled MRI setup.

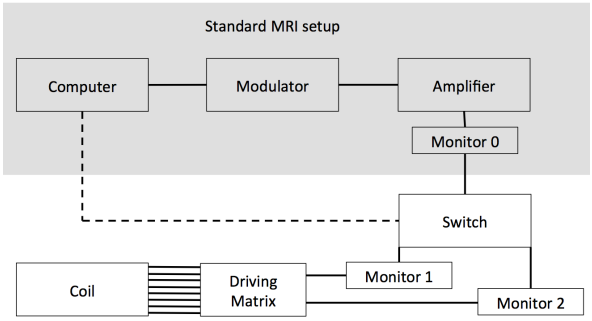

(b) Schematic overview of the sTx system. The gray surface indicates the RF-related components already present in a conventional MRI setup. The inclusion of monitors 1 and 2 may provide additional benefits as detailed in section x.

Figure 9.1

Dual-Channel (dTx)

The dual-channel approach, hereafter referred to as dTx, constitutes a minimalistic pTx setup. Whereas the pTx-enabled MRI implementations consist of multiple independent waveform modulators, amplifiers and power- or waveform-monitors, the dTx system is restricted to only two independent transmit-pathways combined with a specially designed driving matrix to distribute the power over all available transmit-coil-elements (Fig. 9.1a).

Serial-Transmission (sTx)

The serial-transmission approach, hereafter referred to as sTx, requires some comparatively low-cost adaptations to the standard MRI setup. Conventional MRI transmit implementations consist of single waveform modulator, amplifier and power monitor. To facilitate the sTx-method, a switch is included to re-direct the power to one of two transmit-pathways and distribute the energy over all available transmit-coil elements via a specialized driving matrix (Fig. 9.1b). Provided that this switch is fast enough that it can dispatch RF power between the two transmit pathways during a single RF pulse; typically the first half of the pulse could be played on the first pathway, and the second half on the second one.

Linear driving matrix

It is well established that, in order to prevent high local SAR values, it is beneficial to distribute the power over multiple coil-elements surrounding the subject (Lattanzi et al., 2009). However, to obtain a Transmit-SENSE solution, a set of independent transmit-sensitivities is required (Katscher et al., 2005). Instead of driving each of the coil-elements directly, all elements can be driven simultaneously using different linear combinations. One convenient way to drive all coil elements simultaneously on an approximately orthogonal basis of CP eigen-modes can be implemented via a Butler matrix (Butler and Lowe, 1961). Selecting only the N most efficient eigen-modes (dropping the anti-CP modes, Section 2.2), a 2N-element coil can be driven using N independent RF-channels (Alagappan et al., 2008; Setsompop et al., 2008a).

In general, any linear combination can be implemented in the form of a passive RF circuit (Ferrand et al., 2011). Assuming that the transmit-sensitivities do not deviate dramatically between subjects, a set of optimized combinations can be deduced for an average subject. Based on these principles, a set of linear combinations was optimized to produce complementary B_1^+ distributions for both the dTx and sTx approaches (Cloos et al., 2011b; Ferrand et al., 2012). To this end, the normalized standard deviation over all voxels of the sum $\sum_j^2 \left| B_{int}^j(\mathbf{r}) \right|$ produced by two linear combinations of N coil-elements ($B_{int}^j(\mathbf{r})$) was minimized, thus ensuring sufficient magnetic field at every point in the volume of interest.

Safety and local SAR control in the sTx configuration

Each transmit-pathway contributes to the SAR distribution that needs to be considered to guarantee patient safety and compliance with the guidelines (Section 1.3; IEC (2010)). However, in the sTx approach, these transmit pathways are never used simultaneously. This allows the expression of the SAR (Section 2.3; Eq. 2.3) for the sTx system to be simplified to:

$$SAR_{sTx}(\mathbf{r}) = \frac{\sigma(\mathbf{r})}{2\rho(\mathbf{r})}\frac{1}{T}\int_0^T \sum_n^N |a(t)|^2 \left\|\mathbf{E}_n(\mathbf{r})\right\|_2^2 dt \tag{9.1}$$

where N is the number of available transmit-pathways (inputs to the driving matrix), T is the duration, and $a_n(t)$ is the time-dependent modulation of the RF pulse amplitude. This implies that the sum of the power measured on the transmit paths is directly proportional to both the global and local SAR. Thus we can write for the global and local SAR:

$$SAR_{global} = \frac{1}{T}\sum_n^N \left[\overline{SAR_n}\int_0^T |a_n(t)|^2 dt\right] \tag{9.2}$$

$$SAR_{local} = \underbrace{max}_{\mathbf{r}}\left\{\frac{1}{T}\sum_n^N \left[\overline{\overline{SAR_n(\mathbf{r})}}\int_0^T |a_n(t)|^2 dt\right]\right\} \tag{9.3}$$

where $\overline{SAR_n}$and $\overline{\overline{SAR_n(\mathbf{r})}}$ represent the global and local 10-gram-averaged SAR corresponding to the nth transmit-mode, respectively. Consequently, independent average power monitors on each of the transmit channels (Fig. 9.1b) would allow both the global and local SAR to be restricted, without imposing overly conservative approximations or additional constraints.

Nonetheless, optimal performance still requires the time-averaged power limits to be reevaluated for each acquisition. To this end, an approach similar to CEASAR's could be adopted (Chapter 4; Cloos et al. (2010a)). However, due to the simple additive nature of these equations, the local SAR can simply be retrieved from a look-up table, greatly reducing the computational load. Furthermore, the simple relation between local SAR and pulse shapes implies that the weighting factors introduced by the channel-dependent Tikhonov regularization allow direct local and global SAR minimization (Chapter 5, Cloos et al. (2010c)).

To evaluate the global and local SAR produced by each of the considered transmission configurations, full wave (FEM) based electromagnetic field simulations were performed (Chapter 4; Chapter 5; Massire et al. (2012)). The head model used in this study consists of our in-house-developed FEM-compatible implementation of the 49-anatomical-structure model originally presented by Makris et al. (2008), converted to a surface based model containing 20 different tissues (Section 4.7, Massire et al. (2012)). However, it should be noted that the pulse design performance evaluated in this work was based on B_1^+-maps measured with the actual coil in-vivo. Due to variations in coil-loading and anatomical differences between the imaged volunteers and simulated head-model, the obtained SAR profiles can only be considered to provide an indication towards typical distributions produced.

Setup

In the absence of the required switch and driving-matrices, the proposed setups can be emulated by a pTx-setup. For this proof-of-concept, experimental verification was performed on a Siemens 7T Magnetom scanner (Siemens Medical Systems, Erlangen, Germany), equipped with 8 separate transmit-channels. Although the 8-channel system was limited to 1 kW per coil-element, the synthesized dTx and sTx systems were allowed up to 2 kW per driving mode. The same coil configuration and calibration methods were used as described in Chapter 6. FA-maps obtained in 10 human volunteers were used to validate the concept by synthesizing the proposed dTx and sTx systems. Informed consent was obtained from all subjects in accordance with guidelines of our institutional review board.

The first set of data (subject #1) was used to determine appropriate linear combinations to drive the 8 coil-elements from 2 independent transmit-pathways (Fig. 9.1). These combinations were then fixed to evaluate the potential of the proposed methods(Fig. 9.2).

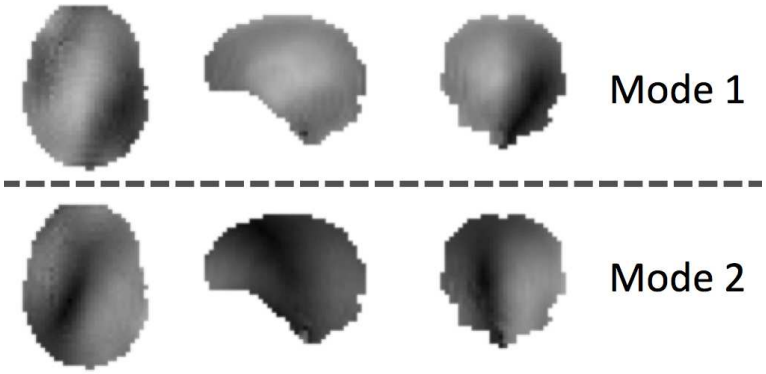

Figure 9.2: B_1^+-maps corresponding to the dual-channel system (based on the measured maps of the individual coil-elements for Subject #1). The two linear combinations are shown side by side in three orthogonal slices through the subject's brain.

Pulse design

Using the synthesized systems, spokes (Saekho et al., 2006) and k_T-points (Cloos et al., 2012) based excitation pulses were designed targeting a uniform excitation profile (FA = 5°) in the human brain. To this end, the spatial domain method (Grissom et al., 2006) was adopted in the framework of the magnitude least squares approach (Setsompop et al., 2008c) as described in Chapters 5 & 6. In order to incorporate the time-switching nature of the sTx approach, the pulse design must enforce only a single active transmit-pathway at any given time-step. Moreover, two sequential pulses have to be played at every k_T-point or spoke to obtain a similar level of performance. Inactive channels are excluded by setting the corresponding matrix elements $a_{i,j}$ in $\mathbf{A}$ (Eq. 5.2) to 0 (Section **5.2**). Obtained excitation pulses were analyzed by numerical evaluation of the full Bloch equations including the measured ΔB_0 evolution. Subsequently, the FA inhomogeneity was quantified by calculating the Normalized Root Mean Square Error (NRMSE) normalized to the mean FA obtained.

9.3 Results

Excitation uniformity

In order to facilitate the proposed dual-channel methods, one of the key requirements is the relative robustness of the transmit-sensitivity profiles corresponding to the two modes in which the transmit-array coil is driven. Due to inter-subject variability, the actual resulting relative phase and effective currents in each of the coil-elements may vary. Regarding the 10 subjects evaluated thus far, the general shape of the transmit-sensitivity profiles appears to be well preserved (Fig. 9.3). Nonetheless, substantial variations between subjects can be observed. Considering the relative phases measured in the approximate center of each brain, phase variations up to 10-20° were observed due to the differences in coil loading.

Based on transmit-sensitivity maps measured in a clinical 3-Tesla MRI system with a body RF coil (Magentom Tim Trio, Siemens Medical Systems, Erlangen, Germany), a reasonably uniform FA distribution may be expected (Fig. 9.4**a**). On the other hand, a strong central brightening effect appears when employing the conventional birdcage mode at 7 Tesla (Fig. 9.4**b** – 29% NMRSE[1]). Confirming earlier findings (Cloos et al., 2012), the k_T-points approach in the context of an 8-channel pTx-extension leads to an excellent FA uniformity throughout the brain (Fig. 9.4**c** – 5% NMRSE). The excitation fidelity thus obtained vastly exceeds the quality achieved with a conventional clinical 3-Tesla system. Merely driving the four most efficient circularly polarized eigen-modes, only minimal deterioration in excitation fidelity was observed (Fig. 9.4**d**). Adopting the proposed dTx-approach, the FA-uniformity is slightly more deteriorated (Fig. 9.4**e** – 9% NMRSE). Nonetheless, the obtained excitation fidelity still outperforms the benchmark set by the conventional clinical MR setup at 3 Tesla (12% NMRSE). Constraining the available degrees of freedom even further by adopting the sTx-approach, a similar excitation quality is reached (Fig. 9.4**f** – 9% NMRSE).

[1] this pseudo-CP mode was found by aligning the phases of all channels in the center of the brain

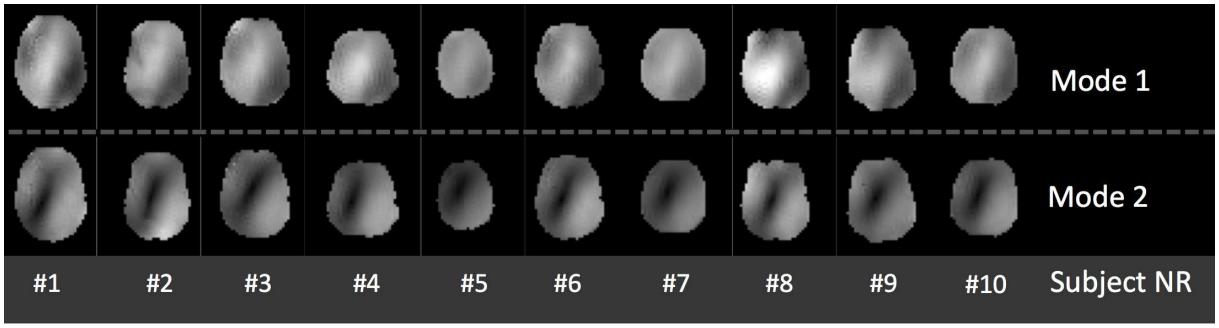

Figure 9.3: Transmit-sensitivity profiles obtained for different subjects. The modes originally designed for the first subject were directly applied to each of the subsequent volunteers (axial slice in at gradient iso-center).

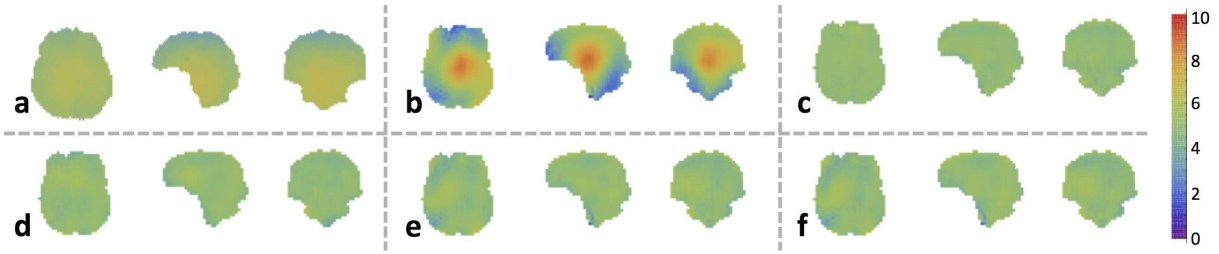

Figure 9.4: Synthesized FA distributions in the human brain (based on B_1^+-mapping measurements from individual pTx channels in Subject #8). **a**: Clinical 3-Tesla MRI setup with a body RF coil (12% NRMSE). **b**: Pseudo CP-mode at 7 Tesla (29% NRMSE). **c**: Eight-channel transmit system, patient-specific 7-kT-points tailored RF excitation (5% NRMSE). **d**: Four-channel transmit system, patient-specific 7-kT-points tailored RF excitation (6% NRMSE). **e**: Dual-channel transmit system, patient-specific 7-kT-point-tailored RF excitation (9% NRMSE). **f**: Serial-transmit system, patient-specific 7-kT-points tailored RF excitation (9% NRMSE).

	RF System	Pulse Design	Mean NRMSE (%±SD)	Min NRMSE (%)	Max NRMSE (%)	Mean Duration (ms±SD)	Total Energy (mJ±SD)
	Conventional system	Square	32.5±3.3	28.3	40.1	0.1±0.0	80±9
	Eight channel RF shim	Square	18.7±1.0	17.7	20.6	0.1±0.0	110±16
3D	pTx system	7–k_T-points	5.1±0.2	5.0	5.7	0.49±0.01	148±13
3D	mTx system	7–k_T-points	6.7±0.8	5.6	8.3	0.49±0.01	134±35
3D	dTx system	7–k_T-points	9.2±1.0	7.8	10.8	0.50±0.01	241±35
3D	sTx system	7–k_T-points	9.3±1.0	7.8	10.7	0.62±0.02	337±79
2D	pTx system	4-Spokes	5.4±0.4	5.0	6.3	3.0±0.0	12.9±2.7
2D	mTx system	4-Spokes	5.7±0.5	5.0	6.4	3.0±0.0	11.6±1.4
2D	dTx system	4-Spokes	7.9±1.3	6.1	10.7	3.0±0.0	29.6±4.4
2D	sTx system	4-Spokes	8.4±1.3	6.8	11.2	6.0±0.0	32.6±3.4

Table 9.1: Measured FA homogeneity and energy-balance obtained with different excitation pulse strategies. The CP-mode and RF-shim pulse amplitudes were scaled to produce an average of 5°. The spatial variation of the FA in different regions (Fore- & midbrain, Cerebellum, Total brain) of the brain is expressed as the standard deviation as percentage of the mean. Total Energy: the total incident energy per RF excitation on all channels. MTE channel: the maximum total incident energy per pulse per channel.

A more extensive evaluation based on measurements performed in 10 different subjects is summarized in Table 9.1. Although in the context of the k_T-points method the sTx-approach allows for a similar level of performance as obtained with the dual-channel setup, the pulse durations are lengthened by almost 25%. Considering a spoke-like pulse design, where the sub-pulse waveforms have a fixed duration, the reduced degrees of freedom available in the sTx-approach impaired the obtainable excitation fidelity due to the inherently enhanced sensitivity to magnetic susceptibility effects. Nonetheless, adequate excitation uniformity could be obtained in all axial slices through the brain using only two sequential channels, albeit a significant increase in both energy deposition and pulse duration (Table 9.1).

Safety considerations

Considering in-vivo applications, both the local and global SAR must be constrained to remain within safe limits (IEC, 2010). Although the time-averaged incident power at the coil level is not directly proportional to the local SAR, it may be considered a first indication towards the global SAR. Compared to the conventional quadrature excitation, all other transmission methods evaluated here demonstrated a reduced level of energy efficiency. However, considering the tailored waveforms assessed in this work, the added value of additional transmit pathways clearly represents itself as a reduction in energy deposition (Table 9.1).

Due to the possibility of high local SAR values, the spatial distribution of the energy deposition needs to be considered. Whereas the conventional CP-mode demonstrates a maximum local to global SAR ratio of approximately a factor 3, the two dual modes demonstrate a ratio about 50% larger (Table 9.2). Therefore, considering the guidelines (Section 1.3; IEC (2010)), the maximum allowed incident power for each of the transmit-pathways would be significantly smaller than in CP-mode due to the occurrence of localized RF hot-spots (Fig. 9.5).

However, the spatial distributions of the SAR produced by Mode 1 & Mode 2 are very different (Fig. 9.5). Therefore, depending on the tailored RF-waveform, the time-averaged local SAR can be reduced substantially. Considering the modes used here, the time averaged optimal combination, corresponds to a maximum local SAR to global SAR ratio of 4.0. Although the simple relation between RF-waveform and local SAR allows this best-case scenario to be found easily, a typical 7-k_T-point-based excitation producing

	CP-mode	Mode1	Mode2	sTx	dTx	mTx	pTx
Maximum local 10-g SAR / global SAR.	3.2	5.4	4.6	4.8	4.4	4.2	3.8
NRMSE for tailored pulses based				9.8%	9.8%	7.0%	5.4%

Table 9.2: Simulated global and peak 10-gram local SAR in the human head (W/kg). The sTx, dTx, mTx and pTx results correspond to 7-k_T-point-based excitations targeting a 5° FA throughout the volume of the brain.

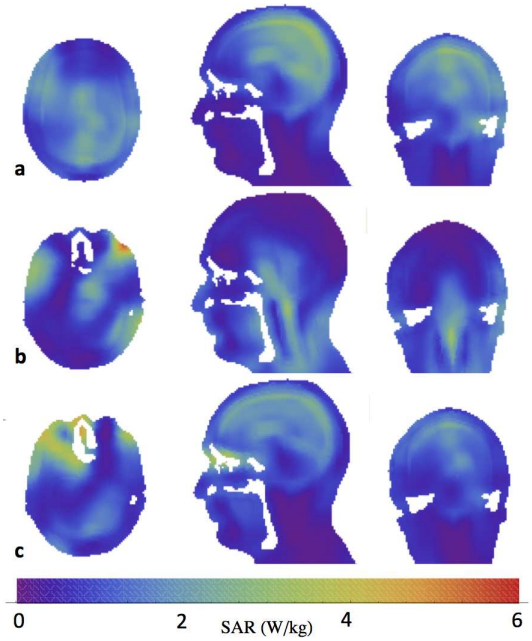

Figure 9.5: Simulated 10-gram local SAR distributions in the human head (all on the same scale). Axial and corneal slices intersect with the hot spot corresponding to the maximum local SAR, while the position of the sagittal slice was fixed through the center of the brain. Top to bottom: (**a**) circularly polarized mode, (**b**) the first transmit-pathway in the dTx and sTx approaches, (**c**) the second transmit-pathway in the dTx and sTx approaches.

adequate FA uniformity (9.8 %) resulted in a local to global SAR ratio of 4.8 (Table 9.2). On the other hand, the dTx-approach allows the interference patterns between the two modes to be exploited. Therefore the RF-energy can be distributed more favorably over the exposed volume while maintaining adequate excitation fidelity (local to global SAR ratio = 4.4) . Extending the available degrees of freedom to four independent transmit-channels, again a slightly lower global to local SAR ratio was found. However, considering that the total energy required is reduced by almost a factor 2 (Table 9.1), the overall system can be considered much less SAR-constrained than the dual channel approaches. Moreover, when driving all available coil-elements individually, the best excitation fidelity was achieved while most favorably distributing the RF energy over the exposed volume (local to global SAR ratio = 3.8).

9.4 Discussion

Considering neuro-imaging applications where the excitation fidelity obtained with a clinical 3 Tesla MR system may be considered sufficient, the proposed dTx and sTx approaches allow adequate excitation uniformity for clinical brain imaging at 7 Tesla. Therefore, the increased signal and contrast enhancements provided by the stronger main magnetic field can be accessed without deterioration of the excitation fidelity. This level of performance was achieved using only two distinct transmit-sensitivity profiles, by minimizing the standard deviation of the sum of magnitudes of the two driving modes. Alternatively, considering the good results obtained by driving an 8-channel coil with mode-compression, a logical choice for a dual channel system would be to adopt only the two most efficient circularly polarized modes. However, based on

the measured B_1^+-maps for our current setup, it appears more difficult to obtain an adequate level of FA uniformity in this way. This may in part be related to the design of our coil (Chapter 3). Other methods to optimize the linear combinations used to drive the coil could be conceived, potentially providing further improvements in excitation fidelity or more favorably distributing the energy over the exposed volume. In particular, considering the relatively high local SAR produced by the modes selected in this work, integration of the electric field distributions in the optimization procedure may prove beneficial. However, considering the interferences produced by the superposition of modes in the dTx configuration, merely optimizing the modes as RF-shimming solutions independently of the pulse design may not be optimal (Zelinski et al., 2008a).

Although the performance of the dual channel systems could be considered adequate, appreciably better FA uniformity could be obtained using either a 4 or 8-channel system. The increased degrees of freedom associated with the additional transmit pathways allow the pulse duration to be shortened and energy deposition to be reduced. Moreover, adopting an 8-channel setup allows the energy to be distributed more evenly over the exposed body, thereby reducing the local SAR compared to the 4-channel configuration. Therefore more RF-energy could be used while remaining in compliance with the safety guidelines when transmitting on 8 independent transmit-channels.

In this work, only small-tip-angle excitations were considered. Whereas the benefits of the 8-channel pTx-system have been established in the large tip angle domain (Chapter 7), adequate performance of the dTx/sTx -approach has yet to be demonstrated for large angles. Initial results based on the optimal control approach (Xu et al., 2008) indicate that it is feasible to design such pulses at least up to 90°. However the tradeoff between SAR minimization and excitation fidelity requires further investigation, especially when considering the high requirements associated with inversion and refocusing pulses.

In conclusion, we have demonstrated the feasibility of a minimalistic 2-channel setup to obtain adequate excitations fidelity for clinical neuro-imaging applications at 7 Tesla in the framework of pTx. We even showed such a setup could be simplified to a serial mode configuration, where no pTx is needed, greatly reducing the cost of the required hardware while still benefiting from the Transmit-SENSE pulse design approach. However, although it is feasible to reduce the number of transmit-channels to a bare minimum, overly constraining the number of available transmit-channels may limit the applicability to SAR lenient protocols only. Nonetheless, the excitation fidelity obtainable with two channels can easily be reduced to an approximately 10% NRMSE. Although this is comparable to what can typically be expected with a clinical system at 3 Tesla, a more extensive 4-channel pTx-implementation improves the excitation fidelity to an approximately 6% NRMSE, while reducing the total energy deposition by a factor of 2.

10 Summary & Recommendations

In pursuit of increasingly better-resolved MR images, ever higher main magnetic field strengths are explored. While progressively ramping up the static field enhances the NMR signal (Ocali and Atalar, 1998), it simultaneously increases the proton Larmor frequency. Considering clinical systems operating at 3 Tesla, the corresponding RF wavelength already becomes comparable to the dimensions of the human body. As a result, when investigating large organs such as the abdomen or thighs, zones of shade and losses of contrast bias the image (Bernstein et al., 2006). Migrating to 7-Tesla, the resulting RF non-uniformities are so strong that contrast artifacts develop even in smaller regions such as the human brain. In anticipation of the first 11.7 Tesla systems now in active development at NeuroSpin and NIH, it becomes increasingly urgent to provide adequate solutions to mitigate these excitation non-uniformities. Otherwise, such ultra-high field systems cannot reach their full potential.

To develop the techniques necessary to tackle the above-mentioned challenges, an 8-channel parallel transmission (pTx) setup was installed in our 7-Tesla MRI system. Whereas most clinical MRI systems only use one transmit-channel at a time, the pTx extension allows different RF waveforms to be played through multiple channels in concert. Although this method provides great flexibility in RF-pulse design, it also allows a plethora of RF-energy distributions to establish in the exposed body (Angelone et al., 2006). Considering that both the localized and global energy deposition has to be limited in order to ensure patient safety (IEC, 2010), RF waveforms that establish the desired excitation pattern without introducing so called RF "hot-spots" are desirable.

The additional degrees of freedom provided by the pTx extension can be used to steer the RF solution towards more favorable energy distributions. This was demonstrated in this work by iteratively optimizing a set of coil-dependent Tikhonov parameters to suppress RF hot-spots (Cloos et al., 2010c). Although this intuitive approach was shown to be robust and computationally manageable, it generally imposes a small degradation in excitation fidelity. Recently more elaborate methods have been published allowing the RF solution to be optimized while retaining a fixed level of performance (Brunner and Pruessmann, 2010; Lee et al., 2010). However, these methods are still limited to the small-tip-angle domain (Pauly and Nishimura, 1989). Considering the robustness and flexibility provided by the optimal control approach (Xu et al., 2008), thorough integration of local and global specific absorption rate (SAR) constraints might be feasible even when targeting arbitrary flip-angles (FA).

During this thesis, the management of local SAR in RF pulse design has mainly been a theoretical exercise to illustrate the flexibility of the pTx approach. So far, the application of such methods has been hampered by the RF safety systems installed, whereby the phase of the power transmitted by each channel is not monitored. Although a practical approach for online SAR assessment was implemented, this conservative method does not allow the desirable effects of destructive E-field interferences to be exploited. Therefore, optimizing the true local SAR provides only limited advantages. However, more sophisticated SAR-management systems will eventually make it possible to reap the benefits of local-SAR-constrained RF-pulse designs (Graesslin, 2008; Gagoski et al., 2009). Nonetheless, our conservative approach did allow new pulse design strategies to be validated in-vivo.

The k_T-points RF pulse design, introduced in this work to homogenize the FA for volumetric applications, was extensively tested in the context of pTx enabled human brain imaging at 7 Tesla (Cloos et al., 2012). The principle idea is to constrain the sampled subset of excitation k-space locations to a sparse cluster surrounding the DC component. In this way, considering that the RF non-uniformities are dominated by low spatial frequencies, limiting the excursions in k-space makes sure that no energy is "wasted" at high frequency components that are of limited interest in the context of flip-angle homogenization. Moreover the time required to cover the few k_T-points is minimized, allowing short pulse durations to be obtained.

Ultimately, the real test for the k_T-points method was to demonstrate the ability to retain excellent tissue contrast when employed in fast 3D sequences such as the MP-RAGE (Mugler and Brookeman, 1990). By generalizing the design to include inversion pulses with an optimal control approach, the SAR-intensive adiabatic pulses could be replaced by the more efficient k_T-points, restoring the expected contrast between

white and gray matter everywhere in the brain. These pTx-enabled inversions simultaneously improve image quality, decrease the energy deposition, and reduce the pulse duration. Nonetheless, the increased magnetic susceptibility effects at 7 Tesla can still pose a challenge for the k_T-point based inversion pulses. Although we have shown that these effects can be mitigated provided that these regions are correctly incorporated into the pulse design, the quality of the final result now also depends strongly on the accuracy with which the region of interest (ROI) is demarcated. Regarding applications in neuroimaging, dedicated software packages are available to extract the brain volume from high quality images. However, when defining the ROI to be used during pulse design, such images are typically not available. Therefore, such programs will have to make do with a low-resolution poor-contrast image, for which they are not optimized. Despite of these non-optimal conditions, we showed that it is possible to automate the ROI demarcation process. Nonetheless, further improvements in robustness are desirable.

In the work presented here, only gradient-recalled sequences were considered. To extend the scope of the k_T-points, the design should be generalized to encompass refocusing pulses. Currently, the first steps have been set to incorporate the k_T-point design into non-selective spin-echo-based methods such as the SPACE sequence (Mugler et al., 2000).

Returning our focus to RF-pulse design, our optimal control approach so far starts with a small-tip-angle-based solution as an initial guess. However this imposes severe limitations on the optimized solution: the found local minimum of the cost function is not guaranteed to be near the global optimum. Moreover, including the k-space trajectory as a set of parameters in the optimization makes the search even more challenging. Intuitively, it seems that by improving the large FA design method, the energy deposition could be reduced even further.

Finally, the pTx implementation itself was reconsidered. Although we were able to demonstrate excellent results with an 8-channel pTx-extension, the costs and technical experience needed to operate the system are a concern for routine operations. Therefore, several simplified implementations were investigated to evaluate the potential of a more cost-effective setup with a reduced number of transmit pathways. These initial results showed that, at least in the small-tip-angle regime, 2 parallel (or even sequential) transmit channels are sufficient to homogenize the FA throughout the human brain at 7 Tesla. So far these initial experiments are limited to Bloch simulations based on B_1^+-maps measured in-vivo with a full-scale pTx system. One of the next steps is to implement the hardware to physically drive an N-element transmit array coil using only 2 parallel transmit pathways. In addition, to enhance the applicability of this approach in a more clinically oriented setting, this concept should be evaluated in other parts of the body and targeting all possible FA. In particular, focusing on the most desired clinical applications, it should be investigated whether the SAR limitations imposed by a 2-channel system are sufficiently lenient or if a larger set of channels is required.

Bibliography

Abraham, T., May 2011. Evolution of brain imaging instrumentation. Semin. Nucl. Med. 41 (3), 202–219.

Adriany, G., van de Moortele, P.-F., Wiesinger, F., Moeller, S., Strupp, J. P., Andersen, P., Snyder, C., Zhang, X., Chen, W., Pruessmann, K. P., Boesiger, P., Vaughan, T., Ugurbil, K., Feb. 2005. Transmit and receive transmission line arrays for 7 Tesla parallel imaging. Magn. Res. Med. 53 (2), 434–445.

Akoka, S., Franconi, F., Seguin, F., Le Pape, A., 1993. Radiofrequency map of an NMR coil by imaging. Magn. Res. Med. 11 (3), 437–441.

Alagappan, V., Nistler, J., Adalsteinsson, E., Setsompop, K., Fontius, U., Zelinski, A., Vester, M., Wiggins, G. C., Hebrank, F., Renz, W., Schmitt, F., Wald, L. L., 2007. Degenerate mode band-pass birdcage coil for accelerated parallel excitation. Magn. Res. Med. 57 (6), 1148–1158.

Alagappan, V., Setsompop, K., Polimeni, J., Potthast, A., Zelinski, A., Wiggins, G., Fontius, U., Schmitt, F., Adalsteinsson, E., Wald, L., 2008. Mode compression of transmit and receive arrays for parallel imaging at 7T. In: Proc. Intl. Soc. Mag. Reson. Med. Toronto, p. 619.

Alon, L., Deniz, C. M., Sodickson, D. K., Zhu, Y., Nov. 2011. Do constrains on |B1+| also constrain |E| and SAR in high field MR? In: Proc. Intl. Soc. Mag. Reson. Med. Montreal, p. 491.

Alperin, N., Vikingstad, E., Gomez Anson, B., Levin, D., 1996. Hemodynamically independent analysis of cerebrospinal fluid and brain motion observed with dynamic phase contrast MRI. Magn. Res. Med. 35 (5), 741–754.

Amadon, A., Boulant, N., 2008. Simultaneous measurement of B0- and B1-maps with modified Actual Flip Angle Imaging sequence. In: Proc. Intl. Soc. Mag. Reson. Med. Toronto, p. 1248.

Amadon, A., Boulant, N., Cloos, M. A., Giacomini, E., Wiggins, C. J., Luong, M., Ferrand, G., Fautz, H.-P., 2010. B1 mapping of an 8-channel TX-array over a human-head-like volume in less than 2 minutes: the XEP sequence. In: ISMRM. p. 2828.

Amadon, A., Cloos, M. A., 2010. Method And Apparatus For Compensating For B1 Inhomogeneity In Magnetic Resonance Imaging By Nonselective Three-Dimensional Tailored RF Pulses. Patent: EU (10290205).

Amadon, A., Cloos, M. A., Boulant, N., Hang, M.-F., Wiggins, C. J., Fauzt, H.-P., 2012. Validation of a very fast B1-mapping sequence for parallel transmission on a human brain at 7T. In: Proc. Intl. Soc. Mag. Reson. Med. Melbourne, p. in press.

Angelone, L., Makris, N., Vasios, Christos ans Wald, L., Giorgio, B., 2006. Effect of Transmit Array Phase Relationship on Local Specific Absorption Rate (SAR). In: Proc. Intl. Soc. Mag. Reson. Med. Seattle, p. 2038.

Ardekani, B. A., Guckemus, S., Bachman, A., Hoptman, M. J., Wojtaszek, M., Nierenberg, J., 2005. Quantitative comparison of algorithms for inter-subject registration of 3D volumetric brain MRI scans. J. Neurosci. Methods. 142 (1), 67–76.

Ashburner, J., Friston, K. J., 2005. Unified segmentation. NeuroImage 26 (3), 839–851.

Barna, J., Arezzo, J., Vaughan Jr, H., 1981. A new multielectrode array for the simultaneous recording of field potentials and unit activity. Electroencephalogr. Clin. Neurophysiol. 52 (5), 494–496.

Baum, J., Tycko, R., Pines, A., 1985. Broadband and adiabatic inversion of a two-level system by phase-modulated pulses. Phys. Rev. A 32 (6), 3435–3447.

Bazaraa, M. S., Sherali, H. D., Shetty, C. M., 1993. Nonlinear Programming: Theory and Algorithms, 2nd Edition, 2nd Edition. Wiley.

Bernstein, M., Huston III, J., Ward, H., 2006. Imaging artifacts at 3.0 T. J. Magn. Reson. Imaging. 24 (4), 735–746.

Bernstein, M., King, K., Zhou, X., 2004. Handbook of MRI Pulse Sequences. 2004. Elsevier Academic Press, Burlington, MA.

Bloch, F., 1946. Nuclear Induction. Phys. Rev. 70 (7 and 8), 460–474.

Bottomley, P. A., Andrew, E. R., 1978. RF magnetic field penetration, phase shift and power dissipation in biological tissue: implications for NMR imaging. Phys. Med. Biol. 23 (4), 630–643.

Boulant, N., 2009. T1 and T2 effects during radio-frequency pulses in spoiled gradient echo sequences. J. Magn. Reson. 197 (2), 213–218.

Boulant, N., Cloos, M., Amadon, A., 2010a. A simple and analytical way to correct for B0 inhomogeneity in the evaluation of B1 maps relying on flip angle measurements and nons-elective square pulses. In: Proc. Intl. Soc. Mag. Reson. Med. Stockholm, p. 4918.

Boulant, N., Cloos, M., Amadon, A., Ferrand, G., Luong, M., Wiggins, C., Le Bihan, D., Hoult, D. I., 2010b. Flip angle and SAR maps induced by a head displacement in parallel transmission and with Cartesian feedback. In: Proc. Intl. Soc. Mag. Reson. Med. Stiockholm, p. 1453.

Boulant, N., Cloos, M., Luong, M., Ferrand, G., Wiggins, C., Amadon, A., 2011. Method for monitoring safety in parallel transmission systems based on channel-dependent average powers. In: Proc. Intl. Soc. Mag. Reson. Med. Montreal, p. 3850.

Boulant, N., Hoult, D. I., 2012. High tip angle approximation based on a modified Bloch-Riccati equation. Magn. Res. Med., in press.

Boulant, N., Le Bihan, D., Amadon, A., 2008. Strongly modulating pulses for counteracting RF inhomogeneity at high fields. Magn. Res. Med. 60 (3), 701–708.

Boulant, N., Mangin, J.-F., Amadon, A., 2009. Counteracting radio frequency inhomogeneity in the human brain at 7 Tesla using strongly modulating pulses. Magn. Res. Med. 61 (5), 1165–1172.

Breyer, T., Wanke, I., Maderwald, S., Woermann, F., Kraff, O., Theysohn, J., Ebner, A., Forsting, M., Ladd, M., Schlamann, M., 2010. Imaging of patients with hippocampal sclerosis at 7 Tesla: initial results. Acad. Radiol. 17 (4), 421–426.

Brunner, D., Pruessmann, K., 2008. A matrix approach for mapping array transmit fields in under a minute. In: Proc. Inl. Soc. Mag. Reson. Med. Toronto, p. 354.

Brunner, D. O., de Zanche, N., Fröhlich, J., Paska, J., Pruessmann, K. P., 2009. Travelling-wave nuclear magnetic resonance. Nature 457 (7232), 994–998.

Brunner, D. O., Paska, J., Froehlich, J., Pruessmann, K., 2008. SAR assesment of transmit arrays: Deterministic calculation of worst- and best-case performance. In: Proc. Inl. Soc. Mag. Reson. Med. p. 4803.

Brunner, D. O., Pruessmann, K. P., 2010. Optimal design of multiple-channel RF pulses under strict power and SAR constraints. Magn. Res. Med. 63 (5), 1280–1291.

Bryson, J. A. E., Ho, Y.-C., 1975. Applied Optimal Control: Optimization, Estimation and Control. Taylor & Francis.

Buchenau, S., Haas, M., Hennig, J., Zaitsev, M., 2010. On the SAR averaging nature of parallel excitation pulses and its impact on conservative worst-case analysis. In: Proc. Inl. Soc. Mag. Reson. Med. Stockholm, p. 3884.

Buonomano, D., Merzenich, M., 1998. Cortical plasticity: from synapses to maps. Annu. Rev. Neurosci. 21 (1), 149–186.

Busse, R. F., Hariharan, H., Vu, A., Brittain, J. H., 2006. Fast spin echo sequences with very long echo trains: design of variable refocusing flip angle schedules and generation of clinical T2 contrast. Magn. Res. Med. 55 (5), 1030–1037.

Butler, J., Lowe, R., 1961. Beam-forming matrix simplifies design of electronically scanned antennas. Electron. Des. 9 (8), 170–173.

Cao, Y., Vikingstad, E., Huttenlocher, P., Towle, V., Levin, D., 1994. Functional magnetic resonance studies of the reorganization of the human hand sensorimotor area after unilateral brain injury in the perinatal period. Proc. Nat. Acad. Sci. 91 (20), 9612.

Carr, H., 1952. Free Precession Techniques in Nuclear Magnetic Resonance. Ph.D. thesis, Reprinted in Encyclopedia of Nuclear Magnetic Resonance, Vol.I, J.Wiley & Sons 1996, Boston.

Carr, H., Purcell, E., 1954. Effects of Diffusion on Free Precession in Nuclear Magnetic Resonance Experiments*t. Phys. Rev. 3, 630–638.

Cheung, K. C., 2007. Implantable microscale neural interfaces. Biomed. Microdevices. 9 (6), 923–938.

Chung, S., Kim, D., Breton, E., 2010. Rapid B1+ mapping using a preconditioning RF pulse with TurboFLASH readout. Magn. Res. Med. 64 (2), 439–446.

Cloos, M. A., Bonmassar, G., 2009. Towards Direct B1 Based Local SAR Estimation. In: Proc. Intl. Soc. Mag. Reson. Med. Honolulu, p. 2966.

Cloos, M. A., Boulant, N., Ferrand, G., Luong, M., Wiggins, C. J., Le Bihan, D., Amadon, A., 2011a. T1-nonlinearity corrections for fast Transmit-Array B1+-mapping of the human brain in the small-tip-angle regime. In: Proc. Intl. Soc. Mag. Reson. Med. Montreal, p. 4409.

Cloos, M. A., Boulant, N., Luong, M., Ferrand, G., Bihan, D. L., Amadon, A., 2010a. Specific absorption rate monitor for in-vivo parallel transmission at 7 Tesla. In: Proc. Intl. Soc. Mag. Reson. Med. Stockholm, p. 3871.

Cloos, M. A., Boulant, N., Luong, M., Ferrand, G., Giacomini, E., Le Bihan, D., Amadon, A., 2012. k(T) - points: Short three-dimensional tailored RF pulses for flip-angle homogenization over an extended volume. Magn. Res. Med. 67 (1), 72–80.

Cloos, M. A., Boulant, N., Luong, M., Ferrand, G., Wiggins, C. J., Giacomini, E., France, A., Bihan, D. L., Amadon, A., 2010b. Kt points: Fast Three-Dimensional Tailored RF Pulses for flip-angle homogenization over an extended volume. In: Proc. Intl. Soc. Mag. Reson. Med. Stockholm, p. 102.

Cloos, M. A., Ferrand, G., Boulant, N., Luong, M., Wiggins, C. J., Le Bihan, D., Amadon, A., 2011b. Dual-channel transmit-SENSE for flip-angle homogenization in the human brain at 7 Tesla: a feasibility study. In: Proc. Intl. Soc. Mag. Reson. Med. Stockholm, p. 325.

Cloos, M. A., Luong, M., Ferrand, G., Amadon, A., Le Bihan, D., Boulant, N., 2010c. Local SAR reduction in parallel excitation based on channel-dependent Tikhonov parameters. J. Magn. Reson. Imaging. 32 (5), 1209–1216.

Collins, C. M., Smith, M. B., 2001. Signal-to-noise ratio and absorbed power as functions of main magnetic field strength, and definition of "90 degrees " RF pulse for the head in the birdcage coil. Magn. Res. Med. 45 (4), 684–691.

Collins, C. M., Zhangwei, W., Smith, M. B., 2007. A Conservative Method for Ensuring Safety Within Transmit Arrays. In: Proc. Intl. Soc. Mag. Reson. Med. Berlin, p. 1092.

Conolly, S., Nishimura, D., Macovski, A., 1986. Optimal control solutions to the magnetic resonance selective excitation problem. IEEE Trans Med Imaging. 5 (2), 106–115.

Cunningham, C. H., Pauly, J. M., Nayak, K. S., 2006. Saturated double-angle method for rapid B1+ mapping. Magn. Res. Med. 55 (6), 1326–1333.

Deichmann, R., Good, C. D., Josephs, O., Ashburner, J., Turner, R., 2000. Optimization of 3D MP-RAGE sequences for structural brain imaging. Neuroimage 12 (1), 112–127.

Dickerson, B. C., Bakkour, A., Salat, D. H., Feczko, E., Pacheco, J., Greve, D. N., Grodstein, F., Wright, C. I., Blacker, D., Rosas, H. D., Sperling, R. A., Atri, A., Growdon, J. H., Hyman, B. T., Morris, J. C., Fischl, B., Buckner, R. L., 2009. The Cortical Signature of Alzheimer's Disease: Regionally Specific Cortical Thinning Relates to Symptom Severity in Very Mild to Mild AD Dementia and is Detectable in Asymptomatic Amyloid-Positive Individuals. Cerebral Cortex 19 (3), 497–510.

Duensing, G., Peterson, D., Wolverton, B., Fitzsimmons, J., 1998. Transcieve Phased Array Design for Imaging at 3.0T. In: Proc. Intl. Soc. Mag. Reson. Med. Sydney.

Eichfelder, G., Gebhardt, M., 2011. Local specific absorption rate control for parallel transmission by virtual observation points. Magn. Res. Med. 66 (5), 1468–1476.

Fautz, H., Vogel, M., Gross, P., Kerr, A., Zhu, Y., 2008. B1 mapping of coil arrays for parallel transmission. In: Proc. Int. Mag. Reson. Med. Torronto, p. 1247.

Feinberg, D., Hoenninger, J., Crooks, L., Kaufman, L., Watts, J., Arakawa, M., 1985a. Inner Volume MR Imaging: Technical Concepts and their Applications. Radiology 156 (3), 743–747.

Feinberg, D., Mills, C., Posin, J., Ortendahl, D., Crooks, L., Watts, J., Kaufman, L., Arakawa, M., Hoenninger, J., Brant-Zawadzki, M., 1985b. Multiple spin-echo magnetic resonance imaging. Radiology 155 (2), 437–442.

Ferrand, G., Luong, M., Amadon, A., Cloos, M. A., Giacomini, E., Darrasse, L., 2012. Generalized double-acquisition imaging for radiofrequency inhomogeneity mitigation in high-field MRI: Experimental proof and performance analysis. Magn. Res. Med. 67 (1), 175–182.

Ferrand, G., Luong, M., Cloos, M. A., France, A., Amadon, A., Boulant, N., Darrasse, L., 2011. SVD-based Hardware Concept to Drive N Transmit Elements of a Phased Array Coil with M<N Channels for Height Field MRI. In: Proc. Intl. Soc. Mag. Reson. Med. Montreal, p. 3888.

Ferrand, G., Luong, M., France, A., 2010. Antenne pour systeme IRM. Patent: EU (1050905).

Fischl, B., Dale, A., 2000. Measuring the thickness of the human cerebral cortex from magnetic resonance images. Proc. Natl. Acad. Sci. USA. 97 (20), 11050–11055.

Friston, K., Ashburner, J., Frith, C., Poline, J., Heather, J., Frackowiak, R. S. J., 1995. Spatial registration and normalization of images. Human brain mapping 3 (3), 165–189.

Fukunaga, K., Watanabe, S., Sato, K., 2005. Dielectric properties of non-toxic tissue-equivalent liquids for radiowave safety tests. In: IEEE Int. Conf. on Dielectric Liquids.

Gabriel, S., Lau, R. W., Gabriel, C., 1996. The dielectric properties of biological tissues: II. Measurements in the frequency range 10 Hz to 20 GHz. Phys. Med. Biol. 41 (11), 2251–2269.

Gagoski, B. A., Gumbrecht, R., Hamm, M., Setsompop, K., Keil, B., Lee, J., Makhoul, K., Mareyam, A., Fujimoto, K., Witzel, T., Fontius, U., Pfeuffer, J., Adalsteinsson, E., Wald, L. L., 2009. Real time RF monitoring in a 7T parallel transmit system. In: Proc. Intl. Soc. Mag. Reson. Med. Stockholm, p. 781.

Graesslin, I., 2008. Parallel Transmission: A Comprehensive RF Safety Concept. In: Proc. PIERS. Boston, pp. 698–700.

Graesslin, I., Biederer, S., Annighoefer, B., Homann, H., Stahl, H., Vernickel, B., Katscher, U., Glaesel, D., Harvey, P., 2009. Real-time global and local SAR monitoring for parallel transmission systems. In: Proc. Intl. Soc. Mag. Reson. Med. Honolulu, p. 302.

Graesslin, I., Schweser, F., Annighoefer, B., Biederer, S., Katscher, U., Nehrke, K., Stahl, H., Dingemans, H., Mens, G., Brnert, P., 2008. A minimum SAR RF pulse design approach for parallel Tx with local hot spot suppression and exact fidelity constraint. In: Proc. Intl. Soc. Mag. Reson. Med. Toronto, p. 621.

Griffiths, D. J., 1994. Introduction to Quantum Mechanics, 3rd Edition. Prentice Hall.

Grinvald, A., Slovin, H., Vanzetta, I., 2000. Non-invasive visualization of cortical columns by fMRI. Nat. Neurosci. 3 (2), 105–107.

Grissom, W., Yip, C.-y., Zhang, Z., Stenger, V. A., Fessler, J. A., Noll, D. C., 2006. Spatial domain method for the design of RF pulses in multicoil parallel excitation. Magn. Res. Med. 56 (3), 620–629.

Grissom, W. A., Pauly, J., 2010. Joint Design of Dual-Band Large-Tip-Angle RF and Gradient Waveforms in Parallel Excitation. In: Proc. Inl. Soc. Mag. Reson. Med. Stockholm, p. 99.

Grissom, W. A., Xu, D., Kerr, A. B., Fessler, J. A., Noll, D. C., 2009. Fast large-tip-angle multidimensional and parallel RF pulse design in MRI. IEEE Trans. Med. Imaging. 28 (10), 1548–1559.

Grissom, W. A., Yip, C.-y., Wright, S. M., Fessler, J. A., Noll, D. C., 2008. Additive angle method for fast large-tip-angle RF pulse design in parallel excitation. Magn. Res. Med. 59 (4), 779–787.

Griswold, M. A., Jakob, P. M., Heidemann, R. M., Nittka, M., Jellus, V., Wang, J., Kiefer, B., Haase, A., 2002. Generalized autocalibrating partially parallel acquisitions (GRAPPA). Magn. Res. Med. 47 (6), 1202–1210.

Gur, R., Mozley, P., Resnick, S., Gottlieb, G., Kohn, M., Zimmerman, R., Herman, G., Atlas, S., Grossman, R., Berretta, D., 1991. Gender differences in age effect on brain atrophy measured by magnetic resonance imaging. Proc. Natl. Acad. Sci. USA. 88 (7), 2845.

Haacke, E. M., Brown, R. W., Thompson, M. R., Venkatesan, R., Jun. 1999. Magnetic Resonance Imaging: Physical Principles and Sequence Design, 1st Edition. Wiley-Liss.

Haase, A., Frahm, J., Matthaei, D., Hanicke, W., Merboldt, K., 1986. FLASH imaging. Rapid NMR imaging using low flip-angle pulses. J. Magn. Reson. 67 (2), 258–266.

Hahn, E., 1950a. Nuclear induction due to free Larmor precession. Phys. Rev. 77 (2), 297–298.

Hahn, E., 1950b. Spin echoes. Phys. Rev. 80 (4), 58.

Han, X., Jovicich, J., Salat, D., van der Kouwe, A., Quinn, B., Czanner, S., Busa, E., Pacheco, J., Albert, M., Killiany, R., Maguire, P., Rosas, D., Makris, N., Dale, A., Dickerson, B., Fischl, B., 2006. Reliability of MRI-derived measurements of human cerebral cortical thickness: the effects of field strength, scanner upgrade and manufacturer. NeuroImage 32 (1), 180–194.

Hansen, P. C., 1992. Analysis of Discrete Ill-Posed Problems by Means of the L-Curve. SIAM Rev. 34 (4), 561–580.

Hornak, J. P., Szumowski, J., Bryant, R. G., 1988. Magnetic field mapping. Magn. Res. Med. 6 (2), 158–163.

Hoult, D., 2000a. Sensitivity and Power Deposition in a High-Field Imaging Experiment. J. Magn. Reson. Imaging. 12 (1), 46–67.

Hoult, D., 2000b. The principle of reciprocity in signal strength calculations: a mathematical guide. Concept Magnetic Res. 12 (4), 173–187.

Hoult, D., Bhakar, B., 1997. NMR signal reception: virtual photons and coherent spontaneous emission. Concept Magnetic Res. 9 (5), 277–297.

Hoult, D., Lauterbur, P.C., 1979. The sensitivity of the zeugmatographic experiment involving human samples. J. Magn. Reson. 34 (2), 425–433.

Hoult, D. I., Kolansky, G., Kripiakevich, D., King, S. B., 2004. The NMR multi-transmit phased array: a Cartesian feedback approach. J. Magn. Reson. 171 (1), 64–70.

Ibrahim, T. S., Abduljalil, A. M., Baertlein, B. A., Lee, R., Robitaill, P. M., 2001a. Analysis of B1 field profiles and SAR values for multi-strut transverse electromagnetic RF coils in high field MRI applications. Phys. Med. Biol. 46 (10), 2545–2555.

Ibrahim, T. S., Lee, R., Abduljalil, A. M., Baertlein, B. A., Robitaille, P.-M.-L., 2001b. Dielectric resonances and B(1) field inhomogeneity in UHFMRI: computational analysis and experimental findings. Magn. Reson. Imaging. 19 (2), 219–226.

IEC, Dec. 2002. International Electrotechnical Commission. International standard, medical electrical equipment. Part 2. Particular requirements for the safety of magnetic resonance equipment for medical diagnosis, 2nd ed. . Geneva: International Electrotechnical Commission.

IEC, Mar. 2010. International Electrotechnical Commission. International standard, medical electrical equipment. Part 2. Particular requirements for the safety of magnetic resonance equipment for medical diagnosis, 3nd ed. . Geneva: International Electrotechnical Commission.

Jankiewicz, M., Zeng, H., Moore, J. E., Anderson, A. W., Avison, M. J., Welch, E. B., Gore, J. C., 2010. Practical considerations for the design of sparse-spokes pulses. J. Magn. Reson. 203 (2), 294–304.

Jaynes, E., 1955. Matrix treatment of nuclear induction. Phys. Rev. 98 (4), 1099–1105.

Jin, J., Sep. 1998. Electromagnetic Analysis and Design in Magnetic Resonance Imaging (Biomedical Engineering), 1st Edition. CRC Press.

Kassakian, P., 2006. Convex Approximation and Optimization with Applications in Magnitude Filter Design and Radiation Pattern Synthesis. Ph.D. thesis, University of California at Berkeley.

Katscher, U., Boernert, P., Leussler, C., 2003. Transmit sense. Magn. Res. Med. 49 (1), 144–150.

Katscher, U., Lisinski, J., Börnert, P., 2010. RF encoding using a multielement parallel transmit system. Magn. Res. Med. 63 (6), 1463–1470.

Katscher, U., Röhrs, J., Bornert, P., 2005. Basic considerations on the impact of the coil array on the performance of Transmit SENSE. Magma 18 (2), 81–88.

Katscher, U., Vernickel, P., Graesslin, I., Boernert, P., 2007. RF Shimming Using a Multi-Element Transmit System in Phantom and In Vivo Studies. In: Proc. Intl. Soc. Mag. Reson. Med. Berlin, p. 1693.

Katscher, U., Voigt, T., Findeklee, C., Nehrke, K., Weiss, S., Doessel, O., 2008. Estimation of local SAR using B1 mapping. In: Proc. Intl. Soc. Mag. Reson. Med. Toronto, p. 1191.

Kerr, A. B., Zhu, Y., Pauly, J. M., 2007. Phase Constraint Relaxation in Parallel Excitation Pulse Design. In: Proc. Inl. Soc. Mag. Reson. Med. Berlin, p. 1694.

Kini, L., Wald, L. L., Adalsteinsson, E., 2009. Fast E1, B1 and SAR simulation with the use of graphics processors. In: Proc. Intl. Soc. Mag. Reson. Med. Honolulu, p. 4776.

Kirk, G. R., Haynes, M. R., Palasis, S., Brown, C., Burns, T. G., McCormick, M., Jones, R. A., 2009. Regionally Specific Cortical Thinning in Children with Sickle Cell Disease. Cerebral Cortex 19 (7), 1549–1556.

Kozlov, M., Turner, R., 2009. Fast MRI coil analysis based on 3-D electromagnetic and RF circuit co-simulation. J. Magn. Reson. 200 (1), 147–152.

Kozlov, M., Turner, R., 2011. Analysis of RF Transmit Performance for a 7T Dual Row Multi-Channel MRI Loop Array. In: Conf Proc IEEE Eng Med Biol Soc. Boston, pp. 547–53.

Kumar, A., Welti, D., Ernst, R., 1975. NMR Fourier zeugmatography. J. Magn. Reson. 18 (1), 69–83.

Kuroda, K., Oshio, K., Chung, A. H., Hynynen, K., Jolesz, F. A., 1997. Temperature mapping using the water proton chemical shift: a chemical shift selective phase mapping method. Magn. Res. Med. 38 (5), 845–851.

Lattanzi, R., Sodickson, D. K., Grant, A. K., Zhu, Y., 2009. Electrodynamic constraints on homogeneity and radiofrequency power deposition in multiple coil excitations. Magn. Res. Med. 61 (2), 315–334.

Lauterbur, P.C., 1973. Image formation by induced local interactions: examples employing nuclear magnetic resonance. Nature 242 (5394), 190–191.

Lauterbur, P.C., 1974. Magnetic resonance zeugmatography. Pure Appl. Chem 40 (1-2), 149–157.

Lee, D., Lustig, M., Grissom, W. A., Pauly, J. M., 2009. Time-optimal design for multidimensional and parallel transmit variable-rate selective excitation. Magn. Res. Med. 61 (6), 1471–1479.

Lee, J., Gebhardt, M., Wald, L. L., Adalsteinsson, E., 2010. Parallel Transmit RF Design with Local SAR Constraints. In: Proc. Intl. Soc. Mag. Reson. Med. Stockholm, p. 105.

Liu, Y., Feng, K., McDougall, M. P., Wright, S. M., Ji, J., 2008. Reducing SAR in parallel excitation using variable-density spirals: a simulation-based study. Magn. Res. Med. 26 (8), 1122–1132.

Ma, C., Xu, D., King, K. F., Liang, Z.-P., 2010. Joint Design of Spoke Trajectories and RF Pulses for Parallel Excitation. Magn. Res. Med. 65 (4), 973–985.

Maier, S., Hardy, C., Jolesz, F. A., 1994. Brain and cerebrospinal fluid motion: real-time quantification with M-mode MR imaging. Radiology 193 (2), 477–483.

Makris, N., Angelone, L. M., Tulloch, S., Sorg, S., Kaiser, J., Kennedy, D., Bonmassar, G., 2008. MRI-based anatomical model of the human head for specific absorption rate mapping. Med. Biol. Eng. Comput. 46 (12), 1239–1251.

Malik, S. J., Keihaninejad, S., Hammers, A., Hajnal, J. V., 2012. Tailored excitation in 3d with spiral nonselective (spins) rf pulses. Magn. Res. Med. 67, 1303–15.

Mansfield, P., 1977. Multi-planar image formation using NMR spin echoes. J. Phys. C: Solid State Phys. 10, L55.

Mansfield, P., Maudsley, A., 1976. Planar spin imaging by NMR. J. Phys. C: Solid State Phys. 9, L409.

Mao, W., Smith, M. B., Collins, C. M., 2006. Exploring the limits of RF shimming for high-field MRI of the human head. Magn. Res. Med. 56 (4), 918–922.

Mao, W., WANG, Z., Smith, M., 2007. Calculation of SAR for transmit coil arrays. Concept Magn. Reson. B. 31 (2), 127–131.

Marques, J. P., Kober, T., Krueger, G., van der Zwaag, W., van de Moortele, P.-F., Gruetter, R., 2010. MP2RAGE, a self bias-field corrected sequence for improved segmentation and T1-mapping at high field. NeuroImage 49 (2), 1271–1281.

Massire, A., Cloos, M. A., Luong, M., Amadon, A., Vignaud, A., Wiggins, C. J., Feb. 2012. Thermal simulations in the human head for high field MRI using parallel transmission. J. Magn. Reson. Imaging., in press.

Matson, G., Liu, H., 2010. Computer Simulations of 3D MPRAGE in Human Brain with Inclusion of Inadvertent Magnetization Transfer Effects. In: Proc. Intl. Soc. Mag. Reson. Med. Stockholm, p. 3008.

Meiboom, S., Gill, D., 1958. Modified Spin-Echo Method for Measuring Nuclear Relaxation Times. Rev. Sci. Instrum. 29 (8), 688–691.

Metzger, G. J., Snyder, C., Akgun, C., Vaughan, T., Ugurbil, K., van de Moortele, P.-F., 2008. Local B1+ shimming for prostate imaging with transceiver arrays at 7T based on subject-dependent transmit phase measurements. Magn. Res. Med. 59 (2), 396–409.

Meyer, J., Roychowdhury, S., 1996. Location of the central sulcus via cortical thickness of the precentral and postcentral gyri on MR. AJNR Am. J. Neuroradiol. 17 (9), 1699–1706.

Minkoff, L., Damadian, R., Thomas, T. E., Hu, N., Goldsmith, M., Koutcher, J., Stanford, M., 1977. NMR in cancer: XVII. dewar for a 53-inch superconducting NMR magnet. Physiol. Chem. Phys. 9 (1), 101–104.

Mugler, J., Brookeman, J., 1990. Three-dimensional magnetization-prepared rapid gradient-echo imaging (3D MP RAGE). Magn. Res. Med. 15 (1), 152–157.

Mugler, J. P., Bao, S., Mulkern, R. V., Guttmann, C. R., Robertson, R. L., Jolesz, F. A., Brookeman, J. R., 2000. Optimized single-slab three-dimensional spin-echo MR imaging of the brain. Radiology 216 (3), 891–899.

Nehrke, K., 2009. On the steady-state properties of actual flip angle imaging (AFI). Magn. Res. Med. 61 (1), 84–92.

Nehrke, K., Bornert, P., 2010. Eigenmode analysis of transmit coil array for tailored b1 mapping. Magn. Reson. Med. 63 (3), 754–764.

Nelder, J., Mead, R., 1965. A simplex method for function minimization. Comput. J. 7 (4), 308–313.

Nowakowski, R. S., 2006. Stable neuron numbers from cradle to grave. Proc. Natl. Acad. Sci. USA. 103 (33), 12219–12220.

Ocali, O., Atalar, E., 1998. Ultimate intrinsic signal-to-noise ratio in MRI. Magn. Res. Med. 39 (3), 462–473.

Ohanian, H., 1986. What is spin? Am. J. Phys. 54 (6), 500–505.

Ohliger, M. A., Sodickson, D. K., 2006. An introduction to coil array design for parallel MRI. NMR Biomed. 19 (3), 300–315.

Oppelt, A., 1986. FISP-a new fast MRI sequence. Electromedica 54 (1), 15–18.

Pauly, J., Le Roux, P., Nishimura, D., Macovski, A., 1991. Parameter relations for the Shinnar-Le Roux selective excitation pulse design algorithm [NMR imaging]. IEEE Trans. Med. Imaging. 10 (1), 53–65.

Pauly, J., Nishimura, D., Macovski, A., 1989. A linear class of large-tip-angle selective excitation pulses. J. Magn. Reson. 82 (3), 571–587.

Pauly, J. M., Nishimura, D., 1989. A k-space analysis of small-tip-angle excitation. J. Magn. Reson. 81 (1), 43–56.

Pohmann, R., 2011. An experimental comparison of B1-mapping Techniques at two field strengths. In: Proc. Inl. Soc. Mag. Reson. Med. Montreal, p. 4410.

Pruessmann, K., Weiger, M., Scheidegger, M., 1999. SENSE: sensitivity encoding for fast MRI. Magn. Res. Med. 42 (5), 952–962.

Robitaille, P.-M., Berliner, L., 2006. Ultra High Field Magnetic Resonance Imaging (Biological Magnetic Resonance). Springer.

Roemer, P., Edelstein, W., Hayes, C., 1990. The NMR phased array. Magn. Res. Med. 16 (2), 192–225.

Rooney, W. D., Johnson, G., Li, X., Cohen, E. R., Kim, S.-G., Ugurbil, K., Springer, C. S., 2007. Magnetic field and tissue dependencies of human brain longitudinal 1H2O relaxation in vivo. Magn. Res. Med. 57 (2), 308–318.

Röschmann, P., 1987. Radiofrequency penetration and absorption in the human body: limitations to high-field whole-body nuclear magnetic resonance imaging. Med. Phys. 14 (6), 922–931.

Saekho, S., Boada, F. E., Noll, D. C., Stenger, V. A., 2005. Small tip angle three-dimensional tailored radiofrequency slab-select pulse for reduced B1 inhomogeneity at 3 T. Magn. Res. Med. 53 (2), 479–484.

Saekho, S., Yip, C.-y., Noll, D. C., Boada, F. E., Stenger, V. A., 2006. Fast-kz three-dimensional tailored radiofrequency pulse for reduced B1 inhomogeneity. Magn. Res. Med. 55 (4), 719–724.

Sbrizzi, A., Hoogduin, H., Lagendijk, J. J., Luijten, P., Sleijpen, G. L. G., van den Berg, C. A. T., 2012. Fast design of local n-gram-specific absorption rate–optimized radiofrequency pulses for parallel transmit systems. Magn. Res. Med. 67, 824–834.

Schneider, J. T., Kalayciyan, R., Haas, M., Ruhm, W., Doessel, O., Hennig, J., Ullmann, P., 2010. Inner-Volume-Imaging Using Three-Dimensional Parallel Excitation. In: Proc. Inl. Soc. Mag. Reson. Med. Stockholm, p. 103.

Schroeder, D. V., Aug. 1999. An Introduction to Thermal Physics, 1st Edition. Addison Wesley.

Sersa, I., Macura, S., 1998. Excitation of complicated shapes in three dimensions. J. Magn. Reson. 135 (2), 466–477.

Setsompop, K., Alagappan, V., Gagoski, B., Witzel, T., Polimeni, J., Potthast, A., Hebrank, F., Fontius, U., Schmitt, F., Wald, L. L., Adalsteinsson, E., 2008a. Slice-selective RF pulses for in vivo B1+ inhomogeneity mitigation at 7 tesla using parallel RF excitation with a 16-element coil. Magn. Res. Med. 60 (6), 1422–1432.

Setsompop, K., Alagappan, V., GAGOSKI, B. A., Potthast, A., Hebrank, F., Fontius, U., Schmitt, F., Wald, L. L., Adalsteinsson, E., 2009. Broadband slab selection with B1+ mitigation at 7T via parallel spectral-spatial excitation. Magn. Res. Med. 61 (2), 493–500.

Setsompop, K., Alagappan, V., Zelinski, A. C., Potthast, A., Fontius, U., Hebrank, F., Schmitt, F., Wald, L. L., Adalsteinsson, E., 2008b. High-flip-angle slice-selective parallel RF transmission with 8 channels at 7 T. J. Magn. Reson. 195 (1), 76–84.

Setsompop, K., Wald, L. L., Alagappan, V., Gagoski, B., Hebrank, F., Fontius, U., Schmitt, F., Adalsteinsson, E., 2006. Parallel RF transmission with eight channels at 3 Tesla. Magn. Res. Med. 56 (5), 1163–1171.

Setsompop, K., Wald, L. L., Alagappan, V., Gagoski, B. A., Adalsteinsson, E., 2008c. Magnitude least squares optimization for parallel radio frequency excitation design demonstrated at 7 Tesla with eight channels. Magn. Res. Med. 59 (4), 908–915.

Silbert, L., Quinn, J., Moore, M., Corbridge, E., Ball, M., Murdoch, G., Sexton, G., Kaye, J., 2003. Changes in premorbid brain volume predict Alzheimer's disease pathology. Neurology 61 (4), 487–492.

Silver, M., Joseph, R., Hoult, D., 1985. Selective spin inversion in nuclear magnetic resonance and coherent optics through an exact solution of the Bloch-Riccati equation. Phys. Rev. A. 31 (4), 2753–2755.

Smith, S. M., 2002. Fast robust automated brain extraction. Hum. Brain. Mapp. 17 (3), 143–155.

Sodickson, D. K., Manning, W. J., 1997. Simultaneous acquisition of spatial harmonics (SMASH): fast imaging with radiofrequency coil arrays. Magn. Res. Med. 38 (4), 591–603.

Staewen, R. S., Johnson, A. J., Ross, B. D., Parrish, T., Merkle, H., Garwood, M., 1990. 3-D FLASH imaging using a single surface coil and a new adiabatic pulse, BIR-4. Invest. Radiol. 25 (5), 559–567.

Stollberger, R., Wach, P., 1996. Imaging of the active B1-field in vivo. Magn. Res. Med. 35 (2), 246–251.

Strumwasser, F., 1958. Long-term recording' from single neurons in brain of unrestrained mammals. Science 127 (3296), 469–470.

Styner, M., Brechbühler, C., Székely, G., Gerig, G., 2000. Parametric estimate of intensity inhomogeneities applied to MRI. IEEE Trans. Med. Imaging. 19 (3), 153–165.

Thieben, M. J., Duggins, A. J., Good, C. D., Gomes, L., Mahant, N., Richards, F., McCusker, E., Frackowiak, R. S. J., 2002. The distribution of structural neuropathology in pre-clinical Huntington's disease. Brain 125 (8), 1815–1828.

Triantafyllou, C., Hoge, R. D., Krueger, G., Wiggins, C. J., Potthast, A., Wiggins, G. C., Wald, L. L., 2005. Comparison of physiological noise at 1.5 T, 3 T and 7 T and optimization of fMRI acquisition parameters. NeuroImage 26 (1), 243–250.

Ullmann, P., Junge, S., Wick, M., Seifert, F., Ruhm, W., Hennig, J., 2005. Experimental analysis of parallel excitation using dedicated coil setups and simultaneous RF transmission on multiple channels. Magn. Res. Med. 54 (4), 994–1001.

Vahedipour, K., Stocker, T., Brenner, D., Shah, N., 2010. Parallel excitation of a 3D ROI inside a post mortem brain. In: Proc. Intl. Soc. Mag. Reson. Med. Stockholm, p. 4917.

Van de Moortele, P.-F., Akgun, C., Adriany, G., Moeller, S., Ritter, J., Collins, C. M., Smith, M. B., Vaughan, J. T., Ugurbil, K., 2005. B(1) destructive interferences and spatial phase patterns at 7 T with a head transceiver array coil. Magn. Res. Med. 54 (6), 1503–1518.

Van de Moortele, P.-F., Auerbach, E. J., Olman, C., Yacoub, E., Ugurbil, K., Moeller, S., 2009. T1 weighted brain images at 7 Tesla unbiased for Proton Density, T2* contrast and RF coil receive B1 sensitivity with simultaneous vessel visualization. NeuroImage 46 (2), 432–446.

Van De Moortele, P.-F., Snyder, C., Delabarre, L., Gregor, A., Vaughan, T., Ugurbil, K., 2007. Calibration Tools for RF Shim at Very High Field with Multiple Element RF Coils: From Ultra Fast Local Relative Phase to Absolute Magnitude B1+ Mapping. In: Proc. Inl. Soc. Mag. Reson. Med. Berlin, p. 1676.

Van der Kouwe, A., Benner, T., Salat, D., 2008. Brain morphometry with multiecho MPRAGE. NeuroImage 40 (2), 559–569.

Vaughan, J. T., Hetherington, H., Otu, J., Pan, J., Pohost, G., 1994. High frequency volume coils for clinical NMR imaging and spectroscopy. Magn. Res. Med. 32 (2), 206–218.

Vogel, M., Kleihorst, R., 2007. Large-scale simulations including a human-body model for MRI. In: IEEE Int. Microwave Symp. Honolulu, pp. 1345–1348.

Voigt, T., Doessel, O., Katscher, U., 2009. Imaging conductivity and local SAR of the human brain. In: Proc. Intl. Soc. Mag. Reson. Med. Honolulu, p. 4513.

Von Economo, C., Koskinas, G., 1927. Die Cytoarchitektonik der Hirnrinde des erwachsenen Menschen. Springer, Berlin.

Wald, L. L., Carvajal, L., Moyher, S. E., Nelson, S. J., Grant, P. E., Barkovich, A. J., Vigneron, D. B., 1995. Phased array detectors and an automated intensity-correction algorithm for high-resolution MR imaging of the human brain. Magn. Res. Med. 34 (3), 433–439.

Wang, J., Qiu, M., Yang, Q. X., Smith, M. B., Constable, R. T., 2005. Measurement and correction of transmitter and receiver induced nonuniformities in vivo. Magn. Res. Med. 53 (2), 408–417.

Wangsness, R., Bloch, F., 1953. The dynamical theory of nuclear induction. Phys. Rev. 89 (4), 728–739.

Weiger, M., Pruessmann, K. P., Österbauer, R., Bornert, P., Boesiger, P., Jezzard, P., 2002. Sensitivity-encoded single-shot spiral imaging for reduced susceptibility artifacts in BOLD fMRI. Magn. Res. Med. 48 (5), 860–866.

Wiggins, C. J., Caillat, M., Bihan, D. L., Schmitt, F., Eberlein, E., 2010. Use of Opposed Shim Currents for Infold Reduction on a UHF MRI System with Head Gradient. In: Proc. Inl. Soc. Mag. Reson. Med. Stockholm, p. 2339.

Wiggins, G. C., Triantafyllou, C., Potthast, A., Reykowski, A., Nittka, M., Wald, L. L., 2006. 32-channel 3 Tesla receive-only phased-array head coil with soccer-ball element geometry. Magn. Res. Med. 56 (1), 216–223.

Xu, D., King, K., Zhu, Y., McKinnon, G. C., Liang, Z.-P., 2008. Designing multichannel, multidimensional, arbitrary flip angle RF pulses using an optimal control approach. Magn. Res. Med. 59 (3), 547–560.

Xu, D., King, K. F., Zhu, Y., McKinnon, G. C., Liang, Z.-P., 2007. A noniterative method to design large-tip-angle multidimensional spatially-selective radio frequency pulses for parallel transmission. Magn. Res. Med. 58 (2), 326–334.

Yacoub, E., Harel, N., Ugurbil, K., 2008. High-field fMRI unveils orientation columns in humans. Proc. Natl. Acad. Sci. USA. 105 (30), 10607–10612.

Yang, Q. X., Mao, W., Wang, J., Smith, M. B., Lei, H., Zhang, X., Ugurbil, K., Chen, W., 2006. Manipulation of image intensity distribution at 7.0 T: passive RF shimming and focusing with dielectric materials. J. Magn. Reson. Imaging. 24 (1), 197–202.

Yang, Q. X., Wang, J., Collins, C. M., Smith, M. B., Zhang, X., Ugurbil, K., Chen, W., 2004. Phantom design method for high-field MRI human systems. Magn. Res. Med. 52 (5), 1016–1020.

Yang, Q. X., Wang, J., Zhang, X., Collins, C. M., Smith, M. B., Liu, H., Zhu, X.-H., Vaughan, J. T., Ugurbil, K., Chen, W., 2002. Analysis of wave behavior in lossy dielectric samples at high field. Magn. Res. Med. 47 (5), 982–989.

Yarnykh, V. L., 2007. Actual flip-angle imaging in the pulsed steady state: a method for rapid three-dimensional mapping of the transmitted radiofrequency field. Magn. Res. Med. 57 (1), 192–200.

Yip, C., Fessler, J. A., Noll, D. C., 2005. Iterative RF pulse design for multidimensional, small-tip-angle selective excitation. Magn. Res. Med. 54 (4), 908–917.

Yip, C., Fessler, J. A., Noll, D. C., 2006. Advanced three-dimensional tailored RF pulse for signal recovery in T2*-weighted functional magnetic resonance imaging. Magn. Res. Med. 56 (5), 1050–1059.

Zanchi, M. G., Stang, P., Kerr, A., Pauly, J. M., Scott, G. C., 2011. Frequency-offset Cartesian feedback for MRI power amplifier linearization. IEEE Trans. Med. Imaging. 30 (2), 512–522.

Zelinski, A., Alagappan, V., Goyal, V., Adalsteinsson, E., Wald, L., 2008a. Sparsity-Enforced Coil Array Mode Compression for Parallel Transmission. In: Proc. Intl. Soc. Mag. Reson. Med. Toronto, p. 1302.

Zelinski, A., Goyal, V. K., Angelone, L., Bonmassar, G., Wald, L., Adalsteinsson, E., 2007. Designing RF Pulses with Optimal Specific Absorption Rate (SAR) Characteristics and Exploring Excitation Fidelity, SAR and Pulse Duration Tradeoffs. In: Proc. Intl. Soc. Mag. Reson. Med. Berlin, p. 1699.

Zelinski, A. C., Angelone, L. M., GOYAL, V. K., Bonmassar, G., Adalsteinsson, E., Wald, L. L., 2008b. Specific absorption rate studies of the parallel transmission of inner-volume excitations at 7T. J. Magn. Reson. Imaging. 28 (4), 1005–1018.

Zelinski, A. C., Wald, L. L., Setsompop, K., Alagappan, V., GAGOSKI, B. A., GOYAL, V. K., Adalsteinsson, E., 2008c. Fast slice-selective radio-frequency excitation pulses for mitigating B+1 inhomogeneity in the human brain at 7 Tesla. Magn. Res. Med. 59 (6), 1355–1364.

Zelinski, A. C., Wald, L. L., Setsompop, K., GOYAL, V. K., Adalsteinsson, E., 2008d. Sparsity-enforced slice-selective MRI RF excitation pulse design. IEEE Trans. Med. Imaging. 27 (9), 1213–1229.

Zhu, Y., 2004. Parallel excitation with an array of transmit coils. Magn. Res. Med. 51 (4), 775–784.

Zumdahl, S. S., Zumdahl, S. A., 1999. Chemistry), 5th Edition. Brooks Cole.

Nomenclature

ADC	analog-to-digital converter
AFI	actual flip-angle imaging sequence
B0	static magnetic field
B1+	transmit sensitivity
B1-	receive sensitivity
BOLD	blood oxygen level dependent effect
BW	bandwidth
cGM	cortical gray matter
CNR	contrast-to-noise ratio
CP	circularly polarized
CSF	cerebrospinal fluid
CT	Computed Tomography
dTx	2-channel setup where an 8-element coil is driven with two optimized linear combinations in parallel
EMF	electromotive force
FA	flip-angle
FEM	finite element methods
FID	free induction decay
FLASH	fast low angle shot (sequence)
fMRI	functional magnetic resonance imaging
GM	gray matter
GRAPPA	generalized autocalibrating partial parallel acquisition
GRE	gradient recalled echo (sequence)
IET	inter echo time
IRFU	institute de recherche sur les fondamentales de l' univers
kT-points	k-space transmission points: non-selective excitations based on a series of arbitrarily shaped RF-waveforms interleaved with gradient blips to transverse a sparse set of k-space locations.:
LTA	large-tip-angle
MOCA	magnetude optimal control approach
MP-RAGE	magnetization-prepared rapid gradient echo (sequence)
MR	magnetic resonance
MRI	magnetic resonance imaging

mTx	4-channel setup where an 8-element coil is driven using the four most efficient circularly polarized modes.
NMR	nuclear magnetic resonance
NRMSE	normalized root mean square error
NRMSIE	normalized root mean square inversion error
OCA	optimal control approach
PET	Positron Emission Tomography
pTx	In chapter 9: parallel transmission with an 8-channel setup where every coil-element is driven independently
pTx	parallel transmission
RF	radio frequency
SAR	specific absorption rate
SE	spin echo (sequence)
SENSE	sensitivity encoding
SMASH	simultaneous acquisition of spatial harmonics
SNR	signal-to-noise ratio
SPACE	sampling perfection with application optimized contrasts using different flip angle evolution (sequence)
Spokes	slice-selective excitation based on a series of frequency-selective pulses played at a select set of locations in k-space 2D k-space while densely sampling a 3rd dimension
STA	small-tip-angle
sTx	1-channel setup where an 8-element coil is sequentially driven with two optimized linear combination.
sWM	subcortical white matter
TE	time of echo
TI	inversion time
TR	time of repetition
UHF	ultra high field (3-Tesla and up)
WM	white matter